Karlsruher Institut für Technologie

Growth, microstructure and properties characterization of multiferroic heterostructures

Zur Erlangung des akademischen Grades eines
DOKTORS DER INGENIEURWISSENSCHAFTEN
(Dr.-Ing)

von der KIT-Fakultät für Machinenbau des
Karlsruher Instituts für Technologie (KIT)
angenommene

DISSERTATION
von

M.Sc. Berkin Nergis

Tag der mündlichen Prüfung: 19.12.2024

Referent: Prof. Dr. rer. nat. Sven Ulrich
Korreferentin: Prof. Dr. rer. nat. Astrid Pundt
Korreferent: Prof. Dr. Tilo Baumbach

Declaration

I hereby declare that I have written this PhD thesis independently and have used only the sources and aids cited. In every instance, I have clearly identified the sources of any passages that have been quoted or paraphrased from other works. This work was conducted in accordance with the rules of good scientific practice of the German Research Foundation. Furthermore, I have neither applied for a doctoral degree in the past, nor am I currently applying for one elsewhere. An academic degree has not been revoked from me.

Karlsruhe, 22.10.2024 Berkin Nergis

Kurzfassung

Diese Dissertation beinhaltet eine detaillierte Studie zur Optimierung des Wachstums von dünnen Schichten und Schichtsystemen mit dem Ziel, Heterostrukturen zu entwickeln, die bei Raumtemperatur multiferroische (MF) Eigenschaften aufweisen. Die Schichtsysteme bestehen aus einer Bodenelektrode, einer ferromagnetischen (FM) und einer ferroelektrischen (FE) Schicht und wurden mittels gepulster Laserabscheidung (PLD) hergestellt. Die vielfältigen Untersuchungen zielen darauf ab, die Zusammenhänge zwischen geeigneten PLD-Wachstumsparametern, charakteristischen strukturellen Merkmalen und den funktionellen Eigenschaften von Heterostrukturen zu verstehen, die für die magnetoelektrische Kopplung in multiferroischen Systemen relevant sind. Die Dissertation ist deshalb in verschiedene Kapitel untergliedert, die jeweils die Eigenschaften der verschiedenartigen Materialschichten und deren Optimierung behandelt, die für das Design der magnetoelektrischen Heterostruktur relevant sind.

Der erste Optimierungsschritt beinhaltet das Verständnis der morphologischen und strukturellen Eigenschaften von mittels PLD hergestellten Platinfilmen bei unterschiedlichen Wachstumstemperaturen und Schichtdicken, die auf Yttriumoxid-stabilisierten, (111)-orientierten Zirkoniumoxid (YSZ) Substraten deponiert wurden. Die ermittelten optimalen PLD-Wachstumsparameter, d.h. optimale Schichtdicke und eine erhöhte Wachstumstemperatur, wurden bei den nachfolgenden Schichtabscheidungen beibehalten. Unter diesen Bedingungen reduziert sich die Defektdichte erheblich, verbessert die Robustheit gegen Entnetzung und minimiert strukturelle Änderungen durch nachfolgende Hochtemperatur-Bearbeitungsschritte.

Der zweite Optimierungsschritt ist die Deposition einer ferromagnetischen Schicht Bariumhexaferrit, $BaFe_{12}O_{19}$ (BaM), mit dem Ziel, geeignete PLD-Wachstumsbedingungen für die besten magnetischen Eigenschaften in Hinblick auf potenzielle multiferroische Anwendungen zu ermitteln. Diese Optimierung fand in zwei Schritten statt: (1) Es wurden Experimente mit verschiedenen Dicken der Pt Bodenelektrode durchgeführt, um die optimale Schichtdicke der Pt Bodenelektrode für BaM Wachstum zu bestimmen. (2) Nachfolgend wurde die Energiedichte des Lasers von 1.5 J/cm^2 bis 5.1 J/cm^2 während des BaM Wachstums auf der optimierten Pt Bodenelektrode variiert. Zuerst wurde gezeigt, dass eine Platin-Zwischenschicht die c-Achsen-Orientierung, das Anisotropiefeld und die Koerzitivkraft der BaM-Schichten erheblich verbessert. Sie verhindert auch eine chemische Vermischung von BaM mit dem YSZ(111)-Substrat. Darüber hinaus wurde festgestellt, dass eine Erhöhung der Platindicke die strukturelle Kontinuität der BaM-Schichten verbessert, da der Oberflächenfüllfaktor von Platin erhöht wird. Im nächsten Schritt wurden die Wachstumskinetik und die magnetischen Eigenschaften durch Anpassung der Energiedichte des Lasers während der Abscheidung verändert. Geringere Fluenzwerte führen zu glatteren Oberflächen und einer geringeren Defektkonzentration., was darauf hindeutet, dass sie sich besser für eine mehrschichtige Gerätearchitektur eignen, während höhere Fluenzwerte tendenziell zu Ba-reduzierten, nicht-stöchiometrischen Phasen führen.

Im dritten Optimierungsschritt wurde hexagonales Ytterbiumferrit *h*-$YbFeO_3$ (YbFO) optimiert, das mittels gepulster Laserabscheidung auf YSZ(111) abgeschieden wurde. YbFO ist ein vielversprechender Kandidat für ein multiferroisches Material, das Ferroelektrizität und Antiferromagnetismus (AF) vereint, mit potenziellen Anwendungen bei niedrigen Temperaturen. Es wurde eine detaillierte Analyse der Mikrostruktur und der temperaturabhängigen magnetischen Eigenschaften durchgeführt, wobei direkt auf YSZ(111) gewachsene YbFO Schichten mit auf Platin-Pufferschichten abgeschiedenen Schichten verglichen wurden. Die Dicke der Platin-Zwischenschicht wurde variiert, wie schon im ersten Optimierungsschritt beschrieben. Ziel ist es, ein umfassendes Verständnis für den Einfluss der Kristallqualität und Morphologie der Pt-Pufferschicht auf die Mikrostruktur, Morphologie und daraus resultierenden physikalischen Eigenschaften der YbFO-Schicht zu erlangen. Die Ergebnisse deuten darauf hin, dass die Homogenität, Kontinuität und Hügelbildung der Pt-Pufferschicht die YbFO-Mikrostruktur, Mosaizität, Korngrenzen und Defektverteilung beeinflussen. Die Resultate der hochauflösenden Transmissionsmikroskopie (HRTEM) und der Röntgenbeugung (XRD) zeigen, dass eine Pt-Zwischenschicht die Kristallqualität der YbFO Schicht verbessert, insbesondere nach Optimierung der Pt Schichtdicke. Die optimale Schichtdicke der Pt-Bodenelektrode für YbFO ist Th_{Pt} = 70 nm. Das Fehlen einer Bodenelektrode führt zu Störungen der Kristallstruktur, der alternierenden atomaren Ausrichtung der ferroelektrischen Domänen und der Yb-Fe Austauschwechselwirkung. Im Gegensatz dazu wurden eine Erhöhung der remanenten und der Gesamtmagnetisierung bei Temperaturen unterhalb von 50 K für h-$YbFeO_3$ Schichten erzielt, die auf Pt-gepufferten YSZ(111) Schichten mit ThPt=70 nm deponiert wurden.

Die Variation der Stapelreihenfolge von ferromagnetischen und ferroelektrischen Schichten in multiferroischen Heterostrukturen ist ein entscheidender Aspekt dieser Arbeit. Insbesondere vergleicht die Studie die Strukturen von M1 ($BaFe_{12}O_{19}$/*h*-$YbFeO_3$) und M2 (*h*-$YbFeO_3$/$BaFe_{12}O_{19}$), bei denen die Stapelreihenfolge invertiert wurde. Die temperaturabhängige magnetische Charakterisierung dieser Strukturen ergab Unterschiede in der Koerzitivkraft, den Anisotropiefeldern und den Anisotropiekonstanten. Diese Eigenschaften wurden mit der Defektkonzentration und Grenzflächenvermischung korreliert. Die M1-Konfiguration ($BaFe_{12}O_{19}$/*h*-$YbFeO_3$) weist eine klar definierte Grenzfläche ohne chemische Vermischung und eine bessere c-Achsen-Orientierung auf, was zu höheren Anisotropiekonstanten und Koerzitivkräften führt. Deshalb eignet sich diese Anordnung ($BaFe_{12}O_{19}$/*h*-$YbFeO_3$) für magnetische Speicheranwendungen. Strukturuntersuchungen wurden mit Röntgendiffraktometrie und Transmissionselektronenmikroskopie (TEM) durchgeführt. Änderungen der Stöchiometrie wurden mit Rasterelektronenmikroskopie/energiedispersiver Röntgenspektroskopie (SEM/EDX), Röntgen-Photoelektronenspektroskopie (XPS) und TEM/EDX untersucht. Rasterelektronenmikroskopie (REM) und Rasterkraftmikroskopie (AFM) wurden für Untersuchung der Morphologie verwendet, die dann mit dem magnetischen Verhalten verknüpft wurde, welches mit Hilfe von Vibrationsmagnetometrie (VSM), supraleitendem Quanteninterferometer (SQUID) und Magnetkraftmikroskopie (MFM) gemessen wurde.

Diese Dissertation hat das Verständnis der Wachstumskinetik und der Optimierung von PLD-Schichtsystemen vertieft, zukünftig multiferroische Heterostruktur-Bauelemente herzustellen, deren magnetoelektrische Kopplung auf atomarer Skala an den Grenzflächen über die Mikrostruktur der Schichten kontrolliert wird. Sie bietet einen systematischen Rahmen für die

Entwicklung maßgeschneiderter magnetischen Eigenschaften von BaM und gibt wertvolle Informationen für deren Entwicklung.

Abstract

This dissertation conducts a deep and valuable study dedicated to the optimization of pulsed laser deposition (PLD) growth of individual and combined layers of bottom electrode, ferromagnetic (FM), and ferroelectric (FE) thin films to develop room-temperature multiferroic (MF) heterostructures devices. The performed and versatile investigations aim to understand the interconnection between suitable PLD growth parameter, characteristic structural features and the functional heterostructure properties relevant for magneto-electric coupling in multiferroic systems. This has directed the thesis in a scheme consisting of different optimization steps of the different material layers relevant for the design of the magneto-electric heterostructures. The first optimization step involves the understanding of morphological and structural modification of PLD deposited platinum (Pt) films on yttria-stabilized zirconia (YSZ) (111) substrates under varied growth temperature and thickness conditions. We conclude that the optimized PLD growth parameters involve elevated growth temperatures aligned with the deposition temperatures of subsequent layers, as well as an increased platinum layer thickness. These significantly reduce defect densities, improve robustness against dewetting at high temperatures, and minimize structural modifications during high-temperature processing stages.

The second step focuses on the optimization of barium hexaferrite, $BaFe_{12}O_{19}$ (BaM), deposition as the ferromagnetic layer with the aim of identifying the most appropriate PLD growth conditions that yield to the most favorable magnetic properties for potential multiferroic applications. This optimization was achieved first, by experimenting with different thicknesses of the Pt bottom electrodes to determine the optimum thickness of Pt bottom electrode for BaM growth; and second, by varying the laser fluence (from 1.5 J/cm² to 5.1 J/cm²) for BaM grown on optimized Pt bottom electrodes. At first, the Pt buffer layer has been demonstrated to significantly enhance the c-axis orientation, anisotropy field, and coercivity of BaM layers. It also prevents chemical intermixing of BaM with the YSZ(111) substrate. Furthermore, it has been discovered that increasing the thickness of the Pt buffer layer improves the structural continuity of BaM layers, due to increase of the surface filling factor of platinum. Secondly, the growth kinetics and magnetic properties were altered by adjusting the laser fluence during deposition. Lower fluence leads to smoother surfaces and reduced defect concentrations, which indicates layers grown at lower fluence more suitable for a multilayered device architecture, whereas higher fluence tends to generate Ba deficient non-stoichiometric phases.

In the third step, hexagonal ytterbium ferrite *h*-$YbFeO_3$ (YbFO) grown on YSZ(111) by pulsed laser deposition is optimized. It is a promising single phase multiferroic candidate where ferroelectricity and antiferromagnetism (AF) coexist, with potential applications at low temperatures. A detailed analysis was conducted on the microstructure and temperature-dependent magnetic properties by comparing YbFO layers grown directly on YSZ(111) and YbFO layers deposited on Pt buffered substrates. The platinum buffer film thickness was varied as investigated in the first optimization step. The objective is to gain a comprehensive understanding of the influence of the Pt underlayer crystal quality and morphology on the YbFO layer crystal quality, surface

morphology, and resulting physical properties. The findings indicate that the homogeneity, continuity, and hillock formation of the Pt buffer layer influences YbFO microstructure, mosaicity, grain boundaries, and defect distribution. The findings of high-resolution transmission microscopy (HRTEM) and X-ray diffraction (XRD) reciprocal space mapping characterizations conclude that existence of a Pt buffer layer and optimizing film thickness improves the crystal quality of the YbFO layers. For YbFO layers, Th_{Pt} = 70 nm is found to be the optimum Pt thickness. The absence of a bottom electrode leads to perturbations in the crystal structure, the so-called '2up-1down' (or vica versa) ordering of rare earth atoms in the crystal structure for ferroelectric domains, and the Yb-Fe exchange interactions. In contrast, improved remanent and total magnetization were obtained at low temperatures below 50 K for *h*-$YbFeO_3$ films, when YbFO films deposited on Pt buffered YSZ(111) where Th_{Pt} = 70 nm.

The variation of stacking orders in the multiferroic heterostructures between ferromagnetic and ferroelectric layers is a crucial aspect of this work. Specifically, the study compares the structures of M1 ($BaFe_{12}O_{19}$/*h*-$YbFeO_3$) and M2 (*h*-$YbFeO_3$/$BaFe_{12}O_{19}$) where the stacking order was inversed. The temperature-dependent magnetic characterizations of these structures reveal differences in the coercivity, anisotropy fields, and anisotropy constants. These properties were correlated with defect concentrations and interface intermixing. The M1 ($BaFe_{12}O_{19}$/*h*-$YbFeO_3$) configuration exhibits a well-defined interface without chemical intermixing and better c-axis orientation which results in increased anisotropy constants and coercivity. This makes the designed M1 ($BaFe_{12}O_{19}$/*h*-$YbFeO_3$) heterostructure suitable for magnetic storage applications. Structural analyses were conducted by using XRD and transmission electron microscopy (TEM). Stoichiometric variations were investigated with scanning electron microscopy/energy dispersive X-ray spectroscopy (SEM/EDX), X-ray photoelectron spectroscopy (XPS), and TEM/EDX. Scanning electron microscopy (SEM) and atomic force microscopy (AFM) were used for morphological assessments, which were then linked to magnetic behavior measured by means of a vibrating sample magnetometry (VSM), superconducting quantum interference device (SQUID), and magnetic force microscopy (MFM).

This dissertation has deepened the understanding of the growth kinetics and PLD growth optimization with the goal to produce multiferroic heterostructure devices with structurally controlled magnetoelectric coupling at the interfaces at the atomic scale. It also provides a systematic framework for tailoring the magnetic properties of BaM layers and provides valuable information for the development of high performance multiferroic systems operating at room temperature.

Acknowledgement

In this work, I faced not only scientific challenges but also the task of adapting, surviving, and managing work and life simultaneously while being far away from most of my loved ones. Many obstacles arose, starting from adapting to a new work environment, dealing with the COVID-19 pandemic and quarantine, to having to learn nearly everything in a short time, experiencing personal losses, and tackling numerous academic and experimental difficulties. This journey turned out to be much more challenging than it seemed when I first applied for the position.

For all these challenges, I would like to express my greatest appreciation and thanks to **Dr. Sondes Bauer**. She was always there, offering unwavering support both scientifically and mentally. This work wouldn't have reached this level without her immense efforts and support. I also want to thank her for pushing me into different fields, allowing me to develop in many aspects, and helping me overcome several difficulties with her encouragement and assistance. I am deeply grateful to **Dr. Sondes Bauer** for her support in adapting to the work environment, and for sharing her knowledge without reservation. I extend my gratitude to **Dr. Adriana Rodrigues**, whose support was fundamental not only during our time working together but also in laying the foundation for my thesis work. The knowledge transfer from data processing to experimental details has been invaluable. Additionally, her kind personality and goodwill provided significant support in adapting to the work environment. I cannot express how much I owe to **Dr. Sondes Bauer** and **Dr. Adriana Rodrigues**. I am grateful to **Dr. Martin Bauer** for his prompt and helpful responses to our needs, assistance with calculations, and for allowing us to use his program for the beamline.

At the NANO beamline, I would like to thank **Andre Scheibe** and **Erhan Cilbir** for their technical and personal support. I also thank **David Haas** for his fast technical IT support. They shared the technical stress of accomplishing the project's needs with me, and I am thankful for their presence.

I express my gratitude to **Prof. Dr. Tilo Baumbach** for his support throughout the project and my PhD process. He tried to be there as much as he could, responding to my needs and facilitating a more relaxed working environment. His support in securing contract extensions was also invaluable.

Thanks to **Dr. Xiaowei Jin** and **Prof. Dr. Reinhardt Schneider**, who were always ready to support the project and my thesis, even after fulfilling their initial roles. Their support in microscopy work significantly impacted the quality of this thesis and related publications.

I appreciate the efforts of **Dr. Lukas Horak** and **Prof. Dr. Vaclav Holy** for their immediate support, suggestions, and scientific advice. They were always available to help when needed.

My thanks also go to **Dr. Klaus Seemann** for his assistance with the scientific content, VSM measurements, and language-related suggestions for the thesis. I also thank **Prof. Dr. Sven Ulrich** for accepting me as a PhD student, which allowed me to pursue this thesis work in the Mechanical Engineering Department, and for granting me access to their VSM machine at IAM.

I am grateful to **Dr. Bärbel Krause** and **Dr. Svetoslav Stankov** for allowing me to use their laboratory devices, teaching me how to operate them, and letting me conduct experiments even during inconvenient times.

I thank my colleague and friend **Dr. Byeongchan So** for his insights into my work, his opinions about the PhD process, and his friendly support, including our shared meals. His kindness, positive attitude, and support made my time in the laboratory and institute enjoyable.

I deeply appreciate my friend and supporter **Dr. Burak Akdeniz**, who was always there for me despite his own challenges. He was a true companion *'yol arkadasi'* with whom I could discuss anything, and his presence was invaluable. Similar thanks go to **Nilsu Parlakyıldız** and **Can Atılgan**, who provided support, long talks, and suggestions, despite being thousands of kilometers away.

Not that I give less value to any of my friends that I mention less, or that I don't mention their names here, or I mention early or late in the text, all of my friends have very important place for me, I will be able to mention some which were there mostly for me during my PhD period for that I extend my thanks to **Deniz Kalkan** for our long phone calls, shared emotions, and same interests; **Deniz Aydın** for sharing a flat and encouraging me for the time period, becoming very close friend of mine and thanks for sharing all those fun moments at the flat; **Selin Özgür** and **Doğa Yahşi** for listening and enjoying cooking sessions; **Anıl Aslan** for being a close friend and flatmate during a difficult period; **İlyas Böcek** for always being positive and friendly; **Gamze Seda Şentürk** for always being available to talk and consult on difficult issues; **Bassem Riad** and **Tuğçe Demiral** for their encouragement; and **Alexandra Szabo** and **Gizem Yartaş** for their friendship and support. Special thanks to **Evren Emre Üstün** for understanding and listening during tough times.

I also thank **Oliver Seubert**, **Tetiana Driabova**, and **Yannic Frank** for accompanying me in bouldering sessions, seeing my stressed side in the gym, and being good friends. Similar thanks go to **Jonas Göckel** and **Kristin Olböter** for teaching me lead climbing, and to **Jonas Fröhlich** for sharing good times in the climbing gyms.

Lastly, I cannot adequately express my gratitude to my family. Words fall short of describing their lifelong support, patience, and unconditional love. Their mental and financial support has been my constant source of strength. Therefore, I thank my mother **Gülten Nergis**, my father **Gazi Nergis**, and my sister **Ayçıl Nergis**, as well as my uncle and aunt for their huge support during my journey in Germany. I also extend my thanks to my uncles and grandparents. Your unwavering support has brought me to this point, allowing me to complete my PhD thesis.

This acknowledgment expresses my heartfelt thanks to everyone who supported me throughout this challenging journey. Your contributions have been invaluable and deeply appreciated.

Contents

Abreviations

AFM	Atomic force microscopy
AF	Antiferromagnetic
APB	Antiphase boundary
BaM	$BaFe_{12}O_{19}$
BSE	Back-scattered electron
CAF	Canted-antiferromagnetic
EB	Exchange-bias
EDX	Energy dispersive X-ray spectroscopy
FE	Ferroelectric
FC	Field cooling
FFT	Fast Fourier Transform
FIB	Focussed ion beam
FM	Ferromagnetic
FWHM	Full-width at half maximum
HAADF	High-angle annular dark- field
HR-RSM	High-resolution reciprocal space map
HR-TEM	High-resolution transmission electron microscopy
HR-STEM	High-resolution scanning transmission electron microscopy
HR-XRD	High-resolution X-ray diffraction
IP	In-plane
MAE	Magneto-crystalline anisotropy
MF	Multiferroic
MRAM	Magnetic random access memory
PLD	Pulsed laser deposition
OOP	Out-of-plane
PM	Paramagnetic
RT	Room temperature
SE	Secondary electrons
SEM	Scanning elecron microscopy
SF	Stacking fault
SOC	Spin-orbital coupling

SR	Sweeping rate
STEM	Scanning transmission electron microscopy
SXRD	Symmetric X-ray diffraction
SZD	Structure zone diagram
TEM	Transmission electron microscopy
VSM	Vibrating sample magnetometer
WH	Williamson-Hall
XPS	X-ray photoelectron spectroscopy
XRD	X-ray diffraction
XRR	X-ray reflectometry
YbFO	*h*-$YbFeO_3$
YSZ	Yttria-stabilized zirconia
ZFC	Zero-field cooling

Preface

The objective of this thesis is to publish the resulting research during the PhD period, in parallel with the dissertation writing process. The research yielded several results, which were published in the following manner. Given that the principal objective was to generate empirically robust and reliable data that was consistent with the narrative and motivation of the dissertation, the figures and data from the published journals have been incorporated into this thesis.

The figures are presented in the same form as in the original publications, but the accompanying text, and interpretations are written in the my own language and tailored to the flow and style of this dissertation. The text has not been copied from the publications. Instead, the figures are incorporated into the narrative of the thesis, creating a coherent and seamless storyline. This approach was chosen over writing a cumulative thesis to provide a more engaging and fluent dissertation.

Publication 1:

- Bauer, S., Rodrigues, A., Horák, L., **Nergis, B.**, Jin, X., Schneider, R., Gröger, R., Baumbach, T., Holý, V. **(2021).** Time-Resolved Morphology and Kinetic Studies of Pulsed Laser Deposition-Grown Pt Layers on Sapphire at Different Growth Temperatures by in Situ Grazing Incidence Small-Angle X-ray Scattering. *Langmuir*, *37*(2), 734-749.

Publication 2:

- Gabriel, V., Kocán, P., Bauer, S., **Nergis, B.**, Rodrigues, A., Horák, L., Jin, X., Schneider, R., Baumbach, T., & Holý, V. **(2022).** Effect of pulse laser frequency on PLD growth of LuFeO3 explained by kinetic simulations of in-situ diffracted intensities. *Scientific Reports*, *12*(1), 5647.

Publication 3:

- **Nergis, B.**, Bauer, S., Jin, X., Seemann, K., Horak, L., Schneider, R., Holý, V., Ulrich, S., Baumbach, T. **(2023).** Effect of the laser fluence on the microstructure and the relating magnetic properties of BaFe12O19 films grown on YSZ (111) by PLD for optimized perpendicular recording. *Journal of Materials Science*, *58*(2), 718-739.

Publication 4:

- Bauer, S., **Nergis, B.**, Jin, X., Schneider, R., Wang, D., Kübel, C., Holý, V., Horák, L., Seemann, K., Ulrich, S., Baumbach, T. **(2023).** Effect of Interface Layer Quality on Microstructure, Stoichiometry, and Magnetic Properties of Hexaferrite BaFe12O19 Grown on YSZ (111) by Pulsed Laser Deposition. *Langmuir*, *39*(40), 14308-14327.

Publication 5:

- Bauer, S., **Nergis, B.**, Jin, X., Schneider, R., Wang, D., Kübel, C., Machovec, P., Horák, L., Holý, V., Seemann, K., Baumbach, T., Ulrich, S. **(2024)**. Dependence of the Structural and Magnetic Properties on the Growth Sequence in Heterostructures Designed by YbFeO3 and BaFe12O19. *Nanomaterials*, *14*(8), 711.

Publication 6:

- **Nergis, B.**, Bauer, S., Jin, X., Horak, L., Schneider, R., Holy, V., Seemann, K., Ulrich, S., Baumbach, T. **(2024)**. Structural and Morphological Studies of Pt in the As-Grown and Encapsulated States and Dependency on Film Thickness. *Nanomaterials*, *14*(8), 725.

Publication 7:

- Bauer, S., **Nergis, B.**, Jin, X., Horak, L., Schneider, R., Holy, V., Seemann, K., Baumbach, T., Ulrich, S. **(2024)**. Relevance of Platinum Underlayer Crystal Quality for the Microstructure and Magnetic Properties of the Heterostructures YbFeO3/Pt/YSZ(111). *Nanomaterials*. *14*(12), 1041.

Karlsruhe, 22.10.2024 Berkin Nergis

1 Motivaton, introduction and goals

1.1 Motivation

The objective of this thesis is to fabricate designed multiferroic heterostructures comprising ferromagnetic and ferroelectric layers with controllable stoichiometries, crystal structure, and morphology using the PLD method. Previous research has demonstrated the successful combination of ferrimagnetic and ferroelectric layers to create multiferroic heterostructures, including $Pr_{0.85}Ca_{0.15}MnO_3/Ba_{0.5}Sr_{0.4}TiO_3$[1] and $La_{0.7}Ca_{0.3}MnO_3/BaTiO_3$[2]. In this thesis, $BaFe_{12}O_{19}$ is selected as the ferromagnetic layer due to its room temperature ferromagnetic behavior, and *h*-$YbFeO_3$ is chosen as the ferroelectric layer for its room temperature ferroelectric properties. Additionally, this combination addresses the emerging interest in these individual layers and fills a gap in the existing literature. Therefore, the thesis focuses on identifying the most optimal PLD growth conditions for single layers (a platinum (Pt) bottom electrode layer, a ferromagnetic layer ($BaFe_{12}O_{19}$, BaM), and a ferroelectric layer (*h*-$YbFeO_3$, YbFO)) and their combination into heterostructures to investigate the resulting structure and its relevance to the obtained properties.

These heterostructures are meant to be multifunctional at room temperature (RT) with the capabilities of magneto-electric coupling at the bilayer's interfaces. The aim is to construct a room temperature operating multiferroic heterostructure system. The strategy is to detune the PLD growth conditions in an iterative way based on the obtained crystal qualities of the layers, surface morphologies, interface quality as well as chemical compositions with interrelation to the magnetic and ferroelectric properties of the individual layers. The focus on RT multiferroic heterostructures originate from the limited availability of materials that simultaneously exhibit a FE and FM behavior at RT. In order to overcome these constrains, the combination of different functional individual layers into a heterostructure system would enables us to achieve multifunctional multiferroic heterostructures envisaged for the application in recording media devices at room temperature.

Prior to the investigation of the interfacial interaction in the heterostructure, which are extremely relevant to the magneto-electric coupling at the interfaces between FM and FE layers, it was worthwhile to carefully optimize the growth conditions of each layer by examining the effect of the varied growth parameters on the structural characteristics, and therefore, on the physical properties.

Each layer was analyzed highlighting specific improvements aligned with the overall goal of potential device assembly. The overall goal not only includes the development of the device production by any method but also includes fabrication of the device in a single run of PLD growth due to PLD's capabilities of growing metals and complex oxide films at high temperatures with

very high crystalline quality. The current PLD setup has device limitations - which could be resolved by improving the system with an integrated cooling system - (such as overheating of the mechanical components due to long-lasting high temperature growth) that does not allow continuous growth through the bottom electrode to the final MF heterostructure. This limitation hindered the combination of each individual layer, which is the overall aim of the project. However, these limitations do not block to progress with strategic approach towards a final device fabrication. These limitations can be overcomed by combining the FM and FE layers without a platinum interface layer. This describes the optimal stacking order for achieving a functional RT multiferroic heterostructure.

The thesis and research do not only establish a path for creating RT MF heterostructures, but also include the development of a possible future MF device fabrication. The thesis also describes the analysis of the structure, stoichiometry, morphology, and in relation functional properties of the layers that are essential for the development of a multiferroic device technology.

1.2 Introduction

This section introduces the foundational concepts and the methodological relevance for the study of growth optimization of multiferroic heterostructure bilayer systems. It dives into the description of the pertinent properties of single ferromagnetic and ferroelectric layers as well as heterostructure multiferroics and their applications. This was followed by an in-depth look into the material growth techniques with a special focus on the epitaxial growth and particularly on PLD methods.

This introductory chapter progresses to discuss various techniques employed for the detailed structural characterization of these materials, including XRD, microscopy and spectroscopy methods. It also explores the specialized methods such as the VSM and the relating theoretical background for assessing the behavior of magnetic properties. The introduction culminates with a thorough examination of the specific materials studied, covering sample preparation and the PLD growth process for Platinum, Barium Ferrite ($BaFe_{12}O_{19}$), and Ytterbium Ferrite (*h*-$YbFeO_3$) which offer insights into their complex deposition and characterization processes.

Multiferroic materials: Multiferroic materials are a rare class of materials that exhibit both ferromagnetism and ferroelectricity simultaneously[3,4,5,6] shown in Figure 1.1. Due to their extraordinary potential in the electronics industry, multiferroics have attracted much attention since their discovery[4]. Energy efficient electronics[7], CMOS[8], spintronics[9], multiple state memory elements[10], non-volatile memories[11], high frequency devices[12], photovoltaics[13], gas sensing[14] are some of the proposed and already researched applications. Ramesh et al. in 2021 have drawn attention to the importance of controlling magnetism by an electric field[15], by pointing out the extreme increase in the use of transistors over the decades which would lead to an energy problem in the future. Additionally, applications of multiferroics are also suggested to offer enhanced energy efficiency[16] and better properties compared to their bulk forms[5,17]. It was fairly proved in the data storage field that the electrical tuning of the magnetic field for multiferroic materials is more beneficial than simply tuning the magnetic field by applying an external magnetic field[15].

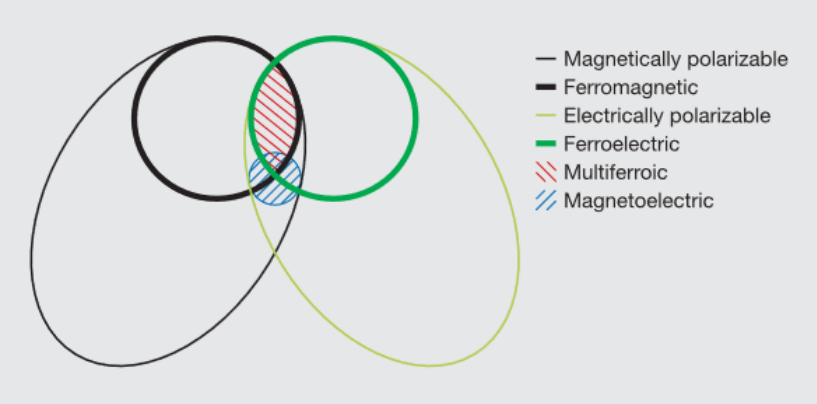

Figure 1.1: The relationship between the magnetically and electrically polarizable materials[18].

1.3 Objectives and scope of the work

1.3.1 Objectives

The objectives of this work are to conduct a comprehensive and systematic study with the goal to understand the growth kinetics of each individual layer (Pt, BaM, YbFO) and its relevance to the resulting film quality in terms of the crystal structure, chemical composition, and morphology. For these layers, the importance of microstructural parameters, the stoichiometry, the determination of electrical, magnetic and ferroelectric properties will be individually investigated. The final goal is to combine these individual layers with their optimized growth parameters into a multiferroic heterostructure system. For that purpose, the first attempt of functional layer growth has been performed on YSZ (111) without any Pt bottom electrode. BaM and YbFO layers grown on YSZ (111) are named as BaMPtTh0 and YbPt_Th0nm.

Therefore, the first step of the work must be the optimization of the platinum interface layer which serves as a bottom electrode for the future ferroelectric/multiferroic application. The bottom conductor layer is a must. On the other side, it improves the lattice mismatch between the BaM (resp. YbFO) and YSZ (111) substrate which in turn decreases the defect concentration and enhances the films qualities.

The objectives of the thesis can be listed as following:

1) Understanding the effect of the PLD growth parameters for the different individual layers (Pt, BaM and YbFO) on the layer crystal quality, continuity, homogeneity as well as on the interface qualities by using complementary characterization methods such as XRD, TEM, SEM/EDX and AFM.

2) Separate determination of the key and the optimum PLD growth parameters which lead to conductive Pt and producing BaM as a strong room-temperature ferromagnetic layer and YbFO as a strong room-temperature ferroelectric layer.

3) Optimizing the individual properties, i.e., conductivity, ferroelectric and ferromagnetic properties by iterating the relevant growth parameter to approach/or to exceed and improve the state-of-the-art properties. This is for the individual improvement of the layers, in order to decide which growth parameters ought to be applied into the heterostructure.

4) This step involves the combination of each individual layer, optimized in the previous stages, a heterostructure where the order of functional layers is alternated. The objective is to investigate the resulting multiferroic properties of this alternated heterostructure to propose which one is more applicable at room temperature. By strategically arranging the layers in this manner, while aiming at enhanced multiferroic properties at room temperature, the efficiency of functional electronic devices can be improved.

1.3.2 Outline

The outline of this work is schematically illustrated in Figure 1.2. The achievable milestones through the considered steps are show a strategical approach to the final aim of the thesis which is the production of magnetoelectric heterostructures devices suitable for the magnetoelectric coupling characterization as presented in the step 5. In this work, preliminary results were obtained at step 0, and the work continued through the steps starting with the Pt bottom electrode optimization. Due to time limitation, step 5 could not be realized. Therefore, the work was concluded with step 4. Step 1 is explained in chapter 4, step 2 can be found in chapter 5, step 3 in chapter 6 and step 4 in chapter 7.

Chapter 4: Platinum layer optimization

This chapter focuses on the improvement of the applicability of the PLD grown Pt bottom electrode. The effect of the Pt layer growth parameter variation such as the temperature, deposition rate on the morphology and film continuity, crystal quality and on the conductivity is investigated. The goal is to explore modifications in the Pt film structure, the subsequent growth as a function of the film thickness with the aim to address potential problems in the Pt bottom electrode due to the Pt layer discontinuity as well as hillock formation.

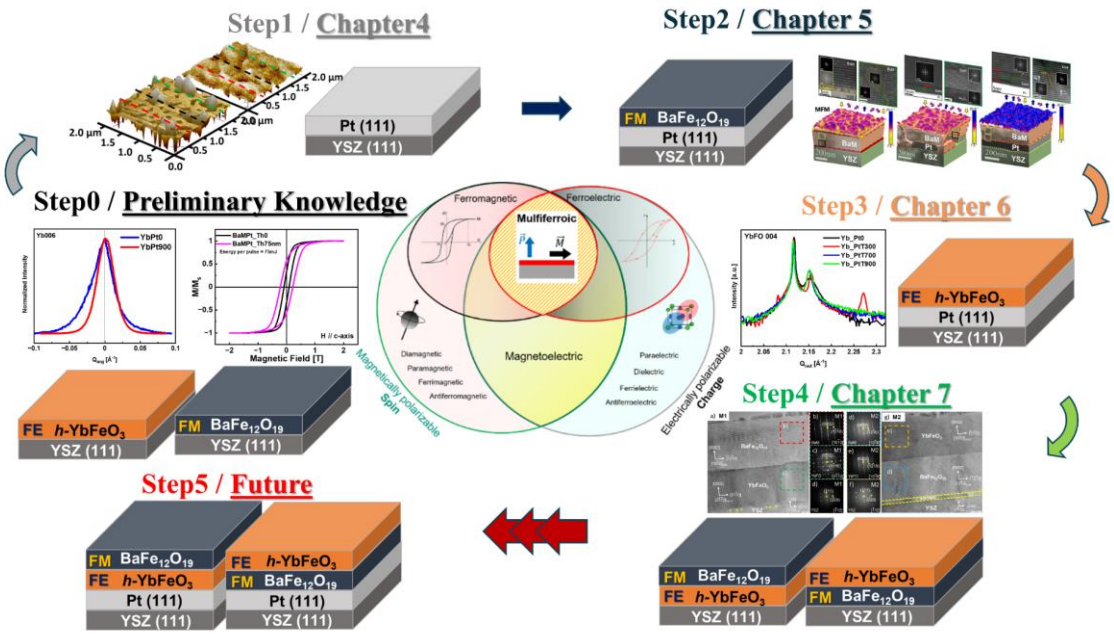

Figure 1.2: Schematic representation of the overall scheme for the thesis path, for detailed view, refer to Figure A-1.

Investigation of Pt film growth parameters: To find the optimum conditions for obtaining a conductive, continuous, hillock-free single-crystal Pt film with a surface orientation in the [111] direction. The effects of the growth temperature and film thickness on the Pt layer are investigated. This optimization is crucial to improve the performance of the Pt bottom electrode, especially to obtain flat, continuous, and conductive bottom electrodes.

Physical stability of Pt bottom electrode: Changes in the Pt layer during the subsequent growth of the functional ferromagnetic and/or ferroelectric layers are also studied in detail to assess the physical stability of the Pt bottom electrode. Understanding the behavior of the Pt film during and after the postgrowth of other layers is essential to ensure the overall structural integrity of the multiferroic heterostructure.

Chapter 5: YbFO layer optimization

Influence of bottom electrode on ferroelectric ordering: In this chapter, the focus is on the investigation how the bottom electrode layer impacts the ferroelectric order in subsequently grown YbFO layers at room temperature (RT) in terms of varying the thickness and morphology. The study analyzes the effects of the bottom electrode thickness on the crystalline structure, morphology, and ferroelectric order of the YbFO layers, with the aim of understanding and optimizing the ferroelectric properties.

Chapter 6: BaM layer optimization

Influence of laser fluence and bottom electrode thickness: This chapter is focused on investigating the modifications required to improve the RT ferromagnetic behavior of BaM layers. The aim is

to achieve enhanced magnetic properties in the BaM layers by optimizing the Pt interlayer thickness and the laser fluence which is used to grow the BaM layer. In this chapter investigation reveals the results on the RT magnetic properties of BaM, by the modifications on the crystalline structure, morphology, chemical composition, and interface quality.

Chapter 7: Combination of layers into heterostructure multiferroics

Influence of the stacking order on the structure and magnetic properties of multiferroic heterostructures: Combining BaM and YbFO in heterostructures with alternating layer order: This chapter explores a unique combination of BaM and YbFO in the field of heterostructure multiferroics. The study aims to significantly enhance the room temperature multiferroic properties of these materials by changing the growth sequences of the BaM and YbFO layers within the heterostructure. The crystalline structure and interfaces quality of the two heterostructures with two stacking orders are presented in detail and are evaluated according to the results which are derived from a combination of high resolution microscopic and diffraction methods. Furthermore, the local domain microstructure with atomic resolution and macroscopic magnetic properties will be discussed in relation to the chemical composition. Through the strategic pairing of BaM, known for its room temperature ferromagnetic properties with YbFO, this work presents a promising approach to achieve enhanced multiferroic behavior. The results of this investigation may have the potential to revolutionize the field of multiferroic materials and bear exciting new possibilities for advanced applications.

2 Fundamentals and methods

2.1 Theory of magnetism

Magnetisation is an interesting phenomenta which was first discovered in antique ages as magnetic material as the forms of 'lodestone' (which is actually magnetized pieces of magnetite) where the pieces of lodestones were rotating around themselves, without any external 'visible' force[12,19]. The first uses of the lodestones were believed to detect the magnetic field of the earth so to use it as a compass in the time of around Olmec society of North America (1400 BCE to 400 BCE).

Thales of Miletus is known to be the first reporter of magnetism in their era in ancient Greek Society, together with Aristotle, it is known to be that the first scientific discussion of magnetism was being done[12]. The name of 'Magnet' believed to be originated from the 'magnesia stone' for the lodestones found in city of Magnesia ad Sipylumin Lydia, in Modern day Manisa, Turkey.

Magnetisation is the vectoral quantity that describes the response of the matter as magnetic field. And the magnetization is a vectoral sum of all magnetic dipole moments which are originated by individual electrons, atoms and molecules per unit volume of the material[20].

2.1.1 Magnetic Dipole Moments

The understanding of magnetism is subject upon the comprehension of magnetic dipole moments. A magnetic dipole moment is a vector quantity that is linked with the magnetic properties of a particle, such as an electron[20]. It represents the strength and direction of the magnetic field produced by the particle.

2.1.1.1 Magnetic Dipole Moment of Electrons

In the perspective of atoms, the magnetic dipole moments that are observed can be attributed to the electrons. These moments are a consequence of both the spin of the electrons and their orbital motion around the nucleus[20]. Each electron is therefore provided with an intrinsic magnetic dipole moment due to its spin, which is often referred to as the electron's spin magnetic moment.

2.1.1.2 Bohr Magneton

The Bohr magneton (μ_B) is a physical constant that quantifies the magnetic dipole moment of an electron caused by its orbital or spin motion. It is a fundamental unit of magnetic moment in atomic physics. The Bohr magneton is defined as[20]:

$$\mu_B = \frac{e\hbar}{2m_e} \tag{2-1}$$

Where e is the electron charge, $\hbar$ is the reduced Planck constant, and m_e is the electron mass. The value of the Bohr magneton μ_B is approximately 9.274×10^{-24} joules per tesla (A m^2)[20].

2.1.1.3 Magnetic Moments in Atoms

In an atom, the total magnetic moment is the vector sum of the magnetic moments of all its electrons. According to the Pauli Exclusion Principle, electrons in the same orbital must have opposite spins, resulting in their magnetic moments cancelling each other out. However, in atoms with unpaired electrons, the magnetic moments do not cancel, leading to a net magnetic moment. The arrangement and interaction of these magnetic dipole moments determine the magnetic properties of the material[20].

2.1.2 Exchange Interactions

Exchange interactions represent a fundamental quantum mechanical force that determines the alignment of spins in magnetic materials[20,22]. These interactions arise due to the Pauli exclusion principle, which states that the total wave function of a system of electrons must be anti-symmetric with respect to the exchange of any two electrons. This leads to an energy difference between parallel and antiparallel spin alignments of neighbouring electrons[20,22].

2.2 Types of Magnetism

The magnetic behaviour of magnetic materials can be categorised according to the alignment of their magnetic dipole moments, the schematic representations are given in Figure 2.1.

2.2.1 Ferromagnetism

In ferromagnetic materials, the exchange interaction causes unpaired electron spins to align parallel to each other. This parallel alignment minimises the system's energy, resulting in a net macroscopic magnetisation even in the absence of an external magnetic field[20,21]. The exchange interaction is positive in ferromagnetic materials, favouring parallel spin alignment[20].

2.2.2 Paramagnetism

Paramagnetism is a magnetic behaviour exhibited by materials where the magnetic dipole moments are randomly oriented in the absence of an external magnetic field. Upon the application of an external field, these moments partially align with the field, resulting in a weak, positive magnetization[20].

2.2.3 Diamagnetism

Diamagnetism is defined by the presence of paired electrons in materials that lack unpaired electrons. When an external magnetic field is applied, the orbital motion of electrons generates a weak, negative magnetisation that opposes the applied field[20,21].

2.2.4 Antiferromagnetism

In antiferromagnetic materials, the magnetic dipole moments of adjacent atoms align in an antiparallel manner, resulting in the absence of a net macroscopic magnetization. The exchange interaction is negative in antiferromagnetic materials, thereby favouring the alignment of spins in an antiparallel direction[20].

2.2.5 Ferrimagnetism

Ferrimagnetism is analogous to antiferromagnetism, yet with unequal opposing magnetic moments, resulting in a net magnetization. Ferrimagnetic materials exhibit a more intricate magnetic structure due to the varying magnitudes of the magnetic moments[20].

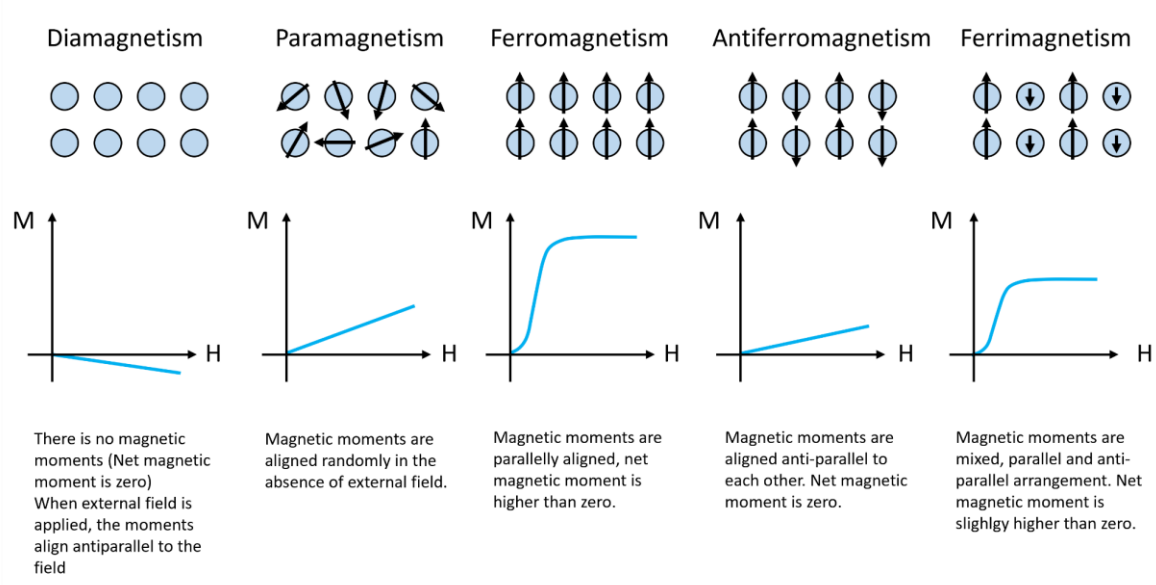

Figure 2.1: Typical magnetization curves of different type of magnetic materials.

2.3 Magnetic Anisotropy

Magnetic anisotropy refers to the directional dependence of a material's magnetic properties. In other words, the energy required to magnetise a material can vary depending on the direction of the applied magnetic field. This phenomenon is crucial in determining the behaviour and applications of magnetic materials. The presence of magnetic anisotropy in a material indicates that there are preferred directions along which the magnetic moments tend to align more easily[20,22].

2.3.1 Types of Magnetic Anisotropy

There are several types of magnetic anisotropy, each arising from different physical mechanisms:

- **Magnetocrystalline Anisotropy:** This type of anisotropy originates from the crystal lattice of the material. The interaction between the magnetic moments and the crystal lattice leads to preferred directions of magnetization[21]. The energy associated with magnetocrystalline anisotropy depends on the crystallographic direction. To illustrate, in cubic crystals, the axes of magnetisation that are most favourable and those that are least favourable are determined by the crystal structure[21]. For example, in a cubic lattice, the <100> and <111> directions are the most and least favourable, respectively.

- **Shape Anisotropy:** Shape anisotropy is a phenomenon that arises from the geometric shape of the magnetic material. In elongated or irregularly shaped particles, the demagnetising field, which opposes magnetisation, varies with the shape. For instance, in a long, thin needle-like particle, it is easier to magnetise along the length of the needle than across its width. This phenomenon can be attributed to the distribution of magnetic charges on the surface, which results in the formation of different energy states for varying directions of magnetization[20].

- **Stress Anisotropy:** This type of anisotropy is induced by mechanical stress. When a magnetic material is subjected to stress, the magnetic moments may preferentially align along specific directions, thereby minimising the strain energy[20]. This effect is significant in materials where the magnetostriction (the change in shape or dimensions of a material in response to magnetisation) is pronounced[20].

2.3.2 Magnetocrystalline Anisotropy

Magnetocrystalline anisotropy (Figure 2.2) represents one of the fundamental property of ferromagnetic materials. It arises from the spin-orbit coupling, which links the spin of the electrons to the crystal lattice[20,22]. The energy associated with magnetocrystalline anisotropy can be expressed in terms of the anisotropy energy density E_A, which depends on the direction cosines of the magnetization with respect to the crystallographic axes[20,22].

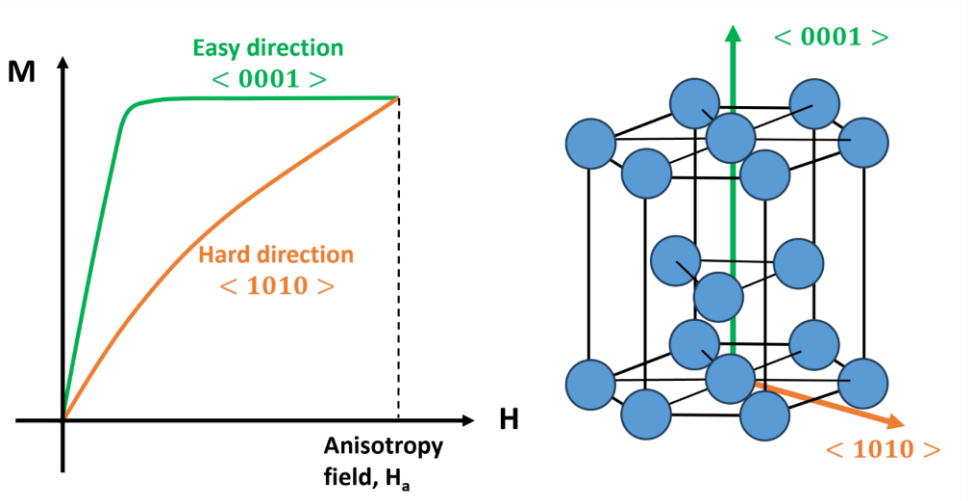

Figure 2.2. A schematic initial magnetization to explain magnetocrystalline anisotropy of a hexagonal material.

For example, in a cubic crystal, the anisotropy energy can be approximated by[20,22]:

$$E_A = K_1(\alpha_1^2\alpha_2^2 + \alpha_2^2\alpha_3^2 + \alpha_3^2\alpha_1^2) + K_2(\alpha_1^2\alpha_2^2\alpha_3^2) \quad (2\text{-}2)$$

where K_1 and K_2 are the anisotropy constants, and α_1, α_2, and α_3 are the direction cosines of the magnetization vector with respect to the crystallographic axes.

In hexagonal crystals, such as cobalt or BaM, the anisotropy energy is typically dominated by a single term[20]:

$$E_A = K_u \sin^2\theta \quad (2\text{-}3)$$

where K_u is the uniaxial anisotropy constant and θ is the angle between the magnetization vector and the easy axis.

2.3.3 Shape Anisotropy

The phenomenon of shape anisotropy can be attributed to the demagnetising field, which is dependent on the geometry of the magnetic material. The demagnetising field is a self-induced field that acts in opposition to the external magnetic field. For an ellipsoidal particle, the demagnetising factors N_x, N_y and N_z are dependent upon the axes of the ellipsoid. The shape anisotropy energy can be expressed as[20,21]:

$$E_{shape} = \frac{1}{2}N_xM_x^2 + \frac{1}{2}N_yM_y^2 + \frac{1}{2}N_zM_z^2 \quad (2\text{-}4)$$

where M_x, M_y and M_z are the components of the magnetization along the principal axes of the ellipsoid.

In elongated particles, such as nanowires or thin films, the demagnetising factor along the length is significantly less than that along the width or thickness, resulting in the length becoming the easy axis of magnetisation.

2.3.4 Stress Anisotropy

Stress anisotropy is a phenomenon whereby mechanical stress influences the magnetic properties of a material. This is of particular significance in materials with high magnetostriction, where the magnetic energy is affected by the strain induced by an external stress[20,21].
The phenomenon of magnetic anisotropy is of great importance in numerous technological applications. It plays a pivotal role in determining the stability of the magnetisation state, coercivity, and magnetic resonance frequencies. In magnetic storage devices, the presence of high magnetic anisotropy is of significant benefit, as it ensures that the stored information remains stable against thermal fluctuations. In magnetic sensors and actuators, the ability to control magnetic anisotropy allows for the precise tuning of the device's response to external magnetic fields[20].

2.4 Magnetic Domains and Domain Walls

2.4.1 Magnetic Domains

Magnetic domains are small, localized regions within a ferromagnetic or ferrimagnetic material where the magnetic moments are aligned in the same direction. Each domain acts as a single magnetic unit, with its magnetization vector pointing uniformly in one direction. The existence of magnetic domains minimizes the material's overall magnetic energy by reducing the magnetostatic energy, which is the energy associated with the external magnetic field produced by the material[20,22].

The formation of domains is driven by the energetic preference for the material to break up into smaller regions with varying magnetisation directions rather than maintaining a single, uniformly magnetised state. This arrangement reduces the external magnetic field, thus lowering the magnetostatic energy[20,22].

2.4.2 Domain Walls

Domain walls are the boundaries between adjacent magnetic domains with different magnetisation directions. The magnetic moments within a domain wall gradually rotate from the direction of one domain to the direction of the neighbouring domain[20,22]. The thickness of the domain wall and the manner in which the moments rotate depend on the material's properties and the type of wall. There are two primary types of domain walls:

Bloch Walls: In Bloch walls, the magnetization rotates within the plane of the wall. This type of wall is commonly found in bulk materials and is characterized by a gradual, smooth rotation of magnetic moments[20,22].

Néel Walls: In Néel walls, the magnetization rotates perpendicular to the plane of the wall. These walls are typically observed in thin films or small particles where surface effects are significant[20,22].

The energy associated with domain walls encompasses exchange energy, which is inclined to align spins, and anisotropy energy, which is inclined to magnetisation along specific crystallographic directions. The equilibrium between these energies determines the domain wall structure and thickness[20,22].

2.5 Magnetic Hysteresis

2.5.1 Hysteresis Loop

The phenomenon of magnetic hysteresis describes the lag between the applied magnetic field and the resulting magnetisation of a material. When a ferromagnetic material is subjected to a varying external magnetic field, its magnetisation does not follow the field in a linear manner. Instead, it

traces out a loop, known as the hysteresis loop, which represents the history of the material's magnetisation and demagnetisation process[20,22]. A typical hysteresis loop (M-H curve) has the following features and shown in Figure 2.3:

Saturation Magnetization (M_s): The maximum magnetisation attained by the material is defined as the value of the magnetic moment aligned with the direction of the applied field.

Remanent Magnetization (M_r): The residual magnetisation is the magnetisation remaining in the material when the external magnetic field is reduced to zero. This value indicates the material's ability to retain magnetisation.

Coercivity (H_c): The magnitude of the external magnetic field required to reduce the magnetisation to zero. Coercivity is a measure of the material's resistance to demagnetisation.

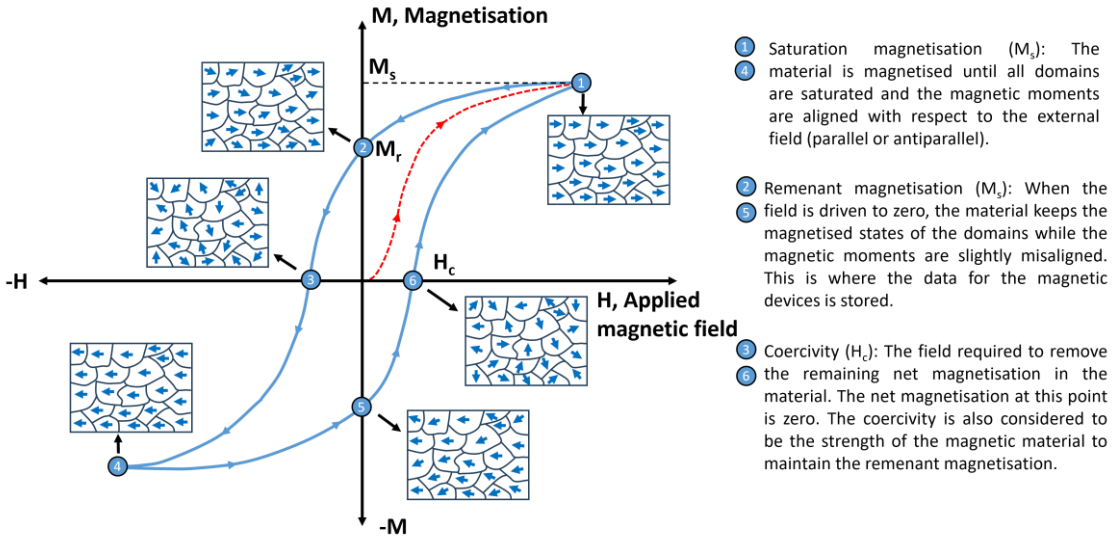

Figure 2.3: (a) A typical hysteresis loop explaining the important features in it together with the schematic represetations of the domain structures on specific magnetic states, the red dotted line represents the initial magnetization.

Coercivity is also a measure of a material's ability to retain stored magnetic data for data storage devices. Few models were published to explain the mechanisms that control the coercivity. The Stoner-Wohlfahrt model attempted to explain coercivity mechanisms in terms of thermal energy and anisotropy[23]. However, magnetic materials also exhibit multiple mechanisms, such as domain wall pinning at defects and boundaries, and domain nucleation[24,25,26]. While the micromagnetic model assumed that the material is a continuous medium and is governed by various energy terms that include exchange energy, anisotropy energy, Zeeman energy, and demagnetizing energy[27]. Exchange energy deals with the interaction between neighboring magnetic moments which favor parallel alignment in ferromagnetic materials. The anisotropy energy refers to the dependence of energy on the direction of magnetization. Therefore, if a material prefers to orient its magnetic moments in a certain direction, it leads to the formation of easy and hard axes. The easy axis describes the direction where the anisotropy energy is high. It makes the material more resistant against magnetization switching in this direction, while the hard axis is the weak axis. Magnetic

storage devices are designed to operate along the direction of the easy axis[28]. This model investigates the driving mechanism of coercivity, whether it is domain wall pinning or domain nucleation[25]. Equation (2-5) shows the well-known micromagnetic model formalism.

$$\frac{H_{c\perp}(T)}{M_{s\perp}(T)} = \alpha * \frac{H_a(T)}{M_{s\perp}(T)} - N_{eff} \tag{2-5}$$

N_{eff} is the demagnetization factor which results from magnetic grain surface and volume charges, and α correspond to a microstructural parameter which is called structural reduction factor[25].

The temperature-dependence coercive field $H_c(T)$, the saturation magnetization $M_s(T)$ and the anisotropy field $H_a(T)$ shows the following relation for which α delivers the information about the coercivity whether it is driven by the domain wall pinning mechanism or by domain wall nucleation[25].

2.5.2 Types of Hysteresis Loops

Different materials exhibit distinct hysteresis loops, which can be broadly categorized as[20,22]:

Hard Magnetic Materials: The materials exhibit a considerable coercivity and a broad hysteresis loop. They retain a notable magnetisation even after the external field is removed, rendering them suitable for use in permanent magnets.

Soft Magnetic Materials: The materials exhibit a relatively low coercivity and a narrow hysteresis loop. They are readily magnetised and demagnetised, rendering them optimal for applications such as transformer cores and magnetic shielding.

2.6 Exchange Bias

2.6.1 Definition of Exchange Bias

Exchange bias is a magnetic phenomenon observed in ferromagnetic/antiferromagnetic (FM/AF) bilayers, where the hysteresis loop of the ferromagnetic material is shifted (Figure 2.4) along the magnetic field axis[29,30]. This shift is typically induced after the FM/AF system is cooled through the Néel temperature (the temperature below which an antiferromagnetic material becomes ordered) of the antiferromagnet while an external magnetic field is applied[29,30]. The exchange bias effect results in the ferromagnetic layer having a preferred direction of magnetisation, which manifests as a unidirectional anisotropy. This effect is characterised by two main parameters:

Exchange Bias Field (H_{EB}): The field offset of the hysteresis loop in the direction of the magnetic field axis.

Coercivity (H_c): The coercive field may be enhanced or modified as a consequence of the exchange interaction at the FM/AF interface.

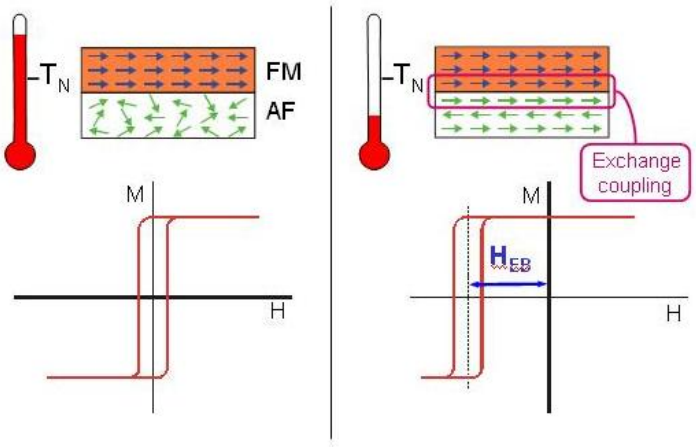

Figure 2.4: Schematic representation of the mechanism of exchange bias phenomenon, the figure is adapted from[30].

2.6.2 Mechanism of Exchange Bias

The underlying mechanism of exchange bias is the exchange interaction at the interface between the ferromagnetic and antiferromagnetic layers. When the FM/AF bilayer is cooled in an external magnetic field, the antiferromagnetic spins at the interface become pinned in a particular direction[29,30]. This pinning creates an effective field that biases the hysteresis loop of the ferromagnetic layer[29,30]. Key points in the mechanism include:

Cooling Field: The application of an external magnetic field during cooling through the Néel temperature results in the alignment of the AF spins at the interface.

Interfacial Exchange Interaction: The exchange coupling between the AF spins and the adjacent FM spins induces a unidirectional anisotropy in the ferromagnet.

2.6.3 Applications of Exchange Bias

Exchange bias has a multitude of applications in various fields, particularly in magnetic storage and sensing technologies. This is due to its ability to stabilise the magnetic state of ferromagnetic layers and enhance magnetic anisotropy[29,30]. Some key applications include:

Magnetic Recording Media: Exchange bias is employed for magnetic tunnel junctions (MTJs)[31], which are indispensable components in hard disk drives (HDDs)[32] and magnetic random-access memory (MRAM)[31]. The reliability afforded by exchange bias guarantees the consistency of data read/write operations.

Spintronics: In spintronic devices, such as MTJs, exchange bias enhances the magnetic stability of the free and pinned layers, thereby improving device performance and reliability. This is of crucial importance for the development of non-volatile memory technologies and advanced computing architectures[33].

Magnetic Sensors: Exchange-biased sensors, such as anisotropic magnetoresistance (AMR) and giant magnetoresistance (GMR) sensors, are enhanced by the stabilised magnetic states provided by exchange bias, resulting in improved sensitivity and accuracy in detecting magnetic fields[34].

2.7 Single multiferroics

Single multiferroics: The coexistence of ferromagnetism and ferroelectricity in a single material known as single-phase multiferroics is often challenging due to the conflicting requirements of these properties[5]. Ferromagnetism typically arises from the presence of unpaired d-orbitals which promote magnetic ordering, while ferroelectric polarization is often associated with the presence of empty d-orbitals[35]. Consequently, the simultaneous appearance of both ferromagnetism and ferroelectricity in a material is rare and complex due to the conflicting orbital configuration[3,5]. Although single-phase multiferroics can occur in the nature, they can also be engineered through the heterostructures[36].

Material layers which vary from a few nanometers to a few micrometers in thickness are called thin films[37,38]. Thin films have been extensively utilized for decades due to novel properties and diverse applications. One of the most well-known examples of thin film applications is the household mirror, which features a coated reflective metal layer on its backside to generate a mirror image, a process commonly referred as 'silvering'[39,37]. Advances in thin film techniques occurred in the 20th century via technological breakthroughs in magnetic recording media[40,41], electronic semiconductor devices[42,38], LEDs[38], optical coatings[43], hard coatings[37,38], energy storage[38], in pharmaceutical industry via thin film drug delivery[38] and multiferroic combination[36]. These advances have revolutionized numerous sectors and continue to drive innovation across various fields.

Multiferroic heterostructures: Multiferroic heterostructures are one of the very new approaches to complex layer-by-layer structures and heterostructures[36]. Thin film heterostructures also allow magnetostrictive coupling at the interfaces of the ferroelectric layers[37]. As a practical solution to the rarity of single-phase multiferroics and the challenge of obtaining strong multiferroic properties within a single material which combine different films in a heterostructure system provide an effective approach to the multiferroic field. This enables the improvement of physical properties like the generation of magnetoelectric (ME) coupling at the interfaces and the engineering of materials for specific applications (i.e. low or high-temperature applications), this opens new possibilities in materials science and engineering.

Multiferroics heterostructure are an advanced field in material science, which involves different ferromagnetic and ferroelectric material layers, in order to create novel multiferroic systems[44,45]. The distinct properties of each layer could be used to produce composite materials with enhanced multiferroic behavior. Furthermore, the biggest challenge of the multiferroics is to have both ferroelectric and the magnetic properties at the room temperature to be suitable for functional devices [45]. Engineering of heterostructures requires careful a consideration of the layer interfaces, as they significantly influence the properties of the system[45]. The interaction between ferroelectric and ferromagnetic layers at the interfaces is of particular interest, as it can lead to unique phenomena

such as enhanced magnetoelectric coupling, where changes in the magnetic properties affect electric polarization and vice versa[15,46]. The control of layer/stacking thickness[47], material composition[48,49], and crystals alignment[50,51] allows a precise tuning of interactions at the interfaces which enables the customization of heterostructure properties for specific applications. Multiferroics heterostructures are being developed due to their potential for groundbreaking applications in various fields, including advanced electronics, energy-efficient data storage[52,53], and novel sensing technologies[54]. The combination of layers with different functionalities allows devices to operate efficiently at room temperature and to offer superior performance compared to their single-phase counterparts. This is in turn promotes an area of research that could significantly contribute to the development of multifunctional materials and devices[47,52,53,54].

2.8 Material growth techniques

2.8.1 Epitaxial growth modes

Epitaxial growth is a critical technique for thin film production which enables a precise control of the crystallographic orientation on a large single-crystal surface[55]. It is also considered to be a first-order phase transformation where thermodynamics and kinetics plays the main contribution on the so called growth modes such as Frank-van der Merwe, Stranski-Krastanov (SK) and Volmer-Weber (VW)[55,56]. One of the essential parameters in the grown film quality is the film uniformity which could be achieved via Frank-van der Merwe growth mode, known as monolayer-by-monolayer mode (2D growth)[56]. However, VW growth is known as island (3D) growth which could lead to a significant surface roughness due to island formation. The combination of both or an intermediate mode is defined as a combination of Frank-van der Merwe and VW modes[57].

Volmer-Weber (VW) growth: The VW represent the growth mode for which the adatoms have a stronger affinity to the surface of the agglomerate rather than to the substrate surface. Adatoms favor to generate clusters and form three-dimensional objects which are called islands at the substrate surface[57]. Continuation of the deposition leads to growth of islands in vertical and lateral directions where adjacent islands are in contact to each other, coalescence occurs to form a thin film[58]. The driving force behind the any growth is to minimize the surface energy of the system. For VW, both the surface energy and the lattice mismatch between the film and the substrate plays an important role for the interaction of the adatoms. In terms of the surface energy, VW growth is favorable when the surface energy of the substrate γ_{SV} is smaller than the sum of the surface energy of adatoms γ_{FV} and the interface energy between the substrate and the film γ_{SF}, (see Figure 2.5) and Equation (2-6)[57].

$$\gamma_{SV} < \gamma_{SF} + \gamma_{FV} \tag{2-6}$$

The minimization of the energy favors the reduction of the surface/interface area between cluster and vacuum, and between cluster and the substrate which leads to island formation. However, island formation is associated with higher density of defects, which results in an inhomogeneous and discontinuous film consists of coalesced islands with a rough film surface[57].

Frank-van der Merwe growth: The Frank-van der Merwe growth mode occurs when the adatoms have a strong affinity to the substrate rather than the surface of the agglomerate which leads to the formation of a continuous thin film[57]. In this mode, the deposited atoms attach to the surface to form one layer at a time. After completing the first layer, new adatoms attach to form the subsequent monolayer which continues until the deposition has finished. The driving force behind Frank-van der Merwe growth is the minimization of interfacial energy between the film and substrate. Frank-van der Merwe growth is favorable when the surface energy of the substrate γ_{SV} is higher and equal to the sum of surface energy of adatoms γ_{FV}, and the interface energy between the substrate and the film γ_{SF}, see Equation (2-7). This mode is observed when the lattice mismatch between the film and substrate is relatively small. This is shown in Figure 2.5[57]. Frank-van der Merwe growth is characterized by good film uniformity which can lead to films with high quality[59].

$$\gamma_{SV} \geq \gamma_{SF} + \gamma_{FV} \tag{2-7}$$

Stranski-Krastanov (SK) growth: The SK growth mode is an intermediate case between Frank-van der Merwe and VW growth modes[56]. At the first stages of growth, monolayers of the films are grown in a Frank-van der Merwe manner, but as the film thickness increases, strain begins to accumulate in the film due to lattice mismatch or due to the surface energy, Equation (2-7). Eventually, the strain component becomes too large to form islands as a stress relaxation mechanism[60]. SK growth is known to show a balance between interfacial energy minimization and strain relaxation, so that the first layers can grow in the Frank-van der Merwe mode until strain component becomes dominant over the interfacial energy where the thickness exceeds so called critical thickness[57]. As it can be seen in Figure 2.5, the lattice mismatch is in the moderate range for SK growth. Dependent on the resulting film thickness, the morphology consists of the combination of both, planar and three-dimensional islands[57].

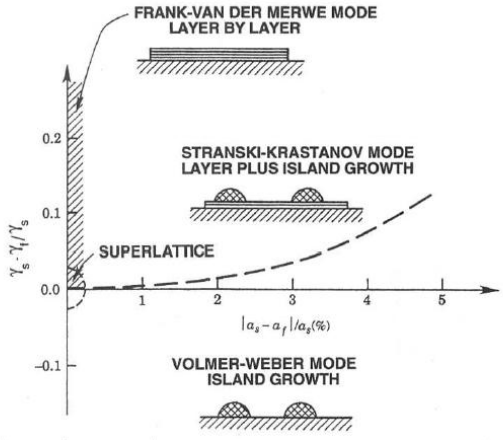

Figure 2.5: Typical growth modes and growth mode variation depending on the lattice mismatch and the surface energy[57].

2.8.2 Growth methods

Understanding and controlling the growth modes is crucial for tailoring thin film properties, in order to obtain desired film structures for the aimed thin film application. Several epitaxial growth methods have been developed so far. Each method offers unique advantages for different types of materials and different types of applications. The deposition process could be divided into three steps to form any deposit. The first one is synthesis/extracting of a material to be deposited. It could be made by the ejection of a material from a source or it could be a chemical reaction of the components of the material which forms from gas or vapor in the chamber[61]. A second step is the transport of the material between the source and the substrate, and the third step is the condensation of the material onto the substrate followed by film nucleation and growth[61]. Physical vapor deposition (PVD) involves the physical principles on ejection and deposition of the material onto a substrate[62]. Transition of the ejected material from the source to the substrate can be caused by thermal processes (i.e., evaporation), plasma-based processes (i.e., sputtering)[62]. An alternative physical process is featured by the deposition of the solid material onto the substrate and could occur by a chemical reaction. This procedure is called chemical vapor deposition (CVD)[62]. Different types of CVD methods are available which depend on the material and the application method, such as atomic layer CVD (ALCVD), metal-organic CVD (MOCVD)[61].

2.8.3 Physical vapor deposition and pulsed laser deposition

Physical Vapor Deposition (PVD) is a fundamental technique for depositing thin films in materials science. It involves the transfer of material without chemical processes in vapor from a source to a substrate. When reaching the substrate, the vapor undergoes condensation which results in the formation of a continuous solid film[57]. PVD is a general term that covers a variety of subtechniques, each characterized by different physical mechanisms for ejecting and depositing material, i.e., sputtering[63], evaporation[64,65], electron-beam physical vapor deposition[66], thermal laser epitaxy[67] or pulsed laser deposition (PLD)[57,65,68]. The most known of these techniques are evaporation and sputtering, which are characterized by their advantages on metallic layer growth with good control on the film thickness, uniformity, deposition rate and less complexity[69]. These attributes particularly make PVD methods suitable for producing specific types of thin films, each tailored for specific applications, highlighting the versatility and adaptability of PVD in the field of thin film technology.

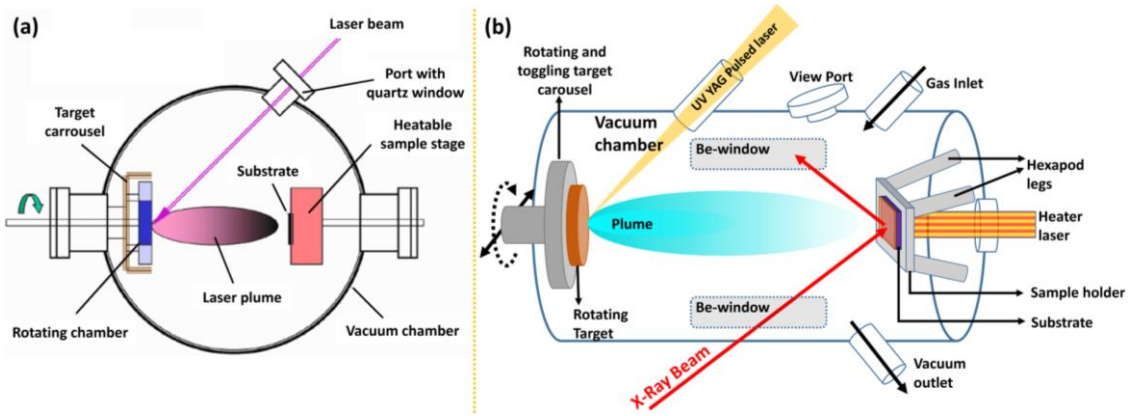

Figure 2.6: (a) A schematic of a commercial PLD chamber[70] and (b) schematic representation of the PLD chamber used in this work. The PLD chamber used in this work differs from the commercial chambers in terms of the Be-windows, and a sample stage mounted on a hexapod which allows in-situ synchrotron experiments. Additionally, the sample holder and the sample heating process is different due to the in-situ experiment concerns.

PLD is emerging as a specialized and highly regarded variant of a PVD process which is well-known for its ability to produce high quality thin films with a particular focus on oxide materials[57,68,71]. The operation principle of PLD involves the use of a high-powered laser, in order to vaporize material from a target[72]. Figure 2.6a shows the schematics of a commercial PLD chamber. Figure 2.6b illustrates the schematic of the PLD chamber used in this work. This vaporized material (called Plume) then propagates, through space to a substrate where it deposits to form a thin film. PLD is able to maintain the stoichiometry of complex materials, which commonly ensures, that the chemical composition of the target material is transferred to the deposited film[65,68,71]. This inherent flexibility of the method in adjusting the film thickness and composition, makes PLD a unique technique in the production of sophisticated thin films for a wide range of applications. In particular, PLD is mentioned for its possibility to grow oxide materials, especially at high temperatures[58], i.e., in the range of 1000 °C. Furthermore, it is even more critical when specific complex oxide films require post-growth annealing, in order to achieve a single crystalline thin film with the desired crystal orientation[73,74], such as BaM and YbFO. The versatility of the technique allows to introduce modifications, such as doping or changing the stoichiometry.

PLD enables the adjustment of the ambient gas pressure, in order to maintain the stoichiometry of the deposited material according to the target. The background gas pressure can range from 10^{-7} mbar (vacuum) to 1 mbar, with the type of gas which depends on the desired material growth. The ambient gas pressure controls the stoichiometry and growth rate. It can also slow down the ablated material through collision with ambient gas atoms[75]. For single film oxides and heterostructures, O_2 is typically used as a background gas[76,77]. Furthermore, the growth rate can also be adjusted by changing the laser pulse frequency, which affects the flux of material which propagates towards the substrate (one monolayer per pulse)[78,79].

Modulating the laser pulse energy or energy density on the target material through PLD can control the stoichiometry of the deposited material[80]. The adjustment of the laser pulse energy and/or spot size affects the energy transferred to the target material and the kinetic energies of the ablated particles[81]. Another advantage of PLD is the ability to grow multiple materials without breaking

the vacuum and without the interruption of the growth process. This allows the growth of multi-layer heterostructures systems in a single run[82].

The optimization of growth parameters is crucial for obtaining high-quality films for specific device applications such as ferroelectric devices and magnetic data storage. Laser pulse energy (i.e., fluence) and energy density transferred to the target (laser fluence) is critical to overcome re-sputtering of the ablated particles and the protection of the substrate from damage caused by the high kinetically energetic particles[83,84]. The kinetic energies of the particles during deposition are of great consequence in determining the resulting film structure and thickness. This concept has been extended to material growth through the introduction of the Structure Zone Diagram (SZD), which allows for the estimation of the resulting structure and film thickness by considering the growth temperature and the energies of the plasma particles. The initial simple model was introduced by Movchan and Demchishin in 1969[85] and was subsequently refined by Anders in 2009[86]. The SZD is for estimating and optimising the growth process of simple structures. However, its application to more complex structures, such as BaM and YbFO, becomes challenging due to the multi-ion nature and tricky composition of these materials. Furthermore, it is important to note that different elements have different energy distributions which depends on their molecular weight. This also affects the stoichiometry of the developing film. However, since the species of particles with higher kinetic energy compete with the background gas to reach the substrate surface, the energy of each becomes important. In some cases, the stoichiometry may not be achieved due to the loss of energy with certain species in the high-pressure background gas[87,88]. It is well recognized that PLD is a highly versatile and valuable deposition method which offers large capabilities in the production of cutting-edge materials for science and technologies fields.

2.9 Study of the crystal quality, microstructure, morphology and stoichiometry

Various methods were utilized, in order to investigate thin film and multiferroic heterostructures materials in terms of crystal quality, microstructure, morphology and stoichiometry. X-ray diffraction (XRD) is commonly used for structural and crystalline quality analysis, often complemented by transmission electron microscopy (TEM) for detailed examination. Atomic force microscopy (AFM) and scanning electron microscopy (SEM) are typically used for morphological studies providing topographical and surface details. X-ray photoelectron spectroscopy (XPS) and energy-dispersive X-ray spectroscopy (EDX) are essential tools for determining stoichiometry which provide insights into bonding states and the elemental composition, respectively.

2.9.1 X-ray diffraction

In this study, XRD represent an essential tool in characterizing the crystalline structure of the PLD-grown thin films and multilayers heterostructures. It provides insights into the film quality by the determination of defect concentration such as grain boundaries, mosaic boundaries and mosaic tilt, dislocations and lattice strain[89,90,91,92,93,94,95,96,97,98]. XRD patterns offer a fundamental understanding of the crystallographic structure of the material. Deep and more detailed analysis could be performed by means of two dimensional 2-D reciprocal space mapping, recorded with

high-resolution (2D-HR-RSM) by using a well collimated X-ray beam, a single counting detector with fast read-out in the millisecond range and small pixel size in the micrometer range. These XRD capabilities can reveal in-depth microstructural details and enables to distinguish between defects in lateral and vertical growth directions of the film and to detect any structural fluctuation along the growth direction of the heterostructures as well as in the transverse direction[96,97,98].

$$2d_{hkl}sin\theta = n\lambda \tag{2-8}$$

The fundamental part of XRD is based on the Bragg's Law (Equation 2-3)[95]. It describes the relation between a diffracted X-ray beam at successive crystal planes with distance d_{hkl} at an angle θ and the n-multiple of the X-ray wavelength λ. The equation is satisfied if the difference of the path length of the incident and diffracted beams at successive lattice planes is equal to $n*\lambda$ for certain angles[99]. Constructive interference of the x-rays takes place if both sites of Equation (2-8) are equal. In the equation, n is then an integer and represents the diffraction order. The (h, k, l) are the miller indices of the crystal planes. A schematic representation of the Bragg diffraction is shown in Figure 2.7a. Bragg's law allows us to determine the crystal lattice parameters, and the orientation of the film[95,96,97]. XRD and Bragg's law are crucial in the study of thin films, i.e., the crystalline structure and elemental phases of materials. This approach is the key to statistically identifying materials and gaining a deeper understanding of their properties. Here we distinguish in the coplanar diffraction between the symmetric X-ray diffraction (SXRD) where the diffracting crystal planes (0, 0, l) are parallel to the film surface and the asymmetric X-ray diffraction (ASXRD) which originates from the diffraction planes inclined to the surface with the miller indices (h, k, l, ≠0).

2.9.1.1 High-resolution reciprocal space mapping

High-Resolution Reciprocal Space Mapping (HR-RSM) is a sophisticated X-ray diffraction technique that provides detailed insights into the crystallographic structure of thin films[95]. HR-RSM is particularly valuable for understanding the epitaxial relationships and strain states within multilayered structures[97]. Due to the development of the X-ray detection systems (i.e., fast read out, high counting rate, pixel size), the acquisition of the 2D-(HR-RSMs) are frequently employed in the X-ray laboratory facilities as well as in the synchrotron facilities. Nevertheless, thanks to throughput of high photon flux at the synchrotron, the acquisition time for 2D-(HR-RSM) is in the range of a few minutes. By using a linear detector or 2D-dimensional areas detectors, it is possible to scan the Ewald sphere in the three dimensions and to produce 3D-(HR-RSMs). Several structural parameters could be accurately determined from the HR-RSMs after applying the background correction considering the instrumental function of the setup such as in-plane and out-of-plane lattice parameters, strain relaxation and lattice mismatches between the film and substrate[95,97].

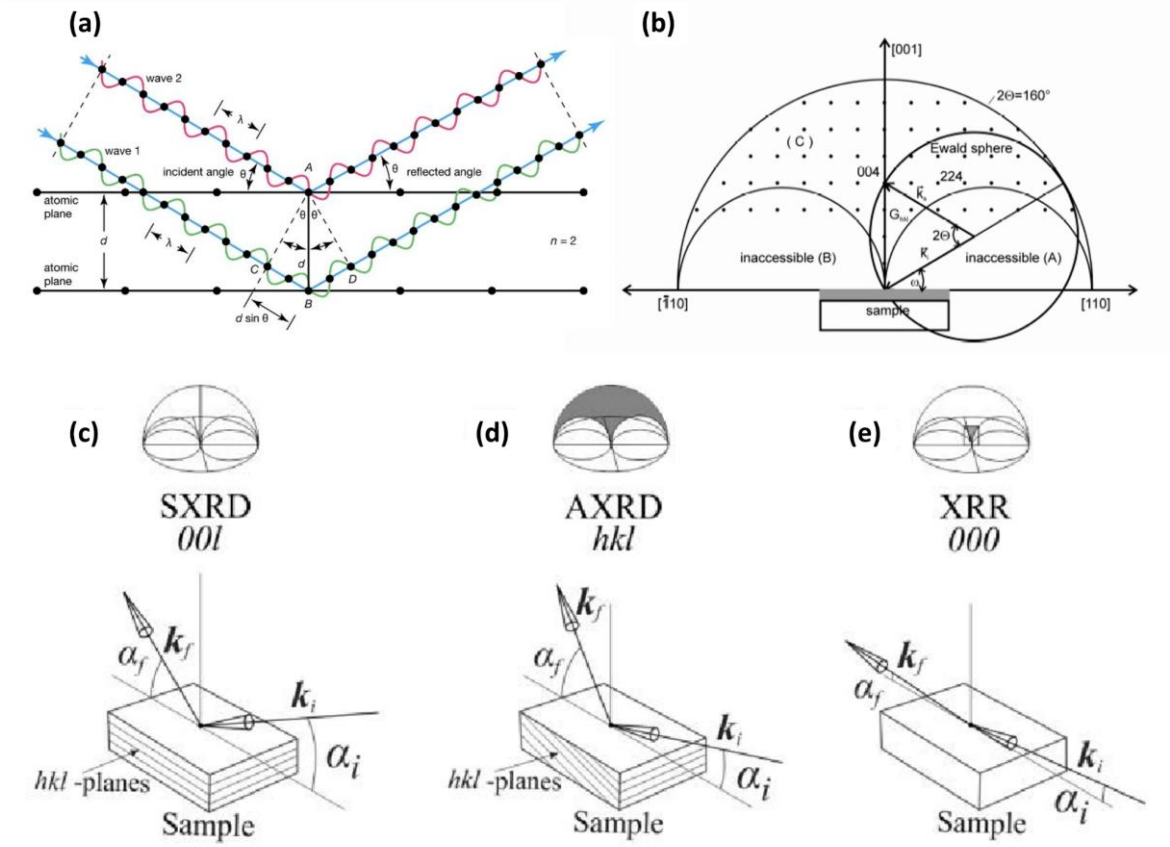

Figure 2.7: (a) Schematics of X-ray diffraction, the illustration shows the incident beam and the reflected beam together with the representative crystalline structure where Bragg diffraction occurs[100], (b) a representative section from reciprocal space of a film grown along [001] direction, indicated that accessible and inaccessible regions in reciprocal space and Ewald's Sphere[101] and (c-e) diffraction geometries of thin films and corresponding regions indicated in reciprocal space (c) symmetrical XRD (SXRD), (d) asyymetrical XRD and (e) X-ray reflectivity[101], for detailed view, refer to Figure A-2.

Figure 2.7b shows a segment of the reciprocal space map of a film grown along the [001] direction which highlights both the accessible and inaccessible reflection regions. It also illustrates the Ewald's sphere and the diffraction vectors which provides a comprehensive view of the film's crystallographic structure. Figure 2.7c displays symmetric and asymmetric XRD patterns in coplanar geometries as well as the X-ray reflectivity (XRR) geometry. The diagram shows the correlation between these patterns and their corresponding regions in the reciprocal space which provides a visual representation of the various scattering phenomena.

2.9.1.2 Williamson-Hall approach

The Williamson-Hall (W-H) is an analytical approach dedicated for the determination of the film microstructure. It is based on the mosaic model and assimilates the film as a system composed of mosaic blocks which have lateral $< L_H >$ and vertical $< L_V >$ mean sizes and are misaligned with respect to the surface normal with a degree of misorientation. This model can be used, in order to evaluate the microstructural properties of crystalline materials from the angular and radial broadening of a set of symmetric reflections. By plotting the full width at half maximum (*FWHM*) of

the angular and the radial diffraction profiles against the scattering vector, the W-H method allows for the estimation of the mean crystallite size, mean value of the lattice strain distribution and mean mosaic tilt[98,147]. The slope and intercept of the linear plot of radial direction provide insights into the average vertical mosaic block size and the degree of strain in the material, respectively. Similarly, the slope and the intercept of the linear plot of the angular broadening provide the information about the average lateral mosaic block size and the mean mosaic tilt, respectively.

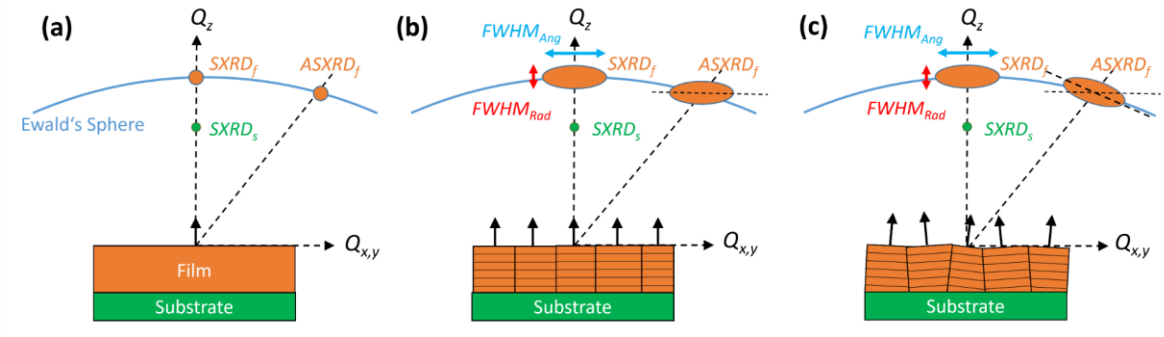

Figure 2.8: A schematic of the thin films and the representative RSM influence due to the defects originated in the film structure where (a) there is no defect in the film and the reflections appear as points, no broadening, (b) there is mosaic blocks and but no tilt which appears to be the broadening in both RSMs of SXRD and ASXRD, (c) there is mosaic blocks and mosaic tilt which appears as broadening and tilt of RSM of ASXRD. ($SXRD_f$ and $ASXRD_f$ stand for film reflections, $SXRD_s$ stands for substrate reflections), for detailed view, refer to Figure A-3.

Figure 2.8 shows a schematic representation of thin films which compare defect-free structures with those that exhibit mosaicity as a form of defect. It also demonstrates how these microstructural variations theoretically appear in reciprocal space maps (RSMs) of symmetric (SXRD) and asymmetric (ASXRD) X-ray diffraction. The diagram shows that an increase in defect concentration usually results in the broadening of reflections in the corresponding reciprocal direction. This effectively illustrates the impact of crystal quality on the diffraction pattern.

2.9.2 X-ray reflectometry

X-ray reflectometry (XRR) is a non-destructive analytical technique which is used to characterize thin films multilayer heterostructures[102]. It provides insights into the film thickness, density, roughness, and interfacial quality of the material layers[102]. The principle of XRR is based on measuring the intensity of X-rays reflected from a material as a function of the incident angle. X-rays undergo a total external reflection when they impinge on a material surface at very low angles[102] (i.e. incident angles ranging from 0-3 degrees). As the angle increases, reflectivity sharply decreases, and this behavior is sensitive to the electron density profile perpendicular to the surface[103]. By analyzing the reflected intensity oscillations (Kiessig fringes[104]), which result from the constructive and destructive interference of X-rays reflected from different interfaces, one can extract information about layer thickness, density variations, and interface roughness[102]. The reflectivity curve, obtained by recording the intensity of the reflected X-ray beam as a function of the incident angle, is analyzed to determine the structural parameters of the film. XRR is espe-

cially useful for analyzing thin films because of its high sensitivity to surface and interface structural features. It can probe layers with thicknesses ranging from a few to several hundred nanometers[102].

2.9.3 Microscopy methods

Microscopy methods offer a window into the microstructure, morphology and surface characteristics of materials at the microscopic level. These techniques are indispensable in complementing the information obtained through X-ray diffraction and spectroscopy and provide a more comprehensive understanding of the material structure.

2.9.3.1 Transmission electron microscopy

Transmission electron microscopy (TEM) stands as a pivotal technique in the study of thin films and nanostructures. It provides high-resolution images which allow for the visualization of atomic arrangements, defects, and interfaces within materials[80,105,106]. TEM is particularly useful in elucidating the crystalline structure, phase identification, and defect analysis at the atomic scale[107]. High resolution TEM gives an image within spatial resolution at the atomic level and contributes to deeply understand the influence of the microstructural features on the resulting physical properties[107].

2.9.3.2 Scanning electron microscopy

Scanning electron microscopy (SEM) is an essential tool for examining the surface morphology and topography of materials[58]. SEM utilizes a focused beam of electrons to create high-resolution images which allow detailed observation of surface features at the nanometer scale[108]. This method is particularly effective for analyzing the surface roughness, grain size, and texture of thin films[109,110]. SEM images can reveal surface defects, cracks, and the homogeneity of coatings which delivers vital information for understanding the relationship between surface characteristics and material properties.

2.9.3.3 Atomic force microscopy

Atomic force microscopy (AFM) is a high-resolution imaging technique that maps the surface topography at the atomic level[58]. AFM operates by scanning a sharp tip over the sample surface and measures the forces between the tip and the sample to produce 3D topographical maps[80]. This method excels in determining surface roughness, particle size, and material homogeneity[80]. AFM is invaluable for studying the nanoscale features of thin films, including surface irregularities[111] and layer thickness[112] which significantly contributes to the comprehensive analysis of material morphology.

2.9.4 Spectroscopy

Spectroscopy techniques are important in analyzing the chemical composition and electronic structure of materials[113,114]. These methods provide insights into elemental distribution[115], bonding states[116], and the presence of impurities or secondary phases[117] which are crucial for understanding material properties.

2.9.4.1 X-ray photoelectron spectroscopy

X-ray photoelectron spectroscopy (XPS) is a surface-sensitive technique that measures the elemental composition and chemical states of materials up to 10 nm film thickness. XPS analyzes the energy distribution of electrons ejected from the material surface when irradiated with X-rays which enables the determination of the chemical environment and oxidation states of elements within ten nanometers from the film surface.

2.9.4.2 Energy dispersive X-ray spectroscopy

Energy dispersive X-ray spectroscopy (EDX) was often coupled with SEM or TEM in our investigation for the single and multiferroic heterostructures. It provides elemental analysis and chemical characterization of materials[118]. EDX detects X-rays emitted from the sample during electron beam irradiation allow the determination of the chemical composition along the growth direction at the cross-section[80]. This method is essential for the determination of the elemental distribution and stoichiometry in thin films, multilayer heterostructures[80] and nanostructures.

2.10 Characterization of magnetic properties

Characterizing magnetic properties is essential for understanding the behavior of materials in different magnetic states as mentioned before, including paramagnetic, diamagnetic, ferromagnetic, antiferromagnetic, and ferromagnetic[20]. It involves examining how materials respond to external magnetic fields under various conditions such as temperature and field orientation. Magnetic characterization reveals key properties like magnetic susceptibility, coercivity, remanence, and magnetic anisotropy[20]. Insights like magnetic susceptibility, coercivity, remanence, and magnetic anisotropy are crucial for applications ranging from data storage to medical imaging and sensor technologies[20,80,107,119]. In the following, we introduce the different key parameters related to magnetic properties of the single layer and heterostructures. For those parameters Vibrating Sample Magnetometry (VSM), Superconducting Quantum Interference Device (SQUID) magnetometry, and Magnetic Force Microscopy (MFM) techniques are used in this work.

Different Magnetic States: An in-depth exploration of various magnetic states, such as paramagnetism, ferromagnetism, ferrimagnetism, and antiferromagnetism, with a focus on their distinct characteristics and occurrences in different materials[20].

Curie Temperature T_C: The temperature at which a ferromagnetic material transitions to a paramagnetic state which represents thermal stability and phase transitions[20].

Exchange Bias (EB): A phenomenon observed in heterostructures composed of ferromagnetic and antiferromagnetic layers. This effect, characterized by a shift in the hysteresis loop along the applied field H, is crucial in understanding magnetic interfacial coupling and its applications in spintronic devices[120,121].

2.10.1 Vibrating Sample Magnetometry (VSM)

Vibrating sample magnetometry (VSM) is a technique used to measure the magnetic properties of a material by detecting the voltage induced in pickup coils by a vibrating sample. The sample is placed in a uniform magnetic field and is mechanically vibrated. The magnetic dipole moments in the sample generate a time-varying magnetic flux, which induces a voltage in the surrounding pickup coils. VSM (see Figure 2.9a and 2.9b) is often used to measure the hysteresis loops to determine coercivity, remanent magnetization, and saturation magnetization, to measure magnetic anisotropy, domain behaviour, to analyse the magnetic phase transitions and temperature-dependent magnetization.

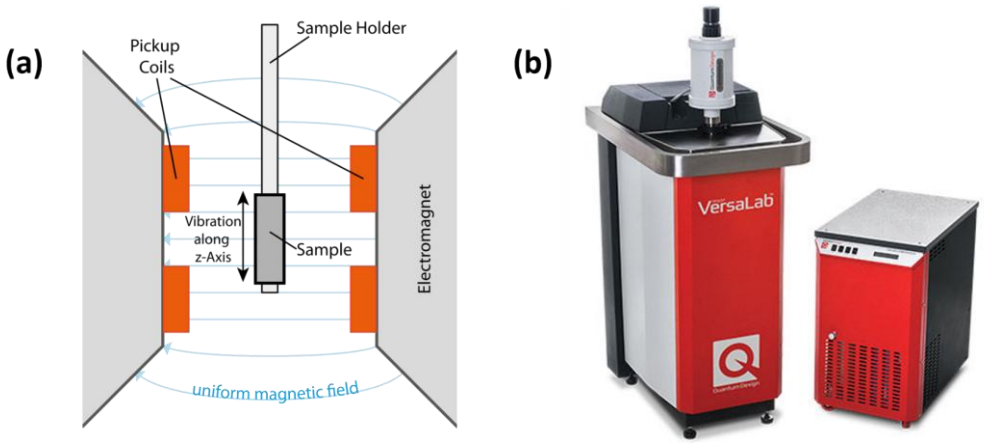

Figure 2.9: (a) Schematic representation of a typical VSM, (b) the VSM device used in this work from Quantum Design (see reference for the specifications)[122].

It is advantageous because of high sensitivity (lower than E-7 range)[123] and precision, capabilities to measure wide range of magnetic fields and temperatures, additionally it is non-destructive and versatile for various sample types. On the other hand, it has some limitations such as, sample shape and size and limited spatial resolution compared to microscopic techniques. These affect the quality of the measurement.

2.10.2 Superconducting Quantum Interference Device (SQUID) Magnetometry

SQUID magnetometry is one of the most sensitive techniques for measuring extremely small magnetic signals. It operates based on the quantum interference of superconducting loops. A SQUID consists of two Josephson junctions in a superconducting loop. When a sample is placed in an external magnetic field, the magnetic flux through the SQUID changes, leading to a change in the current through the Josephson junctions[124]. This change is detected as a voltage, which is proportional to the magnetic moment of the sample. SQUID is often used to measure the weak magnetic signals (lower than E-8 range)[125], to measure the magnetic properties at low temperatures, and characterizing the superconducting materials and small magnetic particles. It is advantageous due to high sensitivity, high precision, capability to reach higher applied fields and capabilities to operate at very low temperatures (i.e. 2K). On the other hand, it is an expensive method

and it is a complex setup to set for cryogenic temperatures where the calibration and handling of the setup must be done carefully.

2.10.3 Magnetic Force Microscopy (MFM)

Magnetic Force Microscopy (MFM) is a type of scanning probe microscopy that maps the magnetic forces near the surface of a sample. A sharp magnetic tip scans the surface of the sample, and the magnetic interactions between the tip and the sample's magnetic domains are detected. The deflection of the cantilever holding the tip is measured, providing information about the magnetic landscape of the sample. The typical applications of the MFM are high-resolution imaging of magnetic domain structures, study of magnetic materials at the nanoscale and investigation of magnetic storage media, thin films, and patterned magnetic structures. MFM is advantages such as high lateral resolution (around 10 nm)[126,127], capable of image the magnetic domains and domain walls and it is non-destructive method where the prior sample treatment is not necessary[128]. On the other hand, it is limited to the surface magnetic states, it requires specialized cantilevers having low lifetime, cantilever calibration is crutial and it is very sensitive to environmental effects such as vibrations, noise and external electromagnetic fields[129].

3 Material of interest

Studying multiferroic thin films requires electrodes on both sides of the film, in order to obtain a contact during multiferroic measurements[130]. To address the conductivity issue, several options can be considered for the bottom electrode, including using a conductive substrate i.e. $SrTiO_3$ doped with Nb (STO:Nb)[16,131] conductive oxides such as $LaNiO_3$ (LNO)[130], (La,Sr)CoO_3 (LSCO)[132,133], $SrRuO_3$[134] or a conductive metal film, e.g., Platinum[135,136].

A suitable electrode for the multiferroic heterostructure is crucial to carefully select the material and the appropriate deposition method for obtaining a conductive layer with good adhesion and high crystalline filling factor beneath the multiferroic structure with high quality and desirable properties. The epitaxial growth of films requires a low lattice mismatch to promote the desired metastable phases of the functional layer[137]. The desired orientation of the multiferroic layer should also be supported by the crystal symmetry of the substrate/bottom electrode[106,137,138]. In addition, the bottom electrode must be chemically and physically stable to withstand the high temperature processes which are involved in the growth or in the annealing of multiferroic oxide films. These processes often occur at elevated temperatures (> 900 °C)[106,137,138].

Considering the bottom electrode and the following growth sequences, a general roadmap of the thesis, selected materials and the steps are shown in Figure 1.2, where platinum bottom electrode to be first optimized and following the optimized material, BaM and YbFO layers will be investigated to open the pathway for combination of all 3 materials to produce a multiferroic device.

Platinum

As mentioned above, there are several bottom electrode options that could be used which depend on the specific material and application. Concerning conductive substrates, there has been a significant amount of research on oxide conductive layers as well as thin metallic films, including gold, silver and platinum[139,140,141,142,143].

Platinum bottom electrodes offer several advantageous properties that make them suitable for multiferroic thin film investigations. They can be produced as high-quality single crystalline films by using PLD[144] with a preferred orientation of (111) on YSZ(111)[138] and Al_2O_3(0001)[106] substrates which promotes the formation of desired metastable phases multiferroic materials, i.e., *h*-$YbFeO_3$, *h*-$LuFeO_3$[106]. Additionally, the lattice mismatch between interplanar spacing of Pt(-110) planes and the in-plane lattice parameter a_0 of some thin films becomes smaller in the case of a platinum interlayer integration into the system compared to the layers grown on the bare substrates[107]. This facilitates epitaxial growth with a preferred orientation of the functional films.

Platinum serves as a dual role when it is used as a bottom electrode. On one hand, it acts as an effective buffer layer, which improves the overall quality of subsequent layers by reducing the lattice mismatch between the layer and substrate[107]. On the other hand, platinum functions as a reliable bottom electrode which is essential for ferroelectric measurements[106,144].

The combination of these properties makes platinum a versatile and advantageous element as a bottom electrode in multiferroic thin film research that facilitates the exploration and understanding of unique multiferroic phenomena. One of the important milestones in the thesis is to find the most optimum PLD-growth parameter for the Pt bottom electrode for the FM and FM layers.

Barium Hexaferrite $BaFe_{12}O_{19}$

Barium Hexaferrite (BaM) is a widely recognized hard ferromagnetic material, known for its high coercivity and excellent chemical stability, which makes it a strong contender for various magnetic applications, particularly in high-density magnetic recording media. Its robust magnetic properties are primarily due to its structure and strong anisotropy. The epitaxial growth of BaM thin films requires a precise control over the deposition conditions, in order to achieve the desired crystallographic orientation and magnetic properties. This work focuses also on proposing optimum growth conditions for BaM films to ensure a high-quality crystal structure and superior magnetic characteristics. The magnetic properties of the films were analyzed in terms of coercivity, magnetization, and anisotropy. The study focused on understanding the influence of microstructural characteristics such as grain size, orientation, and strain on their magnetic behavior. The integration of BaM as a ferromagnetic layer in multiferroic heterostructures offers new possibilities for creating advanced magnetoelectric devices. BaM has suitable (i.e. possibility to grow in c-axis orientation for perpendicular recording medium)[107] magnetic properties and is compatible with ferroelectric materials.

***h*-$YbFeO_3$**

YbFO is a rare-earth orthoferrite material that exhibits multifunctional properties that include ferroelectricity and antiferromagnetism. It is of particular interest for multiferroic applications due to its canted antiferromagnetic structure which allows the coexistence of magnetic and electric orders. The synthesis of high-quality YbFO thin films is crucial for harnessing its multiferroic potential. This thesis thoroughly investigates the optimization of the PLD epitaxial growth of YbFO films for proper crystallographic orientation, defect-free crystals and stoichiometry. Special attention is paid to interface investigation of YbFO heterostructures, in order to enhance magnetoelectric coupling and to achieve functional multiferroic devices. The study examines the magnetic and ferroelectric properties of YbFO depending on the PLD growth conditions and how this could affect the heterostructure design.

Multiferroic heterostructures $BaFe_{12}O_{19}$/*h*-$YbFeO_3$

This thesis focuses on the investigation of BaM and YbFO as integral components of multiferroic heterostructures with two stacking sequences. The study considers the complex interdependencies of structural, magnetic, and ferroelectric properties in these advanced material systems. The knowledge gained from this study shall pave the way for the rational design of next generation multiferroic devices with optimized performance and novel functionalities.

3.1 Pulsed laser deposition of investigated materials

The samples were subjected to a three-step-pre-treatment procedure prior to the PLD growth process. As first YSZ (111) substrates were cleaned by sonication in three consecutive steps by using acetone, isopropanol and ultrapure water, 15 minutes each, followed by drying with nitrogen gas. Secondly, cleaned substrates were annealed in a tube furnace at 1200 °C under air for 2 hours, in order to improve the surface roughness[145]. As a last step, annealed substrates were re-cleaned by applying the first step to avoid contamination during annealing. The substrates were measured by AFM and XRR to confirm their surface roughness and cleanliness. This section will deal with a detailed listing of the PLD growth conditions which were selected after an iterative to figure out the most optimum deposition parameters.

Platinum growth

For the platinum growth, the substrates were heated up under vacuum (~$1x10^{-7}$ mbar) by a rate of 25 °C/min. The layers were grown by using an energy per pulse of 60 mJ (12.5 J/cm^2), a laser pulse frequency of 5 Hz and a target to substrate distance of 35 mm. The samples were produced by varying growth temperatures T_g = 300 °C, 500 °C, 700 °C and 900 °C and by employing 25586, 18900, 19900 and 16470 shots, respectively. The number of shots were calibrated by using the growth rates from a previous publication, in order to have similar thicknesses of around 100 nm[58]. In order to vary the thickness at the growth temperature T_g = 900 °C the number of shots were varied by 1647, 4100, 8235, 12350 and 16470 which resulted in thicknesses of around 10 nm, 25 nm, 40 nm, 55 nm and 70 nm, respectively. After the growth the samples were cooled down to room temperature by a rate of 5 °C/min.

Table 3-1: Sample names and growth parameters used for platinum layers with varied growth temperature, investigated in Chapter 4.

Sample name (in Chapter 4)	**PtT300**	**PtT500**	**PtT700**	**PtT900**
Growth temperature (T_g) [°C]	300	500	700	900
Number of shots (*Nsh*) [#]	25586	18900	19900	16470
Chamber pressure [mTorr]	Vacuum	Vacuum	Vacuum	Vacuum
Estimated films thickness (*Th*) [nm]	90	88	90	108
Laser frequency (*F*) [Hz]	5	5	5	5
Energy per pulse [mJ] / Laser fluence [J/cm^2]	60 / 12.5	60 / 12.5	60 / 12.5	60 / 12.5
Target-substrate distance (*TS*) [mm]	35	35	35	35
Applied characterization methods	XRR, TEM, HRXRD, HRTEM/EDX, investigated in Chapter 4			

Table 3-2: Sample names and growth parameters used for platinum layers with different thicknesses, investigated in Chapter 4.

Sample name (in Chapter 4)	**Pt_Th10nm**	**Pt_Th25nm**	**Pt_Th40nm**	**Pt_Th55nm**	**Pt_Th70nm**
Growth temperature (T_g) [°C]	900	900	900	900	900
Number of shots (*Nsh*) [#]	1647	4100	8235	12350	16470
Chamber pressure [mTorr]	Vacuum	Vacuum	Vacuum	Vacuum	Vacuum
Film thickness (*Th*) [nm]	13	30	49	63	80
Laser frequency (*F*) [Hz]	5	5	5	5	5
Energy per pulse [mJ] / Laser fluence [J/cm^2]	60 / 12.5	60 / 12.5	60 / 12.5	60 / 12.5	60 / 12.5
Target-substrate distance (*TS*) [mm]	35	35	35	35	35
Applied characterization methods	XRR, TEM, HRXRD_RSMs, HRTEM/EDX, investigated in Chapter 4				

$BaFe_{12}O_{19}$ growth

The BaM films were grown on Pt templates and YSZ (111) substrate. The Pt films with varying film thickness, mentioned above, were used as templates for a subsequent BaM film growth. The samples are heated up to T_g = 900 °C under an O_2 partial pressure of P_{O_2} = 400 mTorr with a heating rate of 25 °C/min. Three BaM samples (BaMPtTh0, BaMPtTh25 and BaMPtTh75) were produced for which Pt_Th0 (YSZ (111)), PtTh25 and PtTh75 was used as templates. BaMPtTh0, BaMPtTh25 and BaMPtTh75 were grown by using T_g = 900 °C, P_{O_2} = 400 mTorr, pulse energy 75 mJ (5.1 J/cm^2), laser pulse frequency 1 Hz, target-to-substrate distance 40 mm and number of shots 6666sh, 8465sh and 6666sh, respectively. Another sample was grown by varying pulse energy to 25 mJ (1.5 J/cm^2) with the number of shots of 20000 by using the same growth parameters as the other BaM samples on template Pt_Th75. The number of shots is calibrated to have similar thicknesses which is obtained by 75 mJ. Grown samples were cooled down to room temperature under O_2 partial pressure of 400 mTorr with a cooling rate of 5 °C/min.

Table 3-3: Sample names and growth parameters used for BaM layers with varied laser fluence and interface layer Pt thickness, investigated in Chapter 5.

Sample name (in Chapter 5)	**BaMPtTh0**	**BaMPtTh25**	**BaMPtTh75**
Growth temperature (T_g) [°C]	900	900	900
Number of shots (*Nsh*) [#]	6666	8465	6666
Oxygen pressure [mTorr]	400	400	400
BaM Film thickness (Th_{BaM}) [nm]	169	151	163
Laser frequency (*F*) [Hz]	1	1	1
Energy per pulse [mJ] / Laser fluence [J/cm^2]	75 / 5.1	75 / 5.1	75 / 5.1
Target-substrate distance (*TS*) [mm]	40	40	40
Interface layer type	No Pt	Pt	Pt
Interface layer thickness (Th_{Pt}) [nm]	0	25	75
Pt Interface layer growth condition	Table 3-2		
Applied characterization methods	XRR, TEM, VSM HRXRD_RSMs, HRTEM/EDX, investigated in Chapter 5		

Table 3-3: continued.

Sample name (in Chapter 5)	**BaMF25mJ**	**BaMF75mJ**
Growth temperature (T_g) [°C]	900	900
Number of shots (*Nsh*) [#]	20000	6666
Oxygen pressure [mTorr]	400	400
BaM Film thickness (*Th*) [nm]	140	140
Laser frequency (*F*) [Hz]	1	1
Energy per pulse [mJ] / Laser fluence [J/cm^2]	25 / 1.5	75 / 5.1
Target-substrate distance (*TS*) [mm]	40	40
Interface layer type	Pt	Pt
Interface layer thickness Th_{Pt} [nm]	75	75
Pt Interface layer growth condition	Table 3-2	
Applied characterization methods	XRR, TEM, VSM HRXRD_RSMs, HRTEM/EDX, investigated in Chapter 5.	

h-$YbFeO_3$ growth

YbFO films were grown on Pt templates and YSZ (111) substrates. Pt films with varying film thicknesses (Pt_Th10nm, Pt_Th25nm, Pt_Th40nm, Pt_Th55nm and Pt_Th75nm) and varying growth temperatures (PtT300, PtT500, PtT700 and PtT900) were used as templates as well as YSZ (111) (PtTh0) substrates for a subsequent YbFO film growths The growth parameters of *h*-

$YbFeO_3$ films were not varied, in order to investigate the effect on the YbFO film quality by means of an interface layer. The templates were heated up to the growth temperature T_g = 900 °C under 400 mTorr O_2 partial pressure with a rate of 25 °C/min. The laser pulse energy is adjusted to 25 mJ per pulse (1.5 J/cm^2). The laser frequency is set to 1 Hz and target-to-substrate distance is fixed to 40 mm. 20000 shots were used to grow YbFO films which possess a thickness of *Th* = 100 nm. The grown films were cooled down to room temperature under the same partial ambient pressure P_{O_2} = 400 mTorr O_2 with a cooling rate of 5 °C/min.

Table 3-4: Sample names and growth parameters used for YbFO layers with varied interface layer Pt thickness, investigated in Chapter 6.

Sample name (in Chapter 6)	**YbPt_Th 0nm**	**YbPt_Th 10nm**	**YbPt_Th 40nm**	**YbPt_Th 55nm**	**YbPt_Th 70nm**
Growth temperature (T_g) [°C]	900	900	900	900	900
Number of shots (*Nsh*) [#]	20000	20000	20000	20000	20000
Oxygen pressure [mTorr]	400	400	400	400	400
YbFO Film thickness ($Th_{Y\text{-}bFO}$) [nm]	95	129	126	106	120
Laser frequency (*F*) [Hz]	1	1	1	1	1
Energy per pulse [mJ] / Laser fluence [J/cm^2]	25 / 1.5	25 / 1.5	25 / 1.5	25 / 1.5	25 / 1.5
Target-substrate distance (*TS*) [mm]	40	40	40	40	40
Interface layer type	No Pt	Pt	Pt	Pt	Pt
Interface layer thickness (Th_{Pt}) [nm]	0	10	40	55	70
Pt Interface layer growth condition	NA	Table 3-2			
Applied characterization methods	XRR, TEM, SQUID, HRXRD_RSMs, HRTEM/EDX, investigated in Chapter 6				

Multiferroic heterostructures $BaFe_{12}O_{19}$ /*h*-$YbFeO_3$

BaM and YbFO were grown sequentially on YSZ111 substrates by using two stacking sequences named M1 ($BaFe_{12}O_{19}$/*h*-$YbFeO_3$/YSZ111) and M2 (*h*-$YbFeO_3$/$BaFe_{12}O_{19}$/YSZ111), in order to design multiferroic heterostructures. The PLD growth conditions applied for M1 and M2 are summarised in the table below.

Prior to any characterization, structure and property investigations involved in the thesis, for all samples, which are listed in Table 3-1, 3-2, 3-3, 3-4 and 3-5, the surfaces were sequentially cleaned by sonication in acetone, isopropanol and ultrapure water, 5 min each. After ultrapure

water sonication the sample surface was dried with nitrogen gas. This procedure was conducted before the MFM measurements, in order to avoid the destruction of the remanent magnetic domain structure of the sample.

Table 3-5: Sample names and growth parameters used for multiferroic heterostructures with alternated stacking sequence, investigated in Chapter 7.

Sample name (in Chapter 7)	**M1 ($BaFe_{12}O_{19}$/$YbFeO_3$/YSZ111)**	**M2 ($YbFeO_3$/$BaFe_{12}O_{19}$/YSZ111)**
Growth temperature (T_g) [°C]	900	900
Number of shots BaM (*Nsh*) [#]	10000	10000
Number of shots YbFO (*Nsh*) [#]	10000	10000
Oxygen pressure [mTorr]	400 mTorr for BaM and YbFO	400 mTorr or BaM and YbFO
Target-substrate distance (*TS*) [mm]	40 mm for BaM and YbFO	40 mm or BaM and YbFO
Laser frequency (*F*) [Hz]	1 Hz for BaM and YbFO	1 Hz for BaM and YbFO
Energy per pulse [mJ] / Laser fluence [J/cm^2]	25 mJ (1.5 J/cm^2) for BaM and YbFO	25 mJ (1.5 J/cm^2) for BaM and YbFO
Interface layer type	No	No
Applied characterization methods	XRR, HRXRD_RSMs, TEM, HRTEM/EDX, investigated in Chapter 7	

3.2 Description of applied characterization techniques

The goal on this section is to present all technical details for the applied characterizations methods which include the specifications of the device resolutions, type of the detection systems, sample and geometrical configurations which were utilized in the different studies organized in the different chapters. This part summarizes the experimental section of the whole work.

3.2.1 X-ray reflectivity measurements

X-ray reflectivity measurements were systematically applied for all the samples listed in the Table 3-1, 3-2, 3-3, 3-4 and 3-5. They were recorded at room temperature in air by using the X-ray diffractometer Rigaku SmartLab with a rotating anode for a monochromatic beam of wavelength of $\lambda_{Cu_{K\alpha}} = 1.5419$ Å. The beam width was set to 3 mm by a horizontal slit and was set to 0.05 mm by a slit in the vertical direction. The data were collected over a range of angles from 0.0° to 6.0° with a step size of 0.01° and an exposure time of 1.5 sec/step.

The data analysis was carried out by using the Bruker Leptos 7 software package. The thickness, roughness and the density of the films as well as the interface properties between the layers were calculated by utilizing the fitting model provided by the software, which assumes a multilayer structure. The quality of the fits was assessed by the reduced chi-squared statistic.

3.2.2 High-resolution X-ray diffracton reciprocal space mapping

High-resolution X-ray diffraction reciprocal space mapping (HRXRD_RSM) was performed at the NANO beamline at the synchrotron facility KARA Karlsruhe Germany by using a well collimated and monochromatic beam with an energy of 15 keV. The utilized experiment set-up for the thesis was formerly described in detail by Bauer et al.[146] It includes a heavy-duty diffractometer with eight degrees of freedom for the sample motions and two for one detector arm motion. This diffractometer can be coupled with the in-situ PLD chamber to follow the evolution of the structure during the growth. The experimental setup can be seen in Figure 3.1.

For the different layers Pt, BaM and YbFO which belong to the samples listed in Table 3-1, 3-2, 3-3, 3-4 and 3-5, all the coplanar symmetric and asymmetric reflection orders were recorded by rocking the sample around the Bragg angle. For this measurement a linear Mythen detector was positioned at the Bragg angles which corresponded to the different reflections. An X-ray energy of 15 keV and a distance of 1114 mm from the sample-detector was adjusted, in order to define an angular resolution of 0.0027 degree per channel.

For the Pt film the HRXRD_RSMs of the Pt111, Pt222 and Pt333 reflections were measured. While for the BaM layer, the HRXRD_RSMs of the (004), (006), (008), (0010), (0012), (0014), (0016), (0022), (0024)) symmetric reflections and two asymmetric reflections (i.e. (-2022) and (-2024)) were recorded in same manner. Finally, the HRXRD_RSMs of YbFO004, YbFO006, YbFO008 symmetric reflections and YbFO108 asymmetric reflection were measured. Furthermore, the HRXRD_RSMs of the YSZ substrates YSZ111, YSZ222 and YSZ333 were also measured as references and for the determination of the lattice parameters of the films with respect to the substrate.

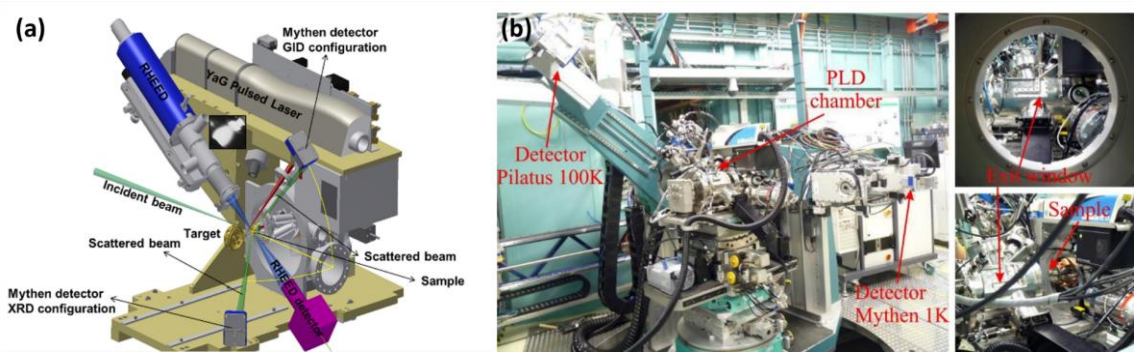

Figure 3.1: (a) 3D schematic and (b) the images of the diffractometer and the PLD setup placed in NANO beamline in KARA light source in KIT Karlsruhe.

A common data analysis procedure, including background subtraction, was applied on the different HRXRD_RSMs which corresponded to the different reflections order of the different Pt, BaM

and YbFO layers. Additionally, the complete diffraction curves of the samples were recorded by moving the sample and the detector in the theta-2theta configuration, simultaneously. All the diffraction profiles were fitted with the pseudo-Voigt function by using the Origin software package which provided R-square values of 0.99 in comparison with the Gaussian and Lorentz fit functions for which the R-square values were lower. The peak positions determined from symmetric, asymmetric reflections were utilized to derive the out-of-plane and in-plane lattice parameters and the lattice mismatches between the YSZ(111) substrate and the Pt interface layer and between the BaM layer and the Pt. The variation of the $FWHM_{ang}$ (resp. $FWHM_{rad}$) as function of the reflection order (*00l*) is equivalent to the Williamson-Hall (WH) plot[147]. It enables the separate determination of the lateral coherent block size $L_{//}$ (resp. vertical coherent block size $L_{\perp}$) from the intercept Y_0 at zero coordinate and the misorientation Δ (resp. the strain fluctuation ε) from the slope of the WH plots. In addition, the Pt, BaM and YbFO mosaicity in the differently grown samples were characterized by deriving the angular as well as the radial diffraction profiles of the corresponding symmetric reflections. As a result, the misorientation α_{Pt} and the mean values of the out-of-plane strain distribution $<\varepsilon_{Pt\perp}>$ of the Pt, BaM and YbFO layers were determined.

3.2.3 Scanning electron microscopy and energy-dispersive X-ray spectroscopy (SEM)

The surface topography and the chemical composition of samples listed in Table 3-1 and 3-2 investigated in Chapter 4. In chapter 4, the samples were characterized by SEM combined with energy-dispersive X-ray spectroscopy (EDXS) by using a FEI Dual beam Helios G4 FX microscope. For secondary electron (SE) imaging of the sample surface, the microscope was operated at 10 kV accelerating voltage in the so-called field-free mode with a beam current of approximately 25 pA. The Everhart-Thornley detector (ETD) was used for image recording.

Chemical analyses were performed by EDXS at a primary electron energy of 20 keV and a beam current of 0.4 nA by applying a Bruker system of the type QUANTAX 400 with a silicon-drift detector (SDD) XFlash 6. In particular, the two-dimensional distribution of the elements Pt, Al, and O was imaged via EDXS mapping, where the acquisition time per map was about 5 min. For mapping and data processing the software ESPRIT 2.1 (Bruker) was used.

3.2.4 Transmission electron microscopy and energy-dispersive X-ray spectroscopy (TEM)

Structural properties and the chemical composition of the samples listed in Table 3-1, 3-2, 3-3, 3-4 and 3-5 were studied by conventional TEM, HRTEM and scanning TEM combined with EDXS. For this purpose, electron-transparent cross-section specimens were prepared by focused ion beam (FIB) milling by using a Helios NanoLab G4 FX dual-beam instrument (Thermo Fisher Scientific). Before the FIB preparation of the TEM lamellas a thin metal layer of gold or silver was sputtered onto the sample surface by means of a Leica sputter coater, in order to protect the BaM films from ion-beam damage. After that, as usual for FIB preparation, an additional Pt/C protection layer was deposited on top of this metal layer. Coarse FIB milling was carried out with Ga^+-ions at an accelerating voltage of 30 kV, whereas for a final sample surface polishing (ca.

5000 scans at each side) 5 kV accelerating voltage with approximately 70 pA ion current was used.

TEM investigations of the BaM films were carried out on two different transmission electron microscopes which possess a thermally assisted field emission cathode (Schottky emitter). In more detail, an aberration-corrected FEI Titan3 80-300 microscope was used for conventional TEM and HRTEM imaging, in order to investigate the general layer properties (e.g., layer thickness, crystal structure) as well as for determining specific microstructural phenomena (Pt/BaM interface, crystal defects). Due to the spherical-aberration corrector in the imaging system of the Titan microscope a point resolution of 0.08 nm can be achieved in HRTEM. For image recording, the microscope is equipped with a 4k × 4k CMOS camera of the F436 type (TVIPS). Selected-area electron diffraction (SAED) was used to determine the crystal orientation of the BaM and Pt interface layers. Microchemical EDXS analyses were carried out by using a 200 kV microscope of the FEI Tecnai Osiris type. This microscope is equipped with a Super-X EDXS detector (FEI) which combines four silicon drift detectors (SDD). X-ray maps were recorded in the STEM mode via the so-called HyperMap mode offered by the ESPRIT software (Bruker). Typical measurement times were in the range from 60 to 90 min, where a possible drift of the sample was automatically corrected by cross-correlation of the corresponding reference images. STEM images were taken by means of a high-angle annular dark-field (HAADF) detector for which the image brightness is a function of the mean atomic number. For combined STEM/EDXS analyses, the lateral resolution amounted to approximately 1 nm in accordance with spot size no. 6 and the use of a condenser aperture of 100 µm in diameter. By employing the ESPRIT 2.3 software, the raw-data X-ray maps were quantified by using the thin-film approximation after Cliff-Lorimer[148], in order to obtain the element-concentration maps and the corresponding line profiles.

3.2.5 Atomic force microscopy and magnetic force microscopy

AFM topography measurements in (Chapters 4, 5, 6 and 7) were carried out by using a Dimension Icon AFM (Veeco Inc, USA) in the tapping mode. As a probe, OPUS HQ:NSC15/Al BS cantilevers (NanoAndMore, Wetzlar, Germany) with a force constant of 40 N/m and a resonance frequency of 325 kHz were used. Images were collected by using a scan rate of 0.5 Hz/line. The AFM topography and MFM images were collected for BaMPtTh0, BaMPtTh25 and BaMPtTh75 (Chapter 4 and 6) on a Dimension Icon AFM (Veeco Inc, USA) in the tapping mode and lift mode at room temperature without an external magnetic field, respectively. As a probe, Bruker's MESP-HM-V2 cantilevers (Bruker, Karlsruhe, Germany) with a force constant of 3.0 N/m, a resonance frequency of 75 kHz and 80 nm tip radius were used for recording the AFM and MFM images. 5 x 5 μm^2 images were collected by using the scan rate 0.5 Hz/line. For the MFM images, a lift height of 50 nm was utilized to identify the magnetic interaction of the sample with the cantilever. The AFM and MFM images were analyzed with the NanoScope software package (Bruker, Karlsruhe, Germany). The particle size analysis on the AFM images were carried out by modulating the color scale in black-and-white to visualize the border areas of the particles. 3D topography images were generated by using height sensor data. The samples were magnetized in the VSM instrument by applying an external magnetic field of 3 Tesla along the c-axis of the film prior to MFM measurements.

3.2.6 X-ray protoelectron spectroscopy

XPS measurements were performed at the IPS UHV analysis laboratory by using a Phoibos 150 analyser and a not monochromated XR-50 Mg K_α X-ray source from SPECS. The angle between the analyser and the X-ray source was fixed to 45°. The pressure inside the analysis chamber was about 3×10^{-10} mbar. All measurements were carried out at room temperature with the pass energy of 20 eV and an energy step of 0.05 eV. The deconvolution of the peaks was performed through the Fityk software and by using Voigt profiles and by applying a linear background. This linear background is more suited to the BaM films as insulating materials rather than the Shirley background which is more adapted to the case of metallic layers, as it has been reported in the CasaXPS manual[149,150]. The binding energy was calibrated by using the Au $4f_{7/2}$ (84.00 eV) photoemission line of a corresponding reference material[151]. Due to the charging effect, the adventitious C 1s (284.5 eV) was acquired as an additional calibration of the binding energy. The fitting process for all components which corresponds to the different chemical elements like Ba, Fe, and O was carried out by constraining the *FWHM* to a constant value.

3.2.7 Vibrating sample magnetometry

The magnetic in-plane (IP) and out-of-plane (OOP) magnetization loops shown in Chapter 5 and 7 were measured by using a VersaLab vibrating sample magnetometer from Quantum design with a magnetic field up to 2 Tesla. The measurements were performed for different temperatures from 50 K to the room temperature. From the magnetization loops, the saturation magnetization Ms, the remanent magnetization Mr, the perpendicular and parallel squareness's $S_\perp = M_{r\perp} / M_{s\perp}$ and $S_{//} = M_{r//} / M_{s//}$, the out-of-plane and in-plane coercivity fields $H_{c\perp}$ and $H_{c//}$, the coercivities ratio $H_{c//} / H_{c\perp}$ and the anisotropy fields H_a were derived. Additionally, the Curie temperature, ZFC and FC measurements were conducted with the VSM as well. The details are described in the next chapters.

4 Comparison of the structure and morphology of Pt grown on YSZ (111) as a function of the film thickness and growth temperature in the as-grown and in the encapsulated states

4.1 Introduction

This chapter aims at the optimization of the platinum (Pt) bottom electrode deposited by PLD. It sustains dewetting which occurs during the subsequent high-temperature layer growth. The focus is to achieve a Pt electrode grown on a YSZ(111) substrate with good chemical stability, sufficient conductivity, and an appropriate lattice misfit with the subsequent layers. This will help to prevent chemical interdiffusion of the oxide layers into the substrate.

Bauer et al. previous study[58] examined the in-situ growth of platinum layers on Al_2O_3 substrates by PLD for different film thicknesses and growth temperatures, in order to obtain the optimum Pt thickness and process temperature for a bottom electrode usable for multiferroic systems. The fabrication of magneto-electric heterostructures requires a stable and reliable bottom electrode capable to withstand high temperature growth conditions which exceed 900 °C[78,80,106,152]. Pt is the material of choice due to its high melting point, resistance to harsh environments, low electrical resistivity and proven performance in ferroelectric devices[153,154,155,156,157]. However, imperfections such as pores or pinholes can significantly degrade the electrical properties of the heterostructure[154]. One of the challenges during the Pt film deposition is the formation of hillocks, especially for ferroelectrics[158]. These formations, often a consequence of residual strain and heat treatment, can occur during the deposition, the subsequent deposition (subsequent deposition will be also called encapsulation thereon) or the annealing process[159,160,161,162,163,164,165,166]. The size and density of these hillocks are closely related to the deposition temperature which affects the internal stresses within the film growth[162,163]. Hillocks show a short circuit hazard by potentially bridging the top and bottom electrodes[163].

Furthermore, the agglomeration process of Pt films is subject to various mechanisms which include capillary and fractal agglomeration influenced by the metal type[167]. Previous studies have highlighted the dual dependence of the film thickness and growth temperature on the hillock formation and dewetting phenomena[139,160,167]. Therefore, the determination of the optimum growth temperature is critical, especially if the film thickness variation in subsequent steps is considered.

Efforts to reduce the film dewetting often involve the use of adhesion layers such as Ta, Ti or Zr, in order to improve the adhesion of Pt to oxide substrates[165]. In addition, the choice of the substrate for Pt deposition (i.e. Al_2O_3[80,152,165], SiO_2[159,160,161,162,163], and YSZ[164,166,167]) plays a key role in the film morphology and hillock formation due to the different lattice mismatch and coefficients of thermal expansion. With the best to our knowledge, detailed studies on the morphological changes of Pt electrodes in an encapsulated state (i.e., sandwiched between the substrate and the over-grown film) remain limited.

The study addresses this gap by employing a comprehensive set of techniques which include high-resolution transmission electron microscopy (HRTEM), atomic force microscopy (AFM), energy dispersive X-ray spectroscopy (EDX), scanning electron (SE) and high-resolution X-ray diffraction (HRXRD). Together, these techniques allow an in-depth study of the morphology and microstructure of Pt films with different thicknesses, both in the as grown and encapsulated states.

4.2 Experimental procedures

The Pt films were deposited on yttria-stabilized zirconia YSZ with (111) orientation after heating the substrate to T_g = 900 °C by using different number of shots 1647, 4100, 8235, 12350 and 16470 with the laser frequency of 5 Hz and energy pulse of 60 mJ (i.e., laser fluence 16 J/cm^2). Prior to the growth, the different substrates were cleaned by isopropanol and then annealed in the furnace for 2 hours at a temperature of 1200 °C, in order to attain low roughness and a good terrace morphology. The target had a distance of 35 mm from the substrate. The Pt films in the as-grown state are named in the manuscript as follow: Pt_Th10nm, Pt_Th25nm, Pt_Th40nm, Pt_Th55nm and Pt_Th70nm. The samples were slowly cooled down with 5 °C/min from T_g = 900 °C to room temperature RT. The substrate used for the Pt growth was 8 mm x 8 mm. We could divide the Pt grown film into the three pieces for three different treatments leading to three different states: as grown, encapsulated and as annealed+uncapped (not shown in this work). In one of the pieces with sizes a of 4 mm x 8 mm, ferroelectric (FE) YbFO layers or ferromagnetic (FM) layers BaM were grown on the different Pt bottom electrodes. For this purpose, the template (Pt/YSZ) was heated from RT to T_g = 900°C with a heating rate of 25 °C/min. The growth of the subsequent YbFO layers was carried out in an oxygen atmosphere with a pressure of 400 mTorr and with a laser frequency of 1 Hz. The deposition time was about 5 hours. The Pt layer were encapsulated between the YSZ and the FE or FM layer systems. The samples are labeled Enc Pt_Th10nm, Enc Pt_Th25nm, Enc Pt_Th40nm, Enc Pt_Th55nm and Enc Pt_Th70nm. Another set of Pt films were grown at different growth temperatures T_g = 300, 500, 700 and 900 °C, and are labeled PtT300, PtT500, PtT700 and PtT900. Since the growth rate depends on T_g, the number of shots was rescaled to obtain Pt films with comparable thicknesses in the range of 90 to 110 nm. The analysis of the AFM images was performed by using the NanoScope software package (Bruker, Karlsruhe, Germany). All the derived topographical parameters are summarized in Table 4-1.

The surface topography and the chemical composition of these nine Pt layers were characterized by SEM combined with energy-dispersive X-ray spectroscopy (EDXS) by using an FEI Dual beam Helios G4 FX microscope. The TEM investigations of the four films Pt_Th40nm, Pt_Th55nm in the as grown state, Enc Pt_Th40nm and Enc Pt_Th55nm were carried out on two

different transmission electron microscopes which possess a thermally assisted field emission cathode (Schottky emitter).

4.3 Morphology and structure dependency on the growth temperature

In order to determine the optimum growth temperature for the Pt bottom electrodes on YSZ (111), the Pt films were grown at different temperatures. This step is critical for the subsequent production of the bottom electrode because of its effect on the stability of the platinum films under harsh, high temperature conditions and O_2 partial pressure during the subsequent layers growth. In this context, we set the conditions at P_{O_2} = 400 mTorr and T_g = 900 °C. At this point, the aim is to assess whether the Pt layers grown at different temperatures showed the same stability and robustness during post-growth annealing. For this purpose, the Pt growth temperatures were varied over a range from 300 °C to 900 °C. Figure 4.1 shows angular and radial sections of the Pt222 and Pt333 reflections for both as-grown and encapsulated Pt layers. In the as-grown state, the curves show significant differences between samples PtT300 and PtT900 grown at 300 °C and 900 °C, respectively. The sample PtT900 in the as-grown has a better crystal quality which makes it more suitable for the growth of metastable films. However, the curves also show that encapsulation by a capping layer growth reduces broadening. In particular, Figure 4.1c, 4.1d. 4.1h and 4.1i compare PtT900 and Enc PtT900 by the angular and radial intensity profiles, respectively. (similarly Figure 4.1a, 4.1b. 4.1f, 4.1g compare for PtT300 and Enc PtT300 by the angular intensity and radial intensity profiles). Comparisons of broadening along radial and angular for as-grown and encapsulated states showed that the film grown at T_g = 900 °C shows less modification through the encapsulation, T_g = 300 °C shows the most (T_g = 500 °C and T_g = 700 °C data are not shown here).

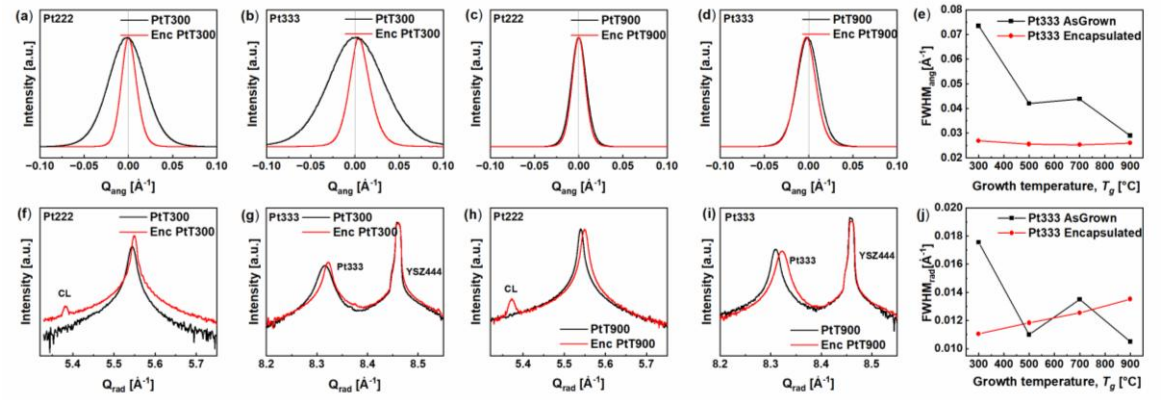

Figure 4.1: (a-d) Angular and (f-i) radial intensity profiles of Pt222 and Pt333 reflections of PtT300, Enc_PtT300, PtT900 and Enc PtT900 films, respectively. (e) Angular (j) radial broadening ($FWHM_{ang}$, $FHWM_{rad}$) values of as-grown and encapsulated films grown at T_g = 300, 500, 700 and 900 °C. For magnified version refer to Figure A-4.

Figure 4.1e and Figure 4.1j shows the angular $FWHM_{ang}$ and radial $FWHM_{rad}$ broadenings of the Pt333 reflections for as grown and encapsulated Pt films at different temperatures. Both $FWHM_{ang}$

and $FWHM_{rad}$ values were obtained by fitting the diffractions profiles by using Pseudo-Voigt function. As the growth temperature T_g increases, $FWHM_{ang}$ follows a decreasing trend, which suggests an improvement of the crystal quality in terms of a defect density reduction. On the other hand, the difference between the broadening of as grown and encapsulated systems becomes small as T_g increases. This means that the structural modification is very small for Pt films grown at high temperatures. This suggests that the structural modification of PtT300 by encapsulation is severe compared to PtT900 which does not undergo critical structural modification through encapsulation. The control of modification by subsequent layer growth is critical to ensure the quality of the capping layer (i.e. FE or FM). This is particularly important for a ferroelectric capping layer which requires a high-quality crystalline film with a specific crystal orientation, essential for ferroelectricity.

The $FWHM_{ang}$ values are used, in order to investigate the mosaicity of the films for as-grown and encapsulated Pt films. Figure 4.2a and 4.2b show a schematic representation of mosaic blocks in a thin film with their surface normal and a Pt111 reflection together with a dashed white line which indicates the angular direction.

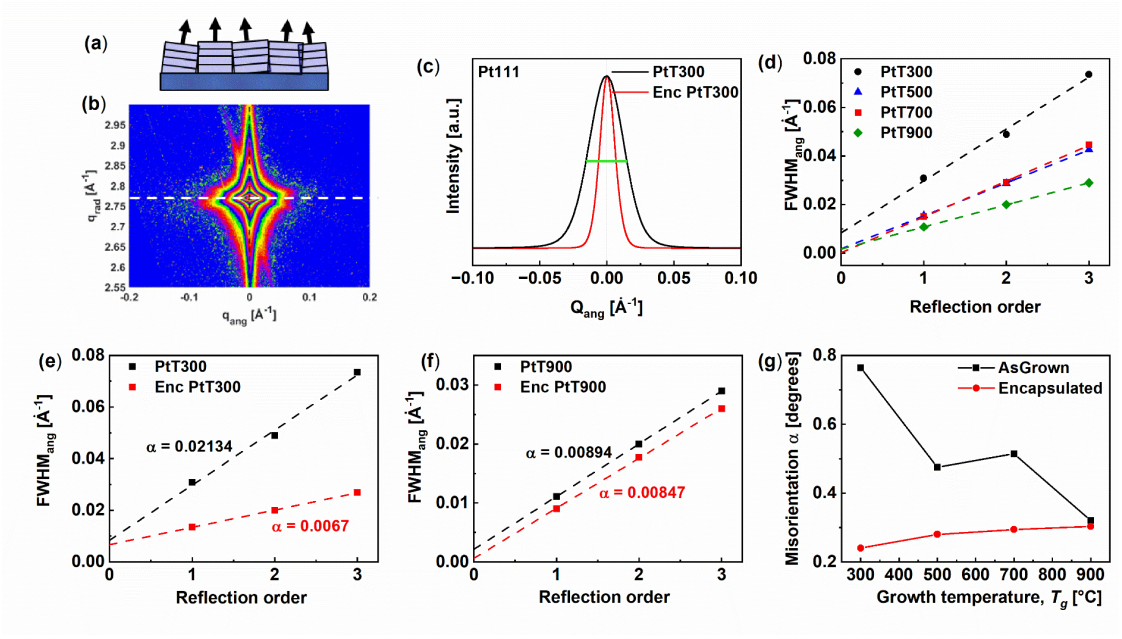

Figure 4.2: (a) A schematic representation of mosaic blocks in a thin film,(b) an examplary Pt111 reflection (in this case for the sample PtT900) and the dashed line shows the angular direction, (c) normalized Pt111 angular intensity profiles of the PtT300 and Enc PtT300, WH-plots of the (d) angular broadenigns of as-grown Pt films, (d) angular WH plot comparison of PtT300 and Enc PtT300, (e) angular WH plot comparison of PtT900 and Enc PtT900. (g) Misorientation comparison of as-grown and encapsulated films.

Figure 4.2c exemlarily shows angular intensity Pt111 profile for the as-grown PtT300 and encapsulated Enc_PtT300 films, where the $FWHM_{ang}$ is marked with a green line, and the difference between as-grown and encapsulated film which are different in their crystal quality. Figure 4.2d shows the angular WH-Plots for the as-grown PtT300, PtT500, PtT700 and PtT900 films where the $FWHM_{ang}$ is the least for PtT900. Figure 4.2e and 4.2f show the WH plots for as-grown and

encapsulated films grown at T_g = 300 °C and at 900 °C, respectively. It demonstrates that using T_g = 900 °C is well suited for the PLD growth of Pt films grown on YSZ (111) substrates for bottom electrode application due to shown less structural modification through encapsulation. The degree of misorientation decreases from α = 0.021 to α = 0.006 as T_g increases from 300 °C to 900 °C. The latter was found to be less affected by the subsequent growth procedure (Figure 4.2f). In Figure 4.3a and 4.3b, the phi scans of the asymmetric Pt331 reflections of the samples produced at T_g = 300 °C and T_g = 900 °C. Here, the as-grown and encapsulated films were compared. PtT300 shows the 6-fold symmetry. On the other hand, PtT900 shows poor 6-fold symmetry and a better crystal quality. Comparisons through the encapsulation reveals that the PtT300 cannot withstand to the encapsulation whereafter 6-fold symmetry is being broken. In the case of PtT900 and Enc PtT900, the film keeps it stability through 5.5 hours of subsequnt growth at T_g = 900 °C and under P_{O_2} = 400 mTorr. Consequently, the PtT900 sample has a stable crystal structure as well as a low degree of misorientation and can be considered as a promising interface layer for the PLD growth of subsequent heterostructures. Despite the 6-fold crystal symmetry found for PtT300 and the relatively small roughness, the degree of misorientation and defect concentration was relatively high for the growth of a single crystalline capping layer. Additionally, the roughness of PtT900, which are obtained by the AFM images shown in Figure 4.4 (a-h), is also the lowest of all growth temperatures experimented in this work.

AFM images show that the PtT300 exhibits island morphology (Figure 4.4) which correlate with the higher degree of misorientation. Increasing the growth temperature into T_g = 500 °C, increases the island sizes and it continues as the temperature was increased to T_g = 700 °C (Figure 4.4b, 4.4f, 4.4c and 4.4g). The morphology of PtT900 is hillocks-free and displays a flat surface with a smaller height variation in comparison with PtT700 which has the hillocks-like height variation. It is worthwile to point out that flatness is important to avoid the formation of out-of-phase boundary (OOB) in the capping layer.

The resulting morphology could also be correlated and understood better by SZD. In the absence of specific data on the energy of platinum atoms in the literature, it was necessary to estimate this parameter during the deposition process. A comparable experimental configuration was employed in a preceding investigation, wherein the energy of Ni atoms during the growth of NiO by PLD was quantified. A laser fluence of 5 J/cm² in a vacuum environment was found to result in an energy of approximately 25 eV for Ni ions[168]. Given that the laser pulse energy density used for platinum in this study is approximately 16 J/cm², it can be assumed that the energy of Pt atoms may exceed 75 eV. By referring to the Anders structure zone diagram (Figure A-5) and the homologous temperature (T_h) listed in Table A-1, one can ascertain the growth regime of platinum. In particular, the growth of platinum at 700 °C and 900 °C is likely to occur within the region of low-temperature, low-energy ion-assisted epitaxial growth. Conversely, growth at 300 °C and 500 °C is expected to fall within the boundaries of zone 1 to zone T, and zone T, respectively. Which explains the morphological variation from 300 °C to 900 °C.

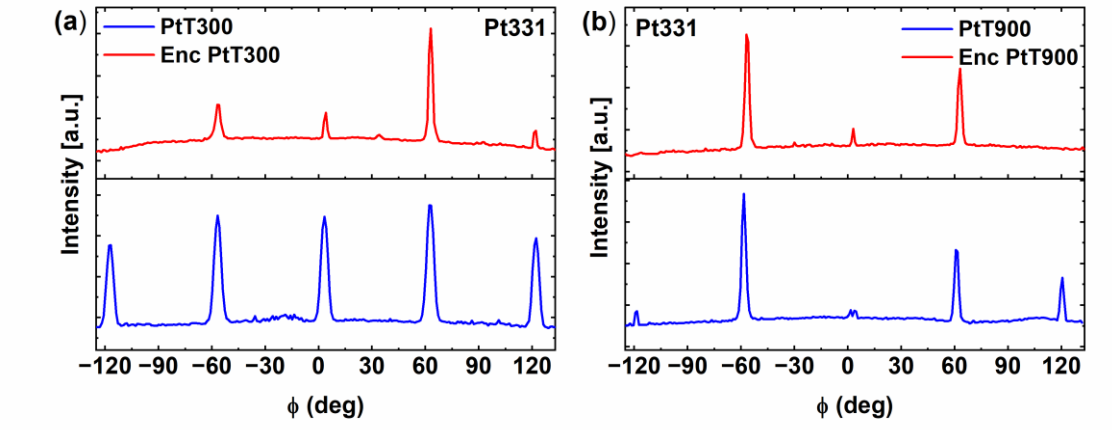

Figure 4.3: Azimuthal scan as function of the phi angle (i.e., rotation around the surface normal) for the asymmetric reflection Pt331 corresponding to the samples (a) PtT300 and Enc PtT300 and (b) PtT900 and Enc PtT900.

In order to explore the morphological changes during the subsequent growth, four segments of the Pt samples (PtT300, PtT500, PtT700 and PtT900) were annealed at T_g = 900 °C under oxygen partial pressure of 400 mTorr for a duration of five hours and 30 min, similarly to the growth conditions applied to the capping layer.

Figure 4.4 (i-l) shows SE_45° images (secondary electron SEM images with a 45° tilt) of the annealed Pt films, hereafter referred to AnnPtT300, AnnPtT500, AnnPtT700 and AnnPtT900. For all films, dewetting of the Pt films was observed at different locations on the film surfaces. The detached Pt films are indicated by yellow arrows in the SE_45° images, where the black contrast represents the substrate, and the grey contrast corresponds to the remaining Pt film on the substrate. Notably, AnnPtT300 showed severe delamination (Figure 4.4i), which was less pronounced in AnnPtT500 (Figure 4.4j). A qualitative comparison of the extent of delamination revealed that AnnPtT700 and AnnPtT900 did not show significant differences, whereas AnnPtT300 showed numerous and large areas of delamination. It was observed that there were grooves in the Pt film for AnnPtT300, AnnPtT700 and AnnPtT900, indicating that Pt atoms migrated or detached from the surface. This implies that film delamination or shrinkage occurred continuously during annealing.

For a better understanding of Pt delamination during the films grown at different temperatures, we considered the thermal strain that occurs as the films cool down from the growth temperature to room temperature. This is calculated by means of the thermal expansion coefficient of Pt, $\alpha_{therm,Pt} = 8.9\,x\,10^{-6}/°C$ (between 0 – 40 °C)[169] and YSZ, $\alpha_{therm,YSZ} = 10.5\,x\,10^{-6}/°C$[170] and by using the Equation (4-1)[171] for the following expression

$$\varepsilon_{Therm} = (\alpha_{therm,Pt} - \alpha_{therm,YSZ}) * \Delta T \qquad (4\text{-}1)$$

for which ε_{Therm} is the film strain while changing the temperature according to ΔT.

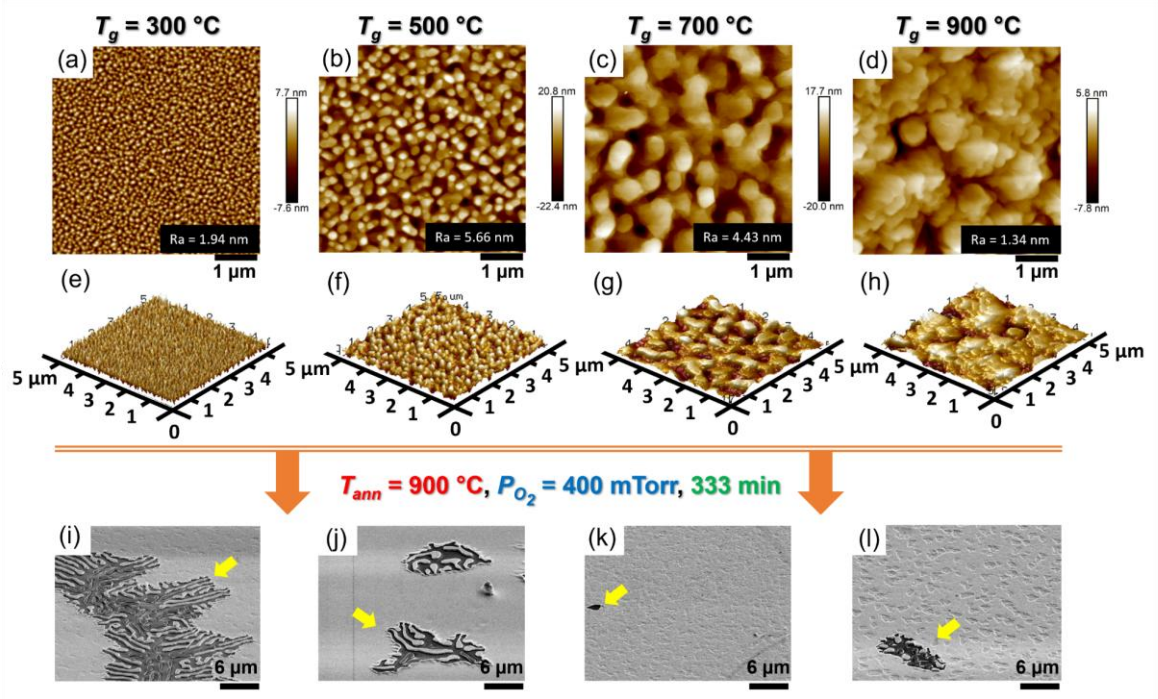

Figure 4.4: (a-d) AFM topograph images of the platinum films grown on YSZ (111) substrates at temperature T_g = 300 °C, 500 °C, 700 °C and 900 °C, respectively. (e-f) 3D AFM representation of the same regions which are shown in (a-d). (i-l) SE_45° images which are collected after an annealing procedure is applied at T_{ann} = 900 °C, P_{O_2} = 400 mTorr for 333 minutes.

The thermal strain increases with T_g (see Figure 4.5) where PtT900 experiences the highest thermal compressive strain ε_{Therm} = - 0.00242 at room temperature. During the annealing process the films are subjected to thermal cycling between 900 °C and room temperature. AnnPtT900 is likely to withstand this thermal cycling. Raising the temperature again for subsequent growth (to T_g = 900 °C) does not cause any additional stress in the film that could exceed it the thermal stress experienced during the growth. Conversely, AnnPtT300 experiences significantly higher strain along the film during annealing (or similarly subsequent layer growth), despite having lower strain in the as-grown layer.

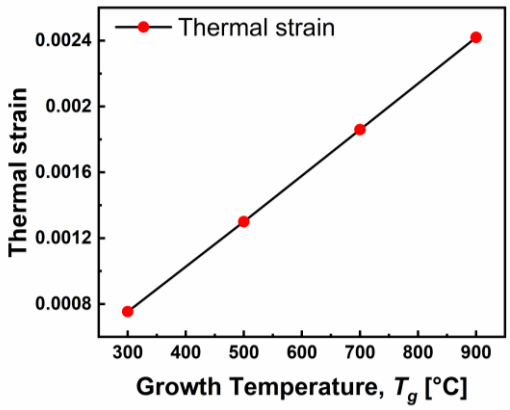

Figure 4.5: Calculated thermal strain of Pt films experienced at room temperature grown at different temperatures.

4.4 Morphology and degree of coverage

Figure 4.6 (b1-f1) show AFM micrographs of the Pt films grown at T_g = 900 °C with different thicknesses, 10 nm, 25 nm, 40 nm, 55 nm, and 70 nm, respectively. The samples are named Pt_Th10nm, Pt_Th25nm, Pt_Th40nm, Pt_Th55nm and Pt_Th70nm. Figure 4.6a1 shows the YSZ(111) substrate prior to the growth with the terrace structure after the heat treatment mentioned in experimental section. In Figure 4.6b1, Pt_Th10nm shows a 3D island morphology where the mean island size (width) is 47 nm (in Table 4-1). It should be mentioned that the mechanisms such as nucleation, coalescence and elongation transition are in competition during the deposition process[58]. As the new adatoms arrive at the surface, they contribute to island growth at a first stages (Th < 10 nm). A high growth temperature, T_g = 900 °C, leads to a higher diffusion rate which allows the adatoms to migrate into the existing islands rather than nucleating new ones. Therefore, high growth temperatures would favor the elongation of the existing islands in expense of generating new nuclei. This result was previously revealed by Bauer et al.[58] Further deposition up to Th_{Pt} = 25 nm leads to the enlargement of the islands and coalescence of islands at the critical thickness and form elongated chains (channel-like structure in Figure 4.6c1). For Pt_Th25nm, the channels width varies in between 41 nm and 141 nm (by AFM) and between 28 nm at a thickness of 25 nm, and the hole sizes (Pt-free regions) appeared to be in the mean size of 41nm (Table 4-1). The increase of the film thicknesses up to 40 nm (Pt_Th40nm) and up to 55 nm (Pt_Th55nm) improves the filling factor by the support of a coalescence mechanism which decreases the distance between the channels. But it increases the channel widths (Figure 4.6d1 and 4.6e1). In Figure 4.6e1, the morphology of Pt_Th55nm appears as a network which contains holes, and which are randomly distributed with a size between 18 nm and 111 nm. The mean size is 61 nm (column#4, row 17). The Pt_Th70nm sample displays a continuous film morphology with a roughness value of R_a = 0.6 nm (column #5, row 10) and hole mean size of 46 nm which varies between 24 nm to 69 nm (column #5, row 18).

Additionally, hillocks formation was also a part of the morphological alterations for Pt grown on a YSZ(111) substrate. These hillocks appeared as bumps/pyramids on the film surface which could be seen as extra elevations. In order to visualize this, line height profiles from the topography were extracted form 3 different locations and are shown with red, green and black dashed lines (Figure 4.6 (b1-f1)). The line profiles are displayed in Figure 4.6 (b2-f2) for Pt_Th10nm, Pt_Th25nm and Pt_Th40nm, Pt_Th55nm and Pt_Th70nm, respectively. These latter are plotted to differentiate between of the hillock heights and the depths. For Pt_Th10nm sample, we measured hillock heights between 5.4 to 44.7 nm in comparison to the 10 nm thick islands. Further deposition of the film caused a decrease in the density of hillocks on the surface. In fact, the density of hillocks steadily decreases until they disappear for Pt_Th70nm at Th_{Pt} = 70 nm (see Figure 4.6b2, 4.6d2, 4.6e2, Figure 4.6f2). Conversely, by comparing Pt_Th40nm (Th_{Pt} = 40 nm) and Pt_Th55nm (Th_{Pt} = 55 nm) in Figure 4.6d2, 4.6e2, the height of the hillocks decreases.

The reduction of the hillock density is accompanied by their reduction of height, while their lateral dimensions increase during the deposition process. The presence of hillocks also has a significant effect on the surface roughness of the layers. As shown in Table 4-1 the roughness values obtained from AFM and denoted as R_a, have higher values when hillocks are present. Conversely, R_a reaches its minimum when hillocks are absent, and the film forms a continuous surface. Figure

4.7 (a-e) represents the secondary electron SEM images of the samples Pt_Th10nm, Pt_Th25nm, Pt_Th40nm, Pt_Th55nm and Pt_Th70nm, respectively where the SEM images are recorded from a region of 1µm x 1.2µm while the sample was not tilted, denoted as SE_0°. The SEM images are complementary to the AFM images in the previous figure (Figure 4.6). The morphology transition behavior from 3D islands to the 2D layer growth when the thickness exceeds Th_{Pt} = 10 nm is visible in the SEM images as well (Figure 4.7a, b). Further deposition above 25 nm results in coalescence of the film to transform Pt-free channels into the Pt-free holes until Th_{Pt} = 55 nm are reached. Further deposition leads to a filling of the holes, at Th_{Pt} = 70 nm (Figure 4.7e). The corresponding EDX maps of the SEM images are collected to identify the Pt-free areas in Figure 4.7 (f-j). The yellow contrast represents the Pt signal, where the dark regions correspond to Pt-free regions.

The SE_0° images as well as the EDX maps are sufficient to clearly identify the hillocks, although, hillocks exist in Figure 4.7c, 4.7d, 4.7h, 4.7i. Especially for the measurement of hillock sizes, edges are not well defined in the EDX maps. Therefore, to be able to quantify the size and the density distributions of hillocks, SEM SE images were collected with a sample stage tilted by 50° and backscattered-electron (BSE) images, in Figure 4.7 (k-o) and (p-t), respectively. By using the SE_50° images, identification of hillocks became relatively easy due to the imaging direction which allows to generate a contrast where the surface heights exist. Hillocks are marked with red circles, as any height bumps from the surface could be considered as hillocks. Furthermore, AFM images give the reliable results for the height of the hillocks.

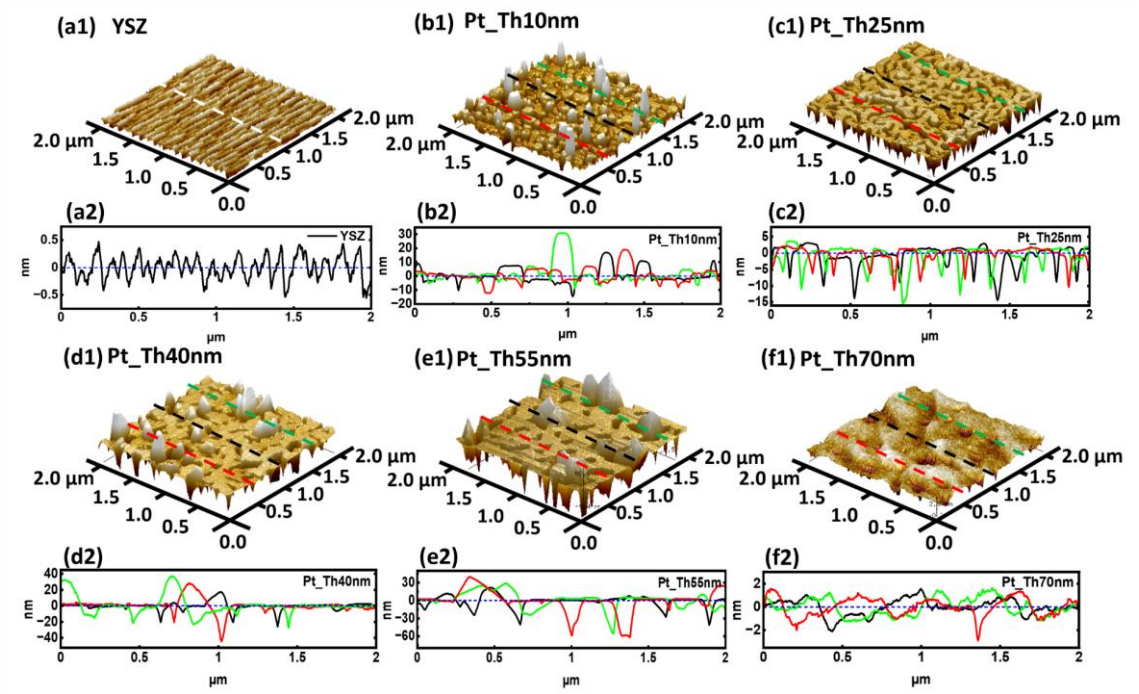

Figure 4.6: (a1-f1) and (a2-f2) are the AFM images with 2 x 2 µm sizes and the corresponding lines profiles drawn by red, black and green dashed lines for the samples YSZ substrate, Pt_Th10nm, Pt_Th25nm, Pt_Th40nm, Pt_Th55nm and Pt_Th70nm, for detailed view refer to Figure A-6[172].

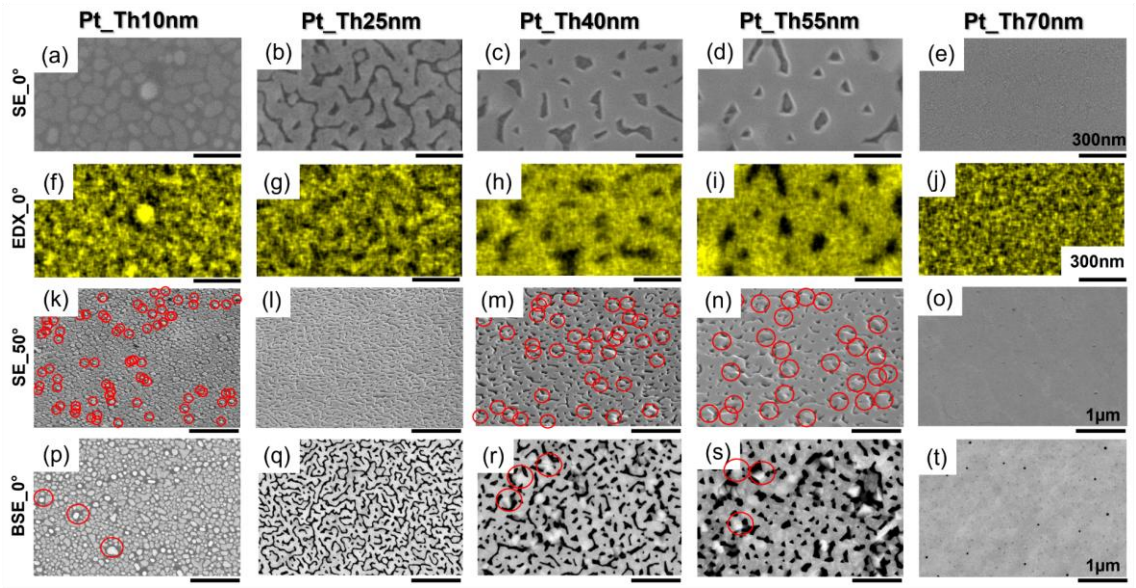

Figure 4.7: (a-f) Images are the SE_0° images recorded with zero degree of inclination. (f-j) are the corresponding EDX maps. (k-o) are the SE_50° measured with an inclination angle of 50 degrees. (p-t) are the BSE images with 5 x 5 µm size. All the SE_0°, EDX maps, SE_50° and BSE correspond to the Pt_Th10nm, Pt_Th25nm, Pt_Th40nm, Pt_Th55nm and Pt_Th70nm in the as-grown state (scale bars are the same for each row as stated (e-t)), for detailed view refer to Figure A-7[172].

However, to make a statistical quantification, many SE_50° images were recorded and an example was shown in Figure 4.7. Additionally, BSE images were collected to provide information about the variation in the atomic number (Z) of the material. This was employed to identify the Pt-free regions where YSZ appears as a dark and Pt as bright contrast. Moreover, BSE images also contain the information from secondary electrons (SE) where SE and BSE together contribute to the height variation and sharp edges such as hillocks. Furthermore, the penetration depth by the electrons is larger than the film thickness which led to a variable brightness contrast of the regions covered by the Pt[173]. Some examples of hillocks, brighter spots, are marked with red circles in the BSE images of Pt_Th10nm, Pt_Th40nm and Pt_Th55nm (Figure 4.7p, 4.7r and, 4.7s). Consequently, BSE method could be employed to easily identify and quantify the hillocks. The distribution density, height of the hillock and hillock sizes were determined by using AFM and BSE images and are compared in Table 4-1. Another advantage of the BSE method is visualizing the internal density fluctuations of the film which might not be visible in the SE images. Figure 4.7e, 4.7o and 4.7t correspond to SE_0 °, SE_50° and to BSE_0° for the Pt_Th70nm film, respectively. Figures 4.7e, and 4.7o do not show any contrast variation while Figure 4.7t shows a black contrast (small holes) and a gray contrast variation over the surface. It means that there exist very small holes or pores in the structure. Additionally, there is a contrast fluctuation in the image which may indicate that the mass density is not constant all over the sample[174].

4.5 Structure and formation of hillocks

Figure 4.8a shows the hillock density [#/µm^2] as function of the Pt film thickness (left y-axis), while on the right y-axis the variation of the hillock volume [µm^3] is plotted. The 3D-2D morphology transition is marked with an orange dashed/dotted line between 10 and 25 nm in which the exact value of the transition thickness is unknown, (see Figure 4.8a). The presence and the absence of the hillocks are also indicated in Figure 4.8a with "H" (i.e., hillocks) and "NH" (i.e., No hillocks), respectively. The Pt_Th10nm sample shows the highest hillocks density whereas the average volume of a single hillock is the lowest. The transition from 3D to 2D growth leads to the formation of hillocks at Th_{Pt} = 25 nm, which appear at Th_{Pt} = 40 nm again, and the hillocks density becomes the highest. Further growth up to Th_{Pt} = 55 nm leads to a decrease of the hillock density, however, the volume becomes the highest. The decrease of the hillock density could be related to the reduction of the grain boundaries as well as the stored energy in the lattice[161]. Due to the increase of the deposition time, the atomic rearrangement resulted in the increase of the lateral Pt sizes of the mosaic blocks.

Figure 4.8b shows the XRR curves of the samples together with the experimental data fit. The fit is done by the multilayer model which was generated by means of a self-developed software package of MATLAB. Table 4-1 shows the thickness values of the as-grown Pt samples, estimated from the density profiles of the layers. The detailed discussion about the density profiles will be mentioned in the following chapters.

Reciprocal space maps (RSMs) of the symmetric Pt111, Pt222, Pt333 reflections and asymmetric Pt224 and Pt331, YSZ224 reflections were recorded for Pt films in the as grown and encapsulated states. The HRXRD measurement was carried out at the NANO beamline in the KARA Light Source located at KIT by using a single photon counting Mythen detector and a high precise multipurpose diffractometer. In Figure 4.9, only RSMs of Pt111, Pt222 are shown.

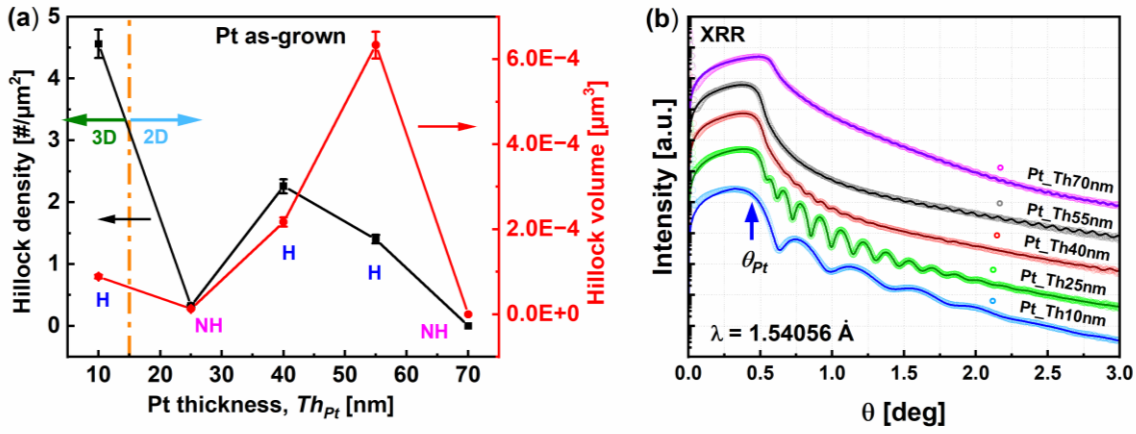

Figure 4.8: (a) Variation of the hillock density (left y-axis) and hillocks volume (right y-axis) with the Pt thickness. The dotted line refers to the morphology transition from 3D-islands growth to 2D-layer-by-layer growth. The labelling "H" and "NH" refers to the hillocks or Non hillocks as it was demonstrated by AFM; SE_50° and by BSE. (b) XRR curves and the corresponding fitting of the samples Pt_Th10nm, Pt_Th25nm, Pt_Th40nm, Pt_Th55nm and Pt_Th70nm[172].

The coordinates of the peak positions where the intensity is at a maximum is derived and used to determine the lattice parameter (*a*), the interplanar spacings d_{111} and $d_{11\text{-}2}$. These latter were determined by assuming the rhombohedral lattice transformation which occur during the growth. In order to estimate the rhombohedral distortion angle δ and the lattice parameter *a*, inputs values for *a* and δ are introduced in the calculation of d_{111}, $d_{11\text{-}2}$ values to derive d_{hkl_cal}. On the other hand, d_{hkl_meas}, values for (111) and (11-2) are calculated from the *Q* positions of the measured reciprocal space maps (shown in Figure 4.9) by using Equation (4-2) and Equation (4-3). By using Equation (4-4) inputs values for *a* and δ were iterated to minimize the difference (Δd_{hkl}) between d_{hkl_cal} and d_{hkl_meas}. On the other hand, it means that the distortion angle and the lattice parameter was fitted to the experimental value.

$$< d_{hkl} >= \frac{2\pi}{l * Q} \tag{4-2}$$

where *Q* is the Q_z of the symmetric reflection and *l* is the reflection order and (*hkl*) = (111), (222), (333).

$$< d_{11-2} >= \frac{3}{2}\frac{2\pi}{Q_{x331}} \tag{4-3}$$

$$\Delta d_{hkl} = d_{hkl\_cal} - d_{hkl\_meas} \tag{4-4}$$

Using the calculated interplanar spacing d_{111} the in-plane ($\varepsilon_{//}$) and out-of-plane ($\varepsilon_{\perp}$) residual strains were calculated (Equation (4-5) and Equation (4-6)) for the rhombohedral distorted lattice. The distortion angle δ (lattice angle is $\alpha = 90 + \delta$) as a function of the thickness Th_{Pt} is plotted in combination with the lattice parameter (Figure 4.10c). In Figure 4.10d, the out-of-plane ($\varepsilon_{\perp}$) residual strain is depicted in combination with the d_{111} lattice parameter.

$$\varepsilon_{//} = \frac{d_{11-2}^{Pt} - d_{11-2}^{Bulk}}{d_{11-2}^{Bulk}} \tag{4-5}$$

Where d_{11-2}^{Bulk} and d_{111}^{Bulk} corresponds to the d-spacing $d_{11\text{-}2}$ and d_{111} of the Pt in the bulk.

$$\varepsilon_{\perp} = \frac{d_{111}^{Pt} - d_{111}^{Bulk}}{d_{111}^{bulk}} \tag{4-6}$$

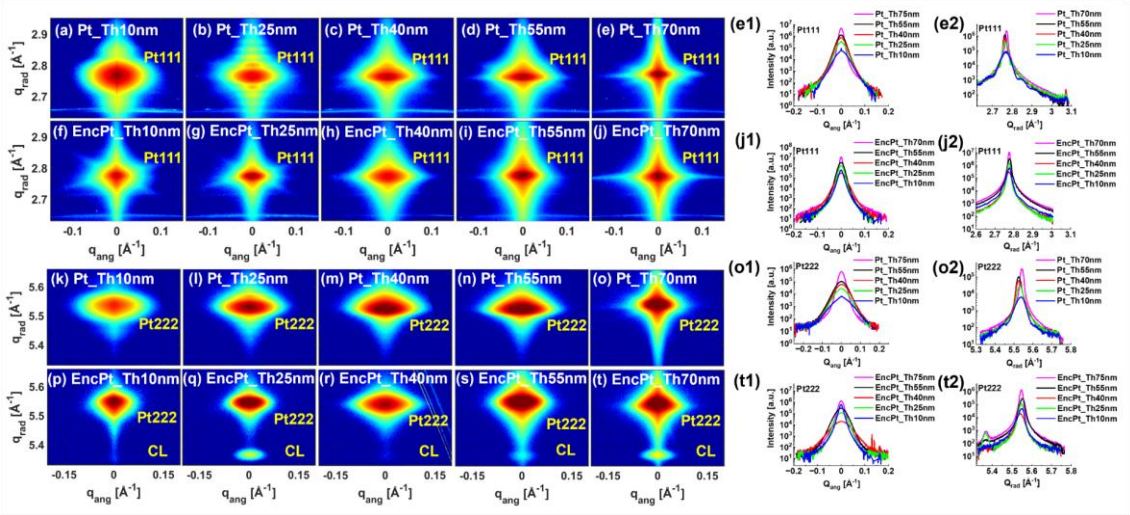

Figure 4.9: Reciprocal space maps of Pt111 reflections for (a-e) as-grown Pt layers and (f-j) encapsulated Pt layers. The corresponding angular and radial Pt111 intensity profiles for as-grown and encapsulated Pt layers with thicknesses Th_{Pt} =10 nm, 25 nm, 40 nm, 55 nm, and 70 nm are shown in (e1, e2) and (j1, j2), respectively. Reciprocal space maps of Pt222 reflections for (k-o) as-grown Pt layers and (p-t) encapsulated Pt layers. The corresponding angular and radial Pt222 intensity profiles for as-grown and encapsulated Pt layers with thicknesses Th_{Pt} = 10 nm, 25 nm, 40 nm, 55 nm, and 70 nm are shown in (o1, o2) and (t1, t2), respectively. For a magnified version refer to Figure A-8[172].

The Q-coordinates of the diffraction peak Pt333 and the YSZ444 (one can consider as a reference reflection from substrate) are close to eachother which allows a simultaneous measurement of the substrate peak and the film reflection. A comparison of the radial and angular diffraction profiles for the Pt333 and YSZ444 reflections of samples with different Pt thicknesses (Pt_Th10nm, Pt_Th25nm, Pt_Th40nm, Pt_Th55nm and Pt_Th70nm) is shown in Figure 4.10a and Figure 4.10b. In Figure 4.10a, the signals from the substrates have been superimposed and used as a reference to determine the peak positions Q_z and the interplanar spacing d_{111}.

The inset of Figure 4.10a exhibits that the maximum intensity (*Imax*) of Pt333 linearly increases with the thickness, with two different slopes as Th_{Pt} varies from 10 to 70 nm. It is noteworthy that the slope of the curve becomes steeper as Th_{Pt} increases from 55 to 70 nm. This increase in Imax can be directly related to the growth of the crystalline film with increasing Th_{Pt}. It may reflect increased coverage, improved crystalline quality (e.g., reduced mosaicity) and increase in diffraction volume (i.e., thickness). Conversely, Q_z*@Imax* decreases with Th_{Pt} in the range of 10 to 40 nm and remains unchanged as Th_{Pt} increases up to 55 nm. Furthermore, an increase in Q_z*@Imax* is observed as Th_{Pt} increases from 55 to 70 nm.

In Figure 4.10c, the lattice parameter (a) and the distortion angle δ follow the same trend along with the variation Pt film thickness Th_{Pt}. This suggests that the lattice parameter is influenced by the distorted lattice δ. As Th_{Pt} increases, there is a peak at Th_{Pt} = 25 nm at which the hillocks are absent followed by the reduction of a and δ when Th_{Pt} becomes higher. This can be interpreted as being related to the formation of hillocks and to stress relaxation. In the case of Th_{Pt} = 70 nm, a and δ took the lowest values. As Th_{Pt} increases to more than 25 nm, the first hillock forms around 40 nm followed by the formation of larger but fewer hillocks. These hillocks disappear at Th_{Pt} =

70 nm. Consequently, with the formation of hillocks, the strain is already relaxed at thicknesses of 40 nm and 55 nm. Subsequent growth results in surface smoothing as Pt-free regions are filled and the remaining hillocks diffuse throughout the layer.

Figure 4.10d shows that the evolution of the tensile out-of-plane residual strains $\varepsilon_{\perp}$ in combination with d-spacing d_{111} of the (111) Pt lattice planes as a function of Th_{Pt}. As indicated in Equation (4-6) both $\varepsilon_{\perp}$ and d_{111} display a similar behavior. It is demonstrated by in-situ stress measurements that the tensile residual stress due to hillocks formation (where T_g > 300 °C) is released during deposition for Pt films sputtered on Si substrates[162].

The focus is on the estimated vertical residual strain ($\varepsilon_{\perp}$) along the growth direction, considering the discontinuity in platinum caused by void formation at lower thicknesses. As deposition time (i.e., Th_{Pt}) increases, competing phenomena such as the transition from 3D to 2D morphology, hillock formation, and void development should be recognized. The Pt film with a thickness of 40 nm, which has the highest density of hillocks and a 2D morphology, exhibits the greatest vertical residual strain ($\varepsilon_{\perp}$ = 0.0035) and a d_{111} spacing of 2.274 Å. Increasing Th_{Pt} in a 2D morphology scenario enhances coverage and reduces hillock density which results in a contraction of the (111) lattice plane spacing and a decrease in $\varepsilon_{\perp}$.

The angular and radial intensity profiles of Pt111 and Pt222 reflections of Pt as-grown and encapsulated samples were derived from the RSMs shown in Figure 4.9 and compared in Figure 4.9 (e1 to t2). From the diffraction radial profiles comparison, it can be seen, that there exist thickness fringes, and oscillations only exists where the vertical coherent length, L_V, is comparable to the film thickness. Thickness fringes are damped in the case of Pt_Th40nm and Pt_Th55nm for the as grown state, which can be correlated to the hillocks. The existence of hillocks disturbs the coherent diffraction and damp the oscillations in the case of Pt_Th40nm and Pt_Th55nm. In the case of Pt_Th70nm, i.e., in the continuous hillocks free film the oscillations appear again which statistically prove that the local hillocks-free images can be correlated with the complete film.

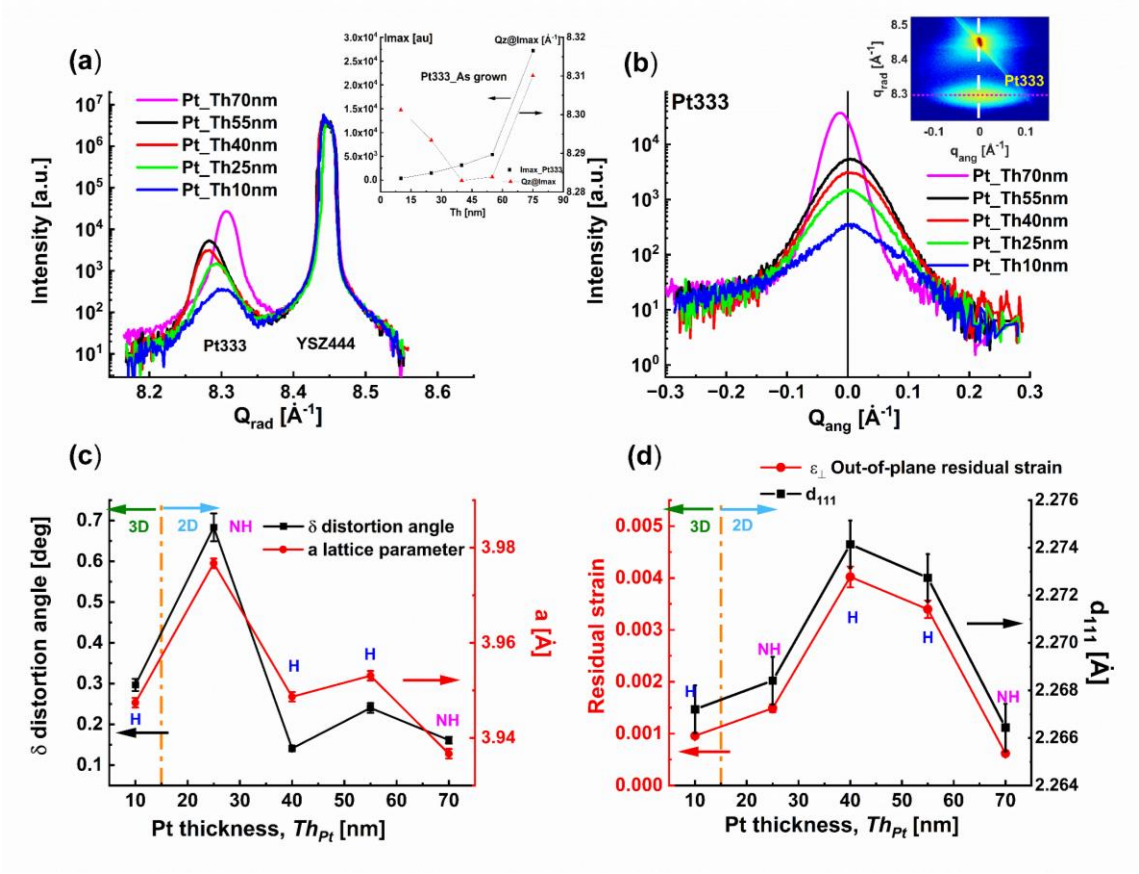

Figure 4.10: (a) The radial diffraction profiles for the Pt333 together with YSZ444 of the Pt_Th10nm, Pt_Th25nm, Pt_Th40nm, Pt_Th55nm and Pt_Th70nm. (b) The corresponding angular diffraction profiles of the Pt333. (c) Variation of the distortion angle and the lattice parameter *a*. (d) Variation of the out-of-plane residual strain and the interplanar spacing d_{111} as function of the of Pt film thickness Th_{Pt}. The labelling "H" and "NH" refers to the hillocks or Non hillocks. The dotted line refers to the morphology transition from 3D-islands growth to 2D-layer-by-layer growth[172].

Angular profiles show that the angular broadening ($FWHM_{ang}$) decreases by increasing Th_{Pt} (Figure 4.11a). The decrease of the $FWHM_{ang}$ could be related to the increase of the lateral coherence length L_H (see Figure 4.11c) and to the decrease of the misorientation shown in Figure 4.11d with the assumption that all the broadening originated from the mosaicity[147]. By employing Pseudo-Voigt fit functions for the radial and angular broadening of the Pt111, Pt222, and Pt333 reflections one can track the changes in $FWHM_{rad}$ and $FWHM_{ang}$ with the reflection order as a function of Th_{Pt}, as shown in the inset of Figure 4.11a and Figure 4.11b. Analyzing the Williamson-Hall plots of $FWHM_{ang}$ and $FWHM_{rad}$ with respect to the reflection order allows to determine the lateral sizes (L_H) and vertical size (L_V) from the intercept, the degree of misorientation (α) and mean value of the vertical strain distribution $(< \varepsilon_\perp >)$ from the slope, respectively. Furthermore, the L_H increase of Th_{Pt} illustrated in Figure 4.11c can be the result of the reduction of the number of the mosaic/grain boundaries, whereby the hillocks density correlated with the triple junctions and grain boundaries at the surface[175]. In the same way, radial intensity profiles were also compared to evaluate the vertical coherent length of the blocks L_V, and mean value of the vertical strain distribution $< \varepsilon_\perp >$.

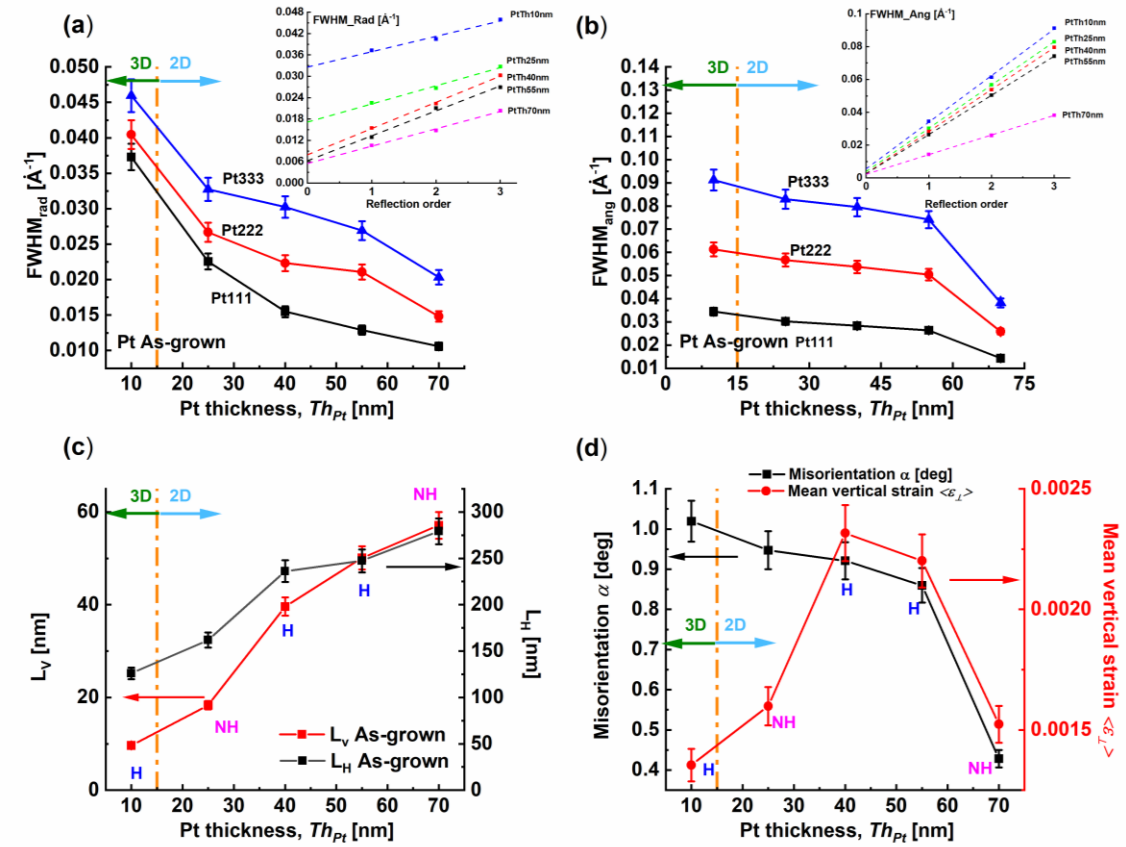

Figure 4.11: (a) And (b) variation of the angular broadening $FWHM_{rad}$ and $FWHM_{ang}$ with Pt film thickness Th_{Pt} respectively. The corresponding inset show the $FWHM_{rad}$ and $FWHM_{ang}$ as function of the reflection order for the Pt_Th10nm, Pt_Th25nm, Pt_Th40nm, Pt_Th55nm and Pt_Th70nm samples. (c) Variation of the lateral L_H and vertical coherence sizes L_V as function of Pt film thickness Th_{Pt}. The dotted line refers to the morphology transition from 3D-islands growth to 2D-layer-by-layer growth. The labelling "H" and "NH" refers to the hillocks or Non hillocks. (d) Variation of the misorientation degree α and the mean value of the vertical strain $<\varepsilon_\perp>$[172].

The increase in block sizes L_H and L_V in Figure 4.11c could also be attributed to the growth time which is directly related to the film thickness via the deposition time. As the growth time increases, the film is exposed to elevated temperatures for a longer period during deposition which consequently influence the sizes L_H and L_V of the Pt mosaic blocks. However, the mean value of vertical strain distribution $< \varepsilon_\perp >$ behaves differently, reaching its peak at Th_{Pt} = 40 nm and Th_{Pt} = 55 nm (Figure 4.11d).

4.6 Modification through encapsulation

The platinum films mentioned above were used as templates for the subsequent growth of the capping "ferroelectric" layer. This involves three steps: the first step heats up the samples Pt_Th10nm, Pt_Th25nm, Pt_Th40nm, Pt_Th55nm and Pt_Th70nm from room temperature to the growth temperature T_g = 900 °C of the capping layer under oxygen environment with an O_2 partial

pressure of P_{O_2} = 400mTorr with a heating rate of 25 °C/min. Heating-up followed by the growth of the capping layer at T_g = 900 °C with P_{O_2} = 400mTorr for 5 hours (which could also be correlated to the previously mentioned annealing for the Pt layer). The last step is a moderate cooling procedure from T_g = 900 °C to room temperature of the bilayer system with a rate of 5 °C/min under P_{O_2} = 400 mT which the Pt layer is encapsulated (Enc Pt) between the substrate and the capping layer. In this part, the morphology and microstructure of both Pt films as in the as-grown and in the encapsulated states will be discussed which were characterized by SEM (SE_0°), EDX, BSE, TEM, XRD and XRR.

Figure 4.12a, 4.12b, and 4.12c and Figure 4.12d, 4.12e, and 4.12f compares the SEM 0°, EDX and BSE images of the Pt film in the as-grown state (Pt_Th25nm) and in encapsulated state (Enc Pt_Th25nm) which hillocks in the as-grown state and in encapsulated state were not detected. The network chain morphology of the Pt film which is transformed into the block morphology during/after the subsequent growth procedure can be visualized by comparing the SEM and EDX images of Pt_Th25nm and Enc Pt_Th25nm (Figure 4.12a, 4.12b and 4.12d, 4.12e). This is often called dewetting, a phenomena of the electrode, which occurs during the annealing procedure at which the Pt atoms are being detached from the surface and agglomerate on the existing Pt islands/layer[164,166]. This consequently decreases the degree of coverage and increases the lateral and the vertical sizes of the blocks. From the evaluation of BSE images, the degree of coverage of the Pt decreases the degree of coverage from 76.3 % to 38.1 %. Furthermore, the blocks seen in the Figure 4.12f are considered to be the bilayer sections of the film whereupon the blocks of Pt below present the capping layer as it was deduced from EDX in Figure 4.12e. For a better understanding of the dewetting phenomena, TEM cross-sections were compared in Figure 4.12g and 4.12h. The TEM images demonstrate that the Pt film thickness is not preserved during the subsequent growth, which results in blocks of around 100 nm vertical size. Additionally, Pt free gaps increase in size. It leads to a growth of the subsequent layer directly on the substrate which is not desired.

The lateral gap sizes (shown via magenta arrows in Figure 4.12g) increase within a range of [15 - 37 nm] to [150 - 690 nm] via dewetting. The thickness change is also verified via mass density profiles obtained by fitting the XRR curves with several layer approximations[176]. This is shown in Figure 4.12i and Figure 4.12j in which Th_{Pt} = 31 nm for Pt_Th25nm, whereas Th_{Pt} = 38 nm for Enc Pt_Th25nm is obtained from the mass density profiles. XRR also justifies the dewetting phenomena during an encapsulation process. Additionally, the mass density profiles of Pt_Th25nm and Enc Pt_Th25nm show a difference in the mass density distribution of the Pt layer as well as in the film thicknesses. As indicated in Figure 4.12j, θ_{CL} and θ_{Pt} show the critical angle for the capping layer and the platinum layer. The comparison between the Pt_Th25nm and Enc Pt_Th25nm shows that the critical angle for the platinum layer is different when Pt is encapsulated. In other words, encapsulation of Pt during the high temperature postgrowth decreases the density of the Pt film (respectively degree of coverage).

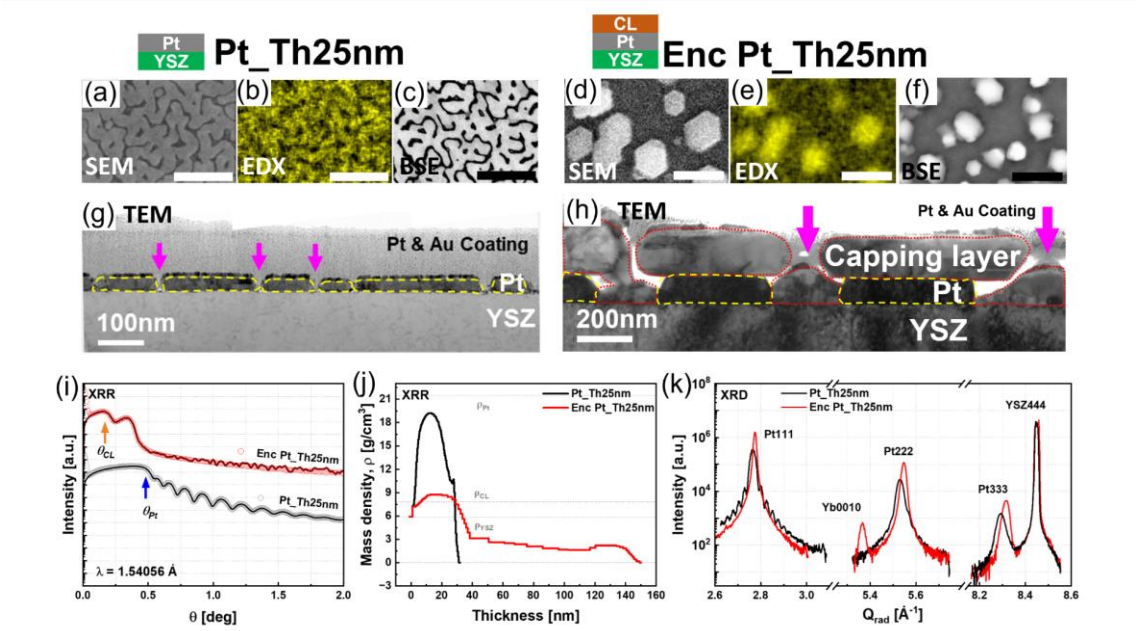

Figure 4.12: (a, b, c, g) And (d, e, f, h) are the SEM, EDX, BSE, TEM images of the Pt_Th25nm and Enc Pt_Th25nm respectively. (i, j, k) Are the comparisons between Pt_Th25nm and Enc Pt_Th25nm of the XRR curves, mass density profiles and the radial diffraction profiles of the Pt111, Pt222 and Pt333 symmetric reflections respectively. Scale bars in (a, b, c, d, e, f) are 500 nm. For magnified version refer to Figure A-9[172].

Additionally, the mass density profile ρ_{Pt} of the Pt_Th25nm film does not remain constant, and it varies across the film thickness up to the film surface without reaching the theoretical bulk value (indicated via the dashed line $\rho_{Pt} = 21.45\ g/cm^3$, $\rho_{YSZ} = 5.85\ g/cm^3$). This mass density fluctuation correlates with the degree of coverage, whereas ρ_{Pt} falls below the theoretical of completely cover film surface. The thickness values obtained from the density profiles are also shown in Table 4-1. It should be noted that the Th_{Pt} values obtained from the mass density profiles are inconsistent with the TEM values due to local aspects of the TEM examination method.

Furthermore, comparing the diffraction patterns a shift in the peak positions of Pt111, Pt222 and Pt333 reflections towards higher scattering wave vectors (Q_{rad}) for the case of Enc Pt_Th25nm can be observed (Figure 4.12k). This shift indicates compression in the out-of-plane interplanar spacing which reduces the lattice plane distance d_{111} = 2.9743 Å to d_{111} = 2.9713 Å. Additionally, the radial intensity profiles show that there is damping of the oscillations of the Pt111 reflections. Visible oscillations indicated that the vertical block sizes of the film were comparable to the thickness and are damped when the sizes are not comparable due to high roughness induced by the dewetting phenomenon.

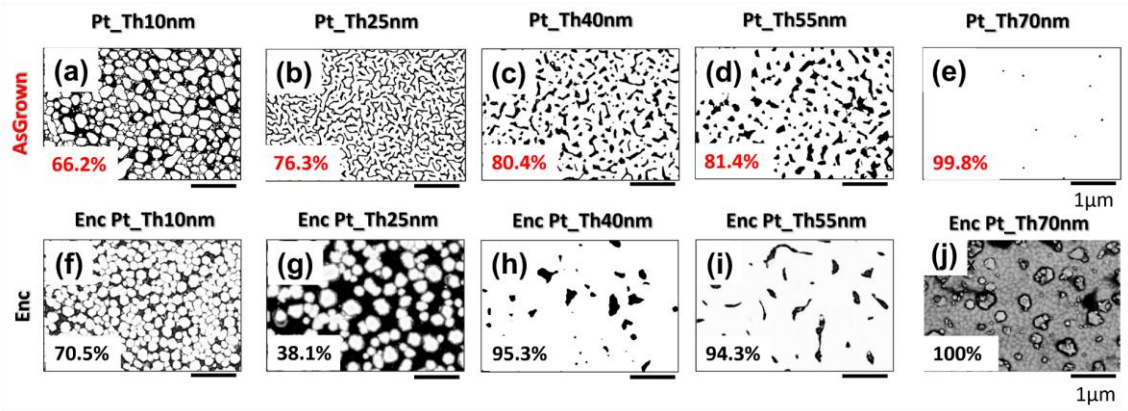

Figure 4.13: Binarised BSE images to investigate the degree of covereage of (a-e) as-grown Pt layers and (f- j) encapsulated Pt layers[172].

The growth of Pt films with varying deposition time led to different morphologies transitioning from 3D-island to 2D-layer-by-layer growth when Th_{Pt} exceeded 10 nm. Above Th_{Pt} = 25 nm the films with Pt_Th40nm and Pt_Th55nm exhibited hillocks at room temperature, likely formed during the cooling phase due to the difference in the thermal coefficient between the Pt film and YSZ substrate. In Figure 4.14, we specifically illustrated the changes in film morphologies and microstructure after post-growth of the subsequent layer for Pt_Th40nm and Enc Pt_Th40nm, where hillocks were present. For comparison, SE_0°, EDX, and BSE images were considered for Pt_Th40nm in its as-grown state (Figure 4.14a, 4.14b, 4.11c) and Enc Pt_Th40nm in its encapsulated state (Figure 4.14d, 4.14e, 4.14f). Due to overgrowth of the subsequent layer, the degree of coverage increased from 80.4 % to 95.3 % (see Figure 4.13c and Figure 4.13h). The BSE images showed a decrease in the hillock density from 2.08 /µm² to 1.64 /µm² (Table 4-1). The formation of hillocks in the 40 nm and 55 nm samples can be attributed to the difference in thermal expansion between Pt and YSZ.

It has been reported that hillock formation serves as a mechanism for stress relaxation in metallic thin films[161,164]. Therefore, the difference between Pt_Th25nm, Pt_Th40nm and Pt_Th55nm can be explained by considering the accumulation and subsequent relaxation of stress due to the film thickness during the cooling phase. From BSE images of Pt_Th40nm and Enc Pt_Th40nm (Figure 4.14c and 4.14f), we derived and summarized the mean sizes of hillock width, the distance between hillocks and channels, as well as the hole diameters (Table 4-1). The hillocks are generally formed by the existence of grain boundaries. In the BSE images the hillocks are present near the black, Pt-free regions which are marked in Figure 4.14c, 4.14f, 4.14k by red circles. In addition, during the subsequent growth phase at T_g = 900 °C the hillocks which are indicated by the magenta arrows in Figure 4.14g, 4.14h, 4.14o become more pronounced. This increased the diffusion energy and induced the reorganization of the Pt film whereupon atoms adjust their positions which in return affects both the morphology and the crystal structure. Consequently, the strain relaxation occurs through the hillock formation. As a speculative interpretation of these results, it can be proposed that at T_g = 900 °C there is a competition between film dewetting, which removes atoms from the surface and/or interface, and atom migration, which leads to the formation of hillocks.

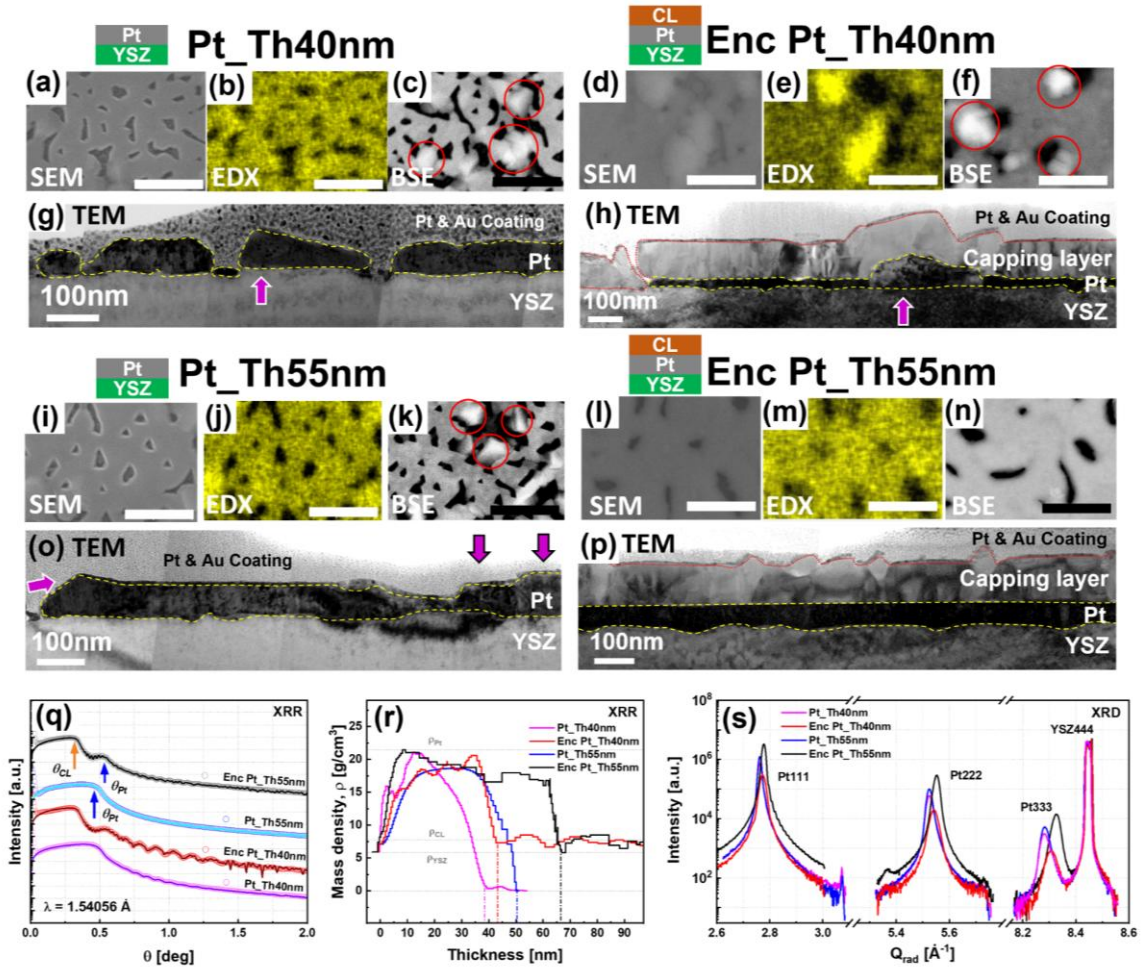

Figure 4.14: (a, b, c, g) And (d, e, f, h) are the SE_0°, EDX, BSE, TEM images of the Pt_Th40nm and Enc Pt_Th40nm respectively. (i, j, k, o) And (l, m, n, p) are the SE_0°, EDX, BSE, TEM images of the Pt_Th55nm and Enc Pt_Th55nm respectively. (q, r, s) Are the comparisons between Pt_Th40nm and Enc Pt_Th40nm and between Pt_Th55nm and Enc Pt_Th55nm of the XRR curves, mass density profiles and the radial diffraction profiles of the Pt111, Pt222 and Pt333 symmetric reflections respectively. Scale bars in (a-f & i-n) are 500 nm. For magnified version refer to Figure A-10[172].

This interplay results in the formation of hillocks or bumps on the surface near the channels during the subsequent growth phase. This in turn contributes to an increase in the degree of coverage and a decrease in the number of hillocks, ultimately leading to a reduction in the hillock density. Simultaneously, the Pt-free area, which are surrounded by the hillocks, were subjected to dewetting caused by the increase of the channel width from 121.75 nm to 237.4 nm and the increase of the hole diameter from 68.35 nm to 96.75 nm for Pt_Th40nm and Enc Pt_Th40nm, respectively. By the rise of the hole diameters detached Pt atoms migrate and pile up around the hillocks, which are near the holes, and enlarge their sizes from 179.8 nm to 376.4 nm. Similar phenomena were investigated in-situ by the group of Jahangir et.al.[159].

Figure 4.14g and 4.14h show the modification by the TEM cross-section images of Pt_Th40nm and Enc Pt_Th40nm. The hillocks are marked with magenta arrows. The film thickness is reduced from 40 nm to 28 nm. XRR and TEM results are in correlation in terms of the thickness of the Pt

film. On the other hand, the hillock sizes were enlarged both in the lateral direction to 200 nm and in the vertical direction to 100 nm. These results support the speculation of the migration of Pt atoms. These results suggest that Pt atoms migrate both from the film surface and from the substrate surface to the existing or appearing hillocks. This rearrangement occurs during the stages of the subsequent growth driven by the diffusion energy at the high temperature T_g = 900 °C.

The SE_0°, EDX, and BSE images of Pt_Th55nm in its as-grown state were compared to Enc Pt_Th55nm in the encapsulated state (see Figure 4.14i, 4.14j, 4.14k and Figure 4.14l, 4.14m, 4.14n, respectively). The analysis of BSE images in Figure 4.13d and 4.13i demonstrates an increase in the degree of coverage from 81.4 % to 94.3 %. Additionally, the hillocks completely disappeared in Enc Pt_Th55nm, as the Pt atoms migrated into the neighboring Pt-free channels which causes a reduction of the number of hillocks (see Figure 4.14k and 4.14n). Therefore, it can be concluded that the competition between dewetting and hillock expansion was influenced by the Pt film thickness under the same growth conditions.

TEM images in Figure 4.14o and 4.14p show that the disappearance of the hillocks happened when the Pt atoms migrated to fill the Pt-free channels in neighboring regions which results in more continuous Pt electrode films. Figure 4.14r demonstrates the mass density profiles obtained by fitting the XRR curves via the several-layers approach of both as-grown and encapsulated states of Th_{Pt} = 40 and 55 nm. In the case of Pt_Th40nm, the mass density profile is not constant and shows a decrease along the film thickness up to the surface. This variation can be attributed to the higher hillock density in Pt_Th40nm which induced the Pt atoms to migrate towards the hillocks rather than filling the gaps in the effective thickness region. This migration contributes to the observed decrease in mass density. Conversely, for Pt_Th55nm, where the hillock density is lower, the density profile of the film remains more consistent. This suggests that the film is homogeneously distributed in the growth direction across the Pt film thickness. As subsequent layers are grown, both layers got smoothed and the density of the hillocks is reduced. As a result, the density profile of the Pt film remains constant throughout the layer without significant fluctuations. The peak position of the Pt333 reflection behaved oppositely for Pt_Th40nm and Pt_Th55nm during encapsulation. Figure 4.14s displays the diffraction patterns of Pt111, Pt222 and Pt333 reflections for the samples in their as-grown and encapsulated states. For the Pt333 higher reflection order, Q_z (light red solid line) of Pt_Th40nm shifted toward lower Q_z values (respectively higher d-spacing, d_{111}) in the case of Enc Pt_Th40nm. Conversely, the Q_z coordinates of the Pt333 peak shifted to higher values when the Pt film changed from its as-grown state (Pt_Th55nm) to the encapsulated state (Enc Pt_Th55nm) which reflected a compressive stress in the out-of-plane d-spacing d_{111}.

Figure 4.15a, 4.15b, 4.15c and 4.15d, 4.15e, 4.15f compare the SE_0°, EDX and BSE of Pt_Th70nm and Enc Pt_Th70nm. The surface of Pt_Th70nm as grown is smooth and without any hillocks. However, subsequent growth could modify the morphology of Pt and consequently the capping layer whereas Figure 4.15d, and 4.15f shows a grain-like morphology.

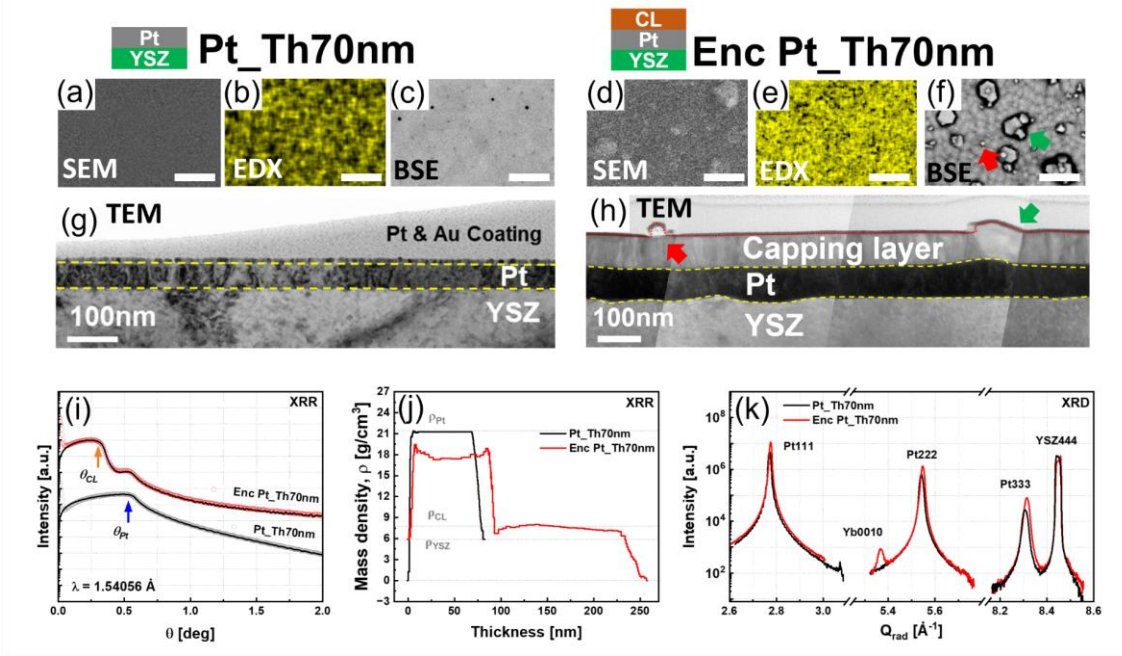

Figure 4.15: (a, b, c, g) And (d, e, f, h) are the SE_0°, EDX, BSE, TEM images of the Pt_Th70nm and Enc Pt_Th70nm respectively. (i, j, k) Are the comparisons between Pt_Th70nm and Enc Pt_Th70nm of the XRR curves, mass density profiles and the radial diffraction profiles of the Pt111, Pt222 and Pt333 symmetric reflections respectively. Scale bars in (a, b, c, d, e, f) are 500 nm. For magnified version refer to Figure A-11[172].

In order to investigate the morphology transformation through the subsequent growth, TEM cross section images were collected. TEM cross section images given by Figure 4.15g and 4.15h, which correspond to Pt_Th70nm and Enc Pt_Th70nm, prove the non-disturbance of Pt film by subsequent growth. Despite the hillock formation was not detected, few bumps were observed in the shape of thickness fluctuations. This latter may generate a disturbance in the crystal structure, orientation and morphology of the subsequent layer which is marked in Figure 4.15f and 4.15h with green arrows. This suggests that the thickness and continuity of the Pt film is crucial for the continuity and microstructural quality of the subsequent grown layer. However, particle-like heights are also visible on the surface of the capping layer, as indicated by the red arrows in Figure 4.15f and 4.15h. These features can be attributed to the growth of the capping layer itself and may not be directly related to the underlying Pt layer.

The XRR fit shown in Figure 4.15i and Figure 4.15j shows the bulk density profiles of the film. It is noticeable that the as-grown sample has a constant density profile throughout the thickness of the film, accompanied by a finely finished surface.. Furthermore, the surface roughness of R_a = 0.6 nm for Pt_Th70nm could be only derived from AFM images due to the inconvenience of the XRR several stack model for the roughness estimation. In addition, the disappearance of the hillocks, which is related with the increased filling factor, indirectly contributes to the sharpness (in other words less rough, smooth, abrupt chemical change) of the Pt film surface. In Figure 4.15, the mass densities profiles of Pt_Th70nm and Enc Pt_Th70nm are consistent and the plateau of mass density profiles which corresponds to the as-grown state (i.e. Pt_Th70nm) is aligned with the theoretical density value. This is in accordance with the obtained local filling factor conducted

by the BSE image analysis. Therefore, it can be concluded that a film thickness of 70 nm is sufficient to completely cover the YSZ(111) surface by using PLD growth. On the other hand, results revealed a slight thickness increase from Th_{Pt} = 70 nm to Th_{Pt} = 88 nm which was accompanied by a small density reduction. This indicates the occurrence of a Pt atoms migration which does not disturb the uniformity and the continuity of the Pt film which is hole-free since the mass the density profile remains constant through the thickness.

In Figure 4.15k, XRD radial intensity profiles of Pt111, Pt222 and Pt333 are compared for Pt_Th70nm and Enc Pt_Th70nm. A peak shift to a higher Q_z position as a result of compression in the d-spacing, d_{111} due to the encapsulation was observed.

To assess the microstructural changes the Pt film as function of thickness Th_{Pt} in the as-grown and encapsulated states, an analysis on the variation of $FWHM_{ang}$ and $FWHM_{rad}$ was performed. It was derived by the Pseudo-Voigt fitting procedure of the diffraction profiles which were determined from the cuts of the RSMs (Figure 4.9). For this purpose, the Williamson-Hall (WH) method was applied to evaluate mosaicity parameters such as misorientation, lateral and vertical coherence lengths, and out-of-plane strain deviation. The degree of misorientation (α) was determined from the slope of the $FWHM_{ang}$ vs. reflection order curve. Figure 4.16a shows the variation of the degree of misorientation α as a function of the Pt film thickness (Th_{Pt}) for the as-grown and encapsulated states of Pt films. In this graph, points labelled by 'H' denote regions with hillocks, while 'NH' denotes regions without hillocks. The dashed/dotted orange line and arrows mark the 3D-2D morphology transition. In the as-grown state, the degree of misorientation α continuously decreases with Th_{Pt}. In addition, Figure 4.16a shows the corresponding hillocks modification at each Pt film thickness Th_{Pt} which occurs due to the subsequent growth. Under subsequent growth, Pt films with Th_{Pt} = 10 nm and 55 nm went from hillock-free ("NH") to hillocks ("H"), while other thicknesses showed no significant change. Thus, as the misorientation decreased, the hillocks disappeared for Pt films with Th_{Pt} = 10 nm and 55 nm. For Th_{Pt} = 25 nm, a strong dewetting caused Pt atoms to migrate onto the Pt blocks which results in a loss of coverage, an increase in the size of voids between Pt blocks and a subsequent reduction in the number of mosaic boundaries. In the case of Th_{Pt} = 40 nm, the presence of the bumps remained unchanged, but their size and density over the surface changed. It is worthwhile to note that the degree of misorientation and out-of-plane residual strain peaked for Enc Pt_Th40nm, as shown in Figure 4.16c. Furthermore, the behavior of the distortion angle δ for both the as-grown and encapsulated layers are studied as a function of Th_{Pt} in Figure 4.16c. The latter generally decreased as the Pt film state changes from the as-grown to the encapsulated. Regardless of the change of the hillock presence between these states, the distortion angle δ was consistently lower in the encapsulated layers, especially for Th_{Pt} = 40 nm and 55 nm. Interestingly, the difference in the distortion angle ($\delta_{as-grown} - \delta_{encapsulated}$) was the smallest in the case of Th_{Pt} = 40 nm whereby hillocks persisted in both states. Encapsulation had a noticeable effect on the reduction of the distortion angle δ, even by causing a drop below zero for the encapsulated Th_{Pt} = 40 nm and 55 nm layers which implies a distortion of the lattice in a different direction.

Figure 4.16d shows the d-spacing d_{111} for both the as-grown and encapsulated layers which followed a similar trend to the distortion angle. For the different Th_{Pt}, the growth of the subsequent layer represented an annealing process of 5 hours duration with an annealing temperature of T_g =

900 °C in an oxygen environment whereupon the Pt interface layer was in an encapsulated state. This annealing process has contributed to the release of the mean value of the vertical strain distribution $<\varepsilon_{\perp}>$ (Figure. 4.16b), the degree of distortion δ (Figure 4.16c) and to the reduction of d-spacing d_{111} in comparison with the as-grown state (Figure 4.16d).

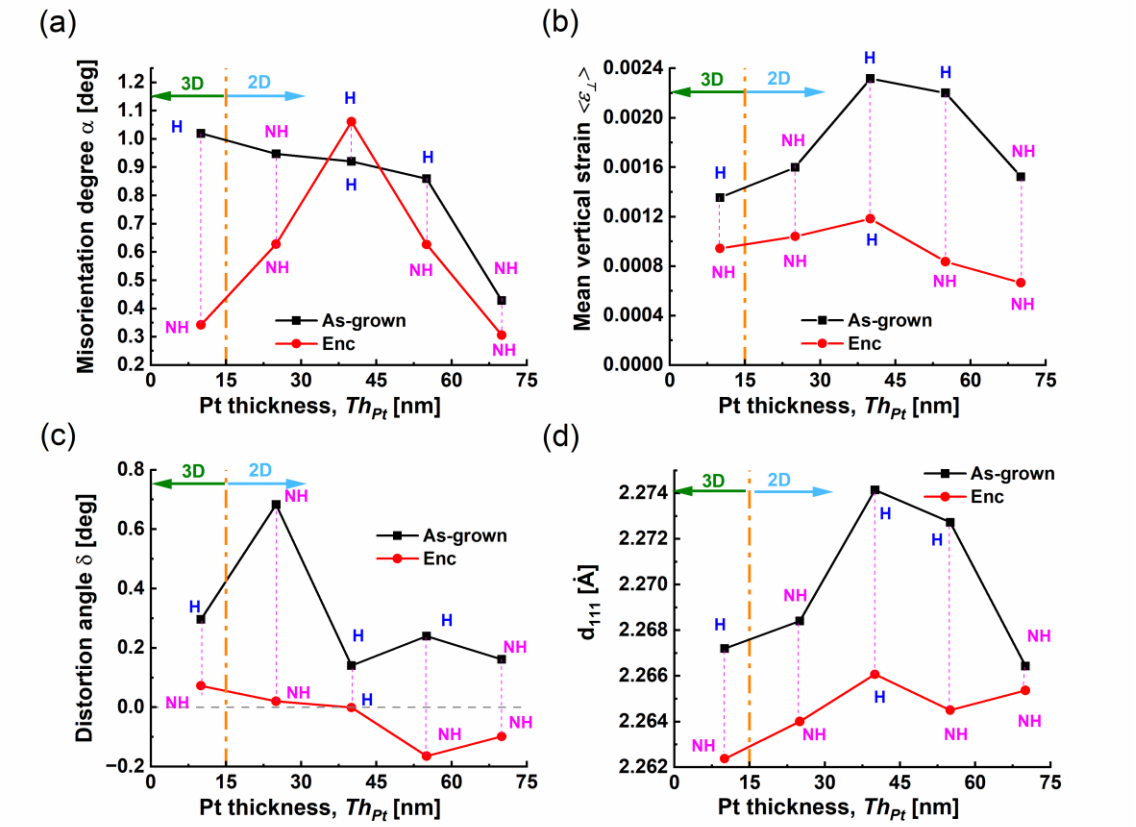

Figure 4.16: (a) Variation in the degree of misorientation, (b) mean vertical strain distribution, (c) cubic to rhombohedral distortion angle, and (d) interplanar d-spacing d_{111} as a function of Th_{Pt} in both as-grown and encapsulated states. The dotted line marks the morphological transition from 3D island growth to 2D layer-by-layer growth. The labels 'H' and 'NH' refer to hillock and no-hillock, respectively[172].

4.7 Summary and conclusions

The study involved the PLD growth of Pt films on YSZ(111) substrates at temperatures which range from T_g = 300 °C to T_g = 900 °C, in order to find out the optimum growth temperature for the future bottom electrode application.

One can conclude from our detailed structure investigation that the platinum films grown at different temperatures exhibit different degrees of mosaicity. The deposited Pt films at T_g = 300°C and 900 °C (i.e. PtT300, PtT900) possess the highest and the lowest degrees of misorientation for the mosaic crystal blocks, respectively. Additionally, PtT900 was found with the smallest angular broadening for a diffraction profile which proves PLD growth to cause a high crystal quality with low defect concentration. Further investigation of morphology revealed that PtT900 had the least

rough surface which makes it a potential candidate for post-growth processes. Additional experiments which simulate subsequent growth processes by annealing, showed that dewetting phenomena occurred in all systems. The phenomena were maximized for PtT300 and minimized for PtT700 and PtT900 as confirmed by SEM images. Further investigation of the crystal structure on annealed samples revealed that PtT300 experienced the maximum modification in terms of angular broadening and mosaic tilt during annealing, while the crystal structure and the morphology of PtT900 underwent minimum modifications. Consequently, one can conclude that the optimum growth temperature is T_g = 900 °C (Homologous temperature, T_h = 0.57, Table A-1) in order to study the thickness effect for an optimum Pt film thickness which may lead to a robust stable functioning bottom electrode. The impact of the Pt film thickness Th_{Pt} was investigated with regard to its morphology, crystal structure, and hillock formation in the as-grown state. By combining various microscopic techniques like SE_50°, EDX, BSE, and TEM, an insight into the role of the Pt thickness was gained by enhancing a film continuity and a reduction of hillocks. The detailed comparison between the as-grown and encapsulated states of the different Pt films revealed several competitive phenomena which includes hillock formation, dewetting, and coalescence driven by an increased diffusion energy at T_g = 900 °C and interactions at grain boundaries. An optimum thickness of Th_{Pt} = 70 nm resulted in a high-quality Pt bottom electrode, free of hillocks, and with minimal thickness fluctuations suitable for the operation at room temperature. Interestingly, the formation of hillocks was observed, dependent on the film thickness and the resulting morphology, despite the high growth temperature. It was concluded that the hillock formation was least pronounced at higher thicknesses, both for the as-grown and encapsulated states. It is important to take the rearrangement of the Pt film during a subsequent growth into account, which effectively represents an annealing process for the Pt bottom electrode. The lattice constants and residual strains of the Pt films decreased after the subsequent growth which indicates compression in the unit cell and stress release due to the Pt film arrangement driven by dewetting and an increased Pt diffusion energy. For the investigated systems, an optimum growth temperature of T_g = 900 °C and an optimum thickness of Th_{Pt} = 70 nm was found which makes Pt to withstand further processes in our multiferroic device production.

Table 4-1: Summary of the morphological parameters in the as-grown and in the encapsulated states for the Pt thicknesses Th_{Pt} = 10, 25, 40, 55 and 70 nm. a: Obtained from AFM. b: Obtained from BSE. s: Obtained from SEM_50°. X: Obtained from XRR. Y: Obtained from TEM. NA: Not-Available[172]

As-Grown State	**Pt_Th10 nm**	**Pt_Th25 nm**	**Pt_Th40 nm**	**Pt_Th55 nm**	**Pt_Th70 nm**
Film thickness Th_{Pt} [nm]	10	25	40	55	70
Topography	Island	Network	Network + Hillocks	Network + Hillocks	Network + Hole
Growth mode	3D	2D	2D	2D	2D
Mismatch [%]	−23.07	−22.25	−23.16	−22.92	−23.37
Morphology					
Thickness[X] [nm]	13.67	30.16	49.08	50.87	80.52
Thickness[Y] [nm]	NA	27.9 [23–31]	58.4 [33–72]	63.7 [30–80]	51.0 [47–55]
Roughness, R_a[X] [nm]	0.54 ± 0.15	1.14	1.18		0.42 ± 0.02
Roughness, R_a[a] [nm]	4.06	1.83	4.24	8.94	0.6
Island size[b] [nm]	47 [10–129]	NA	NA	NA	NA
Channel width[a] [nm]	NA	89 [41–141]	159 [85–247]	213 [104–286]	NA
Channel width[b] [nm]	NA	81 [28–142]	122 [37–308]	137 [48–376]	NA
Depth of channels[a] [nm]	NA	[9–25]	[36–48]	[52–65]	NA
Heights of islands[a] [nm]	[11–45]	NA	NA	NA	NA
Holes					
Hole size[a] [nm]	NA	41 [15–100]	71 [30–176]	61 [18–111]	NA
Hole size[b] [nm]	NA	27 [7–87]	68 [24–182]	95 [28–278]	46 [24–69]
Hillocks					
Hillocks width[a] [nm]	126 [88–171]	NA	187 [87–298]	276 [107–428]	NA
Hillocks width[b] [nm]	NA	NA	180 [117–274]	217 [99–428]	NA
Hillocks density[a] [/µm^2]	4.56	NA	2.26	1.40	NA
Hillocks density[b] [/µm^2]	9.44	NA	2.08	1.78	NA
Hillocks height from the film surface [nm]	21.8 [5.3–44.7]	NA	23.6 [7.2–37.0]	31.8 [16.0–52.8]	NA
Percolation					
Degree of coverage [b] [%]	66.2	76.3	80.4	81.4	99.8
Conductivity [×10^6 1/Ωm]	0	0.25	0.74	1.01	3.69

Table 4-1: Continued[172].

Encapsulated state	**Enc Pt_Th10 nm**	**Enc Pt_Th25 nm**	**Enc Pt_Th40 nm**	**Enc Pt_Th55 nm**	**Enc Pt_Th70 nm**
Resulting topography	Islands	Islands	Network + Hillocks	Network	Hole
Mismatch [%]	−23.68	−23.74	−23.72	−24.09	−23.93
Morphology					
Thickness[X] [nm]	NA	NA	43.72	68.6	NA
Thickness[Y] [nm]	NA	95.4 [89–109]	24.7 [19–35]	54.9 [48–73]	75.0 [70–86]
Island size [nm]	NA	NA	NA	NA	NA
Channel width[b] [nm]	NA	NA	237 [58–1014]	226 [58–1014]	NA
Holes					
Hole size[b] [nm]	NA	NA	97 [29–252]	95 [31–205]	NA
Hole size[Y] [nm]	NA	[150–690]	[45–143]	78	NA
Hillocks					
Hillocks width[b] [nm]	152 [61–278]	179 [58–411]	376 [219–604]	NA	NA
Hillocks density[b] [/µm^2]	NA	NA	1.64	NA	NA
Percolation					
Degree of coverage[b] [%]	70.5	38.1	95.3	94.3	100

5 Microstructure, stoichiometry, and magnetic properties of $BaFe_{12}O_{19}$ films on YSZ(111) substrates: Influence of the platinum interface layer quality and laser fluence

5.1 Introduction

Hexagonal barium ferrite ($BaFe_{12}O_{19}$, BaM) with a magnetoplumbite structure is a well-known material for its microwave applications[177,178,179], magneto-optical recording capabilities[180,181] and specifically for its relatively better magnetic properties for longitudinal recording media[182,183,184]. Several researches were devoted to perform BaM films with a relatively high uniaxial magnetic anisotropy (H_a), high coercivity (H_c) and high perpendicular squareness to make them suitable for perpendicular recording media with a small signal-to-noise ratio (SNR)[80,182,183]. The film thickness has an important role in the properties of thin films, since the accumulated stress, defect density such as threading and misfit dislocations[57] are thickness dependent. For high-density perpendicular recording media (PMR) applications, the necessary thickness would vary from a few tens of nanometers to 200 nm due to the acquired chemical stability, mechanical durability and small grains[80].

Up to date, different growth methods were devoted to the deposition and to investigation of BaM such as sputtering[185,191],pulsed laser deposition (PLD)[80,107,186] , molecular beam epitaxy (MBE)[187] etc. Researchers have reported about a chemical intermixing phenomenon between the BaM layer[186] and the substrates used, i.e., MgO[186], SiO_2[185,188],SiC[187], Al_2O_3[189], YSZ (Bauer et. al. where the BaM grown on YSZ substrates is firstly shown)[80,107]. Furthermore, the c-axis oriented (easy magnetization axis) BaM was fabricated by PLD using Al_2O_3 (0001), MgO(111), SiC(0001), Si(111), GaN(0001) and Ga_5O_{12}(111)[179]. To prevent the chemical intermixing, the formation of an inhomogeneous phase at the substate and additionally grown BaM along the easy magnetisation axis[191,192], several interface layers were investigated such as Au[190], Pt[185,186,191,192], Pd[192] as metallic layers, YSZ[191], TiO_2[193], Fe_2O_3[193], MgO[186,188], ZnO[194] and AlN[195,196] as ceramic interlayers. Pt(111) interlayer was found to be the most effective solution to block the mixture between the substrate and BaM layer. In addition, the Pt interface layer can reduce the lattice mismatch and promote the c-axis orientation[80,197,198]. The effects of the interdiffusion and the variation in the chemical composition on the microstructure and magnetic properties were previously discussed[198]. Few studies have demonstrated the dependence of the coercivity on the chemical composition and magnetic anisotropy[203]. Up to date, several studies were carried out on the impact of

the interface layer film thickness and microstructure on the subsequent grown BaM layer [185,188,189,191,198]. However only few investigations demonstrated the effect of thickness of the Pt interface layer on the BaM coercivity and squareness[185,186,198].

The influence of growth parameters like gas partial pressure (oxygen)[199,200,201,202], substrate surface morphology and temperature[199] on the microstructure, morphology, and magnetic properties was previously studied. However, the laser fluence was not being neither intensively nor systematically investigated. Since the laser fluence affects the growth rate and the kinetic energies of the species the deposited film thickness is consequently dependent on the number of shots as well as on the capability to overcome the environmental gas pressure to reach the substrate. It has been concluded that the laser fluence and the background gas are interrelated[81].

The micromagnetic model developed by Kronmüller et al.[24,203] suggests that the coercivity is controlled by nucleation of reversed domains and/or domain wall pinning[25]. It is also widely accepted that nucleation sites are responsible for reducing coercivity[204], as opposed to pinning sites[20]. In relation to these mechanisms, the investigation of defect types in BaM films by using TEM and complementary diffraction methods have been limited[80,205,206]. This work represents the first demonstration and publication that out-of-phase boundaries are relevant and influenced by the laser fluence used during PLD growth[80]. In terms of defect and coercivity mechanisms, anti-phase/out-of-phase boundaries act as domain wall pinning, while grain misorientation (mosaicity) can reduce the nucleation field. Both can influence the coercivity. Conversely, the mosaicity can reduce the coercivity if the material is slightly out of c-axis orientation[204,207,208]. Therefore, the control of the mosaic tilt and modulation of defect concentration, including out-of-phase boundaries, is important for the coercivity modulation. Few studies have investigated the effect of the interface layer on the c-axis orientation, especially for perpendicular recording media[187,209]. There is a clear need to determine the optimum thickness required for subsequent growth of BaM. Furthermore, while the growth parameters for BaM by using PLD have been extensively investigated, a crucial parameter like the laser fluence, has not been intensively studied. It is important to note that the defect concentration, magnetization and the film thickness are interrelated parameters as highlighted in previous researches[57,210]. Recently, Yu et. al. [211] investigated the dependence of the grain size, the crystal quality and magnetization hysteresis on the laser fluence without considering the variation in the film thickness of their samples which results from the change in the laser fluence. In the chapter, a comprehensive and detailed study, involving versatile and complementary methods such as EDX, STEM, AFM, SEM, MFM, VSM, HRXRD and XPS, will be presented. We attempt to establish the relationship between growth parameter such as laser fluence and stoichiometry, structure, and magnetization. Additionally, we explored the influence of the Pt interface layer on the BaM film quality and properties.

5.2 Influence of platinum interface layer quality on the microstructure, stoichiometry, and magnetic properties

In order to investigate the effect of the interface layer platinum quality on subsequent grown BaM films, two platinum films named PtTh25 and PtTh75 with 25 nm and 75 nm nominal thicknesses were grown on YSZ(111) and structurally and morphologically analyzed by using a combination of diffraction microscopy methods. The detailed structure investigation was performed in Chapter 4. Subsequently, BaM films were deposited on Pt_Th25nm and Pt_Th70nm templates following the growth conditions displayed in Table 3-2 and Table 3-3 of Chapter 3. The obtained bilayers composed of Pt interface layer and BaM layers are termed BaMPtTh25 and BaMPtTh75. To clearly show the influence of the interface layer growth on the film crystal quality and on the resulting magnetic properties, a BaM film was grown without a Pt interface layer named BaMPtTh0.

5.2.1 Comparison of the Pt microstructure between the encapsulated and as-grown state

The templates PtTh25 and PtTh75 were pre-characterized for the BaM growth by XRR, HR-XRD, SEM, and TEM, in order to explore the structural and morphological modifications of the Pt bottom electrode as a function of its thickness. The analysis of the Pt crystal structure was carried out by measuring the Pt-reflections (i.e., Pt111, Pt222, Pt333 and Pt331) by means of HR-XRD for the as-grown state (i.e., PtTh25, PtTh75) and for the encapsulated state (i.e., BaMPtTh25, BaMPtTh75). Figure 5.1 shows reciprocal space maps (RSMs) of the symmetric reflections Pt111, Pt222, Pt333 and YSZ444. RSMs of asymmetric reflection Pt331 are shown for PtTh25, PtTh75, BaMPtTh25 and BaMPtTh75 samples.

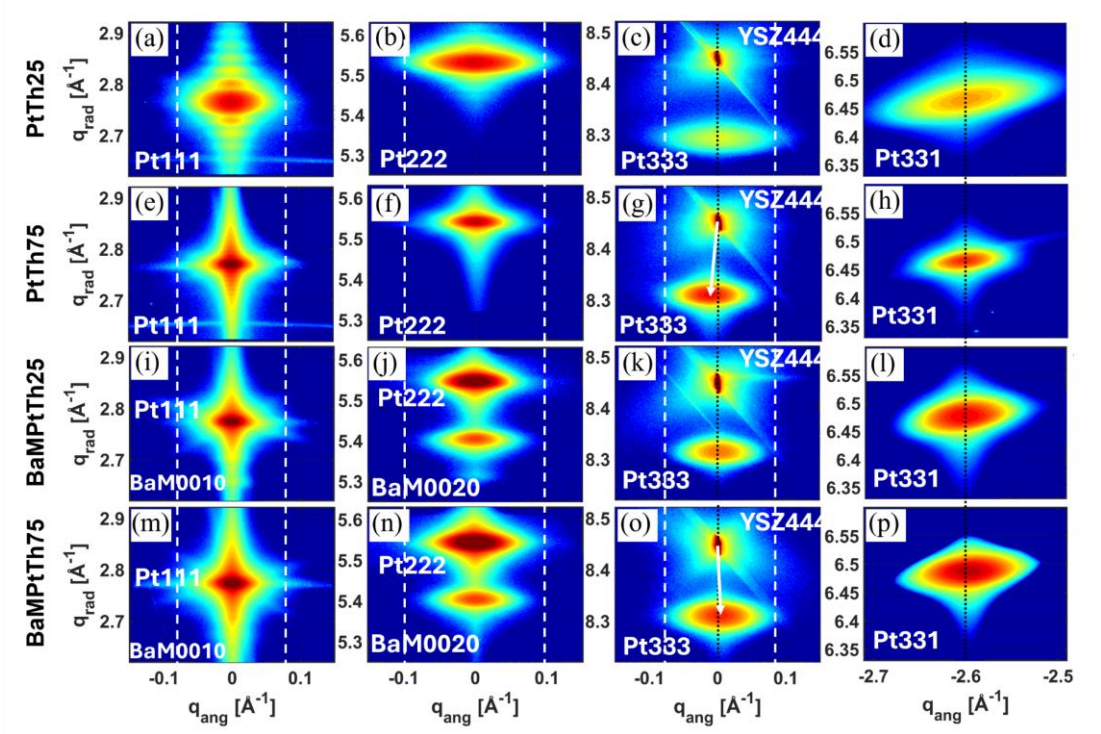

Figure 5.1: (a, b, c, d) And (e, f, g, h), (i, j, k, l), and (m, n, o, p) are reciprocal space maps recorded in high-resolution X-ray diffraction (HR_RSMs) for the symmetric reflections Pt111, Pt222, Pt333 and asymmetric reflection Pt331 for the PtTh25, PtTh75, BaMPtTh25, and BaMPtTh75 samples, respectively[107].

Increasing the Pt film thickness leads to a difference in the distribution of the diffuse scattering around the reflections and therefore in the angular and radial directions of the RSMs. In addition, the radial direction (q_{ang} = 0) of Pt111 reflections, which correspond to PtTh25 and PtTh75, show a decrease in the size of the fringe periodicity (Figure 5.1a, Figure 5.1e). From the oscillation period of the fringes (Figure 5.1a, 5.1e), the vertical coherent block size $L_{\perp, Pt}$ = 23.96 nm for PtTh25 and $L_{\perp, Pt}$ = 68.83 nm for PtTh75 was determined. As a result, the size of the Pt crystal in the growth direction was found to be comparable with the Pt film thickness.

Vertical white dashed lines, inserted in Figure 5.1a, Figure 5.1b and Figure 5.1c for PtTh25 (respectively Figures 5.1e, 5.1f, 5.1g PtTh75) are utilized, in order to compare the extend of diffuse scattering which is distributed along the angular direction for the reflections Pt111, Pt222 and Pt333, respectively. The intensity distributions of the different reflections are larger for PtTh25 than for PtTh75. This can be interpreted as an improvement in the Pt crystal quality induced by the increase of the film thickness up to about 70 nm. Furthermore, RSM of Pt333 reflections combined with the YSZ444 reflections provide an additional information about the c-axis orientation of the Pt crystal film with respect to the substrate (111) lattice planes. By comparing the RSMs (Pt333 & YSZ444) of Figure 5.1c and Figure 5.1g, which correspond to PtTh25 and PtTh75, one can notice that PtTh75 has an off-axis shift of the Pt333 reflection with respect to the YSZ444 reflection as illustrated by the white arrow. This shows that the surface normal of the Pt(111) film is slightly tilted with respect to the YSZ(111) lattice plane normal. RSMs of Pt331 asymmetric reflections (Figure 5.1d, 5.1h) indicate a difference in the diffuse scattering distribution around the reflections of PtTh25 and PtTh75. This refers to a different mosaicity and degree

of misorientation due to the Pt film thickness. It can be seen that the diffraction profiles of PtTh25 (Figure 5.1d) show a larger angular broadening (respectively mosaicity) than in PtTh75 (Figure 5.1h).

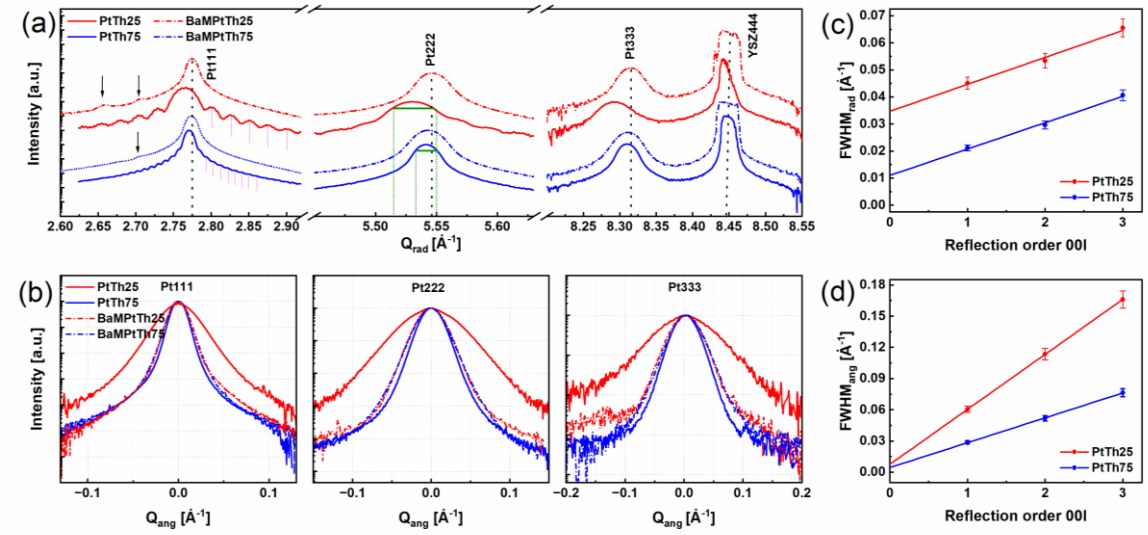

Figure 5.2: (a) Comparison of the radial diffraction profiles of the Pt111, Pt222, and Pt333 derived from vertical cuts along the wave vector Q_z at $Q_x = 0$ of the HR_RSMs illustrated in Figure 5.1. (b) Comparison of the angular diffraction profiles of the Pt111, Pt222, and Pt333 derived from the horizontal cuts at the maximum Q_z values of the corresponding HR_RSMs of Figure 5.1. (c) And (d) variation of the radial and angular broadening as a function of the reflection order 00l drawn for the PtTh25, PtTh75, respectively. For magnified version refer to Figure A-12[107].

In Figure 5.2a and Figure 5.2b, the derived radial and angular diffraction profiles from the RSMs of PtTh25 and PtTh75 are compared. For the Pt111, Pt222 and Pt333 reflections, the radial and the angular broadenings are found to be higher in the case of PtTh25. Furthermore, the high radial broadening shown in Figure 5.2a reflects a higher strain fluctuation along the growth direction (i.e. c-axis of Pt(111)). The variation in angular broadening is illustrated by drawing the FWHM of the Pt222 reflection by dark-green solid and dashed lines in Figure 5.2a. Additionally, Figure 5.2b demonstrates a decrease in the angular broadening for PtTh75, and therefore, in the mosaicity due to the increase of the Pt film thickness. In order to analyze the degrees of mosaicity of Pt films, diffraction profiles of the symmetric reflections Pt111, Pt222 and Pt333 were fitted by Pseudo-Voight functions (Chi-square ~ 0.9999). The determined radial ($FWHM_{rad}$) and angular ($FWHM_{ang}$) values were plotted as a function of the reflection order 00L in Figure 5.2c and Figure 5.2d, respectively. By applying the Williamson-Hall (WH) approach, the mosaic tilt of the blocks (α_{Pt}), the lateral coherent block size ($L_{//, Pt}$), the out-of-plane strain fluctuation ($<\varepsilon_{\perp, Pt}>$) and vertical coherent block sizes ($L_{\perp, Pt}$) are derived and listed in Table 5-1. The WH approach enables the disentanglement of angular broadening contributions which results from the mosaic tilt and lateral coherent block size, as well as from the radial direction of strain fluctuation and vertical coherent block size. WH approach was only applied to the PtTh25 and PtTh75 due to the discontinuity issue of the encapsulated Pt film for the BaMPtTh25 sample, which will be mentioned in (Chapter 4, Pt). It comes out that the lateral coherent block sizes of Pt film increase from $L_{//, Pt}$ = 82.68 nm to $L_{//, Pt}$ = 128.20 nm while the vertical coherent block sizes increase from $L_{\perp, Pt}$ = 18.10

nm to $L_{\perp, Pt}$ = 56.68 nm for PtTh25 and PtTh75, respectively. One can conclude that the increase of the Pt film thickness leads to the enhancement of degree of coverage and therefore to the increase of the block sizes. The low values in ($FWHM_{rad}$) and angular ($FWHM_{ang}$) for PtTh75 is interrelated with the reduced number of the mosaic block boundaries and defects. The degree misorientation of mosaic blocks and vertical strain fluctuation were also improved from α_{Pt} = 1.896 to α_{Pt} = 0.8485 and from $<\varepsilon_{\perp, Pt}>$ = 4.98×10^{-3} to $<\varepsilon_{\perp, Pt}>$ = 4.735×10^{-3}. The Pt film thickness was increased to ~75 nm. In conclusion, the improvement of the microstructure of the Pt film was achieved by increasing the film thickness.

5.2.2 Influence of the interface quality on the $BaFe_{12}O_{19}$ films microstructure

BaMPtTh25 and BaMPtTh75 samples were fabricated by growing BaM on PtTh25 and PtTh75 seed layers. BaM samples which include BaMPtTh0 are taken as a reference and were investigated by several advanced techniques, in order to study the microstructure variation.

5.2.2.1 HR-XRD study

BaMPtTh0 BaMPtTh25 and BaMPtTh75 samples were investigated by analyzing the RSMs of BaM reflections measured by HRXRD. In Figure 5.3, RSMs symmetric reflections of BaM0014, BaM0020, BaM0024 & YSZ333 were shown together with RSMs asymmetric reflections of BaM-2022. BaM-2024, BaM-2025, Pt331 and YSZ224 as well as for the samples BaMPtTh0, BaMPtTh25 and BaMPtTh75. The RSMs of BaM004, BaM006, BaM0010, BaM0012, BaM0016, BaM0020, BaM0022 reflections were also collected (not shown here) and do not reveal any significant difference. From Figure 5.3e, 5.3f and 5.3g, it can be easily seen that for the BaMPtTh25 sample, that an extra RSM-XRD peak in appears at around $Q_Z = 4.0\ \text{Å}^{-1}$ for BaM0014, at around $Q_Z = 5.3\ \text{Å}^{-1}$ for BaM0020, at around $Q_Z = 6.7\ \text{Å}^{-1}$ for BaM0024 and at around $Q_x = -2.43\ \text{Å}^{-1} and\ Q_Z = 6.7\ \text{Å}^{-1}$ for BaM-2024 which is marked with yellow dashed rectangles, respectively. This additional diffraction spots originate from a minor crystalline formation with different out-of-plane lattice parameters. Since the Q_x position is the same as BaM-2022, -2024 and -2025 (Figure 5.3h), the in-plane lattice parameter of this minor phase is the same as of the BaM film but strained in the in-plane direction. Radial diffraction intensity profiles were extracted from the RSMs shown in Figure 5.3 and plotted in Figure 5.4a. In order to improve the visibility, intensities were shifted vertically. Additional peaks were marked with magenta stars and the corresponding Q-positions were indicated by dashed magenta colored lines. It can be clearly seen that an additional peak with a weak intensity appears only for BaMPtTh25 which confirms that the extra phase represents a minor phase only. Radial diffraction profiles do not show a significant difference which prooves similarties in the stoichimetry and out-of-plane strain fluctuation among the BaM samples without a Pt interface layer (i.e. BaMPtTh0) and with a Pt interface layer with two different thicknesses (BaMPtTh25 and BaMPtTh75). Figure 5.4b represents chi-scans of the asymmetric reflection BaM-2022 which shows a six-fold symmetry of the BaM films for all three samples BaMPtTh0, BaMPtTh25 and BaMPtTh75. Extracted symmetric diffraction profiles shown in Figure 5.4a and asymmetric diffraction profiles were fitted by using the Pseudo-Voigt function to extract the Q-positions and FWHM values. Out-of-plane c_{BaM} and in-plane a_{BaM} lattice parameters were calculated and listed in Table 5-2.

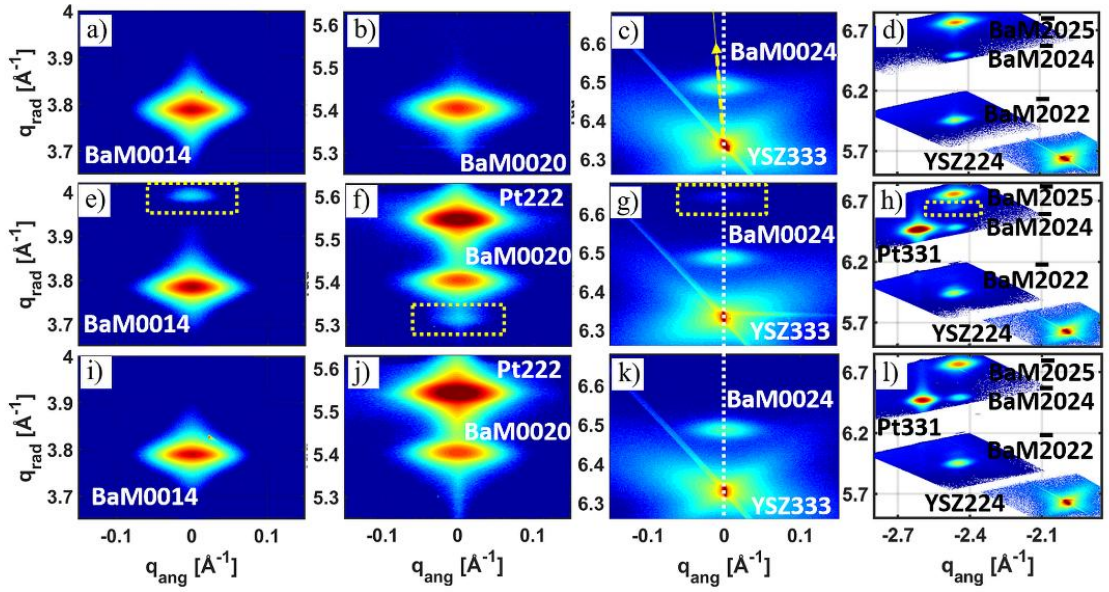

Figure 5.3: (a, b, c, d) And (e, f, g, h), (i, j, k, l) are reciprocal space maps recorded in high-resolution X-ray diffraction (HR_RSMs) for the symmetric reflections BaM0014, BaM0020, BaM0024 and asymmetric reflections BaM-2022, -2024, -2025 for BaMPthTh0, BaMPtTh25 and BaMPtTh75 samples, respectively[107].

The derived radial ($FWHM_{rad}$) and angular ($FWHM_{ang}$) were plotted as a function of the reflection order 00l in Figure 5.5a and in Figure 5.5b, respectively. From the WH approach the degree of mosaicity, sizes of the lateral and vertical coherent blocks and our-of-plane strain fluctuation were determined and listed in Table 5-2. In Figure 5.4c, XRR measurements of PtTh25, PtTh75, BaMPtTh0, BaMPtTh25 and BaMPtTh75 samples are compared. The XRR reflectivity data were fitted by using the Leptos 7 software package. In the used model, BaMPtTh25 and BaMPtTh75 films constist of bilayer systems and PtTh25, PtTh75 and BaMPtTh0 are considered as single layers. Upon the increase of Pt film thickness Th_{Pt}, the oscillations are being damped especially for PtTh75 (Figure 5.4c). This could be due to the increase of the surface roughness. From the of XRR curve fits, the surface roughness of the Pt films decreased from R_{surf} = 2.54 ± 0.33 nm to R_{surf} = 0.42 ± 0.01 when Th_{Pt} was increased from 25 nm to 70nm. Furthermore, it was possible to get obtain better XRR curve fits of PtTh25 by considering a double layer structure which indicate the existence of two different platinum films with different structural parameters. The roughness R_{int} at the Pt/YSZ interface was found to be higher (R_{int} = 1.46 ± 0.24 nm for PtTh75) than for PtTh25 which R_{int} = 0.87 ± 0.08 nm. This in turn explains the loss of oscillations due to the destructive rough interface interferance.

If regarding the comparison between the BaMPtTh25 and BaMPtTh75 films, there exist two interfaces, BaM/Pt and Pt/YSZ. For both films, the roughness at the BaM/Pt interface with R_{int} = 3.7226 ± 0.0140 nm (resp. R_{int} = 2.9587 ± 0.1419 nm) is higher than of the Pt/YSZ interface with R_{int} = 0.3929 ± 0.2597 nm (resp. 0.2273 ± 0.3092) in the case of BaMPtTh25 (resp. BaMPtTh75). One can conclude a defined Pt/YSZ interface and from the roughness of the BaM/Pt interface that there is a loss of thickness oscillations and a steep drop in the XRR intensity. It can be also de-

duced that the quality of the interface BaM/Pt was improved by increasing Th_{Pt}. This was confirmed by the decrease of the surface roughness of PtTh75 with respect to PtTh25. Moreover, for the BaMPtTh0 one-layer system, the roughness of R_{int} = 2.7472 ± 0.6732 nm at the interface BaM/YSZ is higher than the one at the Pt/YSZ interface (R_{int} = 0.3929 ± 0.2597) for BaMPtTh25. In conclusion, the interface quality was improved by inserting a Pt interlayer, not only but also by the increase of the Pt interlayer film thickness.

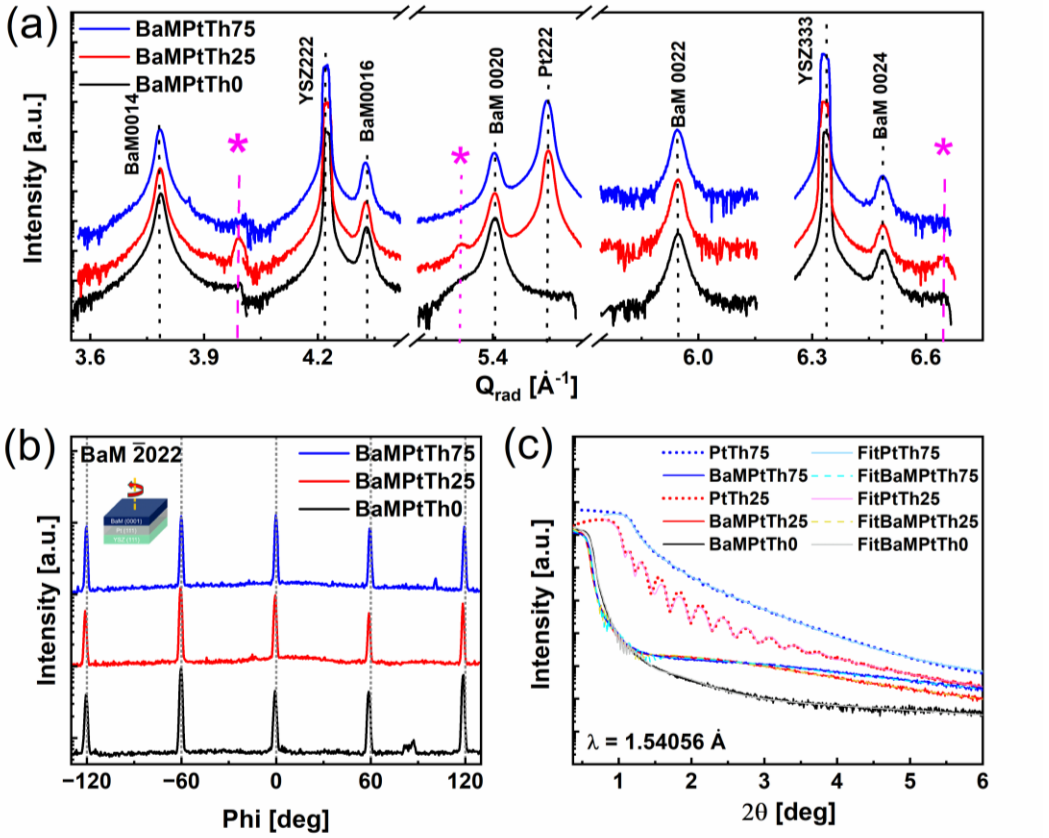

Figure 5.4: (a) Comparison of the radial diffraction profiles of the symmetric reflections BaM0014, BaM0016, BaM0020, BaM0022, and BaM0024 for BaMPthTh0, BaMPtTh25, and BaMPtTh75 samples derived from vertical cuts along the wave vector Q_z at Q_x = 0 of the HR-RSMs partially illustrated in Figure 5.3. (b) Azimuthal scan as a function of the phi angle (i.e., rotation around at the surface normal) for the asymmetric reflection 2022 which corresponds to the BaMPthTh0, BaMPtTh25, and BaMPtTh75 samples. (c) XRR curves for the PtTh25, PtTh75, BaMPthTh0, BaMPtTh25, and BaMPtTh75 samples[107].

In the following, the effect of the Th_{Pt} increase on the microstructure BaM film quality will be investigated. It can be observed from Figure 5.5b, that the $FWHM_{ang}$ values are higher for the case of BaMPtTh75 sample probably due to an increase in the defect concentration associated with the mosaic block boundaries or to their degree of misorientation. This latter is measured to be 0.65 for the BaMPtTh0, while for BaMPtTh25 it is 0.78. For the BaMPtTh75 samples, the value is 0.84. An increase in Th_{Pt} may generate surface irregularities like, for example, roughness. By using Equation (5-1)[57] and (5-2) a lattice mismatch f between BaM and Pt (111) as well as between BaM and YSZ (111) was calculated and listed in Table 5-2.

$$f_{BaM/Pt}[\%] = \frac{a_{BaM} - a_{Pt}}{a_{Pt}} * 100 \quad (5\text{-}1)$$

By using the in-plane (out-of-plane) lattice parameters, a_{BaM}, a_{Pt} and a_{YSZ} (c_{BaM}, c_{Pt} and c_{YSZ}) of the BaM, Pt layers and of the YSZ (111) substrate, in-plane (out-of-plane) residual strain $\varepsilon_{//}$ ($\varepsilon_{\perp}$) values were determined via Equation (5-3) & (5-4)[212].

$$f_{BaM/YSZ}[\%] = \frac{a_{BaM} - a_{YSZ}}{a_{YSZ}} * 100 \quad (5\text{-}2)$$

The magnitudes a_{BaM} and c_{BaM} are the measured in-plane and out-of-plane lattice parameters of the BaM films, whereas $a_{BaM}^{FS} = 5.9281$ Å, $c_{BaM}^{FS} = 23.4070$ Å[107] correspond to the lattice parameters of the BaM bulk in the free standing state.

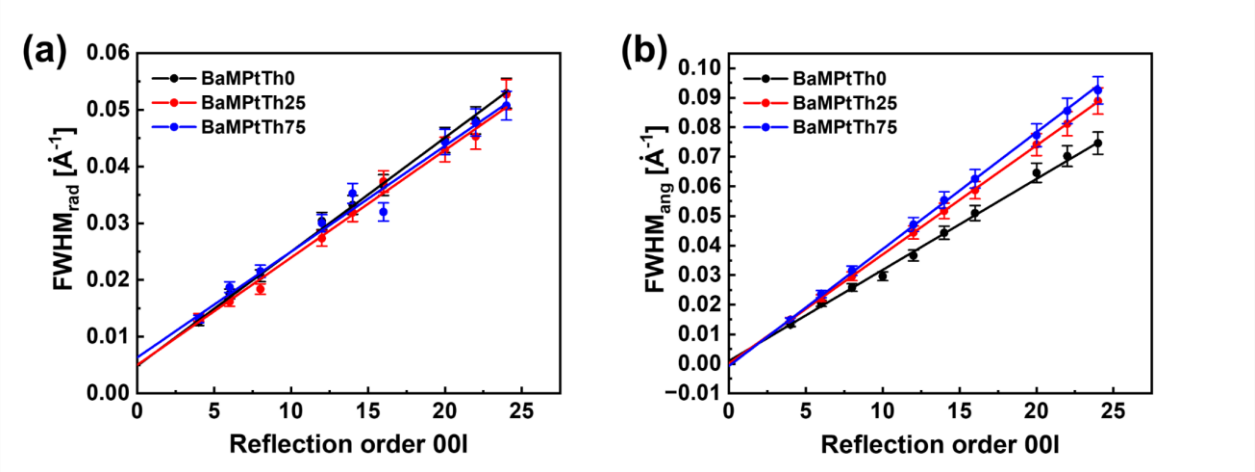

Figure 5.5: (a, b) Variation of the radial and angular broadening with the reflection order 00l employed as Williamson-Hall (WH) approach for the BaMPtTh0, BaMPtTh25 and BaMPtTh75 mosaicity parameters determination. From the $FWHM_{rad}$ as function of the reflection order 00l, the RSM vertical strain $<\varepsilon_{\perp}>$ was determined from the slope $\varepsilon_{\perp,BaM} = \frac{slope}{2}$ while the mean vertical size of the BaM of mosaic block was derived from the intercept at the origin Y0 by $L_{\perp,BaM} = \frac{2\pi}{Y0}$. From $FWHM_{ang}$ as function of the reflection order 00l, the degree of misorientation α [deg] was determined from the slope by $\alpha = slope * (\frac{c_{BaM}}{2\pi})$ [107].

$$\varepsilon_{//,BaM} = \frac{a_{BaM} - a_{BaM}^{FS}}{a_{BaM}^{FS}} \quad (5\text{-}3)$$

$$\varepsilon_{\perp,BaM} = \frac{c_{BaM} - c_{BaM}^{FS}}{c_{BaM}^{FS}} \quad (5\text{-}4)$$

5.2.2.2 Microscopic analysis of the interface quality effect on the $BaFe_{12}O_{19}$ microstructure

As mentioned, the increase of deposited material enhances the film thickness as well as the degree of coverage. In Figure 5.6, SEM and TEM micrographs of as grown samples PtTh25 and PtTh75

are shown. SEM images of PtTh25 and PtTh75 (Figure 5.6a, Figure 5.6b) display different morphology and degree of coverage. This latter is expectedly higher for PtTh75 while PtTh25 contains a network structure with Pt-free channels which indicate an incomplete surface coverage of around 78% calculated by the image processing of SEM data. TEM micrographs of Figure 5.6c and Figure 5.6d, reveal a film composed of Pt disconnected blocks with a thickness variation between Th_{Pt} = 20 nm and Th_{Pt} = 31 nm for PtTh25. The mean value of the thickness obtained by XRR is in accordance with the Pt blocks size derived by TEM.

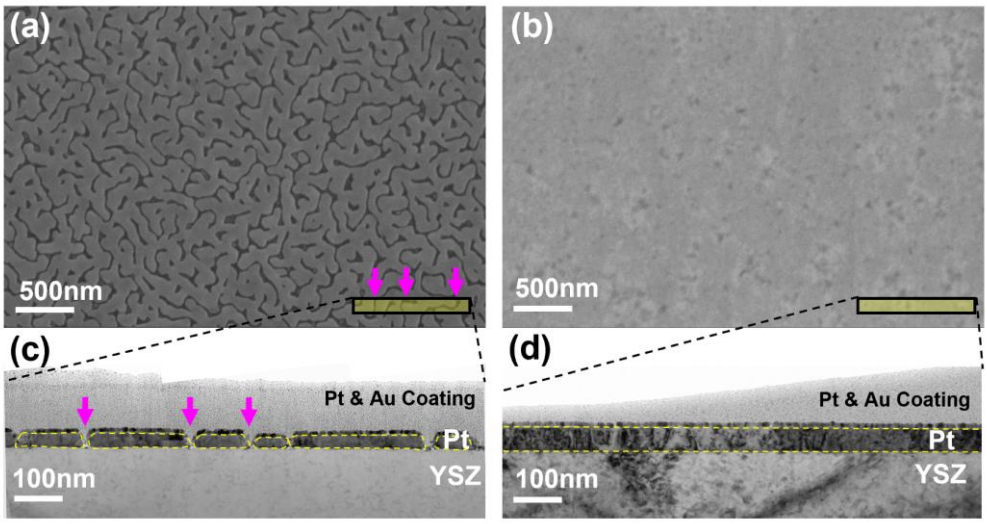

Figure 5.6: (a, c) And (b, d) SEM and TEM micrographs of the PtTh25 and PtTh75 samples respectively. (a) SEM and (c) TEM micrograph of PtTh25 shows the discontinuity of the film. Dark contrast in (a) SEM micrograph corresponds to the channel-like structure which represents non-filled YSZ (111) regions. (b) TEM micrograph also shows the discontinuity from the cross-section. Magenta arrows indicate the channels. (b) SEM and (d) TEM show the continuity of the PtTh75. Black rectangular boxes (a and b) correspond to the representative region and to the size of the TEM lamella shown in (c and d). Yellow-dashed lines in (c, d) indicate the border of the Pt layer to improve visibility[107].

Additionally, the vertical sizes of the mosaic blocks obtained by WH-method were estimated to $L_{\perp, Pt}$ = 24 nm. The findings of XRR and TEM are in accordance with each other and permits us to conclude that the Pt block size extends over the whole film thickness. The width of the Pt-free channels of the PtTh25 sample, i.e., the distances between the Pt blocks, were measured by using SEM images. They vary between 15 and 100 nm. The sizes of the discontinuity regions were estimated between 15 to 37 nm, while the lateral sizes of the Pt blocks vary between 74 to 270 nm for PtTh25. SEM and TEM images of as grown PtTh75 do not reveal any discontinuity. The thickness obtained from a TEM lamella with a size of 1 µm is Th_{Pt} = 55 nm, which is slightly smaller than the thickness obtained from XRR fitting and XRD thickness fringes. This discrepancy of the TEM evaluation can be justified by the limitation of the local region measurement which is provided by TEM micrographs.

The effect of the Pt interlayer thickness on the subsequently grown BaM layers was investigated in detail by using high-resolution STEM imaging and by using HAADF images. BaMPtTh0, BaMPtTh25 and BaMPtTh75 samples were investigated with comparable scaling and are represented in Figure 5.7, Figure 5.8, and, Figure 5.9, respectively. The contrast of HAADF images

depend on the atomic-number and on the specimen thickness. It reveals the element-specific intensity variation due to the similar crystal structure and specimen thickness, especially in the atomically resolved regions. Cross-section TEM Bright-field images of the BaM layer grown on a YSZ substrate were shown in Figure 5.7a. Atomic-resolution images were taken from several regions through the sample, however in Figure 5.7b and 5.7c, representative regions are shown. Figure 5.7b and 5.7c reflects the atomic-resolution real structure of the interface region (BaM/YSZ) (green box) and the bulk region of the film (orange box) in Figure 5.7a, respectively. Figure 5.7b shows the existence of a continuous amorphous layer with 3 nm thickness, located between a BaM layer and a YSZ substrate (see orange dashed lines). The diffractogram (Figure 5.7d) obtained from the interlayer region by fast two-dimensional Fourier transformation (FFT) exhibits an amorphous structure. While the diffractogram of the BaM layer near the interface (Figure 5.7e), obtained from the red square region drawn in Figure 5.7b, proves a highly c-axis oriented BaM crystal structure.

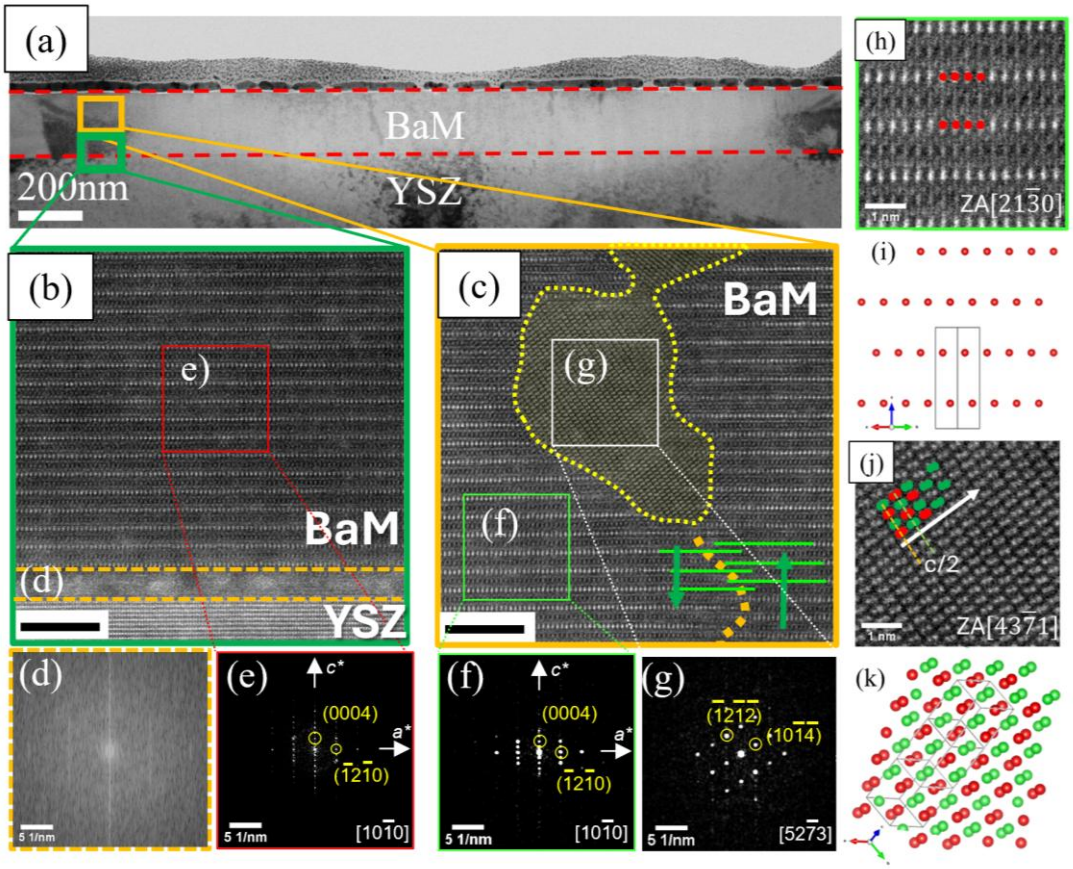

Figure 5.7: (a) Low magnification TEM micrographs for BaMPtTh0 which contains two drawn regions designed by green and yellow squares, (b), (c) high magnification TEM micrographs of 20 x 20 nm corresponding to the green and yellow squares of (a) respectively, scale bars are in the size of 5nm. (d) And (e) Fast Fourier transformation (FFT) images of the interlayer and BaM film regions illustrated by yellow dashed and red solid squares in (b). (f) And (g) are the FFT images for the green and the white BaM regions drawn in Figure showing different crystal orientations. (h, j) HRTEM micrographs of BaMPtTh0, (h, j) HRTEM micrographs of BaM zones indicated by green and white squares respectively. (i) and (k) schematic presentation for the atomic arrangement of the BaM zones which corresponds to the squares white and green, respectively[107].

Additionally, at some locations of the sample out-of-phase (OPB) defects were visualized slightly above the amorphous interlayer and extend through the growth direction without reaching the film surface. The OPB defects are indicated by the vertically dislocated green lines which correspond to the Ba atomic layers in the crystal lattice shown in Figure 5.7c. The extension of the OPB defects through the growth direction, marked with orange dotted lines, was observed to be the origin of the crystal lattice perturbation. In addition, there is a lattice disturbance, highlighted by yellow contour region in Figure 5.7c. The corresponding diffractograms FFT of the white square (Figure. 5.7g) indicates a well embedded BaM with a large degree of misorientation of 15.3 degrees in the c-axis (i.e. [0001] direction of the film). In contrary, the diffractogram of Figure 5.7f, which corresponds to the green square, confirms the formation of highly oriented c-axis BaM crystal outside the disturbed white drawn region. This misorientation detected by the FFT analysis is consistent with the RSM of the diffraction spot BaM0024 (in Figure 5.3c), whereupon the BaM peak position is off-centered in the Qx direction with respect to substrate reflection

of YSZ333, also indicated by the yellow arrow on the RSM. This indicates that there is a misaligned 0001 phase of BaM from the lattice planes normal of the YSZ111 substrate. Figure 5.7h and 5.7j represent the atomically resolved images of the regions (f) and (g) where the orientation of the regions is clearly shown by the red and green dots which represent Ba atoms in the structure. Figure 5.7i and 5.7k display the simulated crystal orientation, the distribution of the Ba atoms and the unit cell of the crystal. Red and green balls both represent Ba atoms. Misalignment of the crystal does not reveal the arrangement of the Ba atoms by itself. The arrangement of the Ba atoms could only be realized when there exists an extra out-of-phase shift in the distance of c/2 of the BaM crystal. This is visualized in Figure 5.7k.

For BaMPtTh25 sample, Figure 5.8 shows the investigation of high-resolution STEM HAADF images and the FFT analysis together with the corresponding regions. In Figure 5.8a, the Pt interface layer in the BaMPtTh25 film appears discontinuous like the PtTh25 sample. During the subsequent growth of the BaM layer, the Pt template undergoes duetting phenomena in such way that atoms of Pt migrate from the surface of YSZ to the already existing Pt blocks. This can be seen from the increase of the height, lateral size of Pt blocks as well as from the expansion of the Pt-free, also called, discontinuity regions. The Pt-free areas were found to vary between 150 and 690 nm. Discontinuity of the Pt interface layer results in discontinuous BaM blocks which grows both on Pt blocks and on YSZ111 Pt-free regions. Those Pt and BaM blocks are visualized by using yellow dotted and red dashed lines. Figure 5.8b and Figure 5.8e compare the quality of BaM/Pt and BaM/YSZ interfaces by high-resolution STEM images of the blue and orange regions drawn in Figure 5.8a. In Figure 5.8e, BaM/YSZ the interface appears to be relatively diffuse which may indicate a gradient of transition, being the origin of OPB (see dislocated green horizontal lines) which ends up with a stacking fault (SF) defect visualized by red arrow. The diffractogram, presented in Figure 5.8d of the BaM film which is grown on YSZ (i.e. Pt free areas). It is obtained from the defined region (green square) and indicates a highly oriented BaM c-axis. Furthermore, the amorphous layer, which was detected in the BaMPtTh0 sample (Figure 5.7) was not observed. Regarding the BaM grown on Pt blocks Figure 5.8b shows a sharp BaM/Pt interface which also contains OPBs and SFs illustrated by green dislocated lines and a red arrow, respectively. The corresponding FFT in Figure 5.8c proves the growth of c-axis oriented BaM on Pt and does not reveal any significant difference with the BaM grown on YSZ. However, few inhomogeneous regions were detected in the regions near the film surface (see Figure 5.8f with low magnification and in Figure 5.8g, Figure 5.8j with higher magnification). There appears a well embedded extra phase layer in between the c-axis oriented BaM layers. From the FFT analysis (Figure 5.8h, 4.8i, 4.8k, 4.8l) of the specified white squares regions in Figure 5.8g and Figure 5.8j, the formation of an extra Ba deficient phase is demonstrated which grew in the orthorhombic structure which corresponds to Fe_2O_3 ICSD 415250 space group $Pna2_1$ which the in-plane and the out-of-plane lattice parameters, projected along the [110] zone axis are a = 5.071 Å, b = 8.736 Å and c = 9.418 Å, respectively. This finding of the extra revealed phase from HRTEM correlates well with the HRXRD RSM results in Figure 5.3e, 5.3f, 5.3g, 5.3h where an extra peak nearby the BaM diffraction spot exists. The comparison between the BaMPtTh25 (Figure 5.8a) and BaMPtTh75 (Figure 5.9a) implies that the continuity and the degree of coverage of the Pt interface layer are dependent on the deposited Pt thickness and, therefore, on the ablated amount of material. One can conclude that the Pt dewetting phenomenon does not conspicuously differentiate between BaM grown on the Pt interface layer and directly grown on YSZ. However, it is well discussed in the

literature that the continuity of the bottom electrode is a crucial to obtain a conductive layer for device applications[213]. Dewetting of Pt during the post-growth process leads to an increase of the lateral distance of Pt-free regions between 15 and 37 nm and 150 to 690 nm, and the lateral Pt block sizes between 110 to 470 nm. In order to understand the formation of two distinct crystal phases during the growth of BaM on BaMPtTh25, BaM1 and BaM2, it is essential to identify the microstructural changes in the Pt interface layer during the BaM growth. For this reason, the Pt crystal structure was compared between the as grown (PtTh25, PtTh75) and in the encapsulated states after subsequent growth (BaMPtTh25 and BaMPtTh75) in Figure 5.2a and 5.2b.

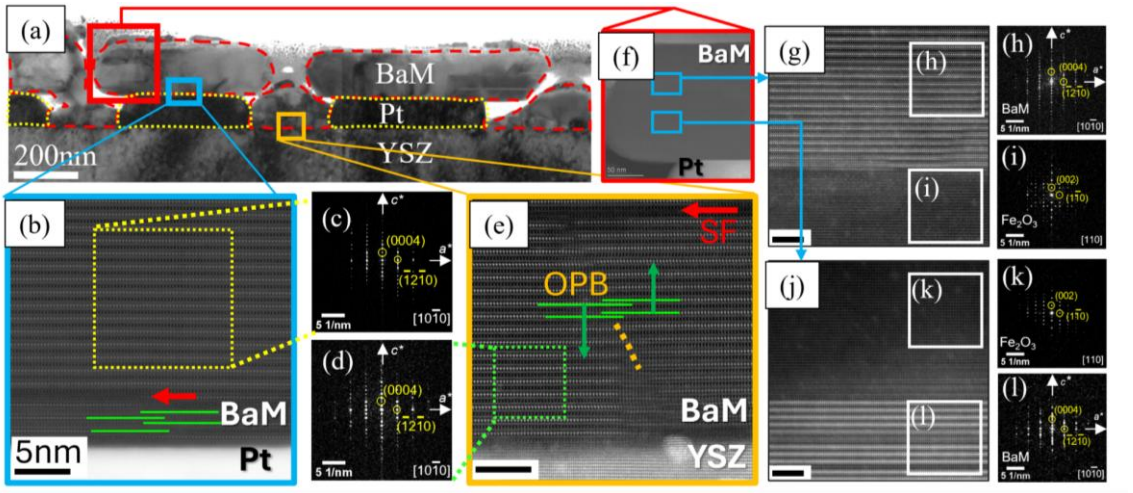

Figure 5.8: (a) Low magnification TEM micrographs for BaMPtTh25 which contains three regions indicated by red, blue, and yellow squares. (b) High magnification TEM micrographs for the blue square of image (a) which correspond to the BaM layer grown on the Pt blocks and (c) FFT images which correspond to the BaM region of the blue square is given in image (b). (e) High magnification TEM micrographs for the yellow square of image (a) which correspond to the BaM layer grown on YSZ substrate in the cavity between the Pt blocks and (d) FFT image of the BaM region designed by the green square in the TEM micrographs of (e). (f) Enlarged TEM micrograph of BaM films grown on Pt, (g), and (j) are high-resolution TEM images which correspond to the two blue regions in image (f). (h) and (i) are the FFT images of two regions with two different atomic contrast in HRTEM micrographs (g). (k) and (l) are the FFT images of two regions with two different atomic contrast in HRTEM micrographs (j). Scale bars (e, g, j) are in the size of 5nm. For magnified version refer to Figure A-13[107].

The shifts in the peak positions of the Pt111, Pt222 and Pt333 reflections are noticeable, especially in the case of BaMPtTh25 and suggest a contraction of the lattice parameter (a_{Pt}) during the deposition of the BaM layer. The derived lattice parameters (see Table 5-1) provide a comprehensive summary of the Pt microstructural changes from the Pt templates (PtTh25, PtTh75) and the bilayer (BaMPtTh25, BaMPtTh75) films. During the subsequent BaM growth the Pt interface layer with a nominal thickness of Th_{Pt} = 25 nm undergoes significant structural changes. This includes the reduction in the lattice unit cell with a_{Pt} decreasing from 3.9388 to 3.9257 Å and the interplanar d-spacing ($d_{111,\,Pt}$) from 5.5638 to 5.5491 Å. In addition, there is a complete relief of the in-plane strain within the Pt layer by following the BaM growth, as shown in Table 5-1. Figure 5.2a shows a smaller shift in the Pt peak positions for BaMPtTh75 compared to PtTh75, and a remarkable displacement observed for the Pt peak position in the case of BaMPtTh25 compared to PtTh25. As a result, the changes in the lattice parameter are relevant for the thinner Pt interface

layers in the case of BaMPtTh25 while BaMPtTh75 exhibits mosaic blocks with slight misorientations in comparison with BaMPtTh25. In the latter case, high-resolution STEM and HR-RSM reveal the presence of two distinct crystal BaM phases. This finding suggests a Pt optimum thickness for the interface layer which ensures the formation of a continuous layer that withstand dewetting during the overgrowth of BaM. The comparison of the crystal structures of the BaM layer grown on the Pt interface layers for BaMPtTh25 (Figure 5.8e) and BaMPtTh75 (Figure 5.9e) underlines the persistence of the same crystalline structure, unaffected by the discontinuity of the Pt interface layer. The BaM film grown on an almost-continuous Pt interface layer was investigated by selecting three distinct regions, denoted by blue, red and green square regions, as shown in Figure 5.9a.

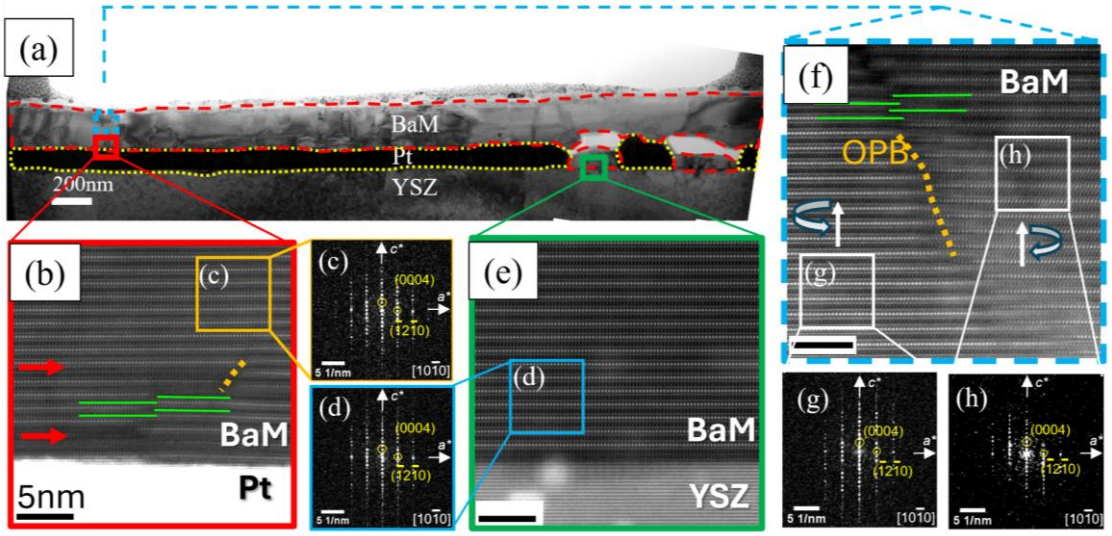

Figure 5.9: (a) Low magnification TEM micrographs for BaMPtTh75, which contains three drawn regions designed by red, blue, and green squares. (b) High magnification TEM micrographs for the red square of image (a) which corresponds to the BaM layer grown on the Pt. (c) FFT images corresponding to the BaM region of the yellow square is given in image (b). (e) HRTEM micrographs of the BaM region grown on YSZ are shown in the green color square in image (a). (d) FFT image which corresponds to the BaM film is highlighted by blue square region in the TEM micrograph image (e). (f) HRTEM micrographs taken from the blue region of TEM image (a). (g) and (h) FFT images which correspond to two BaM regions are given by the white squares of TEM micrographs (f) separated by the out-of-phase boundary defect (OPB). It induces a twist in the BaM crystalline structure. Scale bars in (e, f) are in 5nm size. For magnified version refer to Figure A-14[107].

The well-oriented BaM growth with high crystal quality on the Pt interface layer was confirmed by high-resolution STEM imaging in Figure 5.9b, together with the corresponding diffractogram (Figure 5.9c) of the area marked with orange squares. With respect to the BaM microstructure within the cross section apart from the Pt/BaM interface, the presence of an OPB defect was revealed by the enlarged STEM micrograph of the region outlined by the blue square in Figure 5.9a (Figure 5.9f). This defect separates two regions, labelled 'g' and 'h', which exhibit local twisting around the adjacent OPB. Justification of the twist is provided by the corresponding diffractograms (Figure 5.9g and Figure 5.9h) obtained by the FFT analysis of these distinct regions. The relative change in the diffraction pattern shows that the reciprocal lattice crosses the Ewald's sphere from a different position which indicates a twist in the lattice.

5.2.3 Influence of interface quality on the chemical composition of the subsequent $BaFe_{12}O_{19}$ layer

5.2.3.1 Chemical distribution of the film across the surface

Figure 5.10 shows the surface topography and elemental composition analysis of BaMPtTh0, BaMPtTh25 and BaMPtTh75 by using combined SEM/EDX measurements over a 6 µm x 6 µm area. The intention was to establish a correlation between the microstructures of the Pt interface layer and the BaM layer, and to correlate our findings from STEM/HRXRD-RSM analyses with the spatial distribution of the Ba, Fe, Zr, Pt and O elements. In order to bridge the gap between the microstructures observed in the approximately 2 µm wide cross sections and the surface topography with the corresponding element distributions, one has introduced Figure 5.10a1, 5.10b1 and 5.10c1 as visual reminders of the TEM micrographs shown in Figure 5.7a, Figure 5.8b and Figure 5.9c for the BaMPtTh0, BaMPtTh25 and BaMPtTh75 samples, respectively. The red rectangles in Figure 5.10a2, 5.10b2 and 5.10c2 mark the sample surfaces and refer to our discussions in the previous chapter, supported by cross-sectional TEM/STEM images.

A detailed study of microstructural changes and elemental composition over larger lateral scales was considered valuable to derive reliable information on the influence of the Pt interface layer thickness. Figure 5.10a, 5.10b2 and 5.10c2 provide an overview of the BaM surface topography due to the insertion of the Pt interface layer. For BaMPtTh0, it reveals a homogeneous BaM morphology. For BaMPtTh25, an ensemble of BaM blocks which range from isolated islands to interconnected BaM channels finally generate a BaM network structure with intervening holes for BaMPtTh75.

In order to further understand the corresponding elemental distribution of the morphologies mentioned above, EDX maps were acquired over a 6 µm x 6 µm area and presented in Figure 5.10a4 to 5.10a8, 5.10b4 to 5.10b8 and 5.10c4 to 5.10c8. A uniform distribution of Ba, Fe, O and Zr elements over the measured area was found for BaMPtTh0 (Figure 5.10a4 to Figure 5.10a8). However, the Pt blocks formation of BaMPtTh25 (see Figure 5.10b2 and Figure 5.10b3) is well captured by the corresponding Pt distribution map (Figure 5.10b6) whereupon black regions indicate areas devoid of Pt. In contrast, although Pt defines the block structure, Figure 5.10b4 shows a less distinct block morphology which suggests that Ba encompasses the Pt blocks and the interstitial spaces. Nevertheless, Ba-free voids are present in a regular arrangement within the EDX map visible as black spots similar to the Fe element distribution (Figure 5.10b5). In the case of BaMPtTh75, an almost continuous Pt interface layer which clearly influences the BaM surface morphology and which results in a continuous BaM film interspersed with some voids and channels was obtained. These latter can be seen as dark areas in the SEM images shown in Figure 5.10c2 and 5.10c3. These regions correspond to Pt-free zones at which the Pt layer detached from the substrate during the BaM overgrowth. This was also confirmed by the corresponding EDX mapping data. In Figure 5.10c3, 5.10c5, 5.10c6 and 5.10c8, the elemental characteristics of regions of dark voids and curved channels of varying sizes are readily apparent. Both the voids and channels are Pt-free region but filled with dispersed Ba atoms. However, the Fe and O elements are partially absent in certain regions within the voids and channels.

5.2.3.2 Atomic-scale analysis of the chemical distribution at the interfaces by using atomic-resolution EDX mapping

As mentioned above, the modulation of the BaM/YSZ interface was achieved by the intercalation of a Pt layer. The continuity of the Pt interface layer and the surface morphology of the overlying BaM film was significantly affected by the increase of the Pt thickness from Th_{Pt} = 25 nm to 75 nm. During the subsequent growth of BaM the Pt/YSZ template underwent changes in the microstructure, strain and morphology due to Pt dewetting from the substrate. These processes resulted in the formation of distinct interfaces: a single BaM/YSZ interface in the BaMPtTh0 sample and three types of interfaces (Pt/YSZ, BaM/Pt and BaM/YSZ) in the BaMPtTh25 and BaMPtTh75 bilayer systems. In addition to our focus on interface transitions in terms of the microstructure high resolution EDX mapping for the different samples (BaMPtTh0, BaMPtTh25 and BaMPtTh75) to explore and compare the chemical composition within these interface regions was performed. Figure 5.11a and 5.11b show atomically resolved STEM HAADF images of the BaM layer grown on YSZ near the BaM/YSZ interface for BaMPtTh0 and BaMPtTh25, respectively.

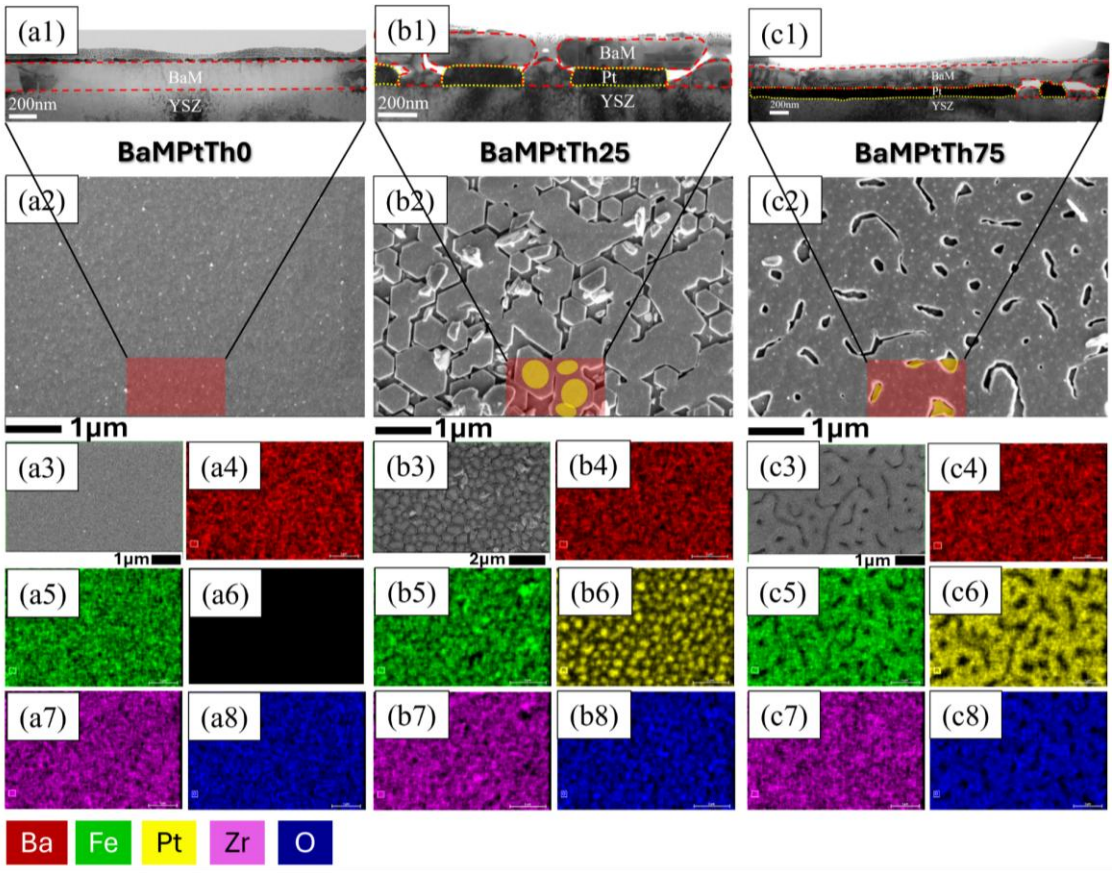

Figure 5.10: (a1, b1, c1) (a2, b2, c2) Present low-resolution TEM and SEM micrographs for BaMPtTh0, BaMPtTh25 and BaMPtTh75, respectively. The red square illustrates the size of the TEM micrographs with respect to the SEM regions investigated. (a3, a4, a5, a6, a7 and a8), (b3, b4, b5, b6, b7, and b8) And (c3, c4, c5, c6, c7, and c8) correspond to the HADDF images and different EDX elemental maps for the Ba, Fe, Pt, Zr, and O_2 for BaMPt0, BaMPtTh25, and BaMPtTh75, respectively[107].

EDX were acquired from regions marked with white and red boxes and subsequently quantified (Figure 5.11d1 to 5.11d5 and 5.11e1 to 5.11e5). The resulting Ba, Fe, Zr and O elements profiles for are shown in Figure 5.11c. Four distinct regions appear: R1 = *Th* < 2.4 nm, R2 = 2.4 nm < *Th* < 4 nm, R3 = 4 nm < *Th* < 5 nm and R4 = 5 nm < *Th* < 12 nm. The R1 region (*Th* < 2.4 nm) has the highest Zr and O concentrations which indicate the YSZ substrate. In the R2 region (2.4 nm < *Th* < 4 nm), the Zr and O signals gradually decrease and finally disappear above *Th* = 4 nm which shows the transition from the YSZ substrate to the BaM layer. This suggests a gradual, rather than an abrupt, interface between YSZ and the BaM layer in both BaMPtTh0 and BaMPtTh25 samples.

The R2 transition region (2.4 nm < *Th* < 4 nm) coincides with a decrease in the Zr and O signals and a simultaneous increase in the Ba and Fe signals. This trend implies diffusion of Ba and Fe atoms into the YSZ. In the R3 region (4 nm < *Th* < 5 nm) Zr is completely absent, replaced by an increase of Ba and O concentrations due to the BaM layer. A decrease in the Fe signal stabilizes when *Th* exceeds 6 nm. In the region 5 nm < *Th* < 12 nm, the Ba signal shows a sinusoidal pattern with a periodicity of about 2 nm which corresponds to the interatomic distance of Ba in the c-axis direction. In the STEM HAADF image of Figure 5.11a, a less regular behavior is observed for the Ba profile within the range of 2.4 nm < *Th* < 5 nm which has structurally smeared characteristics. This phenomenon is evident in both BaM layers directly grown on YSZ substrates which corresponds to the BaMPtTh0 and BaMPtTh25 samples. EDX1154 elemental maps portraying Ba, Fe, O, and Zr distributions for BaMPtTh0 are presented in Figure 5.11d2, 5.11d3, 5.11d4, and 5.11d5. The smeared atomic structure corresponds to the region denoted as R = 2.4 nm < *Th* < 5.0 nm, whereby the sub-region R2 = 2.4 nm < *Th* < 4 nm exhibits an interdiffusion of Ba and Fe atoms into the YSZ substrate. This region (R2) in the various EDX1154 maps shows the presence of the elements Fe, Ba, O, and Zr. Moreover, the dashed line in Figure 5.11c aligns with a minimum of the oxygen profile which corresponds to a dark stripe in the associated O map of the EDX1154 dataset. Furthermore, for BaMPtTh0, when *Th* > 5.0 nm (as seen in Figure 5.11d1), the atomic structure becomes well-defined with relatively constant O and Fe intensities while the Ba intensity oscillates in line with the layered atomic arrangement of Ba (as evident in Figure 5.11c). The FFT analysis of Figure 5.7d demonstrates that the formed interlayer within the R = 2.4 nm < *Th* < 5.0 nm range possesses an amorphous structure. The elemental profiles imply that this interlayer consists of a mixture of Fe, Ba, Zr, and O, which presumably exhibits a disordered or non-crystalline arrangement. For BaMPtTh25, Figure 5.11e1 does not reveal the smeared atomic region observed in Figure 5.11d1 of BaMPtTh0. Nevertheless, within the transition region R2 = 2.4 nm < *Th* < 4 nm the Ba concentration is higher for BaMPtTh0 (Figure 5.11d2) compared to BaMPtTh25 (Figure 5.11e2). This suggests that the diffusion of Ba and Fe into the substrate is more prominent in the case of BaMPtTh0, despite both BaM layers being directly grown on YSZ substrates. Different profiles of element concentrations are compared for both BaM layers in the region R4 = 6 nm < *Th* < 12 nm which the courses of the elements Ba, Fe and O are more stable (see Figure 5.11c). The corresponding elemental profiles almost overlap which suggests that the chemical composition of BaM grown on YSZ does not show significant differences.

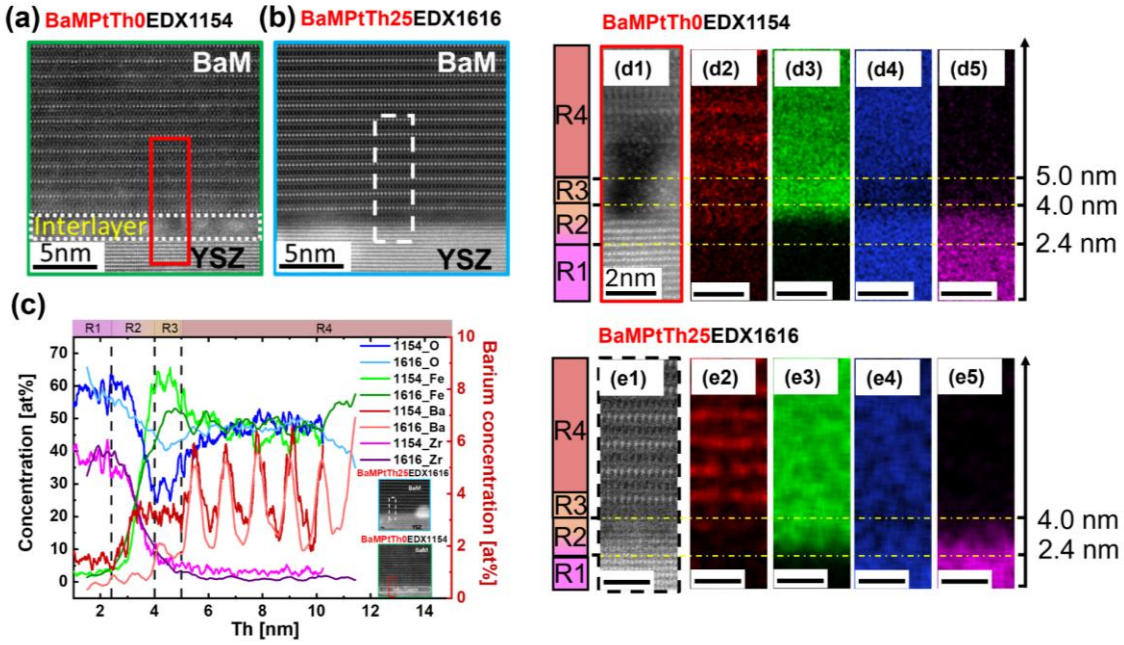

Figure 5.11: (a, b) HRTEM micrographs for the BaM layer grown on the YSZ substrate for the BaMPtTh0 and BaMPtTh25, respectively. The respective regions drawn by the red and the white squares describe the selected regions for the EDX maps BaMPtTh0EDX1154 and BaMPtTh25EDX1616. (c) Comparison of the elemental profiles for the O, Fe, Ba, and Zr elements for the BaMPtTh0EDX1154 and BaMPtTh25EDX1616. (d1, d2, d3, d4, d5) And (e1, e2, e3, e4, e5) correspond to the HADDF images and different EXD elemental maps for the Ba, Fe, O, and Zr for BaMPtTh0EDX1154 and BaMPtTh25EDX1616, respectively. Scale bars in (d1-d5 and e1-e5) are in 2nm size. For magnified version refer to Figure A-15[107].

Figure 5.12a and 5.12b show high-resolution STEM images of the BaM layers grown on Pt substrates for BaMPtTh75 and BaMPtTh25 samples, respectively. Combined high-resolution STEM/EDX analyses were performed in the highlighted rectangular areas marked in yellow and red. Figure 5.12d1 to 5.12d5 and 5.12e1 to 5.12e5 show the corresponding STEM HAADF images and quantified EDX maps for the elements Ba, Fe, O and Pt.

The EDX maps and elemental profiles derived from these maps (see Figure 5.12c) reveal four distinct regions: R1 = *Th* < 1 nm, R2 = 1.0 nm < *Th* < 2.4 nm, R3 = 2.4 nm < *Th* < 3.5 nm, and R4 = 3.5 nm < *Th* < 12 nm. Notably, for both BaMPtTh75 and BaMPtTh25 the region R1 = *Th* < 1 nm shows a maximum concentration of Pt due to its association with the metal interlayer. In this R1 region there is also a trace amount of Ba (around 3.5 at.%) as observed in Figure 5.12c, Figure 5.12d2, 5.12d5, 5.12e2 and 5.12e5. This indicates a possible diffusion of Ba atoms into the upper regions of the Pt interlayer. However, it is also plausible that this is an artefact due to the excitation of Ba X-rays in the adjacent BaM layer by electrons that are significantly backscattered by platinum. The regions R2 = 1.0 nm < *Th* < 2.4 nm and R3 = 2.4 nm < *Th* < 3.5 nm correspond to a Pt/BaM transition region characterized by a sharp decrease in the Pt signals in both elemental profiles for BaMPtTh75 and BaMPtTh25. At the same time, in these transition regions (R1 and R2) an increase in the Fe and O content is observed which stabilizes the subsequent R4 = 3.5 nm < *Th* < 12 nm region. Figure 5.12c illustrates that the Pt decay transition is not abrupt when BaM is grown on a Pt interface layer, unlike the case of Zr decay when BaM is

grown directly on a YSZ substrate. In the regions R1 = *Th* < 1 nm and R2 = 1.0 nm < *Th* < 2.4 nm, the elemental profiles of Ba, Fe, O and Pt show almost an identical behavior for both BaMPtTh75 and BaMPtTh25 samples, and there is no pronounced effect related to the thickness of the deposited Pt. It is noteworthy that the Pt film beneath the grown BaM has undergone significant thickness changes of up to about 100 nm due to dewetting during the BaM post-growth.

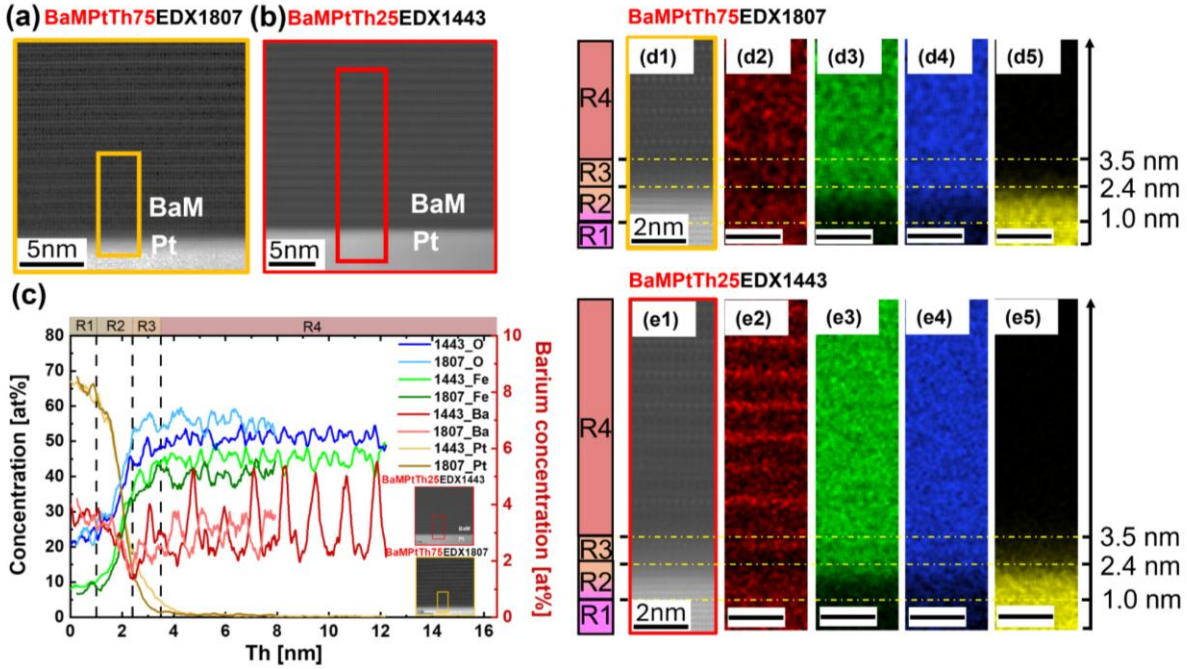

Figure 5.12: (a, b) HRTEM micrographs for the BaM layer grown on Pt for the BaMPtTh75 and BaMPtTh25, respectively. The respective regions (yellow and the red squares) describe the selected regions for the EDX maps BaMPtTh75EDX1807 and BaMPtTh25EDX1443. (c) Comparison of the elemental profiles for the O, Fe, Ba, and Zr elements for the BaMPtTh25EDX1443 and BaMPtTh75EDX1807. (d1, d2, d3, d4, d5) And (e1, e2, e3, e4, e5) correspond to the HADDF images and different EDX elemental maps for the Ba, Fe, O, and Pt for BaMPtTh75EDX1807 and BaMPtTh25EDX1443, respectively. Scale bars in (d1-d5 and e1-e5) are in 2 nm size. For a magnified version refer to Figure A-16[107].

In the region R4 = 3.5 nm < *Th* < 12 nm, at which the elemental profiles of Ba, Fe and O are more stable, and at which the Pt signal is absent, the atomic concentrations of the different elements were compared for both BaM layers. For BaMPtTh25, average values of approximately 2.7 at.% Ba and 45 at.% Fe were determined, while for BaMPtTh75 the values were approximately 3.1 at.% Ba and 40 at.% Fe. This suggests that BaM grown in BaMPtTh75 has a slightly higher Ba concentration and a slightly lower iron content. Correspondingly, the mean oxygen concentration % O was slightly higher for BaMPtTh75. These results suggest the probability of some variation in the chemical composition of BaM near the Pt interface. Due to the non-uniform Pt interface layer in BaMPtTh25, the BaM film was deposited on the Pt blocks as well as the Pt-free mainly on the YSZ substrate. This lead to investigate whether the chemical composition of BaM directly grown on the YSZ substrate in BaMPtTh25 was like this of BaM/YSZ in BaMPtTh0 and BaMPtTh75. Similarly, a comparative analysis of the chemical composition was carried out with BaM films grown on Pt substrates for both, BaMPtTh25 and BaMPtTh75. The aim was to determine whether the chemical composition of BaM, when grown on Pt, is that of BaM grown directly

on YSZ, as observed in BaMPtTh0, BaMPtTh25 and BaMPtTh75 samples. Several X-ray maps from different regions of the three samples (specific maps not shown here) were acquired. The resulting Ba, Fe, O and Pt elements profiles are shown in Figure 5.13b, 5.13c, 5.13e and 5.13f. Figure 5.13b displays a comparison of the elemental concentration profiles of BaMPtTh25.

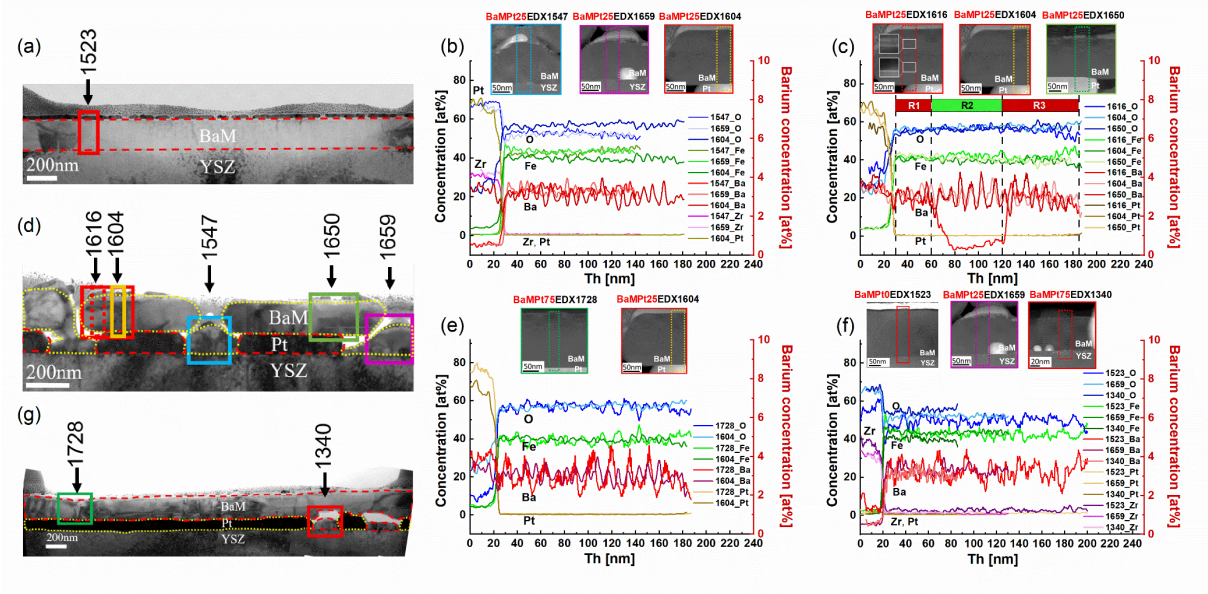

Figure 5.13: (a, d, h) Low magnification TEM micrographs for the BaMPtTh0, BaMPtTh25 and BaMPtTh75 samples, respectively. (b) Comparison of the elemental profiles for the O, Fe, Ba, Zr, and Pt elements derived from the EDX maps BaMPt25EDX1547, BaMPt25EDX1659, and BaMPt25EDX1604 for the BaM film grown on YSZ, YSZ and on Pt, respectively. (c) Comparison of the elemental profiles for the O, Fe, Ba, and Pt elements derived from the EDX maps BaMPt25EDX1616, BaMPt25EDX1604, and BaMPt25EDX1650 for different BaM regions grown on Pt. (e) Comparison of the elemental profiles for the O, Fe, Ba, and Pt elements derived from the EDX maps BaMPt75EDX1728, BaMPt25EDX1604. (f) Comparison of the elemental profiles for the O, Fe, Ba, Pt, and Zr elements derived from the EDX maps BaMPt0EDX1523, BaMPt25EDX1659, BaMPt75EDX1340. For magnified version refer to Figure A-17[107].

These profiles relate to the regions identified in Figure 5.13b and marked by red squares (EDX1604, row 5 in Table A-7), blue squares (EDX1547, row 4 in Table A-7) and magenta squares (EDX1659, row 3 in Table A-7). The blue and magenta squares represent BaM regions grown on the YSZ substrate, located between Pt blocks. In contrast, the red square represents BaM grown on a Pt interface layer block. In Figure 5.13d, five regions within the BaM film have been selected and marked with different colored boxes. From these boxes, three boxes, namely the red dotted box of EDX1616, the yellow solid box of EDX1604 and the green solid box of EDX1650 correspond to the BaM layer grown on Pt interface layer blocks. Meanwhile, two boxes, namely the solid blue box of EDX1547 and the solid magenta box of EDX1659, represent the BaM grown on Pt-free areas due to problems related to the Pt detachment during the BaM post-growth process.

The STEM images of the X-ray map regions EDX1604, EDX1547 and EDX1659 are shown as insets in Figure 5.13b. Element concentration measurements were performed in the thickness range R = *Th* > 33 nm which variations in the film thickness profile were minimal. The resulting

values are summarized in Table A-7. In particular, the concentration values of the elements Ba, Fe and O are similar in the case of EDX1547 and EDX1659 which the BaM layer was directly grown on YSZ in areas not covered by platinum due to the dewetting phenomenon (see Table A-7, rows 3 and 4). However, for the BaMPtTh25 sample with a Ba content of about 3 at.% (data set EDX1604, corresponding to BaM grown on Pt) and 39.50 at.% Fe these concentrations are lower compared to the concentrations of these elements (3.30 at.% Ba and 43 at.% Fe, data set EDX1547 in Table A-7) in BaM grown on Pt-free regions (see rows 4 and 5 in Table A-7). Conversely, for BaM on Pt (data set EDX1604), the oxygen content of about 57 at.% is slightly higher than the 53 at.% found for BaM on YSZ (data set EDX1547), as also shown in Figure 5.13b. This result suggests that BaM regions may show slight variations in the chemical composition which depends on the type of interface layer.

Figure 5.13c shows a comparison of the Ba, Fe, O and Pt elements profiles for the BaMPtTh25 sample. These data are derived from BaM grown on Pt blocks. These are the data sets EDX1616, EDX1604 and EDX1650 selected from appropriate regions of the film (see Figure 5.13d). The atomic concentration values for Ba, Fe and O within thicknesses approximately equal to $Th > 33$ nm are detailed in rows 5, 6 and 7 of Table A-7, respectively. The profiles from the datasets EDX1604 and EDX1650 show a similar pattern with comparable element concentrations in rows 5 and 7. This suggests that BaM grown in these regions is almost identical. However, in some regions of this BaM layer, such as dataset EDX1616, high resolution STEM and associated digital image analysis revealed the presence of two distinct crystalline phases. Within the Ba concentration profile, three distinct regions become apparent: R1 = 30 nm < Th < 60 nm, R2 = 60 nm < Th < 120 nm and R3 = 60 nm < Th < 185 nm. In the R2 region, which extends from 60 nm < Th < 120 nm, the Ba content of about 2.60 at.% indicates a BaM phase deficient in Ba, while iron is enriched which results in an Fe content of about 41.70 at.%. The presence of a secondary BaM phase with a different chemical composition and structure explains the additional diffraction spots observed in Figure 5.3e, 5.3f, 5.3g and 5.3h. In conclusion, the combined use of the HRXRD, HR-STEM and EDX techniques in the case of sample BaMPtTh25 confirmed the presence of a minor secondary BaM phase with different lattice parameters due to its different chemical composition which is Ba deficient. Figure 5.13e shows a comparison between the EDX line profiles of BaMPtTh25 and BaMPtTh75 samples. These data sets, namely EDX1728 and EDX1604, refer to BaM layers grown on a Pt interface layer with thicknesses more than 25 nm. The resulting elements concentration values correspond to rows 9 and 5 of Table A-7 and show only minor differences between the BaMPtTh25 and BaMPtTh75 samples which reflect similar chemical composition as the Pt interface layer had almost identical thicknesses due to the dewetting problem (see Figure 5.13d and 5.13h). Despite the nominal difference in Th_{Pt} of Pt interface layer in the as-grown state for BaMPtTh25 and BaMPtTh75, there was no significant attributable effect. As a result of the Pt detachment during the BaM post growth, Pt-free regions were particularly prevalent in BaMPtTh25, at which the Pt thickness is only 25 nm. In contrast, only a few Pt-free regions were detected in BaMPtTh75. It is pertinent to investigate whether the chemical composition of the BaM material grown in these Pt-free regions in BaMPtTh25 and BaMPtTh75 is like that grown without a Pt interface layer in BaMPtTh0. In order to achieve this, the element-specific EDX profiles of the different BaM regions, shown in Figure 5.13a, 5.13d and 5.13h, are compared in Figure 5.13f (specifically data sets EDX1523, EDX1659 and EDX1340). The corresponding element concentration values are given in Table A-7, rows 2, 3 and 8, respectively. Compared to

BaM in BaMPtTh0, which serves as a reference for BaM without an interface layer, BaMPtTh25 shows a slightly higher Ba and Fe content (dataset EDX1659), about 2 % higher than those in dataset EDX1523. Conversely, data set EDX1659 has an oxygen concentration about 4 % higher than that of EDX1523 (see Table A-7). The percentage increase in the element concentration in data set EDX1659 was calculated as the ratio of the difference between the element concentrations of EDX1659 and EDX1523 to the concentration in EDX1523.

Regarding the BaM layer in BaMPtTh75, the Ba concentration in data set EDX1340 is about 4 % lower than in data set EDX1523. Conversely, the Fe concentration in data set EDX1340 is approximately 6.5 % lower than in EDX1523, and the O content in data set EDX1340 is approximately 9.3 % higher than in EDX1523. The percentage increase/decrease in the element concentration in data set EDX1340 was determined by calculating the ratio of the difference between the element concentrations of EDX1340 and EDX1523 to the concentration in EDX1523.

These results suggest that the chemical composition of BaM grown on YSZ along the growth direction is not consistent among the different samples, namely BaMPtTh0, BaMPtTh25 and BaMPtTh75. It should be emphasized that the same number of shots was utilized for the growth of the corresponding BaM layers. Nevertheless, the thicknesses of the BaM layers differ for BaMPtTh0, BaMPtTh25 and BaMPtTh75 (column (3) of Table A-7) which depends on the type of interface, whether it is BaM/YSZ or BaM/Pt/YSZ. This suggests that the interfacial strain affects the BaM growth rate. For example, for BaMPtTh0 the thickness is Th_{BaM} = 176 nm, whereas the BaM layers grown on YSZ have thicknesses which range from Th_{BaM} = 106 nm to 111 nm for BaMPtTh25 and approximately Th_{BaM} = 62 nm for BaMPtTh75. On the other hand, BaM grown on a Pt substrate has a thickness that ranges from Th_{BaM} = 147 nm to 155 nm for BaMPtTh25 and approximately 160 nm for BaMPtTh75.

5.2.4 Effect of the interface quality on the magnetic properties of $BaFe_{12}O_{19}$ films

5.2.4.1 Macroscopic magnetic properties

Out-of-plane (OOP, H // c-axis) and in-plane (IP, H ⊥ c-axis) magnetization loops for BaMPtTh0, BaMPtTh25 and BaMPtTh75 are compared in Figure 5.14a and 5.14b, respectively. The deposition of the Pt interface layer has led to an increase in the coercivity fields $H_{c\perp}$ and $H_{c//}$ as well as in the OOP and IP magnetization hysteresis loops. There is an increase in dissipation energy for BaMPtTh25 and BaMPtTh75. In addition, the IP magnetization shows a two-sloped hysteresis for BaMPtTh0, BaMPtTh25 and BaMPtTh75 (see Figure 5.14b). This behavior may indicate a multilayer structure along the interface or laterally separated domains, like the properties of BaM/YSZ and BaM grown on Pt blocks, as observed in BaMPtTh25. Figure 5.14a and 5.14b do not reveal a significant difference in the magnetization behavior between BaMPtTh25 and BaMPtTh75, despite the Pt discontinuity problem in the BaMPtTh25 sample. To further investigate the effect of Pt intercalation and its thickness, the OOP coercivity fields $H_{c\perp}$, the anisotropy field H_a, the remanent magnetization M_r and the M_r / M_s ratio were plotted as a function of Th_{Pt} of the Pt interface layer in Figure 5.14c, 5.14d and 5.14e, respectively, and summarised in Table 5-3. By depositing the Pt interface layer, the values of $H_{c\perp}$ and $H_{c//}$ for the BaM layer increased from $H_{c\perp}$= 897 Oe and $H_{c//}$ = 476 for BaMPtTh0 to $H_{c\perp}$= 2070 Oe and $H_{c//}$ = 998 Oe for

BaMPtTh25. In order to understand the reasons for this increase in the coercivity fields H_c, it is important to consider various factors that affect the coercivity H_c, such as the magnetic anisotropy which includes magnetocrystalline and magnetoelastic anisotropies. The absolute value of the in-plane residual strain $\varepsilon_{//,\,BaM}$ determined from HRXRD was found to increase from $\varepsilon_{//,\,BaM}$ = -0.0074 for BaMPtTh0 to -0.0115 for BaMPtTh25 and -0.0193 for BaMPtTh75 (see Table 5-3). This consequently contributes to the increase in the magnetoelastic anisotropy and affects the coercivity H_c and the anisotropy field H_a.

It is worthwhile looking at the relationship between the anisotropy field H_a and the effective anisotropy constant, K_f. K_f is essentially the square root of the sum of two components: the magnetocrystalline constant K_1 and the magneto-elastic anisotropy K_σ. K_σ is closely related to the in-plane residual strain $\varepsilon_{//,\,BaM}$ and can be expressed as follows[25,214]. In Equation (4-7), Y_{BaM} is the Young's modulus (1.115 x 10^{11} N/m^2), μ_{BaM} is the Poisson's ratio (9.86 x 10^{10} N/m^2), λ_{BaM} is the magnetostriction constant (9 x 10^{-6})[215], and $\varepsilon_{//,\,BaM}$ is the in-plane residual strain (Table 5-2). The following equation

$$H_a = \frac{2K_f}{Ms} \tag{5-5}$$

represents the anisotropy field in which K_f and M_s are the effective anisotropy constant and the saturation magnetization, respectively[216,217]. The anisotropy constant is expressed by means of equation

$$K_f = \sqrt{(K_1^2 + K_\sigma^2)} \tag{5-6}$$

in which K_1 and K_σ are the magnetocrystalline anisotropy and magnetoelastic anisotropy constants, respectively.

$$K_\sigma = \frac{3}{2} * \left(\frac{Y_{BaM}}{1 + \mu_{BaM}}\right) * \lambda_{BaM} * \varepsilon_{//,BaM} \tag{5-7}$$

From Equation (4-7), we calculate the values of K_σ to be -9.87 x 10^5, -1.55 x 10^6 and -2.58 x 10^6 N/m^2 for BaMPtTh0, BaMPtTh25 and BaMPtTh75, respectively. Furthermore, by using Equations (4-5) and (4-6), we determined the magnetocrystalline constant K_1 to be 9.52 x 10^5, 1.53 x 10^6 and 2.57 x 10^6 N/m^2 for BaMPtTh0, BaMPtTh25 and BaMPtTh75, respectively. Consequently, one can observe that both the magnetocrystalline K_1 and the magnetoelastic K_σ anisotropy constants significantly increase with the deposition of the Pt interface layer Th_{Pt}. Combining Equations (4-5), (4-6) and (4-7), it is clear that the H_a field is directly proportional to the residual strain. Therefore, an increase in the in-plane residual strain $\varepsilon_{//,BaM}$ results in an increase in the H_a field, as shown in Figure 5.14c. The increase in the coercivity ($H_{c\perp}$ and $H_{c//}$) due to strain induced effects is a phenomenon observed in various materials such as $CoFe_2O_4$[216,218,219] films. In the case of BaMPtTh25, the increase in the coercivity can also be related to the non-uniformity of the BaM layer, mainly caused by the formation of a secondary crystal BaM phase with different lattice parameters and stoichiometry, as previously demonstrated by HR-STEM/EDX and HRXRD-

RSM methods. It is important to note that the lattice misfit ($f_{BaM/Pt}$) and the residual strain have a significant effect on the magnetic properties. Table 5-2 shows a comparison of the microstructural features, which include a lattice misfit and an in-plane residual strain, for BaMPtTh0, BaMPtTh25 and BaMPtTh75. The deposition of a Pt interface layer changes the lattice misfit from tensile ($f_{BaM/YSZ}$ = -19.5087 %) in BaMPtTh0 to compressive ($f_{BaM/Pt}$ = 5.5990 %) for BaMPtTh25 and ($f_{BaM/Pt}$ = 4.7701 %) for BaMPtTh75. In addition, Table 5-2 highlights the significant variation in the in-plane residual strain $\varepsilon_{//,BaM}$ due to the Pt interface layer deposition. The increase in $H_{c\perp}$ could also be related to the defect density as well as to the misalignment of the BaM planes with respect to the substrate lattice planes. However, the $FWHM_{ang}$ of the diffraction spots (BaM0014, BaM0020 and BaM0024) did not show significant differences between BaMPtTh0, BaMPtTh25 and BaMPtTh75 which indicates comparable diffuse scattering and the related defect densities. Furthermore, the misalignment of the BaM lattice planes with those of the YSZ substrate, observed in BaMPtTh0, is absent in BaMPtTh25 and BaMPtTh75. This informs us about the improvement of the c-axis BaM orientation which in return increases the anisotropy field (H_a) from 1.26 T to 1.34 T in Figure 5.14c. By comparing BaMPtTh0 and BaMPtTh25, we deduce that both the M_r and the M_r / M_s ratio remarkably increases with the thickness of the Pt interface layer (see Figure 5.14d and 5.14e). However, the variation in the M_r and M_r / M_s ratio is estimated to be around 5 % to 15 % in the case of BaMPtTh75 due to the continuity of the Pt interface layer. It is important to note that the coercivity is strongly influenced by the magnetic anisotropy H_a and microstructure of the BaM film as extensively analyzed in previous chapters by using SEM/HR-STEM/EDX and HRXRD. In order to understand the dominant mechanisms, which control the coercivity, the micromagnetic theory developed by Kronmüller et al. was applied. This theory involves a H_c / M_s against H_a / M_s plot and should result in a linear relationship for a uniform magnetization reversal process. The slope denoted as (α) of this curve provides an insight into the dominant mechanism: if $\alpha > 0.3$ it suggests a nucleation mechanism, whereas $\alpha < 0.3$ indicates nucleation, pinning of domains or a combination of both.

Figure 5.14f gives the variation of H_c / M_s as a function of H_a / M_s for BaMPtTh0, BaMPtTh25 and BaMPtTh75, whereupon the evaluated slopes (α) were 0.103, 0.116 and 0.142, respectively. These results suggest that none of the samples can be attributed solely to nucleation as the dominant mechanism. Figure 5.15a, 5.15b and 5.15 c show AFM images of samples BaMPtTh0, BaMPtTh25 and BaMPtTh75. Correspondingly, Figure 5.15d, 5.15e and 5.15f show MFM images which the contrast is due to a phase shift in the magnetic domains in the range of 7.5° - 20°. MFM images of the hard disk drive (HDD) were also taken which show positively and negatively magnetized tip states (Figure A-20).

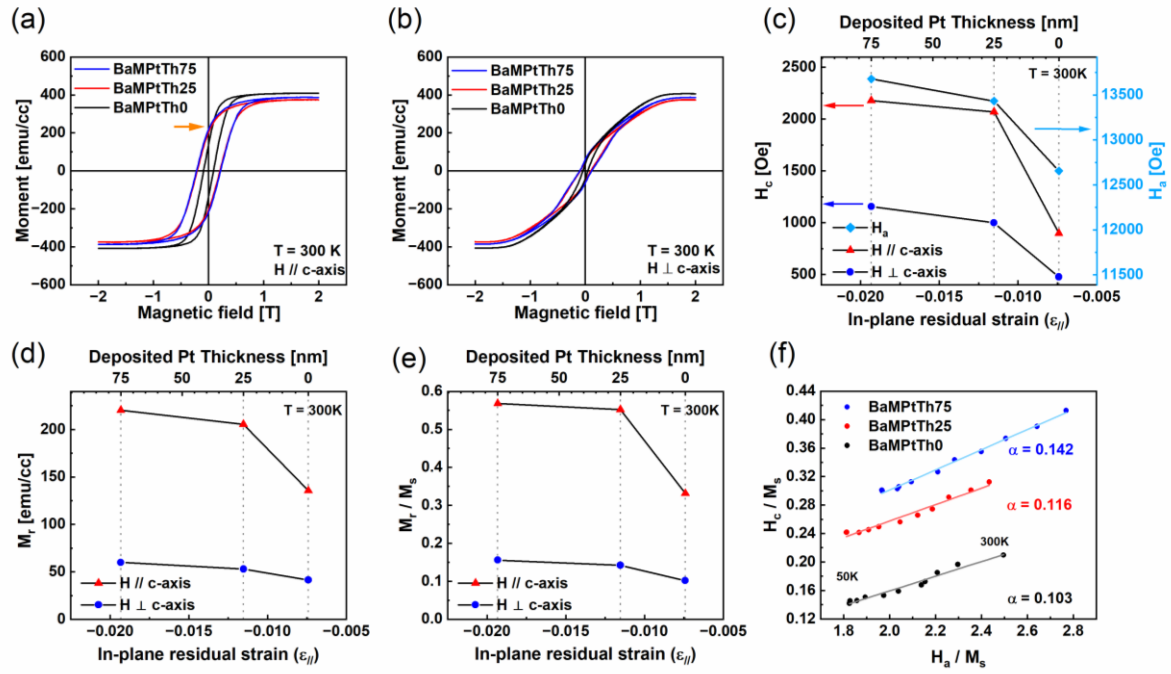

Figure 5.14: (a, b) Out-of-plane and in-plane magnetization hysteresis measured at room temperature for the BaMPthTh0, BaMPtTh25, and BaMPtTh75 samples. Variation of the (c) coercivity fields, anisotropy field, (d) remanent magnetization, (e) squareness M_r / M_s ratio as a function of the in-plane residual strain $\varepsilon_{//}$ (of BaM), (f) plot of H_c / M_s as a function of H_a / M_s for the BaMPtTh0, BaMPtTh25, and BaMPtTh75 where the slope α was evaluated to be 0.103, 0.116 and 0.142, respectively[107].

5.2.4.2 Microscopic magnetic properties

This step confirmed the accuracy of our MFM measurements and ruled out any artefacts due to the MFM hardware, the user image processing, long-range forces (e.g., electrical, adhesion) or phase shifting of the cantilever oscillations. It is important to note that MFM images are taken in the remanent state (M_r), whereupon the BaM film consists of a distribution of magnetic domains oriented parallel to the crystallographic c-axis and anti-parallel to the dipoles of the magnetized tip which is oriented towards the film. The phase shift is directly proportional to the out-of-plane component of the local magnetic field. Consequently, blue and yellow regions correspond to the highest and lowest spin orientations along the c-axis, in the remanent state, respectively while the magenta regions indicate intermediate spin orientations. Compared to BaMPtTh0 and BaMPtTh25, the MFM image of BaMPtTh75 (Figure 5.15f) shows the highest proportion of highly oriented magnetic domains, with blue regions which predominate. Conversely, BaMPtTh0 shows the highest percentage of yellow regions which indicates a significant misorientation of the magnetic domains. Figure 5.15e and 5.15f, which correspond to BaMPtTh25 and BaMPtTh75, clearly show the influence of the Pt interface layer continuity on the local orientation of the magnetic domains parallel to the c-axis. The presence of local and highly oriented magnetic domains in BaMPtTh75 is particularly important for high signal-to-noise ratio performance in perpendicular recording media. For easy comparison, we have evaluated the size of magnetic domains which correspond to three degrees of spin orientation (see Figure A-19) and summarized the results in Table 5-4. These results indicate that BaMPtTh75, which is characterized by a smooth

and continuous Pt interface layer, has the highest percentage (73.31 %) of highly spin-oriented magnetic domains along the c-direction. The degree of spin orientation quantified from the MFM images is relatively consistent, most of it with the lowest spin oriented magnetic domains (47.19 % for BaMPtTh0 and 51.32 % for BaMPtTh25). While the magnetization loops do not reveal significant differences in magnetic properties between BaMPtTh25 and BaMPtTh75, the local magnetic domain orientation confirms the local influence of the Pt interface layer discontinuity.

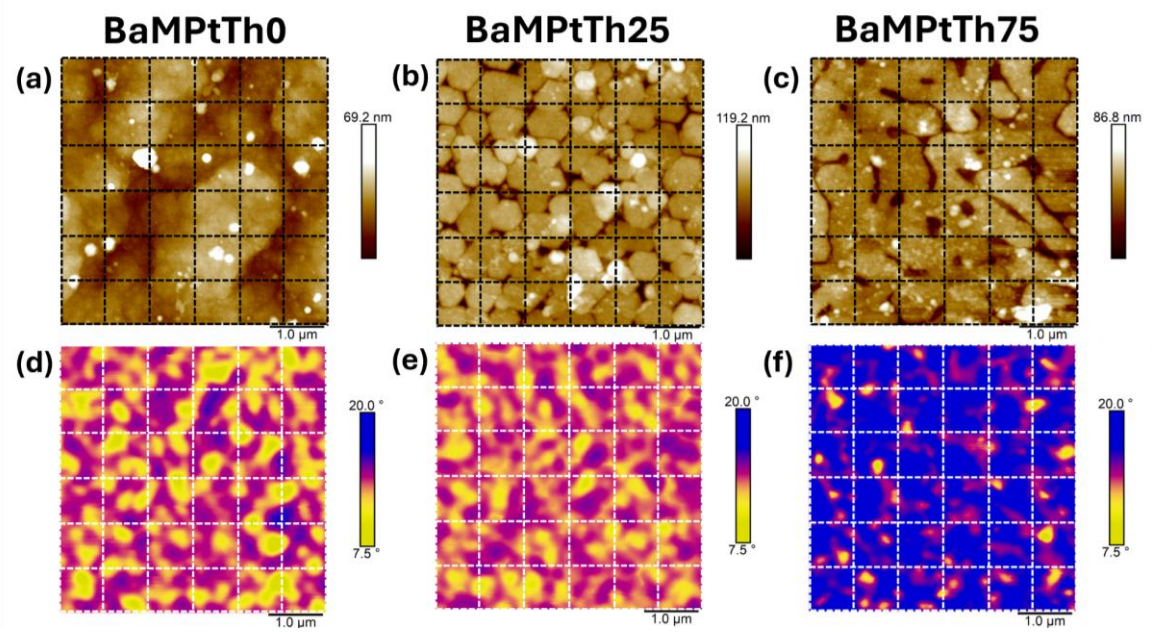

Figure 5.15: (a, b, c) Topography AFM images were recorded for the BaMPtTh0, BaMPtTh25, and BaMPtTh75 samples. (d, e, f) The corresponding MFM images with the phase shift scale of [7.5° - 20°]. The blue and the yellow regions correspond to the highest and the lowest oriented magnetic domains, respectively, while the magenta regions originate from the intermediate spin orientation of the magnetic domains[107].

Before proceeding to the investigation of the fluence parameter, it is worthwhile providing a brief summary of the findings. Extensive microstructural analyses were carried out on the Pt/YSZ templates and BaM bilayer systems by using HRXRD and HR-STEM/EDX/SEM methods. It was observed that BaMPtTh25 with an initial Th_{Pt} = 25 nm exhibited a pronounced dewetting phenomenon of the Pt bottom electrode from the YSZ substrate which results in the formation of a discontinuous Pt film composed of Pt blocks and Pt-free regions. As a result, two different BaM layers developed on two different surfaces: Pt and YSZ. The application of EDX mapping on the BaM regions did not reveal significant stoichiometric differences between BaM grown on YSZ and BaM grown on Pt. However, EDX maps revealed the presence of a minor Ba-deficient secondary crystalline phase identified as Fe_2O_3. In contrast, BaMPtTh0, without an interlayer exhibited misoriented regions near the film surface induced by out-of-phase boundaries. In addition, the formation of an amorphous interlayer was observed at the interface of BaM/YSZ. On the contrary, BaMPtTh25 and BaMPtTh75 exhibited highly oriented BaM c-axis layers with out-of-phase boundaries and stacking faults that could act as pinning domain walls. High resolution STEM micrographs delineated a sharp BaM/Pt interface for BaMPtTh25 and BaMPtTh75, while

interdiffusion between BaM and the YSZ substrate was observed for BaMPtTh0. This has influenced the in-plane residual strain of the BaM film. The presence of the Pt interface layer enhanced the coercivity fields (both $H_{c\perp}$ and $H_{c//}$) and the anisotropy field H_a via an increase in the in-plane residual strain. Conversely, misoriented grains in BaMPtTh0 reduced the coercivity field. Subsequently, micromagnetic modelling was used to investigate the mechanisms which impact the coercivity field, but the effort proved to be inconclusive. In addition, the subsequent investigation by MFM revealed highly oriented c-axis domains in BaMPtTh75 which indicate a remarkable degree of spin orientation along the c-axis. The prevalence of highly oriented magnetic domains in BaMPtTh75 underscores the critical importance of the continuity and the optimum thickness of the Pt interface layer (≥ 70 nm) which makes it suitable for applications in perpendicular recording media. This thickness does not only facilitate the resistance of the Pt film in terms of dewetting during the subsequent growth, as discussed in Chapter 4, but also ensures both continuity and robustness which, thereby, guarantees the development of c-axis oriented magnetic domains.

5.3 Effect of the laser fluence on the microstructure and magnetic properties of $BaFe_{12}O_{19}$

In the previous study, the quality of BaM films were carefully investigated to deeply understand the influence of the Pt interface layer thickness Th_{Pt}, which effectively reduced the lattice mismatch. We conclude that the microstructure, morphology, and stoichiometry of these hexaferrite BaM films were particularly dependent on the Pt film continuity, and its thickness Th_{Pt}. Several PLD growth parameters apart from the laser fluence were varied with the aim to optimize the magnetic properties of BaM[80]. In order to investigate the effect of the laser fluence on the microstructure, chemical composition, and on the resulting magnetic properties of these thin BaM films, two films were grown by using two different laser fluence values, 25 mJ (BaMF25mJ) and 75 mJ (BaMF75mJ), onto the Pt/YSZ templates with an optimized $Th_{Pt} \approx 70$ nm. The objectives are to explore the effects of the laser fluence variation on the growth kinetics of BaM films as well as on the microstructural features such as the lateral coherent block size, mosaic block misorientation and magnetic properties. Understanding these dynamics is essential for achieving high quality BaM films, which are essential for improving perpendicular recording resolution.

5.3.1 Influence of the laser fluence on the BaM microstructure

5.3.1.1 Investigation via HR-XRD

In Figure 5.16, XRD patterns (theta/2theta) of BaMF25mJ and BaMF75mJ are compared. These patterns include BaM (00l) reflections up to BaM0030 together with YSZ (111) substrate reflections up to 4th order and Pt (111) reflections up to 3rd order. Both patterns show the growth of BaM films with a high crystal quality characterized by a pronounced c-axis orientation. Additionally, the intensities of the substrate and platinum peaks almost overlap for both BaMF25mJ and BaMF75mJ while the intensities of (00l) BaM reflections are slightly lower for BaMF75mJ. This may indicate either variations in film the thickness or variations in the crystalline quality along the (00l) direction. Furthermore, the broadening of the (00l) reflections for BaMF75mJ (black

curve) is higher than in the case of BaMF25mJ. Both BaM films include sharp additional peaks (marked with red triangles) around BaM0012 and BaM0014. They coincide with the brag angles of the Fe_2O_3 phase.

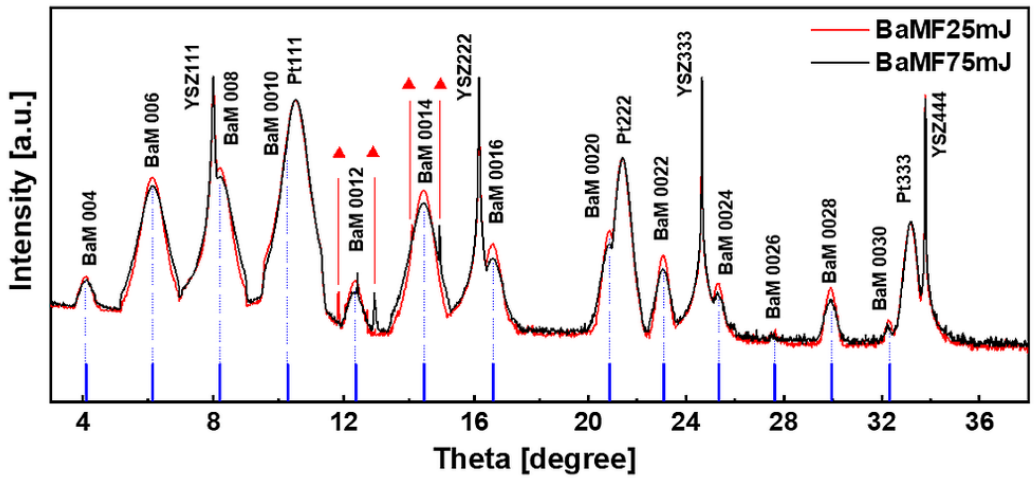

Figure 5.16: Theta/2theta X-ray diffraction scans of BaMF25mJ and BaMF75mJ films which show highly c-axis oriented BaM films. The red triangles indicate the peak positions of a minor secondary phase that have Bragg positions close to the Fe_2O_3 phase[80].

Increasing the fluence from 25 mJ to 75 mJ might induce the formation of the Ba-deficient phase of Fe_2O_3 and two BaM layers with different stoichiometries. HR-RSMs were collected for selected symmetric and asymmetric reflections of YSZ, Pt and BaM, and are shown in Figure 5.17 in which the upper and the lower rows include the plume picture of BaMF25mJ and BaMF75mJ, respectively. The diffuse scattering in HR-RSMs of BaMF25mJ and BaMF75mJ do not show a significant difference along the angular direction. However, the radial broadening seems to be larger for the BaM006 reflection of BaMF75mJ, which will be discussed later. Figure 5.17c and 5.17i simultaneously show Pt222 and BaM0020 reflections in a single scan, as well as in Figure 5.17d and 5.17j which the YSZ333 and BaM0024 HR-RSMs are market with vertical white dashed lines which indicate $Q_{ang} = 0$ Å^{-1}. Figure 5.17c and 5.17i show that the BaM0020 reflection is in-line with the Pt222 reflection which provides that the [001] direction of BaM is parallel to the Pt [111] direction. In the same way, Figure 5.17d and 5.17j show that the BaM0024 reflection is in-line with the YSZ333 reflection as well which indicates that the BaM [001] direction is parallel to the YSZ [111] direction without any layer misorientation. Figure 5.17e and 5.17k show an asymmetric reflection of BaM-2022 whereupon BaMF75mJ shows peak doubling which indicates that there exist two phases with slightly different lattice parameters. By using the RSMs, radial (direction of dashed black lines in Figure 5.17h) and angular (direction of orange dashed lines in Figure 5.17b) intensity distributions of BaM006, BaM0014 and BaM0024 were extracted and compared in Figure 5.18 and Figure 5.19, respectively. The differences in the intensity and broadening are further analyzed in Figure 5.18 which demonstrates that the broadening of radial diffraction profiles for the reflections BaM006 and BaM0014 are larger in the case of BaMF75mJ compared to BaMF25mJ. This could be attributed to the variations in the stoichiometry of the BaM layer as well as to the strain distribution within the layer. Referring to the intensity of the

YSZ333 reflection, Figure 5.18c shows differences in the intensity, peak position and broadening of the BaM0024 reflection between the BaMF25mJ and BaMF75mJ films. The increase of the fluence enhances the amount of ablated material from the target which consequently affects the growth rate and time necessary for the same final thickness. Consequently, the lattice rearrangement would be less influenced by the diffusion in the layer BaMF75mJ due to the shorter growth time compared to BaMF25mJ[226]. Moreover, by increasing the laser fluence the stoichiometric transfer from the target to the substrate is not guaranteed due to the increase of the radial distribution of the plasma caused by the increased kinetic energies of the species which depend on their molecular weight[220]. Additionally, as the kinetic energy increases, species of plasma which reach the target surface are more likely to be bounced back or cause resputtering which can be called desorption[83,221]. Desorption, driven by the higher kinetic energy of Ba atoms, may be responsible for the formation of the Fe_2O_3 phase. Figure 5.18d shows a WH plot which shows that the broadening variation is linearly related to the reflection order. The slope of BaMF75mJ is steeper than that of BaMF25mJ which indicates a greater strain distribution in the film for the 75 mJ grown film. This is consistent with the reduced growth time and diffusion properties.

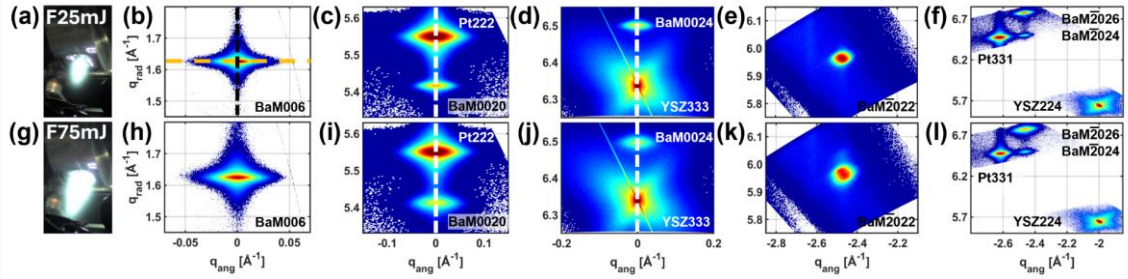

Figure 5.17: (a) And (g) plume pictures during the growth of the samples. Selected HR-RSMs of BaM symmetric (b) & (h) (006), (c) & (i) (0020) together with Pt (222), (d) & (j) (0024) together with YSZ (333) and asymmetric (e) & (k) (-2022) reflections and (f) & (l) (-2024), (-2026) together with Pt (331) and YSZ (224) of BaMF25mJ and BaMF75mJ films on the upper and lower row, respectively. (b) Orange and black dashed lines show exemplary cuts for angular and radial diffraction profiles, respectively. (c) & (i) And (d) & (j) show that the c-axes of Pt(111) & BaM(0001) films and YSZ(111) & BaM(0001) film are parallel to each other, respectively. For magnified view refer to Figure A-18[80].

In particular, the y-intercept of the WH plot in the radial direction delivers the average mosaic block size along the growth direction. It is evident that the y-intercept of BaMF75mJ is smaller than that of BaMF25mJ which indicates a larger mean mosaic block size along the growth direction. Figure 5.19 shows angular diffraction profiles of BaM006, BaM0014 and BaM0024 reflections, together with the WH plot ($FWHM_{ang}$ vs 00l) (Figure 5.19d). The $FWHM_{ang}$ is slightly more pronounced in the case of BaMF75mJ. This higher growth rate due to increase of laser fluence induced the increased kinetic energies of the species which reach the substrate surface. This in turn may contribute to a defect formation during deposition, characterized by a stoichiometric inhomogeneity and the formation of stacking defects[222,223].

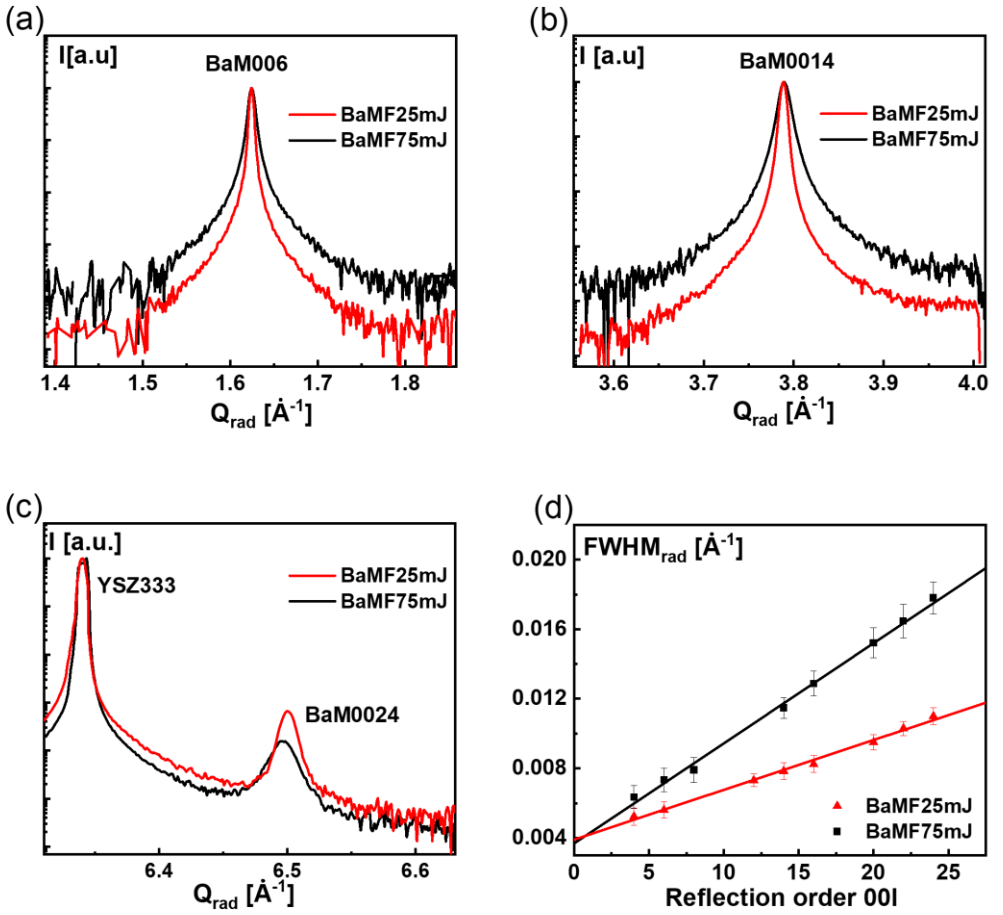

Figure 5.18: Radial diffraction profiles of selected BaM RSMs of (a) (006), (b) (0014), and (c) (0024) reflections together with YSZ (333) reflection of BaMF25mJ and BaMF75mJ. (d) Williamson-Hall plot of $FWHM_{rad}$ as a function of the reflection order (00l)[80].

The $FHWM_{ang}$ increases linearly with *00l*, and the slope is steeper for BaMF75mJ than that for BaMF25mJ. This reflects a higher mean mosaic tilt of the blocks. However, it does not provide information about the number of mosaic block sizes or the number density of mosaic boundaries. These data are determined by the y-intercept of the fitted curve (see Table 5-5). It can be found that the mean lateral size of the mosaic blocks in BaMF75mJ is slightly smaller than that in BaMF25mJ.

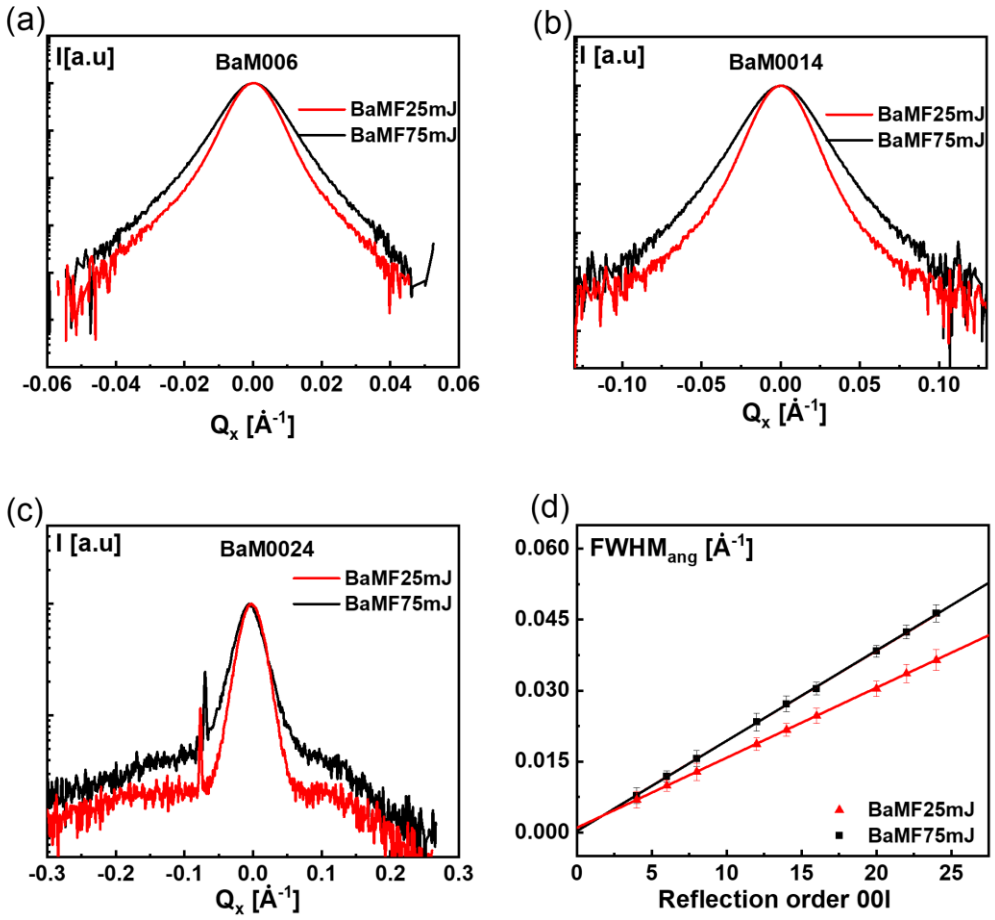

Figure 5.19: Angular diffraction profiles of selected BaM RSMs of (a) (006), (b) (0014), and (c) (0024) reflections of BaMF25mJ and BaMF75mJ. (d) Williamson-Hall plot of $FWHM_{ang}$ as a function of the reflection order (00l)[80].

5.3.1.2 Investigation via HR-TEM

TEM examination of both layers was carried out to obtain conclusive statistical results from the XRD and WH analyses. Figure 5.20 shows the TEM study carried out on BaMF25mJ. In Figure 5.20a, a low magnification TEM image shows the bilayer BaM/Pt system on the YSZ(111) substrate which clearly illustrates the continuity of the BaM and Pt layers along with its thickness and along the lateral direction. The platinum layer has an approximate thickness of Th_{Pt} = 100 nm while Th_{BaM} = 135 nm. The contrast variations within the BaM layer was due to locally different diffraction conditions and reveal slightly different oriented BaM mosaic blocks separated by phase boundaries. The lateral size of mosaic blocks varies from 25 nm to 156 nm. Importantly, there is no distinct contrast variation in the vertical direction which suggests that the vertical size of the mosaic blocks is equivalent to the thickness of the BaM layer. Region of Interest 1 (ROI1) was selected for higher magnification images shown in Figure 5.20b.

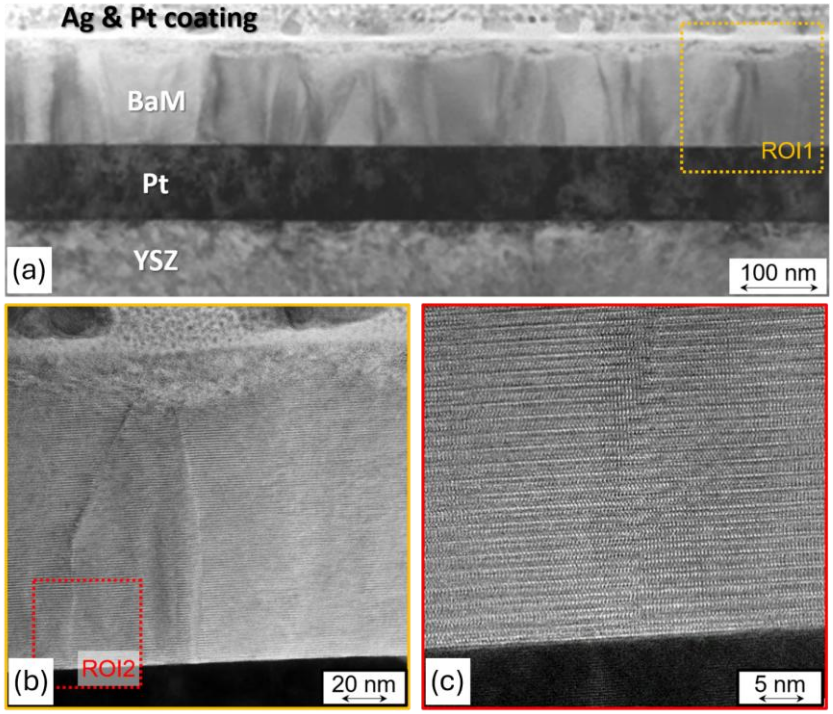

Figure 5.20: (a) TEM bright-field image of the BaM/Pt layer stack on YSZ(111) substrate of the sample BaMF25mJ, dark vertical lines as well as black/white regions hint at the presence of mosaic blocks. (b) Corresponding SAED pattern for orientation relationship between BaM and Pt. (c) HRTEM image of the BaM region ROI1 with three mosaic blocks. (d) HRTEM image of the interfacial region ROI2 between BaM along its [10-10] zone-axis direction and Pt along [11-2] in the vicinity of the mosaic-block boundary marked with a square in (c)[80].

A SAED pattern taken from the BaM/Pt interface confirms the alignment between the layers along BaM [0001] and Pt [111] which shows their parallel orientation (SAED pattern not shown here). This alignment is consistent with the XRD results (see Figure 5.17). Interestingly, the mosaic boundaries are identified as out-of-phase boundaries (OPB), at which the layer shifts by a c/4 lattice parameter. These OPBs originate at the BaM/Pt interface and propagate throughout the layer to the surface. Figure 5.20c shows a higher magnification view of ROI2 selected from Figure 5.20b. It demonstrates the sharpness of separation of the BaM/Pt interface at the atomic scale. Notably, OPBs form steps on the Pt surface, even in the absence of a surface. Furthermore, each individual mosaic block within the layer has a relatively perfect crystal structure. Figure 5.21 shows TEM images obtained by FIB milling of the BaMF75mJ film. The low magnification TEM images in Figure 5.21a illustrate the BaM/Pt/YSZ(111) system, with continuous Pt which possess slight thickness variations noted within the layer. These variations could be due to local sampling in TEM investigations. In particular, the low magnification image suggests a higher number of mosaic blocks, accompanied by an increased number of boundaries (visible as black lines within the layer). This finding is consistent with the XRD results which revealed a higher defect density (Figure 5.19). Furthermore, lateral boundaries are also evident which indicates variable mosaic blocks in the growth direction. This observation is consistent with the XRD results which there is a larger radial broadening for BaMF75mJ compared to BaMF25mJ (see Figure 5.18. ROI3). The higher magnification in Figure 5.21b reveals the presence of mosaic boundaries, again in the form

of out-of-phase boundaries (OPBs) generated at the interface. However, these boundaries do not propagate through the film thickness, but they terminate at the locations of stacking defects. Consequently, the c/4 shift of the lattice appears to be halted by a stacking fault which creates another mosaic boundary for another mosaic block along the growth direction. Outside the boundary regions, a local strain distribution was detected from the subtle contrast variations. This observation is corroborated by the XRD results and the WH analysis. Figure 5.21c shows a HR-TEM image of the BaM/Pt interface in ROI4. Here the OPBs originate from the vicinity of the interface whereas the BaM/Pt interface lacks the sharpness seen in the case of BaMF25mJ. The first few nanometers of BaM/Pt in BaMF75mJ appear to be disturbed and not atomically sharp. This suggests that the fast growth rate and/or high energy species do not effectively rearrange at the platinum surface.

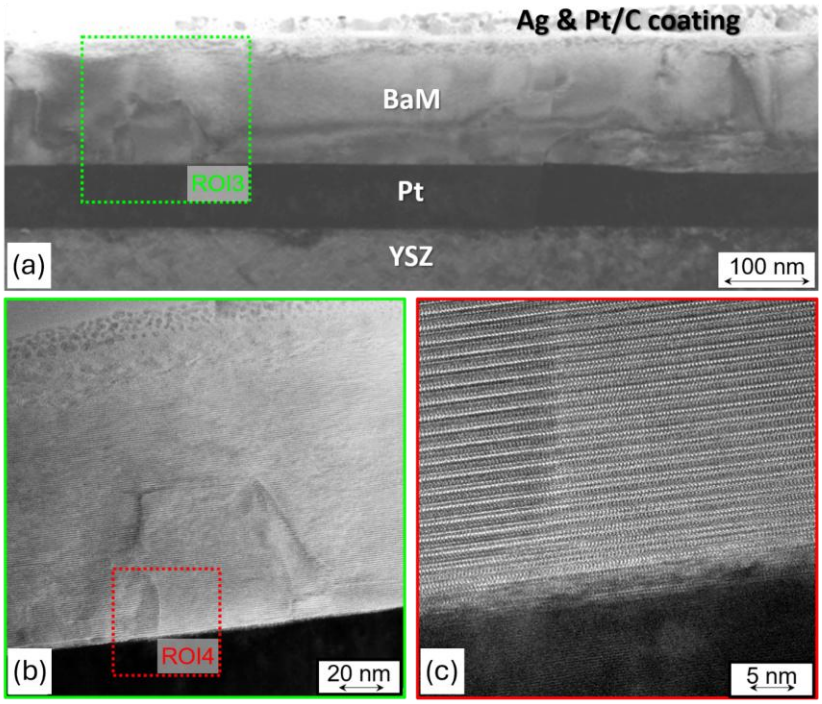

Figure 5.21: (a) TEM bright-field image of the BaM/Pt layer stack on YSZ(111) of BaMF75mJ and (b) corresponding SAED pattern with the orientation relationship between BaM and Pt. In this BaM, the bottom region with a vertical extension of about disturbed region 50 nm than with horizontally separated crystal blocks (c) HR-TEM image of a complex mosaic-block structure (ROI3) with both vertical and horizontal boundaries within the BaM film. (c) HR-TEM image of the interfacial region (ROI4) between BaM along its [10-10] zone-axis direction and Pt along [11-2][80].

Alternatively, the perturbation could be generated by the high kinetic energy species which impinge on the Pt surface and/or the first few atomic layers of BaM during the initial stages of growth. Subsequently, this perturbation may transform into the observed OPBs as the surface loses its flatness.

5.3.2 Influence of the laser fluence on the surface morphology and stoichiometry

Understanding the morphology of the layer is also important to learn about the growth kinetic which is useful for the future investigation of heterostructures. In order to explore the growth kinetics for a quasi-in-situ study, an additional sample was grown at 25mJ and 75mJ. Those samples were grown until so called up to half of the thickness of the actual studied layer. This allowed to examine the surface morphology at this stage and to conduct an in-situ measurement at which the layer is grown until it reaches half of its thickness. These samples were labeled as BaMF25mJ Th70nm and BaMF75mJ Th70nm whereas the original layers were labeled BaMF25mJ Th140nm and BaMF75mJ Th140nm. In Figure 5.22, AFM results are shown for BaMF25mJ Th70nm, BaMF75mJ Th70nm, BaMF25mJ Th140nm and BaMF75mJ Th140nm with different area size, 5µm x 5µm (Figure 5.22a to 5.22d), 2µm x2 µm (Figure 5.22e to 5.22h) and 3D images 2µm x 2µm for the representation of their morphology (Figure 5.22i to 5.22l). The first 2 columns of the figure show the so-called half thickness films whereupon the last 2 columns are the films with nominal conditions, i.e., actual thickness. The micrographs of the films grown at 25mJ confirm well-defined hexagonal grains which the growth time also takes longer (Figure 5.22a, 5.22e, 5.22i and 5.22c, 5.22g, 5.22k).

Increasing the fluence leads to coalescence of the hexagonal grains and to the formation of an interconnected grain network at which the grains become rounded and elongated to form chains. This was induced by the higher energetic species which results from the increase of the ablation fluence. The increase of the film thickness from 70 to 140 nm in the case of BaMF25mJ lead to an increase of the hexagonal grain sizes from 450 nm to 800 nm whereas the increase of the thickness of BaMF75mJ lead to the formation of distributed and the well-defined grains in the range of 80 to 265 nm on top of the elongated and interconnected hexagonal chains. In conclusion, for BaMF75mJ underwent 2 types of outgrowths which the first is composed of the hexagonal interconnected grains. Further deposition lead to the formation of secondary spherical grains on top of the preexisting elongated chains. The growth beyond the 70 nm thickness nuclei with the high kinetic energies diffuse onto the surface and coalesce to form grains which their sizes are dependent on the material flux rate or time given between the pulses. In other words, it is dependent on the competition between the nucleation rate and the crystal growth rate[224]. It was also shown by Zhang et al. that the influence of fluence affects the BaM morphology[225]. It could be deduced that the increase of the fluence from 25 to 75 mJ, due to increase of diffusion energy and decrease the time given for rearrangement, grains become smaller[226]. In order to better meet the requirement of the high-density perpendicular recording media, further tuning would be necessary in the case of the BaMF75mJ film.

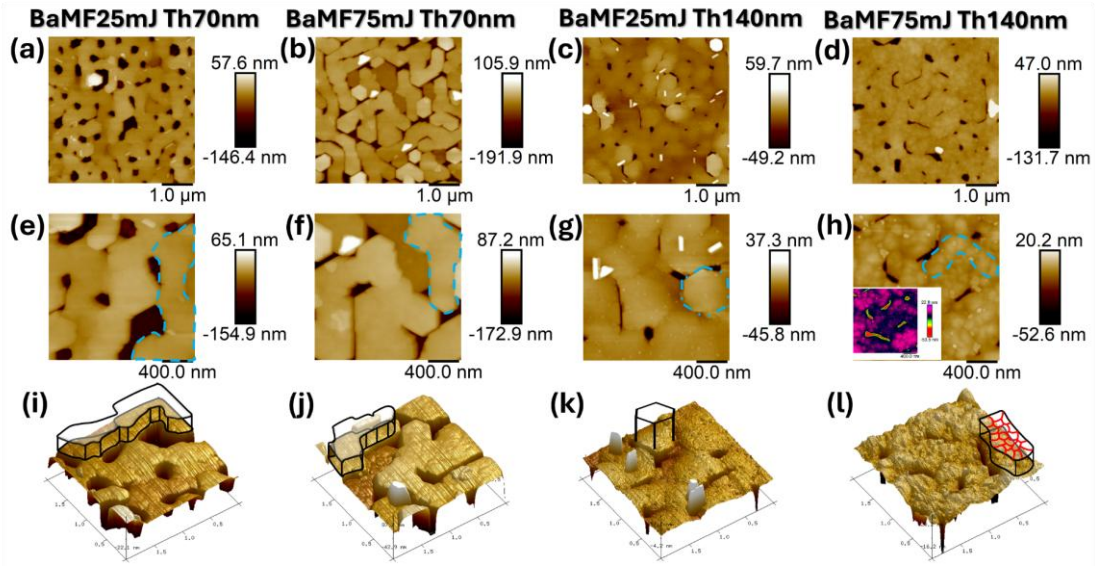

Figure 5.22: Atomic force microscopy (AFM) morphology images (a, b, c, d) from 5µm x 5µm region, (e, f, g, h) from 2µm x 2µm region of BaMF25mJ Th70nm, BaMF75mJ Th70nm, BaMF25mJ Th140nm, and BaMF75mJ Th140nm, respectively. Blue dashed lines show typical topography features. (i, j, k, l) Show the 3D images of the corresponding 2µm x 2µm morphology images in (e, f, g, h), respectively. Representative topographic features are highlighted via extended drawings on 3D topography images (i, j, k, l)[80].

This could be achieved by varying the oxygen pressure or raising the growth rate by means of the repetition rate[227]. The mentioned structures are visualized with a blued dashed line in Figure 5.22e to 5.22h in which the interconnected hexagonal chains and the well-defined hexagonal grains are visible. In the 3D representation, extra drawings were made too to better clarify the mentioned structure at which the secondary growth-related grains of the BaMF75mJ were visualized by means of red lines on top of the black structure (see Figure 5.22l). Since the XRD points out the chemical disturbances on the structure an XPS investigation was conducted to study the chemical variation on the sample's surfaces as XPS is sensitive within a depth of 10 nm only. Figure 5.23 shows the XPS curves of Ba3d (5.23a and 5.23b for BaMF75mJ and BaMF25mJ), Fe2p (5.23c) and O1s (5.23d) and the deconvolution of the species. Figure 5.23b, 5.23c and 5.23d show the spectra for the Ba 3d, Fe 2p and O 1s lines obtained from the BaMF25mJ film. In Figure 5.23b one can observe two distinct peaks for both the Ba $3d_{3/2}$ and Ba $3d_{5/2}$ of the BaMF25mJ sample. The lower binding energy (BE) of the spin-orbit split (SOS) pair at $3d_{3/2}$ BE_{Ba1} = 793.98 eV and $3d_{5/2}$ BE_{Ba1} = 778.65 eV (referred to as Ba1, indicated by blue curves) is attributed to Ba1 atoms in the perovskite phase.

The higher binding energy SOS pair at $3d_{3/2}$ BE_{Ba2} = 795.33 eV and $3d_{5/2}$ BE_{Ba2} = 780 eV (denoted Ba2, indicated by red curves) corresponds to Ba2 atoms in a different chemical environment. The energy separation between Ba1 and Ba2 is about 1.5 ± 0.1 eV. This finding agrees with similar XPS spectra of Ba atoms observed by Atuchin et al.[228] for hexaferrite BaM powder samples. The BE values which correspond to the peak positions of Ba 3d3/2 and Ba 3d5/2 for both BaMF25mJ and BaMF75mJ samples are given in Table A-8 in appendix. Figure 5.23a and Figure 5.23b show a comparison of the Ba spectra of the 25 mJ and 75 mJ samples, respectively. Both spectra show the presence of two types of atoms, Ba1 and Ba2. However, the Ba1/Ba2 ratio is different, with

BaMF25mJ being 1.08 and BaMF75mJ being 1.34. Consequently, this difference in ratio results in different total Ba profiles. It is generally accepted that Ba atoms with a binding energy below 780 eV correspond to Ba1 atoms which are a part of the perovskite BaM phase. As shown in Figure 5.23c, the XPS spectra of Fe 2p show the $2p_{3/2}$ and $2p_{1/2}$ multiplets are indicated by (peak1, peak2) and (peak3, peak4), respectively, together with their corresponding satellites.

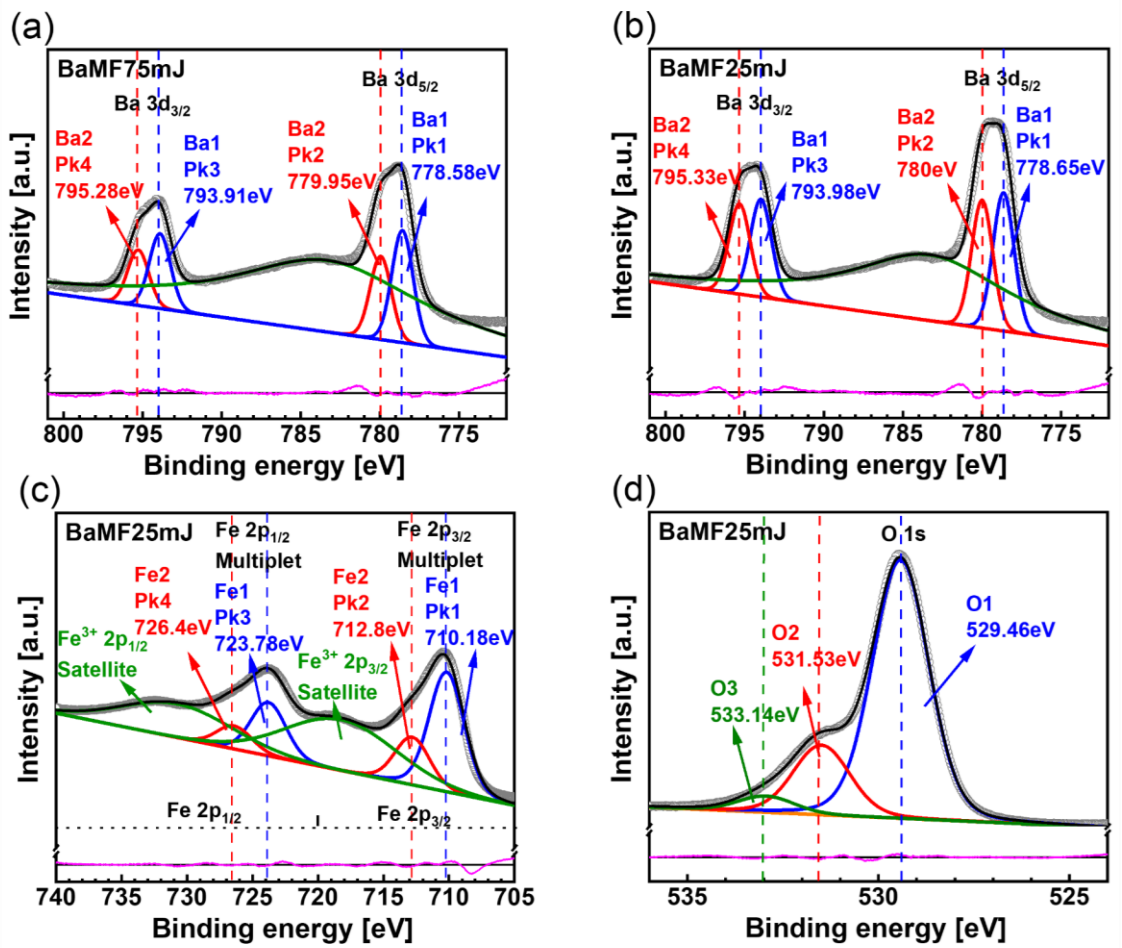

Figure 5.23: Measured and fitted narrow range XPS spectra of BaM films, (a) Ba 3d spectra of BaMF75mJ, (b) Ba 3d spectra of BaMF25mJ, (c) Fe 2p spectra of BaMF25mJ, and (d) O 1s of BaMF25mJ. Open circles correspond to measured XPS data where solid black lines correspond to fitted data, an orange line represents the background intensity, blue, red, and green curves show the fitting peaks, and below the fits solid magenta line corresponds to fit residue. Blue curves of (a, b) correspond to peak 1 (Pk1) and peak 3 (Pk3) of the Ba1 doublet where red curves of (a, b) correspond to peak 2 (Pk2) and peak 4 (Pk4) of Ba2 doublet with spin-orbit splitting SOS = 15.33 eV, with an intensity ratio of $I_{5/2}$:$I_{3/2}$ = 2/3. The solid green line in (a, b) corresponds to the Auger peak of Fe LMM. Blue curves in (c) correspond to peak 1 (Pk1) and peak 3 (Pk3) of the Fe1 doublet and red curves represent peak 2 (Pk2) and peak 4 (Pk4) of the Fe2 doublet separated by SOS = 13.6 eV with an intensity ratio of $I_{3/2}$:$I_{1/2}$=2. Green solid lines in (c) represent satellite peaks of Fe 2p orbitals. (d) Blue, red, and green curves correspond to the O1, O2, and O3 peak fits for the O 1s spectrum, respectively[80].

The curve fits the measured data remarkably well. The BE values which correspond to the peak positions of the $2p_{1/2}$ and $2p_{3/2}$ multiplets for both BaMF25mJ and BaMF75mJ are compared in Table A-9 in the appendix. In addition, the BE values of the SOS pair at $2p_{1/2}$ BE_{Fe1} = 723.78 eV

and $2p_{3/2}$ BE_{Fe1} = 710.18 eV are assigned to Fe1 atoms (peak3 and peak1 is represented by blue curves) for BaMF25mJ. Similarly, the BE values of the SOS pair at $2p_{1/2}$ BE_{Fe2} = 726.4 eV and $2p_{3/2}$ BE_{Fe2} = 712.8 eV correspond to Fe2 atoms (peaks 4 and 2 is represented by red curves). Figure 5.23d shows the O 1s spectral region which can be divided into three sub-peaks. The lower binding energies BE_{O1} = 529.46 eV and BE_{O2} = 531.53 eV are referred to O1 and O2, respectively. These are associated with O_2 ions in the BaM phase. Typically, the O 1s peak falls within the 528 - 531 eV binding energy range characteristic of metal oxides. Another peak at BE_{O3} = 533.14 eV corresponds to an Ox- oxidation state ($0 < x < 2$). This is associated with chemisorbed species and oxygen vacancies.

Our analysis, which includes peak positions and integrated intensities of Ba 3d, Fe 2p and O 1s atoms, is listed in detail for both BaMF25mJ and BaMF75mJ samples in Table A-9 in the appendix. Importantly, percentages to examine variations in the Fe/Ba ratio which result from the change in laser fluence are used. The sum of the intensities for Ba, Fe and O add up to 100 %, as shown in Table A-9 in the appendix.

Our focus here is to understand how the increase of the fluence from 25 to 75 mJ affects the chemical composition of the surface. To do this, we compare the total spectra of all elements, Ba, Fe and O, in Figure 5.24a. The top of the spectra shows changes in Ba and Fe as the laser fluence varies. In particular, for BEs below 700 eV and above 820 eV both spectra match well. However, in the intermediate BE range which corresponds to Fe, the red spectrum of the BaMF25mJ sample has a higher intensity than that of BaMF25mJ. Conversely, in the BE range which corresponds to Ba, the blue profile of BaMF25mJ shows higher Ba intensities compared to BaMF75mJ. Figure 5.24b, 5.24c and 5.24d give a more detailed breakdown of the spectra for Ba, Fe and O in both BaMF25mJ and BaMF75mJ films.

By fitting all the spectra, the corresponding peak positions and intensities, which are compared in Table A-9 in the appendix are determined. The comparison of the spectral profiles shows that the Ba intensity is higher in BaMF25mJ, while the Fe intensity is higher for BaMF75mJ. Specifically, the integrated area shows that I_{Ba} = 14.35 % for BaMF25mJ and 9.62 % for BaMF75mJ. Conversely, I_{Fe} = 72.25 % for BaMF25mJ and 77.75 % for BaMF75mJ. These results indicate that BaMF25mJ is Ba enriched while BaMF75mJ is richer in iron. In addition, I_{O1} = 10.12 % is higher for BaMF25mJ. Since XPS merely provides the information about the surface chemistry, a STEM/EDX (Figure 5.25) study was conducted for 2 different BaM films.

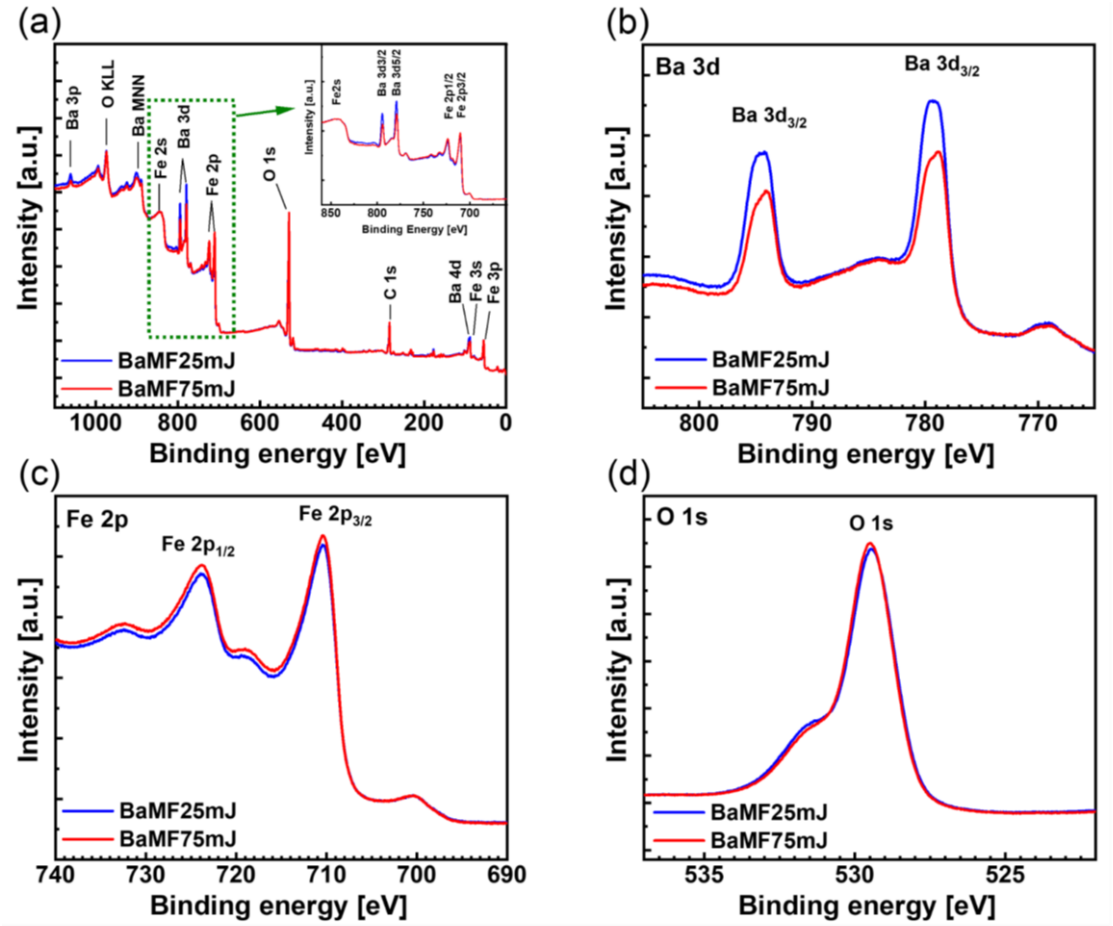

Figure 5.24: Acquired XPS (a) survey spectrum with inset of the magnified region of Fe 2s, Fe 2p, and Ba 3d lines. (b) Ba 3d, (c) Fe 2p, and (d) O 1s spectra of BaMF25mJ and BaMF75mJ films[80].

Figure 5.25a1 to 5.25a4 show the STEM and EDX maps of the BaMF25mJ film and the atomic concentration (Figure 5.25a5) profile along the marked region in Figure 5.25a1 (similarly, Figure 5.25b1 to 5.25b5, and Figure 5.25c1 to 5.25c5 for BaMF75mJ from 2 different regions). EDX maps are measured in the STEM mode by using the electron probe with 1 nm in diameter. The obtained maps were substracted from the background and analysed. For the EDX maps, Ba, Fe and O are shown with the color code of red, green, and blue for the elemental profiles. Elemental maps allow to identify the presence of a chemical fluctuation in the layer and the occurrence of a chemical interdiffusion at the BaM/Pt interface. The overall composition of the two films is close to the nominal values, namely approximately, 3 at.% Ba, 37 at.% Fe and 60 at.% O (see Figure 5.25a5 and 5.25b5). There are some deviations in the concentration of the chemical species, especially towards the film surface. One can see that the variation of the concentration is systematically exists at the film surface. However, the concentrations below the first 20 nm of the surface are consistent for Ba, Fe and O. The change in the microchemistry in near-surface regions can hardly be interpretted as a real inhomogeity of the chemical composition due to the probable artifact generated by the TEM sample preparation. Since a Ga^+-ion beam was used to prepare the FIB lamella the variation in chemistry could be caused by the lamella preaparation. In Figure 5.25b5, a small gradient of Fe and O was visible which the concentration of Fe and O seems to

decrease steadily towards the surface of the film. Here, the Ba content remains constant apart from the surface region. For example, at the interface BaM/YSZ the elemental composition is 3.0 at.% Ba, 39.5 at.% Fe and 57.5 at.% O whereas the composition values are 1.8 at.% Ba, 33.3 at.% Fe and 64.9 at.% O at the surface.

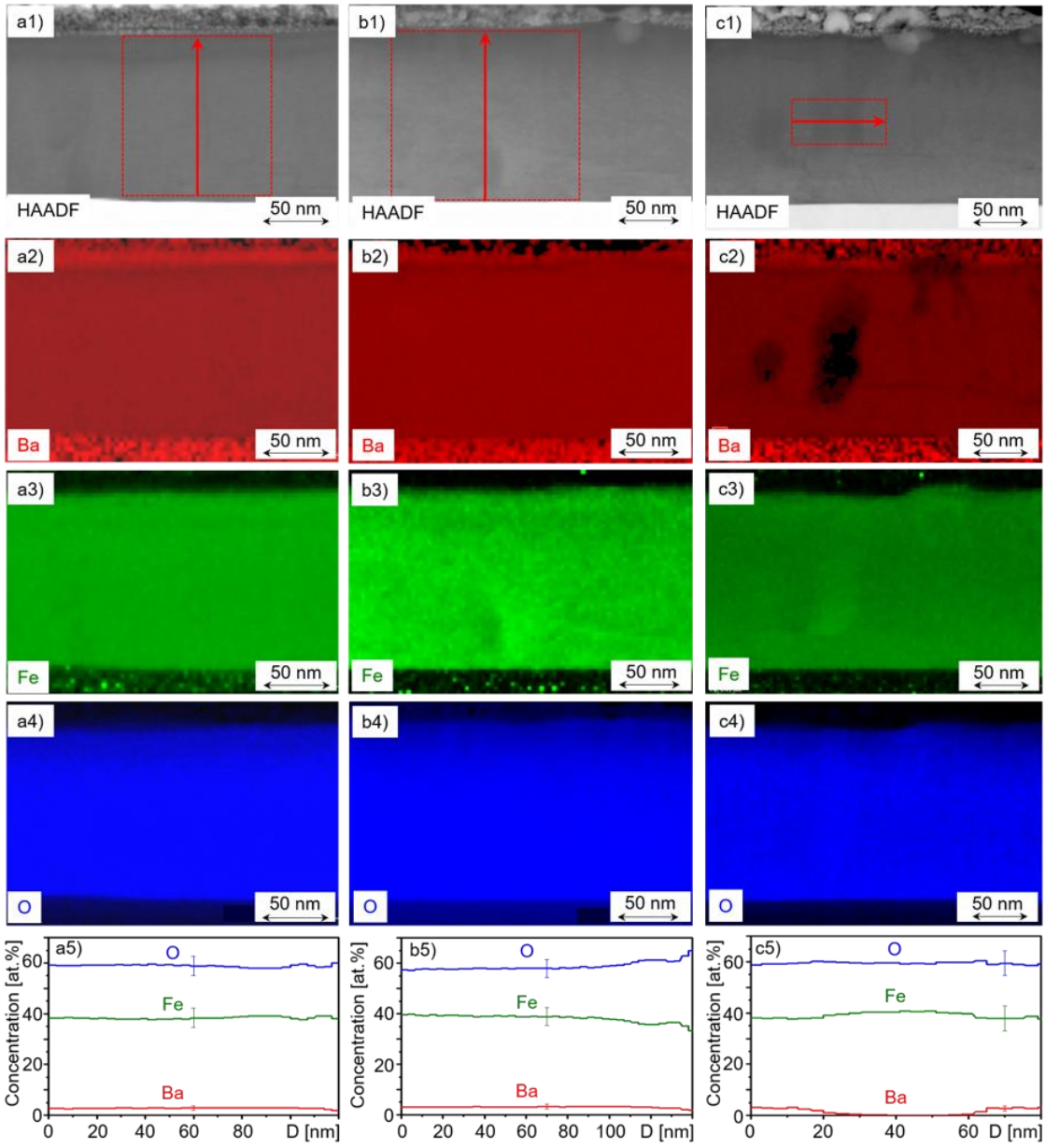

Figure 5.25: Combined STEM/EDXS analysis of the element distribution of the BaM/Pt layers on YSZ in cross-section: STEM HAADF images and X-ray maps of the distribution of the elements Ba, Fe, and O together with corresponding element-concentration profiles of the regions marked in the STEM HAADF images for BaMF25mJ (a1-a5) and for two different regions in BaMF75mJ which figures (b1-b5) represent a typical BaM region and (c1-c5) show a region with a secondary Fe-O rich phase. The individual energy-dispersive X-ray data were quantified by using the thin-film approximation and the noise of the obtained maps was reduced by applying a 3 x 3 mean filter. The error bars in the element-concentration profiles amount to approximately 1 at. % for Ba, 4.5 at. % for Fe, 4.5 at. % for O[80].

Additionally, BaMF75mJ contains a secondary Fe-O phase with the composition of 40 at.% Fe and 60 at.% O at some regions which corresponds to a Fe_2O_3 phase (Figure 5.25c5). In comparison with the BaM matrix, a respective amount of the Fe_2O_3 regions occupied a low volume fraction from the BaM sample. In the TEM lamella, there exist 2 regions which are separated 5µm from each other. On the other hand, a compositional variation was not observed in the BaMF25mJ sample. Therefore, BaMF25mJ is found to possess the same stoichiometry as the BaM target whereas the BaMF75mJ displays slight gradient variations and Ba deficient regions related to the formation of the Fe_2O_3 phase as discussed in the previous chapter. Furthermore, BaMF75mJ shows a gradient in the composition through the film thickness. It must be emphasized that BaMF25mJ and BaMF75mJ display a chemical variation at the surface which could partially correlated with the difference revealed by XPS measurements. However, it should be noted that EDX/STEM analysis is a local analysis method which cannot deliver the overall information unless it does not correlate with the statistical methods.

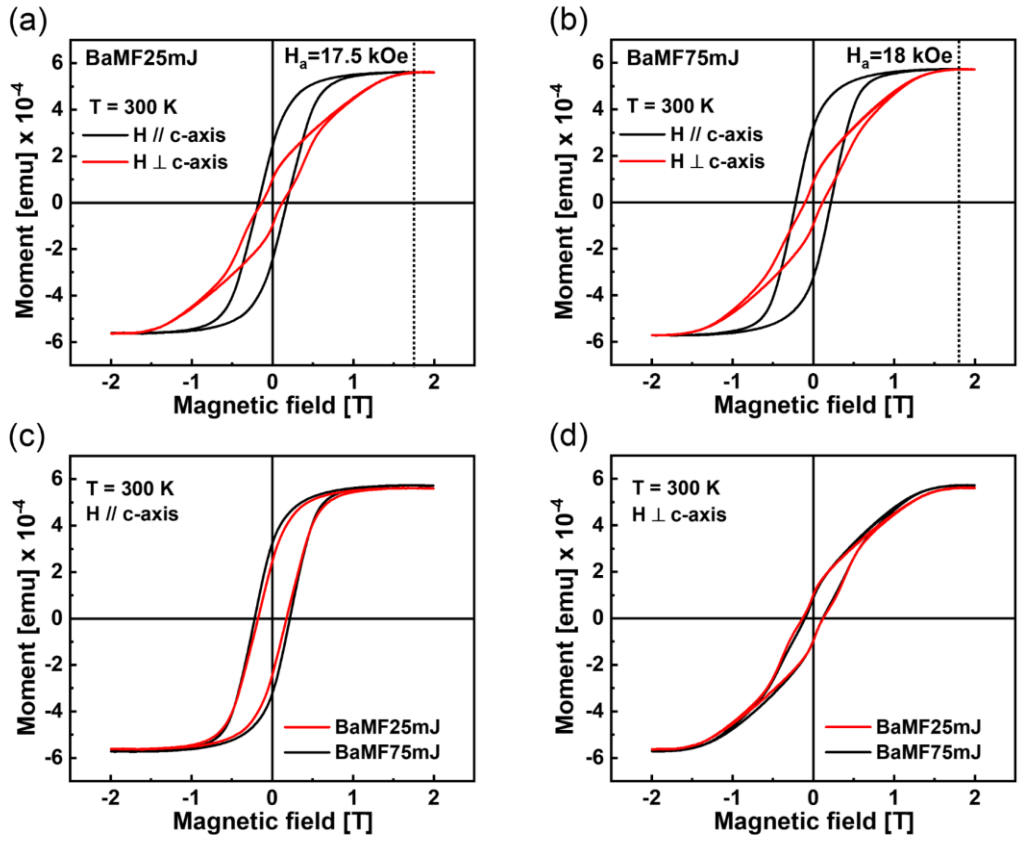

Figure 5.26: In-plane and out-of-plane hysteresis loops of (a) BaMF25mJ, (b) BaMF75mJ, (c) comparison between BaMF25mJ and BaMF75mJ of the out-of-plane magnetization loops, and (d) the in-plane-plane hysteresis loops[80].

5.3.3 Influence of the laser fluence on magnetic properties

Figure 5.26 shows the out-of-plane (OOP) and the in-plane (IP) magnetic hysteresis loops measured from [-2T to 2T] of the samples BaMF25mJ and BaMF75mJ. Both films show a significant difference between the in-plane and out-of-plane hysteresis loops. BaMF75mJ exhibits the high OOP squareness and the low IP squareness ($S_{\perp}$ = 0.56, $S_{//}$ = 0.152) which indicates a high degree of crystallographic c-axis orientation. Additionally, the comparison of the $S_{\perp}$ and $S_{//}$ values between the two films show that the degree of misorientation increases with the increase of fluence. In the case of BaMF25mJ the squareness values are lower than BaMF75mJ, however, still high enough for application ($S_{\perp}$ = 0.43, $S_{//}$ = 0.177) listed in Table 5-7. The anisotropy fields were found to be H_a = 17.5 kOe and H_a = 18.0 kOe for BaMF25mJ and BaMF75mJ, respectively. The magnetization saturation seems to be comparable to each other whereupon the squareness varies due to the variation in the remanence magnetization. The saturation magnetization seems to be relevant to the thickness whereas both films were grown to a thickness of 140 nm. Figures 5.26c and 5.26d compare the OP and the IP hysteresis loops of two films which the hysteresis area is larger than in the case of BaMF75mJ. This reflects a large dissipation energy due to the higher defect density. Therefore the threshold to switch the magnetisazion is higher which explains the higher coercivity H_c = 2166 Oe. Additionally, the presence of the minor Fe_2O_3 secondary phase and the interaction between the BaM and Fe-O phase could also contribute to the additional enhancement of the coercive field H_c.

5.4 Summary and conclusions

The investigation of the interface layer thickness effect and the variation of the BaM growth parameters such as the fluence has allowed to determine of optimal growth conditions for future chip designs which involve heterostructures with room temperature FE and room temperature FM layers. The results of this work have provided a critical insight into the growth of BaM films by applying PLD. The study showed that the thickness of the Pt interface layer plays a crucial role in achieving continuous, stoichiometrically homogeneous, high crystalline quality BaM films with desirable magnetic properties. An insufficient Pt interface layer thickness was found which lead to dewetting and delamination phenomena during the subsequent growth. It resulted in the formation of Pt blocks and voids. In addition, the effects of the laser fluence on the BaM film growth was investigated. Comprehensive study which included HRXRD, HR-STEM and various analytical techniques, revealed microstructural and morphological changes in the BaM films which were attributed to the variation in the kinetic energy of the ablated species. One can conclude that a smooth and continuous Pt layer is essential to obtain high quality BaM films suitable for perpendicular recording media, especially when the Pt interface layer thickness reaches or exceeds 70 nm. This optimized Pt interface layer withstands dewetting phenomena during the BaM growth which results in highly c-axis oriented magnetic domains. It is a critical factor in achieving the desired recording performance. Furthermore, the investigation of the effect of increasing the energy per pulse from 25 mJ to 75 mJ on BaM films highlighted the importance of the laser fluence as a growth parameter. It was found that higher a laser fluence induced more crystal defects in the film which includes mosaic block boundaries and secondary phases. This affected the stoichiometry and magnetic properties of the film, with BaMF75mJ which showed

superior properties for recording media applications compared to BaMF25mJ. In summary, this study highlights the importance of laser fluence as a key PLD growth parameter that can be tailored to modulate the microstructure, morphology and resulting magnetic properties of BaM films. This makes it valuable for specific materials applications.

Table 5-1: Summary of the microstructure parameters for the platinum layer in the as-grown state for the samples PtTh25, PtTh75 and for the bilayers systems BaMPtTh25 and BaMPtTh75. The microstructural parameters include lattice parameters, interplanar spacing along the growth direction ($a_{Pt,}$ $d_{111,\,Pt}$), mismatch *f*. Lateral and vertical sizes ($L_{//,\,Pt}$, $L_{\perp,\,Pt}$) as well as misorientation α_{Pt} and root mean square (RMS) of vertical strain derived from the WH plots. In-plane residual strain $\varepsilon_{//,Pt}$ and vertical size $L_{\perp,\,Pt}$ calculated from fringes of symmetric XRD reflections Pt111. No visible fringes: NVF, NA: Not applicable[107].

Sample Name	**PtTh25**	**PtTh75**	**BaMPtTh25**	**BaMPtTh75**
Underlayer	Pt	Pt	Pt	Pt
Lattice parameter a_{Pt} [Å]	3.9388 ± 0.0004	3.9309 ± 0.0004	3.9257 ± 0.0004	3.9299 ± 0.0004
Interplanar spacing $d_{111,\,Pt}$ [Å]	5.5638 ± 0.0005	5.5539 ± 0.0005	5.5491 ± 0.0005	5.5489 ± 0.0005
Mismatch (Pt/YSZ) $f_{Pt/YSZ}$ [%]	-23.84 ± 0.24	-23.88 ± 0.24	-23.96 ± 0.24	-24.04 ± 0.24
In-plane residual strain $\varepsilon_{//,\,Pt}$	0.00280 ± 0.0003	0.001 ± 0.0001	0.0002 ± 0.0002	0.00013 ± 0.0002
Lateral size WH-Plot $L_{//,\,Pt}$ [nm]	82.70 ± 8.30	128.20 ± 13.0	NA	NA
Vertical size WH-Plot $L_{\perp,\,Pt}$ [nm]	18.10 ± 1.80	56.70 ± 5.60	NA	NA
Misorientation WH-Plot α_{Pt} [deg]	1.90 ± 0.20	0.85 ± 0.08	NA	NA
RMS vertical strain $<\varepsilon_{L,\,BaM}>$ WH-Plot	0.00498 ± 0.5E-3	0.00474 ± 0.5E-3	NA	NA
Vertical size fringes $L_{\perp,\,Pt}$ [nm]	24.00 ± 2.40	67.83 ± 6.80	NVF	NVF

Table 5-2: Summary of the microstructure parameters for the BaM layer for BaMPtTh25 and BaMPtTh75 samples. The microstructural parameters include out-of-plane and in-plane lattice parameters (c_{BaM}, a_{BaM}), mismatch *f*, vertical size $L_{\perp, BaM}$ as well as misorientation α_{BaM} and root mean square (RMS) of vertical strain $< \varepsilon_{\perp, BaM} >$derived from the WH plots. In-plane and out-of-plane residual strain $\varepsilon_{//, BaM}$, $\varepsilon_{\perp, BaM}$ (T): Tensile, (C) : Compressive[107]

Sample name	**BaMPtTh0**	**BaMPtTh25**	**BaMPtTh75**
Out-of-plane lattice parameter c_{BaM} [Å]	23.2448 ± 0.0003	23.2485 ± 0.0003	23.2517 ± 0.0003
In-plane lattice parameter a_{BaM} [Å]	5.8842 ± 0.0005	5.8597 ± 0.0005	5.8136 ± 0.0003
Mismatch $f_{BaM/YSZ}$ *[%]/* $f_{BaM/Pt}$ [%]	-19.5087 (T)	5.599 (C)	4.7701 (C)
In-plane residual strain $\varepsilon_{//, BaM}$	-0.0074 ± 0.001	-0.0115 ± 0.001	-0.0193 ± 0.001
Out-of-plane residual strain $\varepsilon_{\perp, BaM}$	-0.0069 ± 0.0003	-0.0067 ± 0.0007	-0.0066 ± 0.0007
Vertical size WH-Plot $L_{\perp, BaM}$ [nm]	128.49 ± 13	124.66 ± 13	98.95 ± 10
Misorientation WH-Plot α_{BaM} [deg]	0.653 ± 0.05	0.783 ± 0.05	0.838 ± 0.05
RMS vertical strain WH-Plot $<\varepsilon_{\perp, BaM}>$	1.00E-03	9.45E-04	9.30E-04

Table 5-3: Summary of the magnetic properties determined for the BaMPtTh0, BaMPtTh25 and BaMPtTh75 including the magnetization at the saturation M_s, remanence M_r, the perpendicular and parallel squareness's $S_\perp = M_{r\perp} / M_{s\perp}$ and $S_{//} = M_{r//} / M_{s//}$, the out-of-plane $H_{c\perp}$ and in-plane coercivity fields $H_{c//}$[107].

Sample name	**BaMPtTh0**		**BaMPtTh25**		**BaMPtTh75**	
Direction with respect to surface	Out-of-plane	In-plane	Out-of-plane	In-plane	Out-of-plane	In-plane
Deposited Pt thickness Th_{Pt} [nm]	0		25		75	
In-plane residual strain $\varepsilon_{//,BaM}$	-0.0074 ± 0.001		-0.0115 ± 0.001		-0.0193 ± 0.001	
M_s [emu/cc]	409 ± 10	408 ± 10	372 ± 10	372 ± 10	387 ± 10	386 ± 10
M_r [emu/cc]	135.5 ± 5	41.5 ± 5	205.4 ± 5	53.0 ± 5	220.3 ± 5	60.1 ± 5
$S_\perp = M_{r\perp} / M_{s\perp}$	0.33 ± 0.05		0.55 ± 0.05		0.57 ± 0.05	
$S_{//} = M_{r//} / M_{s//}$		0.102 ± 0.05		0.142 ± 0.05		0.156 ± 0.05
H_c [Oe]	897 ± 10	476 ± 10	2070 ± 10	998 ± 10	2180 ± 10	1155 ± 10
$H_{c//} / H_{c\perp}$	0.53 ± 0.05		0.48 ± 0.05		0.53 ± 0.05	
H_a [Oe]	12656 ± 150		13433 ± 150		13678 ± 150	

Table 5-4: Determination of the proportion of the highly, intermediate and low spin orientation magnetic domains from the MFM images recorded in the remanent state Mr after magnetizing the samples with the H field of 3 Tesla at the VSM instrument[107].

Sample name	**BaMPtTh0**	**BaMPtTh25**	**BaMPtTh75**
Highly spin oriented BaM magnetic domains (phase shift Δφ = 20 °) Blue area percentage [%]	4.38 ± 0.50	3.16 ± 0.50	73.31 ± 0.50
Intermediate spin oriented BaM magnetic domains (phase shift Δφ = 13 °) Magenta area percentage [%]	48.50 ± 0.50	46.04 ± 0.50	23.11 ± 0.50
Low spin oriented BaM magnetic domains (phase shift Δφ = 7.5 °) Yellow area percentage [%]	47.19 ± 0.50	51.32 ± 0.50	3.68 ± 0.50

Table 5-5: In and out-of-plane lattice parameters of YSZ (111), Pt (111) and $BaFe_{12}O_{19}$ film together with the in-plane mismatch between YSZ (111) / Pt (111) and Pt (111) / BaM[80].

		BaMF25mJ	**BaMF75mJ**
YSZ(111)	In-plane lattice parameter *a* [Å]	7.2807 ± 0.0001	7.2833 ± 0.0001
	Out-of-plane lattice parameter *c* [Å]	5.1481 ± 0.0001	5.14 ± 0.0001
Pt(111)	In-plane lattice parameter *a* [Å]	5.5449 ± 0.0001	5.5452 ± 0.0001
	Out-of-plane lattice parameter *c* [Å]	3.9255 ± 0.0001	3.9218 ± 0.0001
Mismatch	(YSZ/Pt) [%]	23.841 ± 0.001	23.864 ± 0.001
$BaFe_{12}O_{19}$	In-plane lattice parameter *a* [Å]	5.8632 ± 0.0001	5.8396 ± 0.0001
	Out-of-plane lattice parameter *c* [Å]	23.2001 ± 0.0001	23.2171 ± 0.0001
Mismatch	(Pt/BaM) [%]	5.74 ± 0.002	5.309 ± 0.002

Table 5-6: Vertical and lateral blocks sizes obtained by WH-Plots and TEM images, together with misorientation angle and root mean square deviation of strain along the growth direction for BaMF25mJ and BaMF75mJ films[80].

Parameter / Determination method	**BaMF25mJ**	**BaMF75mJ**
Vertical coherent block size ($L_{\perp}$) / WH-Plot of SXRD [nm]	85 ± 3	85 ± 5
Lateral coherent block size ($L_{//}$) / WH-Plot of SXRD [nm]	293.5 ± 29	925 ± 92
Vertical size of mosaic blocks / TEM [nm]	135	[6 – 122]
Lateral size of mosaic blocks / TEM [nm]	[25-156]	[23-244]
Misorientation angle (Δ) / WH_Plot of SXRD [degree]	0.626 ± 0.1	0.804 ± 0.1
Root mean square deviation of strain (ε) / WH_Plot of SXRD	2.86E-4 ± 0.10E-4	5.75E-4 ± 0.16E-4

Table 5-7: Energy per pulse, growth rate (GR) , saturation magnetization (M_s), remenance magnetization (M_r), out-of-plane magnetic squareness ($S_\perp$), in-plane magnetic squareness ($S_{//}$), magnetic coercivity (H_c), perpendicular anisotropy ($Hc_{//}/Hc_\perp$) and grain sizes of BaMF25mJ and BaMF75mJ films[80].

	BaMF25mJ		**BaMF75mJ**	
	Out-of-plane	**In-plane**	**Out-of-plane**	**In-plane**
Energy per pulse [mJ] (fluence [J/cm^2])	25 (1.5)		75 (5.1)	
GR [nm/min]	0.41	0.41	1.22	1.22
M_s [emu/cc]	430	430	467	462
M_r [emu/cc]	185	76	262	70
$S_\perp = M_{r\perp} / M_{s\perp}$	0.43		0.56	
$S_{//} = M_{r//} / M_{s//}$		0.177		0.152
H_c [Oe]	1768.9	1253.4	2166	1177.3
$H_{c//} / H_{c\perp}$	0.7		0.53	
Interconnected hexagonal chains [min-max] [nm]	[287-983]		[301-740]	
Grain sizes [min-max] [nm]	[450-800]		[80-265]	

6 Relevance of the platinum underlayer crystal quality in the microstructure and magnetic properties of bilayer systems *h*-$YbFeO_3$/Pt/YSZ(111) grown by pulsed laser deposition

6.1 Introduction

The epitaxial growth of rare earth hexaferrites, particularly hexagonal ferrites (*h*-$RFeO_3$, where R = Y, Dy-Lu), including *h*-$YbFeO_3$, has attracted significant interest due to their successful stabilization in a metastable hexagonal structure (space group: $P6_3cm$) [106,229,230.] This has been achieved by depositing these films onto hexagonal substrates which includes sapphire (Al_2O_3)[137,231,232,233], YSZ(111)[137,233,234,235], MgO [232] and buffered substrates with materials promoting the $P6_3cm$ structure. These include platinum (Pt)[231,232,235], Fe_3O_4[236], indium tin oxide (ITO)[234,235,237] and strontium titanate (STO)[233,238,239]. In fact, the study of Jeong et al.[231] demonstrated that *h*-$YbFeO_3$ (YbFO) films possess a thickness of about 60 nm and are grown on sputtered Pt on a Al_2O_3 substrate by using PLD. They exhibited RT ferroelectricity. Furthermore, the observed ferroelectric polarization at RT was P_s = 15 µC/cm² and the magnetic ordering temperature was T_N = 120 K[231]. Recent studies have proved that hexagonal ferrites exhibit a simultaneous and spontaneous electric and magnetic polarization at low temperatures which classifies them as a new multiferroic family. These materials are known for their ferroelectric and antiferromagnetic properties[230,231,234,235,237,239].

Recent attempts to fabricate *h*-$YbFeO_3$-based devices have demonstrated the crucial role of bottom electrodes, such as Pt[231,232,235], ITO[234,235,237] and $La_{2/3}Sr_{1/3}MnO_3$ (LSMO)[238,239], in the characterization of ferroelectric and dielectric properties. The interfacial strain can be tailored by selecting different substrates or introducing an underlayer that also serves as a bottom electrode. Zhang et al. demonstrated that modifying the interfacial misfit impacts the epitaxial quality and magnetism of YbFO[236]. Investigations into the microstructure of YbFO grown on Al_2O_3 without an interlayer revealed the presence of misfit dislocations shown by high-resolution transmission electron microscopy (HRTEM)[232], while antiphase boundaries (APB) were detected in YbFO grown on YSZ(111)[235]. Bauer et al.[106] employed HRTEM in conjunction with high-resolution X-ray diffraction (HRXRD) to demonstrate how PLD grown Pt underlayer moderates the mismatch between *h*-$LuFeO_3$ and an Al_2O_3 substrate, thereby reducing the defect density and enhancing the crystal quality. Furthermore, they emphasized that the thickness optimization of the Pt underlayer was significantly important to ensure continuity and conductivity in Pt bottom electrodes[106].

There is a lack of knowledge regarding the dependence of the YbFO microstructure on growth parameters, particularly in relation to the quality of the underlayer between the YbFO film and the substrate. Bauer et al.[107] recently highlighted the significance of the Pt underlayer quality on both the crystal structure and magnetic properties of $BaFe_{12}O_{19}$ hexaferrite films. Their findings demonstrated that an optimal Pt underlayer thickness, grown by PLD, enhances both the layer quality and the magnetic performance.

In this study, we examined the film morphology and microstructure of YbFO grown on YSZ(111) and Pt-buffered YSZ(111) with the varying Pt film thicknesses in detail. The objective is to investigate how the underlayer quality influences the crystal structure of YbFO and its magnetic properties. This investigation employs a combination of diffraction, scanning, and transmission microscopy as well as superconducting quantum interference techniques.

6.2 Experimntal section

PLD growth of h-$YbFeO_3$ on Pt buffered YSZ(111) substrates

The Pt films were deposited on YSZ with a (111) orientation in the PLD chamber in a vacuum environment after heating the substrate up to T_g = 900 °C by using different number of shots 1647, 4100, 8235, 12350 and 16470 with a laser frequency of 5 Hz, and an energy pulse of 60 mJ (i.e. fluence F = 16 J/cm^2). Prior to the growth, the different substrates were cleaned by isopropanol and then annealed in the furnace for 2 hours at a temperature of 1200 °C, in order to have low roughness and a good terrace morphology. The target was separated by 35 mm from the substrate. The samples were cooled slowly with 5 °C/min from T_g = 900 °C to RT. The substrate used for the Pt growth were 8 x 8 mm^2 in size. One could divide the grown Pt films into the two pieces for the subsequent treatment. In the case of one of the pieces with a size of 4 mm x 8 mm, ferroelectric (FE) YbFO layers were grown on the different Pt bottom electrodes mentioned above. For this purpose, the template (Pt/YSZ) was heated from RT to T_g = 900 °C with a heating rate of 25 °C/min. The growth of the subsequent YbFO layers was carried out in an oxygen atmosphere at a pressure of 400 mTorr and with a laser frequency of 1 Hz and a number of shots of *Nsh* = 20000. The deposition time was about 5 hours. The Pt layer became encapsulated the multilayer system between the YSZ and the FE layer. In the manuscript, the corresponding samples with encapsulated Pt films of different thickness are named as follows: YbPt_Th0nm YbPt_Th10nm, YbPt_Th40nm, YbPt_Th55nm and YbPt_Th70nm.

High-resolution and X-ray diffraction reciprocal space mapping

2D-reciprocal space maps (2D-HRXRD) were recorded for the different Pt and YbFO reflections by using high-resolution X-ray diffraction at the NANO beamline at the KIT light source in Karlsruhe Germany. All the 2D-HRXRD data of the symmetric and asymmetric reflections were measured by using a Mythen linear detector positioned at the corresponding Bragg diffraction angles and by rocking the sample around the Bragg angle. All the X-ray measurements were performed at an energy of E = 15 keV and a wavelength of 0.826 Å. Furthermore, azimuthal Phi (ϕ) scans were also carried out by rotating the samples YbPt_Th0nm YbPt_Th40nm, YbPt_Th55nm and YbPt_Th70nm around the surface normal for the asymmetric reflections YbFO108.

X-ray reflectivity and mass density profiles

The specular X-ray reflectivity (XRR) was measured by using a Rigaku Smartlab diffractometer. The data were measured by using Cu-K_α radiation with a wavelength of λ = 1.5418 Å and a parallel beam with an X-ray mirror. The data were evaluated by the multilayers with rough interfaces method for XRR analysis developed by Parratt[176]. The used model for fitting of the XRR curves of YbPt_Th0nm, YbPt_Th10nm, YbPt_Th40nm, YbPt_Th55nm and YbPt_Th70nm is described as following: a rough YSZ substrate, thin interlayer between the substrate and the first layer, the first layer with a rough interface and a rough top layer. The fit was carried out by using a self-written script based on the least square fitting algorithm. All the fitting parameters are summarized in Table 6-1.

Atomic Force Microscopy

Ex-situ AFM topography measurements were carried out in the tapping mode with a Bruker Dimension ICON (Bruker, Karlsruhe, Germany) for the YSZ(111) substrate, Pt_Th10nm, Pt_Th40nm, Pt_Th55nm and Pt_Th70nm templates as well as for the bilayers systems such as YbPt_Th0nm, YbPt_Th10nm, YbPt_Th40nm, YbPt_Th55nm and YbPt_Th70nm after the subsequent growth of a YbFO layer. As sensors, we used OPUS AC160-NA cantilevers (Nano-AndMore, Wetzlar, Germany), with force constants of 26 N/m and resonance frequencies of 300 kHz. The analysis of the AFM images was performed by using the NanoScope v2 software package (Bruker, Karlsruhe, Germany). All the derived topographical parameters are summarized in Table 6-1.

Scanning Electron Microscopy (SEM) and Transmission Electron Microscopy (TEM)

The surface topography and the chemical composition of these nine Pt layers were characterized by SEM imaging combined with energy-dispersive X-ray spectroscopy (EDX) by using an FEI Dual beam Helios G4 FX microscope. For secondary electron (SE) imaging of the sample surface with 0 degrees of inclination, respectively, an Everhart-Thornley detector (ETD) was used. The microscope was operated at an accelerating voltage of 10 kV in the so-called field-free mode with a beam current of approximately 25 pA. In addition, element-specific information backscattered electron (BSE) images were taken by means of a semiconductor (pn-diode) detector. Moreover, chemical analyses were performed by EDX at a primary electron energy of 20 keV and a beam current of 0.4 nA by applying a Bruker system of the type QUANTAX 400 with a silicon-drift detector (SDD) XFlash 6. For the samples without inclination (EDX_0°) the two-dimensional Pt distribution was imaged by mapping at which the acquisition time per map was about 5 min. By employing the ESPRIT 2.3 software, the raw-data X-ray maps were quantified by using the thin-film approximation after Cliff-Lorimer[148] to obtain element-concentration maps.

For the TEM inspection of the different samples (YbPt_Th0nm YbPt_Th40nm, YbPt_Th55nm and YbPt_Th70nm) cross-sectional specimens were prepared by focused ion beam (FIB) milling and by using the FEI Dual beam Helios G4 FX microscope. Prior to the FIB preparation, a thin gold layer was sputtered on the sample surface to reduce ion-beam damage of the heterostructures. Subsequently, the standard FIB preparation of TEM lamellae was done, where a Pt protection layer was deposited on top of the samples. Then, coarse FIB milling was carried out at a primary ion energy of 5 keV. The lamellae were attached to Cu lift-out grids and finally polished by a

Ga^+-ion beam with a low energy of 1 keV to minimize the Ga^+ implantation and material amorphization. TEM investigations of all the above-mentioned samples were carried out on an aberration-corrected FEI Titan 80-300 microscope. This TEM uses a thermally assisted field emission cathode (Schottky emitter) and was operated at 300 kV high voltage. For image recording, the microscope is equipped with a 4k × 4k CMOS camera of the F436 type (TVIPS). TEM bright-field imaging was performed to obtain information about general layer properties like, e.g., layer thickness and crystal structure.

Degree of coverage

The values of the degree of coverage DoC (BSE) were obtained by processing the BSE images of Figure 6.2f, 6.2g, 6.2h, 6.2i and 6.2j while the Yb degree of coverages Yb_DoC (EDX) were determined from the EDX maps of the Yb elements of Figure 6.2i3, 6.2m3, 6.2n3 and 6.2o3. In detail, the Weka Trainable Segmentation plug-in of the ImageJ software[240] was utilized. Dark contrast groves were marked as the substrate and regions with bright contrast as Yb. The software was iteratively trained by comparing the marked regions with the original image. Weka Trainable Segmentation plug-in allows the identification of the variable contrast regions. Image defects (such as contrast profile, charging contrast etc.) could be eliminated by the iterative training opportunity of the plug-in. The segmentation results were converted into binary images, and the area fractions were measured by ImageJ and determined as the degree of coverage. All the estimated values were summarized in Table 6-1 under the section 'Film morphology'.

Superconducting quantum interference device (SQUID)

Out-of-plane (OOP) magnetization hysteresis loops were performed at the temperatures T = 2 K, 10 K, 20 K, 30 K, 50 K, 100 K, 150 K and 300 K by using the MPMS3 SQUID magnetometer from the company Quantum Design for an applied field in the range of H = 0 to 6 Tesla. The measurement was selectively performed for YbPt_Th0nm YbPt_Th10nm, YbPt_Th55nm and YbPt_Th70nm. Additionally, zero field cooling (ZFC) and field cooling (FC) curves at which the samples were cooled in the absence and the presence of the applied fields (H = 100 Oe, 2000 Oe, H is parallel to the c-axis) respectively, were also recorded in the temperature range T = [2 – 300 K]. From the (OOP) magnetization loops, the saturation magnetization $M_{s\perp}(T)$, the remanent magnetization, $M_{r\perp}(T)$, the out-of-plane (OOP) coercivity field $H_{c\perp}(T)$ were derived and plotted versus temperature T.

6.3 Morphology and structure dependency of YbFO layers on the bottom electrode thickness and uniformity

Figure 6.1a presents the XRD patterns of YbFO films grown directly on YSZ(111) substrates and films grown on YSZ(111) buffered with varying thicknesses of platinum (Th_{Pt}), labeled YbPt_Th10nm, YbPt_Th40nm, YbPt_Th55nm and YbPt_Th70nm. For visual clarity, the XRD patterns are vertically shifted. The XRD patterns show substrate reflections (YSZ111, YSZ222, YSZ333, YSZ444) marked by magenta stars, and these reflections are superposed for different

samples. Additionally, Pt underlayer reflections (Pt111, Pt222, Pt333) are clearly visible with an increase in the reflection intensity with Th_{Pt} and a decrease in broadening which simultaneously indicates a better coverage of Pt on YSZ(111) and an improved crystal quality. Notably, the XRD pattern for YbPt_Th0nm, depicted with a black solid line, does not show Pt reflections and justifies the absence of a Pt underlayer. All patterns confirm the epitaxial growth of YbFO through various reflection orders (YbFO002, YbFO004, YbFO006, YbFO008, YbFO0010, YbFO0012, YbFO0014), though peak intensities and profiles vary, which reflects the influence of the Pt underlayer thickness and quality of the YbFO growth. As the Th_{Pt} increases, the YbFO layer quality improves. Nevertheless, YbFO006 reflection is not visible for YbPt_Th10nm, YbPt_Th40nm. On the other hand, YbFO006 appears for YbPt_Th55nm and its intensity increases for Th_{Pt} = 70 nm. This indicates that the quality of YbFO is influenced by the underlayer quality. Figure 6.1b shows the measured and the simulated XRR curves. The simulation of XRR was based on the multilayer approach and was conducted to estimate the film thickness as well as the mass density profiles.

Distinct critical angles in the XRR curves (θ_{Pt} = 0.55° and θ_{YbFO} = 0.34°) are identified for samples with a Pt underlayer, while a single critical angle (θ_{YbFO} = 0.34°) is observed for YbPt_Th0nm in the absence of a Pt underlayer. From these XRR fittings, the thicknesses of encapsulated Pt and YbFO layers are calculated. The mass density profiles derived from these simulations are displayed in Figure 6.1c, with the YSZ(111) substrate in green, the Pt film in grey, the YbFO layer in orange and the air with turquoise color.

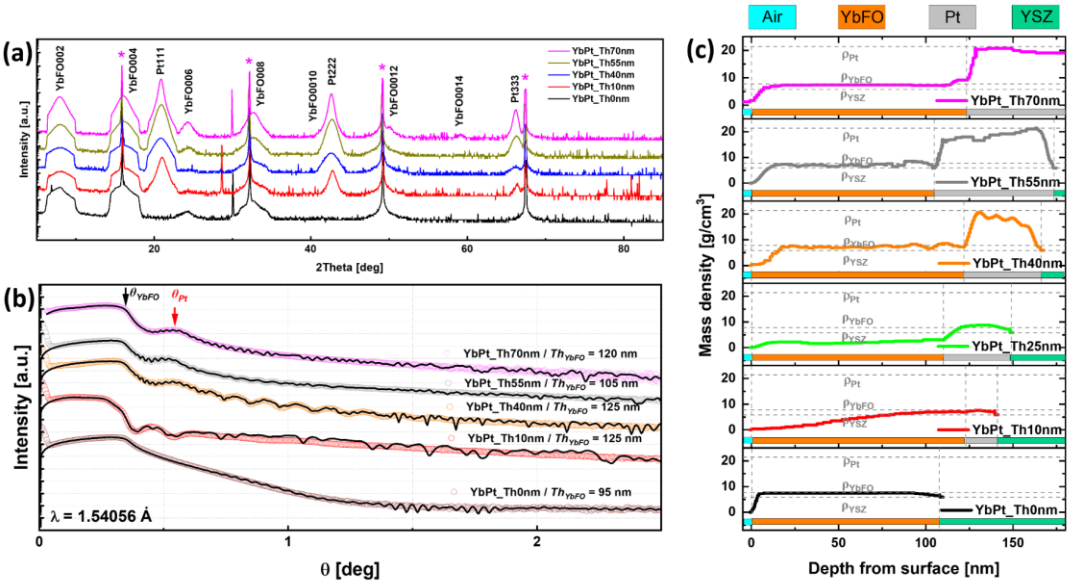

Figure 6.1: (a) X-ray diffraction (XRD) patterns of the YbPt_Th0 nm, YbPt_Th10 nm, YbPt_Th40 nm, YbPt_Th55 nm and YbPt_Th70 nm where the magenta stars indicate the YSZ(111) peaks. The XRD curves are vertically shifted for better clarity. (b) XRR curves of the samples YbPt_Th0 nm, YbPt_Th10 nm, YbPt_Th40 nm, YbPt_Th55 nm and YbPt_Th70 nm whereupon Q_{YbFO} and Q_{Pt} are critical angles of the YbFO and Pt layers. XRR curves are vertically shifted for better visibility. (c) The mass densities profiles along the film depth for the samples YbPt_Th0 nm (lowest panel) , YbPt_Th10 nm, YbPt_Th40 nm, YbPt_Th55 nm and YbPt_Th70 nm (upper panel), the green, grey. The orange and turquoise bars correspond to the YSZ, Pt, YbFO and air ranges for the different samples which serve for the determination of the layers thicknesses. For magnified version, refer to Figure A-21[241].

The grown films (under uniform conditions T_g = 900 °C, P_{O_2} = 400 mTorr, Nsh = 20000) with varied Pt thicknesses (10 nm, 40 nm, 55 nm, 70 nm) were influenced by the growth dynamics of the YbFO layer even the same growth conditions for all the samples were performed. The resulting thickness variations of YbFO (i.e. Th_{YbFO} = 95 nm for YbPt_Th0nm to 120 nm for YbPt_Th70nm, see Figure 6.1a) suggest that the Pt underlayer does not only affect growth kinetics but also the final quality and morphology of the YbFO layers, as indicated by the reduced XRD peak broadening and improved crystal quality in samples like YbPt_Th70nm.

Regarding the mass density of YbFO, for the YbPt_Th0nm sample, the mass density ρ_{YbFO} is equal to 7.82 g/cm^3, which is close to the theoretical value of YbFO. However, for YbPt_Th10nm, ρ_{YbFO} falls below this value which results from a less complete Pt coverage of the substrate surface at Th_{Pt} = 10 nm. This in turn impacts the YbFO layer morphology. This particular issue will be further explored in the subsequent sections. As the thickness of the Pt underlayer exceeds Th_{Pt} = 40 nm, the coverage becomes more complete, and the Pt-buffered YSZ(111) presents a more uniform surface which withstands the commonly observed dewetting phenomena during the subsequent YbFO growth. In chapter 4 and in the related published work[172], the structural and morphological transformations of the Pt underlayer in the as-grown and encapsulated states were investigated in detail as a function of the Pt film thickness. The work highlighted the emergence of competitive phenomena such as dewetting, hillock formation and the infilling of voids by Pt migration which is driven by high diffusion energies during the growth of the capping layer at T_g = 900 °C.

The influence of the Pt underlayer thickness on the YbFO film morphology is shown in Figure 6.2 which displays SEM images in the top row, BSE images in the middle row and EDX maps in the bottom rows. These images illustrate notable changes in the morphology and elemental distribution by a varying Pt thickness. Figure 6.3 presents a comparison between the AFM images of the Pt-buffered YSZ(111) in its as-grown state (upper panel Figure 6.3a1 to 6.3a5) and those of the YbFO films overgrown on the corresponding Pt films (lower panel Figure 6.3b1 to 6.3b5). The comparison demonstrates the influence of modifications in the Pt underlayer on the subsequent layer, as discussed in detail in this work (Chapter 4) and in the published work[172]. In particular, the formation of hillocks at a Pt thickness of 40 nm is noteworthy which persist even after the YbFO deposition as shown in Figure 6.2c and 6.2h, visible as regions of light contrast (hillocks are indicated by the red circles) (see details in Chapter 4, at which the similar comparisons were deeply investigated in terms of hillocks modification through encapsulation).The EDX maps (Figure 6.2m1, 6.2m3, and 6.2m4) demonstrate the presence of Pt hillocks which are enveloped by the YbFO layer as well as black areas corresponding to voids of both Pt and Yb free regions. Furthermore, AFM images (Figure 6.3a4 and 6.3b4) indicate that hillocks formed in the as-grown Pt-buffered YSZ(111) withstand the YbFO growth phase, and therefore affect the YbFO mosaic block arrangement. On the other hand, at a Pt thickness of 55 nm, hillocks formed initially tend to migrate towards voids which facilitates a more uniform Pt underlayer. It results in a more uniform YbFO network film with holes (Figure 6.2d, 6.2i, and Figure 6.2n1). Despite similar YbFO film thicknesses (Th_{YbFO} = 100 ± 5 nm) for YbPt_Th0nm and YbPt_Th55nm, their morphologies differ significantly. The YbPt_Th0nm film exhibits an island-like morphology (Figure 6.3b1), whereas the YbPt_Th55nm film forms a 2D continuous network with holes (Figure

6.3b4). This morphological variance may be due to the layered growth process as well as to the Pt underlayer surface morphology.

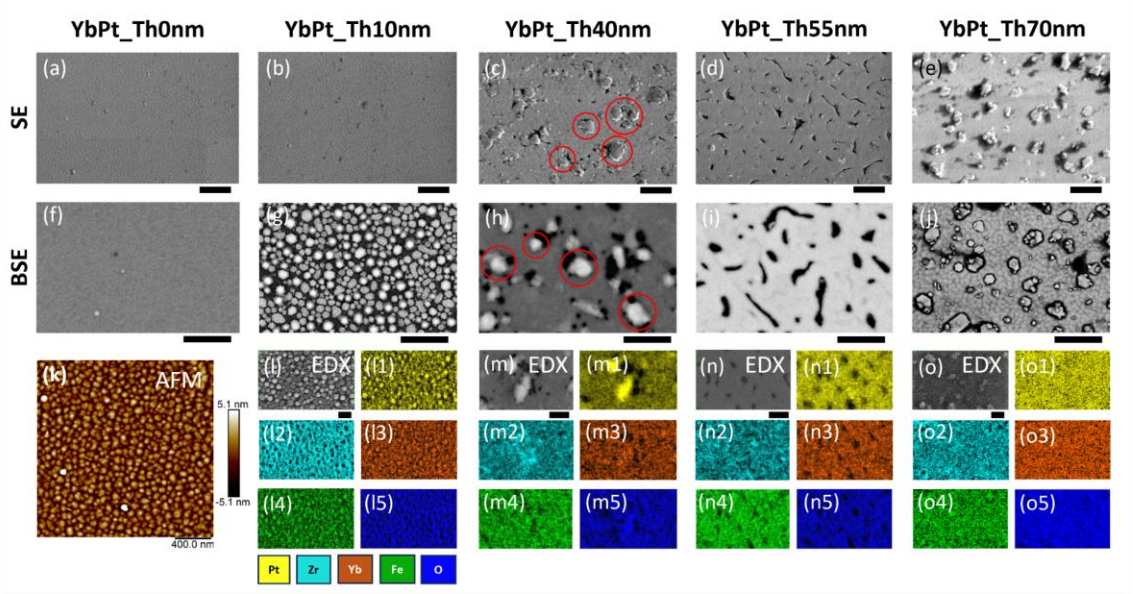

Figure 6.2: (a, b, c, d, e) And (f, g, h, i, j) are the SEM and BSE images of the YbPt_Th0 nm, YbPt_Th10 nm, YbPt_Th40 nm, YbPt_Th55 nm and YbPt_Th70 nm samples with a scale bar of 1 µm. (k) AFM image of the YbPt_Th0 nm film with a scale bar of 400 nm, (l, l1, l2, l3, l4, l5), (m, m1, m2, m3, m4, m5), (n, n1, n2, n3, n4, n5) and (o, o1, o2, o3, o4, o5) are the EDX maps of the elements Pt, Zr, Yb, Fe and O for the YbPt_Th10 nm, YbPt_Th40 nm, YbPt_Th55 nm and YbPt_Th70 nm samples, respectively, with scale bar of 500 nm. For magnified version, refer to Figure A-22[241].

For YbPt_Th70nm (Figure 6.3e, 6.3j), a continuous and homogeneous YbFO film is formed (as the filled surface of the Pt film indicates), followed by an aggregation of YbFO which started as a secondary nucleation over the filled surface when the film exceeds a critical thickness. In order to maintain the continuity and the homogeneity in the YbFO layer, it is crucial to optimize and limit the number of shots (*Nsh*) (i.e. below 20000 for Th_{Pt} = 70 nm).

Based on complementary methods, including SEM, BSE, AFM, and XRR measurements, the evolution of the Pt underlayer morphology was observed from 3D island growth to a 2D network with holes, and finally to a homogeneous and continuous film when the Pt thickness exceeded 55 nm. This progression significantly influenced the surface morphology, homogeneity, and elemental distribution of the YbFO film. Furthermore, the mass density of the resulting YbFO film approached the stoichiometry of the $YbFeO_3$ target (ρ_{YbFeO3} = 7.82 g/cm³) when the Pt underlayer was grown to its optimum thickness.

Figure 6.4a, 6.4b, and 6.4c present the radial diffraction profiles along the crystal truncation rods of selected reflections, including YbFO002, YbFO004, and YbFO0010, for samples, including YbPt_Th0nm, YbPt_Th40nm, YbPt_Th55nm, and YbPt_Th70nm The peak profiles were analysed by using the Pseudo-Voigt function, fitted with a nonlinear least squares method from which peak positions and the full width at half maximum ($FWHM_{rad}$) were determined. The results, plotted in Figure 6.5a, shows variations in the $FWHM_{rad}$ against the reflection order YbFO002 which indicates differences in the crystal quality across the samples. Figure 6.4b shows the

YbFO004 and YSZ(111) substrates peaks which overlap. They were used as a reference for comparing the intensities and broadenings of the YbFO diffraction peaks of the different samples. Analysis of Figure 6.4a to Figure 6.4c reveals that the samples YbPt_Th40nm and YbPt_Th70nm exhibit the lowest and highest peak intensities, respectively. Furthermore, $FWHM_{rad}$ of the YbPt_Th0nm sample is notably larger whereas the $FWHM_{rad}$ decreases by increasing the Pt underlayer thickness Th_{Pt} (see Figure 6.5a). This can be interpreted as an enhancement in the YbFO layer quality due to the Pt underlayer growth and the achievement of an optimum thickness. Notably, the intensity of the Pt222 peak in Figure 6.4c rises with increasing the Th_{Pt}, which is well correlated with the increase of Pt film thickness and interrelated with the improvement of the degree of coverage observed in Figure 6.3. Figure 6.4d. The azimuthal scans of the asymmetric reflection YbFO2014 confirms the epitaxial growth of the YbFO layer with a six-fold hexagonal symmetry across all samples. The peak intensities in the azimuthal scans enhance with increasing the Th_{Pt}, which directly correlates with an improvement in YbFO crystal quality along the film. This latter suggests that YbFO films are promising for ferroelectric properties along the growth c-axis of its non-centrosymmetric hexagonal cell, similar to the findings of Jeong et al.[231] for YbFO films grown on Pt(111)/Al_2O_3(0001). Even though they did not provide any information regarding the Pt thickness used in their study. The lower peak intensities in the azimuthal scans of YbPt_Th0nm, in contrast to YbPt_Th70nm, hint at a weaker ferroelectricity and potential disruptions in the ferroelectric domains within the YbFO layer of the YbPt_Th0nm sample. Additionally, by analyzing the coordinates of symmetric reflections (i.e., YbFO002, YbFO004, YbFO006, YbFO008) and asymmetric reflections (i.e., YbFO2012, YbFO2013, YbFO2014) the in-plane (a_{YbFO}) and out-of-plane (c_{YbFO}) lattice parameters were calculated by using the hexagonal lattice parameter formula. Furthermore, the misfit ($f_{YbFO/YSZ}$) between the YSZ(111) substrate and the YbFO film was determined for the YbPt_Th0nm sample by using (Equation (6-1)) the formula $3 \times d(11\text{-}2)_{YSZ}$ for the substrate relative to the a_{YbFO} parameter of the film which reflects the 3-to-1 lattice site coincidence between the substrate and the film.

$$f_{YbFO/YSZ}[\%] = \frac{a_{YbFO} - 3 * d(11\bar{2})_{YSZ}}{3 * d(11\bar{2})_{YSZ}} * 100 \qquad (6\text{-}1)$$

The growth of hexagonal YbFO on YSZ(111) substrates exhibits an in-plane atomic orientation that aligns YbFO (100) parallel to YSZ (11-2) which results in a misfit value of $f_{YbFO/YSZ}$ = -5.32 % (see Table 6-1). This misfit calculation formalism is comparable to the one used by Xu et al. [2] who reported a misfit of $f_{LFO/YSZ}$ = -5.6 % for hexagonal $LuFeO_3$ (*h*-$LuFeO_3$) grown on YSZ(111). In this case, the oxygen networks of *h*-$LuFeO_3$ and YSZ(111) are well-matched at the interface which leads to strong interfacial bonding. It is noteworthy that *h*-$LuFeO_3$ and *h*-$YbFeO_3$ are isostructural, exhibiting similar lattice parameters[236].

Furthermore, the misfit between the Pt underlayer and the YbFO film was calculated for the YbPt_Th10nm, YbPt_Th40nm, YbPt_Th55nm, and YbPt_Th70nm samples. The misfit was analyzed by using the correspondence $4 \times d(11\text{-}2)_{Pt}$ of the Pt underlayer relative to the a_{YbFO} parameter of the YbFO layer. This indicates a 4-to-1 (Equation (6-2)) conformity between the Pt(111) substrate and the YbFO film in terms of their respective lattice sites.

$$f_{YbFO/Pt}[\%] = \frac{a_{YbFO} - 4 * d(11\bar{2})_{Pt}}{4 * d(11\bar{2})_{Pt}} * 100 \quad (6\text{-}2)$$

It was observed that the misfit between YbFO and the Pt underlayer, designated as $f_{YbFO/Pt}$, gradually decreased from -8.46 % to -6.83 % when approaching the $f_{YbFO/YSZ}$ misfit of -5.32 % as the thickness of the Pt layer increased (see Table 6-1). This reduction indicates an improvement in the matching between the atomic networks of YbFO and Pt(111) at the interface which results from the increased continuity and homogeneity in the thicker Pt layers. Xu et al. [230] also noted a misfit value of $f_{LFO/Pt}$ = -7.5 % for *h*-$LuFeO_3$ (LFO) on platinum, though the details on the thickness of the Pt film were not provided.

The in-plane ($\varepsilon_{//,YbFO}$) and out-of-plane ($\varepsilon_{\perp,YbFO}$) residual strains are calculated using the following formulas (Equation (6-3) and (6-4)) and provided in Table 6-1:

$$\varepsilon_{//,YbFO}\,[\%] = \frac{a_{YbFO} - a_{YbFO}^{FS}}{a_{YbFO}^{FS}} * 100 \quad (6\text{-}3)$$

$$\varepsilon_{\perp,YbFO}\,[\%] = \frac{c_{YbFO} - c_{YbFO}^{FS}}{a_{YbFO}^{FS}} * 100 \quad (6\text{-}4)$$

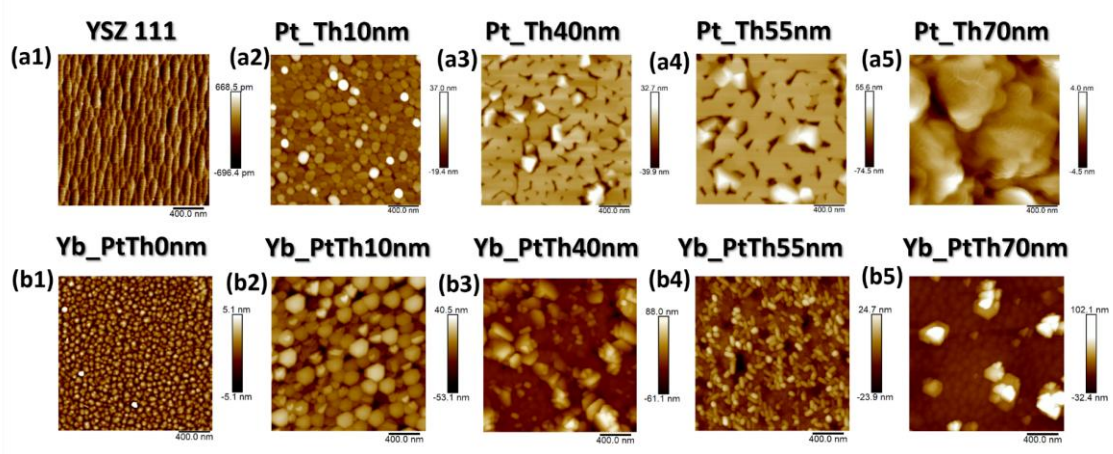

Figure 6.3: (a1, a2, a3, a4, a5) AFM images with a size of 2 µm x 2 µm and a bar scale of 400 nm of the YSZ(111), Pt_Th10nm, Pt_Th40 nm, Pt_Th55nm and Pt_Th70nm, respectively. (b1, b2, b3, b4, b5) Are the corresponding AFM images of the samples after the subsequent growth of YbFO layer with 20000 shots for the samples Yb_PtTh0nm, Yb_PtTh10nm, Yb_PtTh40nm, Yb_PtTh55nm and Yb_PtTh70nm, respectively. For magnified version, refer to Figure A-23[241].

Figure 6.4e, 6.4f, and 6.4g display the radial diffraction profiles along the crystal truncation rod for the YbFO002, YbFO004, and YbFO0010 reflections and compare different samples: YbPt_Th0nm, YbPt_Th40nm, YbPt_Th55nm, and YbPt_Th70nm. The profiles were fitted by using a Pseudo-Voigt function, and the derived $FWHM_{rad}$ values were plotted against the reflection order, as shown in Figure 6.5b. It is evident from these figures that the lowest $FWHM_{rad}$ values are observed for YbPt_Th70nm which indicates an enhancement in the YbFO crystal quality when Th_{Pt} reaches an optimum at 70 nm. The Williamson-Hall (WH) approach[147,242] was employed to analyze the plots presented in Figure 6.5a and Figure 6.5b. It was assumed that the

YbFO films consist of mosaic blocks characterized by lateral ($L_{H,\,YbFO}$) and vertical sizes ($L_{V,\,YbFO}$). They are misaligned with the c-axis to a degree represented by the misorientation α_{YbFO}, and are vertically strained by defects and grain boundaries. From the intercepts and slopes of the $FWHM_{rad}$ plotted against the reflection order, $L_{V,\,YbFO}$ and the mean value of the vertical strain distributions ($<\beta_{\perp,YbFO}>$) of the YbFO mosaic blocks can be derived (Mosaicity section of Table 6-1). The $L_{V,\,YbFO}$ values were found to be 81.8 ± 5 nm for YbPt_Th0nm and 100.35 ± 5 nm for YbPt_Th70nm which is comparable to the respective film thicknesses as measured by TEM. This indicates that the YbFO crystal extends across the entire film thickness.

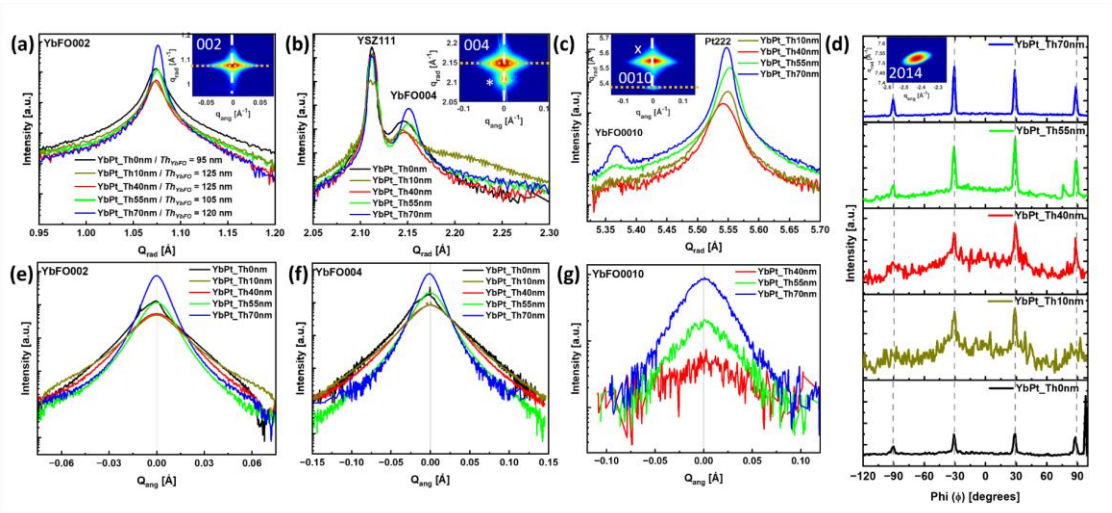

Figure 6.4: (a, b, c) And (e, f, g) are the comparison of the radial and the angular diffraction profiles which correspond to Yb_PtTh0nm, Yb_PtTh10nm, Yb_PtTh40nm, Yb_PtTh55nm and Yb_PtTh70nm samples for the reflections YbFO002, YbFO004 and YbFO0010 respectively. (d) Layout of the azimuthal scans I (Φ) of the asymmetric reflection YbFO2014 for Yb_PtTh0nm, Yb_PtTh10nm, Yb_PtTh40nm, Yb_PtTh55nm and Yb_PtTh70nm ordered from the bottom to top panel, respectively. For magnified version, refer to Figure A-24[241].

For other samples, such as YbPt_Th40nm and YbPt_Th55nm, $L_{V,\,YbFO}$ was found to be less than the film thickness Th_{YbFO} determined by TEM which suggests greater structural discrepancies. These discrepancies were further examined in relation to the film characterization and mosaicity sections. The WH approach also enabled the quantification of radial broadening ($FWHM_{rad}$) due to the vertical size ($L_{V,\,YbFO}$) and strain contributions ($<\beta_{\perp,YbFO}>$) which were notably pronounced in samples without a Pt underlayer as shown in Figure 6.5a and 6.5b. It is notable that the mean vertical strain value for YbPt_Th0nm was $<\beta_{\perp,YbFO}>$ = 3.95E-3 which is significantly higher than for YbPt_Th70nm at $<\beta_{\perp,YbFO}>$ = 1.82E-3. This underlines an improvement in the YbFO layer quality with an optimal Pt underlayer thickness Th_{Pt}. Furthermore, the degree of misorientation (α_{YbFO}) and the mean lateral size ($L_{H,\,YbFO}$) of YbFO crystal mosaic blocks were also derived for each sample and compared under Mosaicity in Table 6-1. The α_{YbFO} values serve as indicators of the defect density within the YbFO layer, and lower values would reflect a better crystal quality. The increased $L_{H,\,YbFO}$ for YbPt_Th70nm at 571.2 ± 5 nm, in comparison to 218.2 ± 5 nm for YbPt_Th40nm, suggests a reduction in the number of grain boundaries and an amelioration in the

continuity of the crystal structure for the YbPt_Th70nm sample. This supports that the Pt underlayer plays a crucial role in developing the structural integrity and properties of the subsequent YbFO films.

In conclusion, the crystal quality of YbFO is significantly improved when the Pt thickness is 70 nm. This is evidenced by a notable decrease in $FWHM_{ang}$ and a reduction in the number of grain boundaries. These improvements are associated with the expansion of the $L_{H,\,YbFO}$ and a decrease in the degree of misorientation. Such structural characteristics were not achieved with Pt thicknesses below 55 nm.

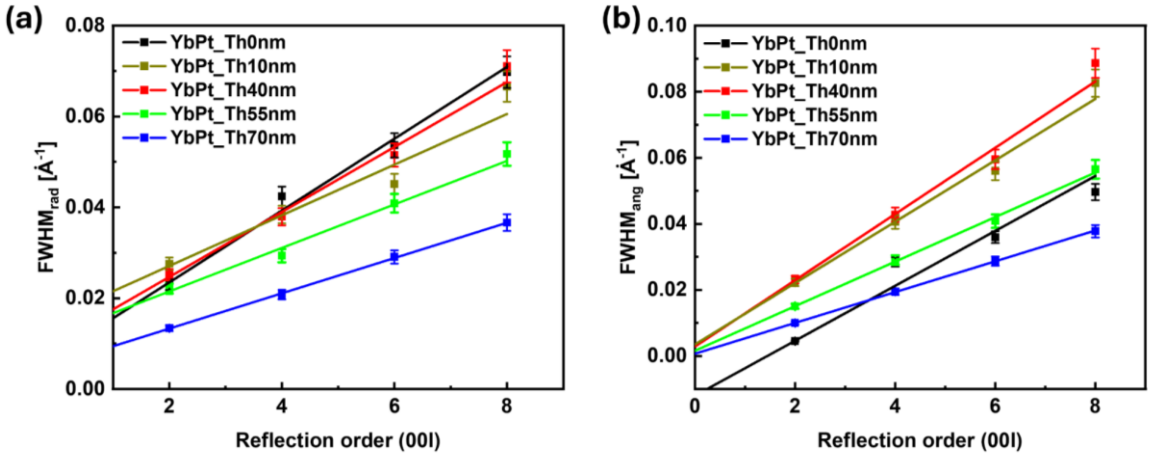

Figure 6.5: Variation of the $FWHM_{rad}$ (a) and $FWHM_{ang}$ (b) with the reflection order 00l for Yb_PtTh0nm, Yb_PtTh10nm, Yb_PtTh40nm, Yb_PtTh55nm and Yb_PtTh70nm samples for the determination of the mosaicity parameters[241].

Figure 6.6 presents TEM cross-section images of the YbPt_Th0nm, YbPt_Th40nm, YbPt_Th55nm, and YbPt_Th70nm samples. The aim is to evaluate the influence of the Pt underlayer quality on the microstructure of subsequently grown YbFO films in comparison with the YbPt_Th0nm sample without a Pt underlayer. The TEM images enabled the measurement of the Pt and YbFO layer thicknesses Th_{Pt} (TEM) and Th_{YbFO} (TEM), respectively, as listed in Table 6-1. The continuous filling of the Pt layer in the YbPt_Th70nm sample (Figure 6.6d0) leads to a uniform YbFO layer thickness with negligeable thickness fluctuations, Th_{YbFO} (TEM) = 95 ± 5 nm, similar to that of YbPt_Th0nm.

One can reveal a remarkable improvement in the quality of the YbFO layer in YbPt_Th70nm by comparing it with YbPt_Th0nm. This is well argued by the reduction of the degree of misorientation (α_{YbFO} = 0.93 ± 0.05 Å) and the vertical strain ($<\beta_{\perp,YbFO}>$ = 3.95E-3 ± 0.5E-4). The promoted quality of YbFO film is evidenced by the distinct contrast differences observed between the TEM images of YbPt_Th0nm and YbPt_Th70nm (Figure 6.6a0 and Figure 6.6d0). Despite comparable YbFO layer thicknesses, the diffraction intensities of reflections such as YbFO002 and YbFO004 are significantly stronger in YbPt_Th70nm compared to YbPt_Th0nm, as evidenced by Figure 6.1a and Figure 6.4a to 6.4c.

Furthermore, intermediate Pt underlayer thicknesses (10, 40, and 55 nm) were also studied, with TEM analyses specifically performed on the YbPt_Th40nm and YbPt_Th55nm samples (Figure 6.6b0 to 6.6b4, and 6.6c0 to 6.6c3). The morphological differences due to hillock formation were more pronounced in the YbPt_Th40nm sample. TEM images of Figure 6.6b0 showed significant fluctuations in the Pt film thickness and revealed hillocks (highlighted by magenta arrow). In contrast, the YbPt_Th55nm sample displayed a more uniform Pt layer without hillocks (Figure 6.6c0) which indicates a better layer continuity and reduced structural defects.

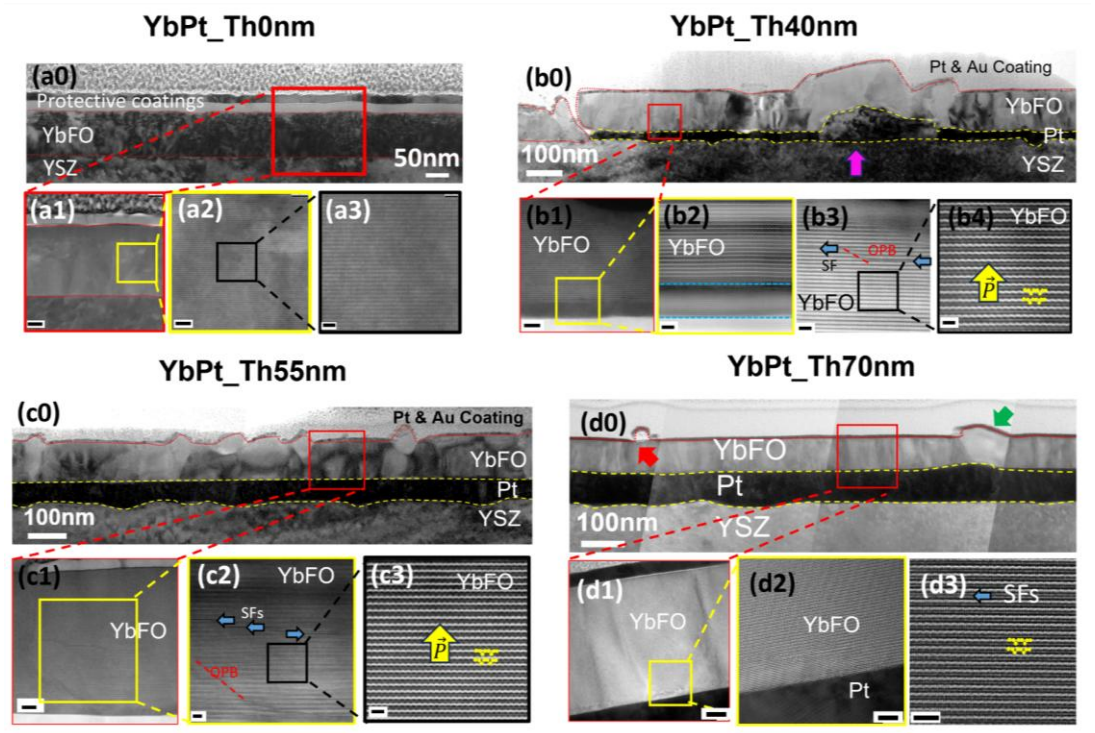

Figure 6.6: (a0, a1, a2, a3) TEM images for YbPt_Th0nm where (a0) image is the overview TEM with the lowest magnification and scale bar of 50 nm, (a1) image corresponds to the red rectangular region drawn in (a0), (a2) image corresponds to the yellow square drawn in (a1) and (a3) is the high magnification images of the black rectangular region shown in (a2). (b0, b1, b2, b3, b4) TEM images for YbPt_Th40nm where (b0) image is the overview TEM with the lowest magnification and scale bar of 100 nm, (b1) image corresponds to the red rectangle region drawn in (b0), (b2) image corresponds to the yellow square drawn in (b1) and (b4) is the high magnification images of the black rectangular region shown in (b3). (c0, c1, c2, c3) TEM images for YbPt_Th55nm where (c0) image is the overview TEM with the lowest magnification and scale bar of 100 nm, (c1) image corresponds to the red rectangular region drawn in (c0), (c2) image corresponds to the yellow square drawn in (c1) and (c3) is the high magnification images of the black rectangular region shown in (c2). (d0, d1, d2, d3) TEM images for YbPt_Th70nm where (d0) image is the overview TEM with the lowest magnification (d1) image corresponds to the red rectangular region drawn in (d0), (d2) image corresponds to the yellow square drawn in (d1) and (d3) is the high magnification images of the black rectangular region shown in (d2). Scale bars of (a1), (a2) and (a3) are 25 nm, 5 nm and 2 nm respectively. Scale bars of (b1), (b2), (b3) and (b4) are 5 nm, 2 nm, 2 nm and 1 nm respectively. Scale bars of (c1), (c2) and (c3) are 10 nm, 5 nm, and 1 nm respectively. Scale bars of (d1), (d2) and (d3) are 10 nm, 5 nm and 2 nm, respectively. For magnified version, refer to Figure A-25[241].

HRTEM images provide further understanding upon the Pt underlayer quality on the microstructure of the YbFO layer. For instance, in YbPt_Th40nm the presence of stacking faults and out-of-phase boundaries are visible near the smeared interface with the Pt underlayer (Figure 6.6b1,

6.6b2, 6.6b3) which correlates with higher vertical strain and misorientation values. This contrasts with YbPt_Th55nm at which improvements in Pt layer quality reduces these defects (shown in Figure 6.6c3). The comprehensive results from XRD and TEM underlines the critical role of the Pt underlayer quality. A sufficient thickness, represented by $Th_{Pt} > 55$ nm, is essential for reducing the defect density and enhances the structural integrity and crystal quality of overlying YbFO films. Optimization of the Pt underlayer, particularly at $Th_{Pt} = 70$ nm, has been shown to significantly improve the crystal quality of YbFO which is an optimal condition for subsequent multiferroic device applications.

The study of the YbFO microstructure using HRTEM provides a comprehensive understanding of the impact of the Pt underlayer microstructure. When the Pt thickness is not optimal, it suffers from discontinuity and hillock formation, which leads to disturbances in the YbFO crystal quality and the formation of defects that inhibit ferroelectric performance. However, outside the defect regions, ferroelectric domains were clearly visualized.

6.4 Magnetic properties of YbFO layers dependent on the bottom electrode thickness

Magnetization measurements were conducted on the samples YbPt_Th0nm, YbPt_Th10nm, YbPt_Th55nm, and YbPt_Th70nm by using the SQUID device. OOP magnetization hysteresis curves were recorded for each sample at various temperatures, specifically at 2 K, 10 K, 20 K, 30 K, 50 K, 100 K, 150 K, and 300 K. For each sample, the OOP curves of the saturation magnetization ($M_{s\perp}$), remanent magnetization ($M_{r\perp}$) and OOP coercivity ($H_{c\perp}$) can be derived and were plotted as a function of the temperature. This is compared in Figure 6.7b, 6.7c, and 6.7d, respectively. Figure 6.3b illustrates a non-linear increase in $M_{s\perp}$ with Th_{Pt} at each temperature, except YbPt_Th0nm. As illustrated, the OOP magnetic hysteresis loops at $T = 2$ K are presented in Figure 6.7a. It can be observed that $M_{s\perp}$ of YbPt_Th0nm and YbPt_Th70nm are slightly different, while YbPt_Th10nm and YbPt_Th55nm exhibit lower values due to the imperfections in the YbFO layer revealed by the structural study. The inset in Figure 6.7a provides a magnified view of the hysteresis loops which clearly shows the variations in $M_{r\perp}$ among the different samples. It is important to note that hysteresis effects were not detected in any of the samples above $T = 100$ K. This findings are in accordance with previous studies on the magnetic properties of YbFO [137,230,231,235].

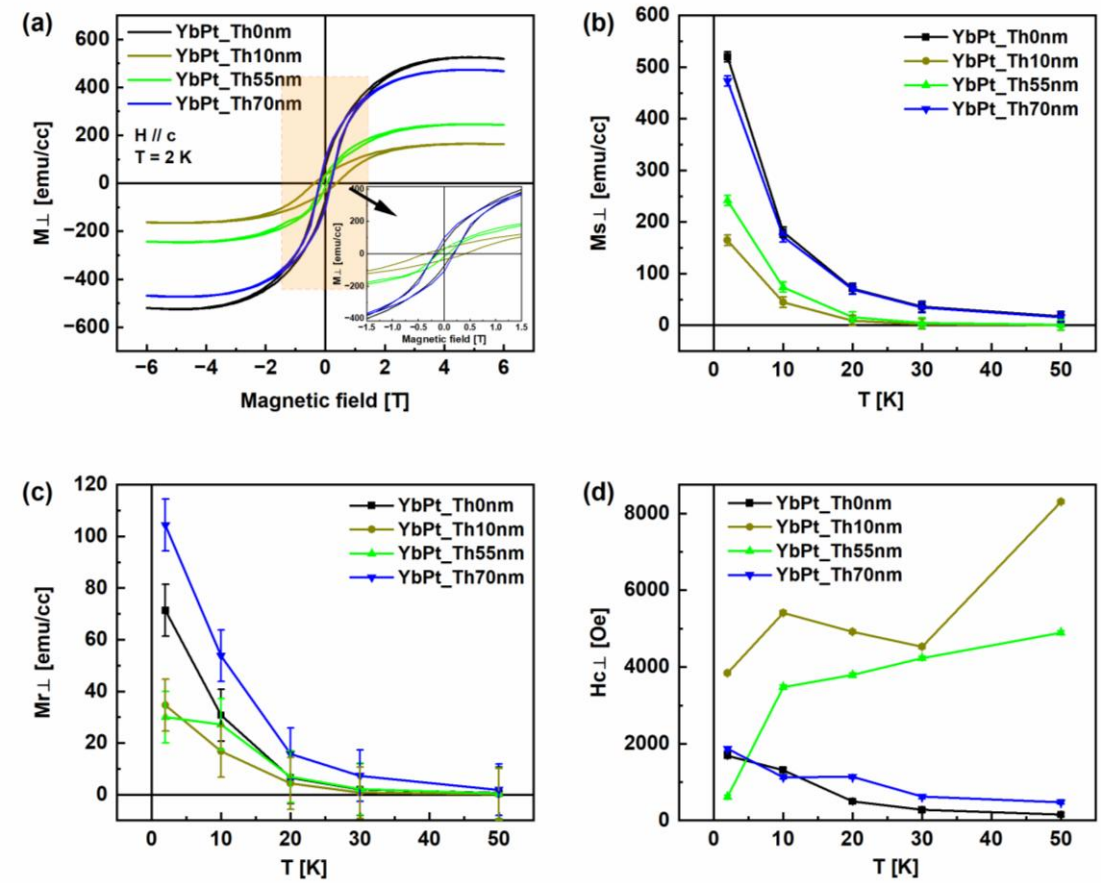

Figure 6.7: (a) Out-of-plane (OOP) magnetization hysteresis loops measured at 2K for an applied field up to 6 Tesla for the YbPt_Th0 nm, YbPt_Th10 nm, YbPt_Th55 nm and YbPt_Th70 nm samples. Dependence of the magnetization at saturation $M_{s\perp}$ (b), remanent magnetization $M_{r\perp}$ (c) and perpendicular coercivity $H_{c\perp}$ on the temperature T for the YbPt_Th0 nm, YbPt_Th10 nm, YbPt_Th55 nm and YbPt_Th70 nm samples[241].

At low temperatures, the total magnetic moment $M_{s\perp}$ is composed of contributions from both the Yb^{3+} and Fe^{3+} sites and their interactions (Fe-Fe, Fe-Yb, and Yb-Yb). The initial order of the Fe^{3+} spins occurs through Fe-Fe interactions followed by the polarization of paramagnetic Yb^{3+} sites and by the exchange field from Fe^{3+} through Fe-Yb interactions. Finally, the long-range order of Yb^{3+} is established through Yb-Yb interactions[230,235,243]. Based on the formalism proposed by Cao et al.[243], the total magnetization can be expressed as follows:

$$M = M_{Fe} * \left(1 + \frac{\chi_{Yb} * \Gamma_{YbFe}}{\mu_{Yb}}\right) + \chi_{Yb} * H \qquad (6\text{-}5)$$

The molecular field of the Yb-Fe interaction, denoted by Γ_{YbFe}, is a function of the external applied field, H, the susceptibility, χ_{Yb}, and the magnetic moment of Yb, μ_{Yb}.

Figure 6.7b and Figure 6.7c demonstrates an increase in the magnitude of $M_{s\perp}$ and $M_{r\perp}$ as the temperature decreases, regardless of Th_{Pt}. This increase becomes more rapid when the temperature drops below 20 K which indicates a significant contribution due to the spin order of Yb^{3+} induced by the molecular field of Fe^{3+}. A similar behavior has been previously reported for YbFO grown on YSZ(111) without an underlayer[235]. In earlier studies, the temperature dependences of $M_{s\perp}$ and $M_{r\perp}$ were not discussed in relation to the effect of the buffer layer which is the focus of this work.

Figure 6.7b illustrates the magnetization-temperature dependence which reveals a significant influence of Th_{Pt} at low measured temperatures (T = 2 K, 10 K). The behavior of $M_{s\perp}$ against the temperature was found to be comparable for the samples YbPt_Th0nm and YbPt_Th70nm. However, the $M_{r\perp}$ (H = 0) was found to be significantly enhanced by optimizing the quality of the YbFO layer on Pt in the case of YbPt_Th70nm, as illustrated in Figure 6.7c. From Equation (6-5) 5 at H = 0, the total moment ($M_{r\perp}$) is dependent on the molecular field of the Yb-Fe interaction (Γ_{YbFe}) as well as on the magnetic moment (M_{Fe}). The rise of $M_{r\perp}$ for YbPt_Th70nm is correlated with the strong Yb-Fe spin interactions which are influenced by the quality of the atomic arrangement. Figure 6.6a0 to 6.6a3 reveal a disturbance in the atomic arrangement that could degrade the strength of Yb-Fe interactions and explain the reduction in $M_{r\perp}$ for YbPt_Th0nm. Conversely, defects such as stacking faults and grain boundaries can also disturb spin interactions and reduce the effects of moments. Furthermore, the reduced remanent $M_{r\perp}$ in the case of YbPt_Th10nm and YbPt_Th55nm can be explained by the presence of defects (see Figure 6.7b, 6.7c). Moreover, the lateral and vertical grain boundaries revealed by TEM in Figure 6.6c0 for YbPt_Th55nm exhibit a considerable influence on the coercivity $H_{c\perp}$ (see Figure 6.7d). Despite the high degree of misorientation in YbPt_Th0nm, the coercivity values $H_{c\perp}$ were comparable to those of YbPt_Th70nm which indicates a reduced number of phase boundaries in YbPt_Th0nm. This is demonstrated by the TEM image in Figure 6.6a0.

Temperature-dependent magnetization curves such as zero field cooling (ZFC) and field cooling (FC) were obtained for the samples YbPt_Th0nm, YbPt_Th55nm, and YbPt_Th70nm (Figure 6.8a to 6.8f). The ZFC and FC curves were recorded at two applied fields, H = 100 Oe and 2000 Oe, in the OOP direction with H parallel to the c-axis. The thermo-magnetic irreversibility temperature (T_{irr}) is defined as the temperature at which the ZFC and FC curves bifurcate[244]. The bifurcation temperature between the ZFC and FC curves can be considered as a magnetic ordering temperature, T_{irr}. The degree of irreversibility ΔM(T) is defined as the difference between the ZFC and FC plots at a specific temperature T and is represented by $\Delta M(T) = M_{FC} - M_{ZFC}$.

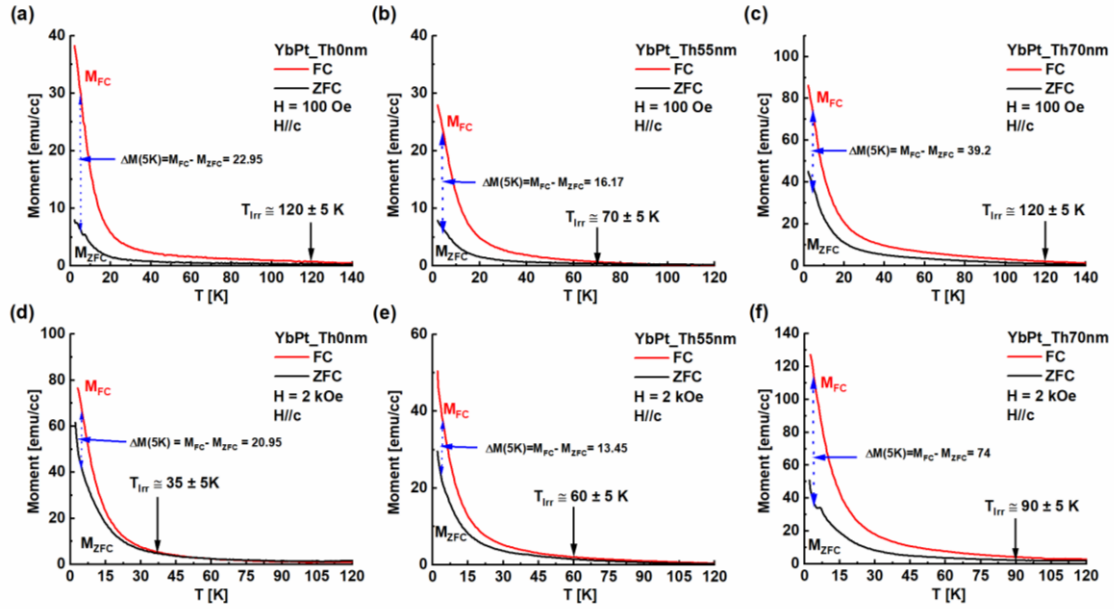

Figure 6.8: Zero field cooling (ZFC) and field cooling (FC) curves, respectively, recorded for YbPt_Th0 nm, YbPt_Th55 nm and YbPt_Th70 nm samples with an applied field H = 100 Oe (a, b, c) and H = 2000 Oe (d, e, f). For magnified version, refer to Figure A-26[241].

An exemplary ΔM(5 K) was determined for comparison purposes, as shown in graphs in Figure 6.8. The magnitude of the irreversibility ΔM between M_{FC} and M_{ZFC} is argued to be a measure of the magnetic anisotropy in the film[245]. Figure 6.8 shows that for $T < T_{irr}$ M_{FC} continuously increased with the decrease in temperature which indicates a magnetic anisotropy in the YbPt_Th0nm, YbPt_Th55nm, and YbPt_Th70nm samples. On the contrary, if the anisotropy was weak in the YbFO films M_{FC} would remain constant. However, this is not the case.

Furthermore, for YbPt_Th0nm the magnitude of bifurcation was found to be ΔM(5 K) ≈ 23 and 21 at applied fields of H = 100 Oe and 2000 Oe, respectively. This indicates that the irreversibility does not strongly depend on the applied field (see Figure 6.8a and 6.8d). This also applies to YbPt_Th55nm, where ΔM(5 K) varies slightly with H, as illustrated by Figure 6.8b and 6.8e. Conversely, the irreversibility ΔM was stronger in the case of YbPt_Th70nm and varied from ΔM ≈ 39.2 to 74 as the applied field H was changed from 100 to 2000 Oe. This can be interpreted as a remarkable difference in the magnetic anisotropy of YbPt_Th70nm compared to YbPt_Th0nm and YbPt_Th55nm which can be attributed to the interfacial differences induced by the Pt underlayer, despite the similarities recorded in the temperature-dependent $M_{s\perp}$ and temperature-dependent $H_{c\perp}$.

Figure 6.8 illustrates that T_{irr} is dependent on the applied field H in the case of YbFO. A comparable phenomenon was observed by Sahu et al. in the case of a $ZnFe_2O_4$ thin film[244]. The measured T_{irr} of approximately 120 K at H = 100 Oe for the YbPt_Th0nm and YbPt_Th70nm samples is consistent with the previously recorded Neel temperature T_N of approximately 125 K[137,231]. However, the measured T_{irr} at H = 2000 Oe was found to be T_{irr} ≈ 35, 60, and 90 K ± 5 K for the

YbPt_Th0nm, YbPt_Th55nm, and YbPt_Th70nm samples, respectively. The transition temperature, $T_{irr} \approx 90$ K ± 5 K, was found to be lower than the value recorded by Jeong et al. [231] ($T_N \approx 120$ K in the case of YbFO films with a thickness of 60 nm grown on Pt(111)/Al_2O_3(0001), where Pt(111) was sputtered and no information was provided about the thickness of the Pt bottom electrode).

A detailed investigation revealed that the structural features of the Pt underlayer significantly influence the magnetic properties of YbFO, particularly in relation to temperature. Achieving an optimal Pt underlayer thickness has markedly improved the crystal quality of YbFO, preventing disturbances in spin interactions caused by atomic arrangement irregularities, as observed in the Yb_Pth0nm sample. It can be concluded that the high quality of the Pt underlayer film, in terms of morphology and homogeneity, achieved in the Yb_PtTh70nm sample, enables superior $M_{s\perp}$, $M_{r\perp}$, and high T_{irr}, in comparison to samples with Pt underlayer thicknesses below 70 nm.

6.5 Summary and conclusions

The ferroelectric characterization of YbFO necessitates the deposition of a bottom electrode, such as Pt as in this work. Up to date, there is a lack of investigations which addresses the optimization process of the Pt bottom electrode, and the resulting effects if the thickness is not at an optimum. This gap extends to how the Pt underlayer impacts not only the ferroelectric properties but also the magnetic properties and therefore the multiferroicity character of YbFO. This work aimed to investigate the influence of the Pt underlayer thickness on the film morphology, crystal structure, and mosaicity of YbFO, as well as on the magnetization parameters which include $M_{s\perp}$, $M_{r\perp}$, $H_{c\perp}$, and T_{irr}.

The results demonstrated that an increase in Th_{Pt} leads to an improvement in the quality of the YbFO layer. The findings were obtained by combining data from HRTEM and HRXRD. These observations revealed a disturbance in the atomic arrangement of the crystal for the YbPt_Th0nm sample. It is necessary to achieve an optimum Th_{Pt} beyond 55 nm to develop a continuous and homogeneous Pt underlayer which ameliorate the mosaicity of YbFO by reducing the number of phase boundaries and stacking faults. The objective of the Pt underlayer is to improve the epitaxial relationship between the YbFO and the YSZ(111) substrate, to serve as a conductive bottom electrode and to maintain or improve the magnetic properties compared to YbFO layers deposited directly on the YSZ(111) substrate.

Those investigation demonstrated that using a high-quality Pt underlayer with an optimum thickness would also contribute to the enhancement of magnetic properties. It was observed that there was an increase in $M_{r\perp}$ and the magnitude of the bifurcation between M_{FC} and M_{ZFC} which indicates that YbFO with a measurable magnetic anisotropy was deposited in the YbPt_Th70nm sample compared to the YbPt_Th0nm sample which both possess the same YbFO layer thickness ($Th_{YbFO} = 95 \pm 5$ nm).

Table 6-1: Summary of the main parameters derived from diffraction and microscopy analysis methods and organized in the following sections: PLD growth conditions, film characterization, film morphology, crystal structure and mosaicity. NA: Not applicable, (C): Compressive[241].

PLD growth conditions	**YbPt_ Th0nm**	**YbPt_ Th10nm**	**YbPt_ Th40nm**	**YbPt_ Th55nm**	**YbPt_ Th70nm**
Number of shots Nsh_{YbFO}	20000	20000	20000	20000	20000
Growth temperature $T_{g,YbFO}$ [°C]	900	900	900	900	900
Number of shots Nsh_{Pt}	NA	1647	8235	12350	16470
Growth temperature $T_{g,Pt}$ [°C]	NA	900	900	900	900
Film characterization					
Th_{YbFO} (XRR) [nm]	95 ± 5	128.61 ± 5	125.8 ± 5	105.6 ± 5	120 ± 5
Th_{Pt} (Mass density) [nm]	NA	13.67 ± 5	49.08 ± 5	50.87 ± 5	80.52 ± 5
Th_{Pt} (TEM) [min-max] <Th_{Pt} (TEM)> [nm]	NA	NA	[18-96] 33.6 ± 5	[50-68] 56.5 ± 5	[64-86] 75.16 ± 5
Th_{YbFO} (TEM) [min-max] <Th_{YbFO} (TEM)> [nm]	NA 94 ± 5	NA	[108-120] 114 ± 5	[103-117] 110 ± 5	NA 95 ± 5
Film morphology, degree of coverage [%]					
Yb_DoC (EDX) [%]	NA	86.36 ± 2	92.62 ± 2	93.83 ± 2	NA
DoC (BSE) [%]	100 ± 2	NA	95.34 ± 2	94.33 ± 2	NA
Crystal structure					
dspacing of YSZ $d(11\overline{2})_{YSZ}$ [Å]	2.0985 ± 0.0005	2.1002 ± 0.0005	2.1004 ± 0.0005	2.1004 ± 0.0005	2.1004 ± 0.0005
dspacing of Pt $d(11\overline{2})_{Pt}$ [Å]	NA	1.60280 ± 0.0005	1.6023 ± 0.0005	1.5944 ± 0.0005	1.5977 ± 0.0005
In-plane lattice parameter a_{YbFO} [Å]	5.9603 ± 0.0005	5.8685 ± 0.0005	5.8750 ± 0.0005	5.9167 ± 0.0005	5.9544 ± 0.0005
Out-of-plane lattice parameter c_{YbFO} [Å]	11.7086 ± 0.0005	11.7292 ± 0.0005	11.7192 ± 0.0005	11.7087 ± 0.0005	11.6990 ± 0.0005
Misfit $f_{YbFO/YSZ}$ [%]	-5.32 (C)	NA	NA	NA	NA
Misfit $f_{YbFO/Pt}$ [%] (Yb/4*Pt)	NA	-8.46 (C)	-8.34 (C)	-7.22 (C)	-6.83 (C)
Misfit $f_{Pt/YSZ}$ [%]	NA	-23.07 (C)	-23.16 (C)	-22.92 (C)	-23.37 (C)
In-plane residual strain $\varepsilon_{//,YbFO}$ [%]	-0.0115 ± 0.001	-0.0268 ± 0.001	-0.0257 ± 0.001	-0.0188 ± 0.001	-0.0126 ± 0.001
Out-of-plane plane residual strain $\varepsilon_{\perp,YbFO}$ [%]	0.0025 ± 0.0002	0.0042 ± 0.0002	0.0034 ± 0.0002	0.0025 ± 0.0002	0.0016 ± 0.0002

Table 6-1: Continued[241].

PLD growth conditions	**YbPt_ Th0nm**	**YbPt_ Th10nm**	**YbPt_ Th40nm**	**YbPt_ Th55nm**	**YbPt_ Th70nm**
Mosaicity					
Degree of misorientation α_{YbFO} [degree]	0.93 ± 0.05	0.99 ± 0.05	1.07 ± 0.05	0.8 ± 0.05	0.48 ± 0.05
Lateral size mosaic blocks $L_{H,YbFO}$ [nm]	NA	179.0 ± 5	218.2 ± 5	NA	571.2 ± 5
Vertical size mosaic blocks $L_{V,YbFO}$ [nm] (2xFWHM)	81.8 ± 5	39.35 ± 5	60.55 ± 5	52.7 ± 5	100.35 ± 5
Mean value vertical strain distribution $<\beta_{\perp,YbFO}>$ (2xFWHM)	$3.95x10^{-3}$ $\pm 0.5x10^{-4}$	$2.80x10^{-3}$ $\pm 0.5x10^{-4}$	$3.58x10^{-3}$ $\pm 0.5x10^{-4}$	$2.40x10^{-3}$ $\pm 0.5x10^{-4}$	$1.82x10^{-3}$ $\pm 0.5x10^{-4}$

7 Dependence of the structural and magnetic properties on the growth sequence in heterostructures designed by *h*-$YbFeO_3$ and $BaFe_{12}O_{19}$

7.1 Introduction

Apart from single phase multiferroics, magnetoelectric heterostructures have recently received immense attention due to the new discovered interfaces effects and the functionalities acquired by combining ferroelectric (FE) and ferromagnetic (FM) layers[246,247]. The heterostructures such as $SrBa_2Ta_2O_9$/BaM[248,249], $Ba_2EuFeNb_4O_{15}$/BaM[250,251], multilayers composed of BaM layers with $Pb(Zr,Ti)O_3$ (PZT)[252] or $(Ba,Sr)TiO_3$ (BST)[253,254,255] or $BaTiO_3$ perovskite layers[256] and multiferroic composite[257,258,259] are examples of magnetoelectric heterostructures. In this thesis the heterostructure was designed by combining a BaM layer as a FM layer with high anisotropy, high coercivity[107] for good perpendicular recording media applications at room temperature, and $YbFeO_3$ as hexagonal rare-earth ferrites which represent a FE layer at room temperature, and which exhibits antiferromagnetism at low temperatures[230]. Furthermore, room temperature ferroelectricity was confirmed for hexagonal-$YbFeO_3$ (YbFO) layers grown on Pt(111)/Al_2O_3(0001)[231] and YSZ (111) by PLD[235,243]. Additionally, YbFO was found to be as a canted antiferromagnet below the Neel temperature of around 125 K. It was carried out by measuring the temperature-dependent saturation magnetization after zero field cooling (ZFC) and field cooling (FC), respectively[137,231,235,238]. This results in weak ferrimagnetism because of the canted spin orientations towards the c-axis of the unit cell[137]. Recently, heterostructures based on YbFO were designed by using a FE/dielectric (DE) bilayer structure[238] which YbFO represents an improper ferroelectric material and $CoFe_2O_4$ a dielectric material to achieve the electrostatic energy tuning for the spontaneous FE polarization. In the latter case, the FE polarization was shown by the atomic arrangement of the rare-earth element by cross-sectional HAADF-STEM images at which the Yb atoms are placed in a way “two-up-one-down” or vica versa[238,260]. The occurrence of spontaneous FE polarization was attributed to the localization of electrons at atoms in a 'two-up' formation which results in an upward electrical field. Aside from its ferroelectric characteristics, Fu et al.'s explored the extent of the lattice misfit and the differences in thermal expansion coefficients across the interfaces of distinct heterostructure layers[233]. This study aimed to evaluate the microstructural strain in various layers, thus modifies the magneto-optical properties. Former investigations demonstrated that interface effects such as epitaxial strain[261], interface quality (i.e. defects, roughness, sharpness)[262,263,264] and interdiffusion/chemical intermixing[265,266] affected the resulting mag-

netic and/or electric properties in the magnetoelectric heterostructures[267,268]. This required an understanding of the structure-property interrelation which influences the magnetic interaction[269], spin reordering[270,271] and coupling across the interfaces between FM and AF bilayers[262,264,265,266,269,270,271]. FM/AF heterostructures are well-known for exhibiting the exchange bias (EB) phenomenon. This latter leads to a horizontal shift in the magnetic hysteresis loop along the applied field[280]. This results in higher remanence, particularly close to saturation, in the absence of an external magnetic field known as the zero-field state. This magnetic property has directed the way for technological advancements in magnetoresistance applications[272], such as MRAMs (Magnetic Random Access Memory)[273], and magnetic tunneling applications[272,274]. However, EB was attributed to the pinning effect of domains caused by the uncompensated surface spins of the AF layer[270]. In contrast, for a fully compensated AF surface, the AF spins align perpendicularly to those of the FM spins which results in minimal interfacial spin frustration[285]. Subsequently, this could increase Hc whereas EB is not detected. It was approved that EB coupling in multiple interfaces can be observed in cases which the heterostructure interface is rough and chemically mixed. In contrast, LSMO/BFO systems with a sharp and chemically distinct interface do not reveal any EB coupling[264,275,276,277,278,279,280,281]. To the best of ones knowledge, few studies explored the effect of the stacking order in heterostructure systems which was previously studied in $BaFe_{12}O_{19}/BaTiO_3$[256], $La_{0.7}Sr_{0.3}MnO_3/BiFeO_3$[264], $LaMnO_3/LaFeO_3$[265], and $LaMnO_3/LaNiO_3$ [282,256,264,265].

In this study, a FM BaM layer was combined with a canted AF and a room temperature ferroelectric YbFO layer, with two different growth sequences on YSZ (111). The variation of the crystal quality, microstructure, chemical compositions of the individual layers and the involved interfaces by using a combination of high-resolution microscopy and diffraction methods was investigated. In addition, we compared the temperature-dependent behavior of the magnetic properties for both stacking orders of heterostructure systems.

7.2 Experimental section

PLD growth

This chapter combines the previous results and the optimization of growth parameters for the single layers and bilayer systems. Two heterostructure systems, named M1 (YSZ/YbFO/BaM) and M2 (YSZ/BaM/YbFO), were grown by using PLD with two different stacking orders on a YSZ (111) substrate. The BaM and YbFO targets with a purity of 99.9 % and a YSZ (111) substrate with a miscut of α_M ± 0.3 degrees were obtained from Surface, Germany (surface.com). Prior to growth, the substrates were cleaned and annealed as described in Chapter 3. The individual BaM and YbFO layers of M1 and M2 systems were grown at T_g = 850 °C with an oxygen pressure of P_{O_2} = 400 mTorr, a target-substrate distance of *TS* = 40 mm, and the number of shots of *Nsh* = 10000. The laser frequency used for growth was *F* = 1 Hz, with an energy per pulse of 25mJ (1.5 J/cm^2) and a laser wavelength of 266 nm. All the growth parameters are summarized in the table below:

Table 7-1: PLD growth parameters and characterization methods used for investigation of M1 and M2 heterostructures.

Sample name	**M1 ($BaFe_{12}O_{19}/YbFeO_3/YSZ111$)**	**M2 ($YbFeO_3/BaFe_{12}O_{19}/YSZ111$)**
Growth temperature T_g	850 °C	850 °C
Ns_{BaM}	10000	10000
Nsh_{YbFO}	10000	10000
Oxygen pressure	400 mTorr for BaM and YbFO	400 mTorr or BaM and YbFO
Target-substrate distance *TS*	40 mm for BaM and YbFO	40 mm or BaM and YbFO
Laser frequency *F*	1 Hz for BaM and YbFO	1 Hz for BaM and YbFO
Energy per pulse Laser fluence	25 mJ (1.5 J/cm^2) for BaM and YbFO	25 mJ (1.5 J/cm^2) for BaM and YbFO
Interface layer type	No	No
Characterization methods	XRR, HRXRD_RSMs, TEM, HRTEM/EDX	XRR, HRXRD_RSMs, TEM, HRTEM/EDX

2D-HRXRD reciprocal space mapping

Theta/2Theta scans were performed by using a Rigaku SmartLab diffractometer with a Cu $K_{\alpha 1}$ (λ = 1.540593 Å) radiation monochromatized by means of a Ge (220) 2-bounce monochromator. The measurements were taken with an incident slit width of 0.5 mm and two receiving slits, 0.5 mm and 1.0 mm wide, positioned in front of a scintillation detector. 2D-HRXRD reciprocal space maps were recorded at the NANO beamline at the KIT light source in Karlsruhe Germany for different reflections of BaM and YbFO layers. 2D-HRXRD maps of symmetric and asymmetric reflections corresponding to the BaM and YbFO layers were measured by using a Mythen linear detector positioned at the corresponding Bragg diffraction angles and by rocking the sample around the Bragg angle. All the measurements carried out in the NANO beamline were performed with a beam energy of E = 15 keV and a wavelength λ of 0.826 Å. Additionally, the azimuthal scans, which correspond to the YbFO108 and BaM-1018 asymmetric reflections, were measured by rotating the samples of M1 and M2 around their surfaces normal.

The miscut measurement was conducted by using an Empyrean diffractometer, for different azimuths angles in the range of ϕ = [0 - 350 °] which the detector was positioned at the Bragg diffraction angle $2*Q_B$ of the symmetric YSZ111 reflection. The deviation $\Delta Q = (Q_{max} - Q_B)$ from the rocking curve were recorded for the crystal lattice plane (111) of YSZ which Q_{max} is the angle of the diffraction peak maximum. ΔQ_{XRD} derived from XRD as function of azimuthal angle ϕ is shown by red open circles in Figure A-27 for M1 and M2.

For each azimuthal angle ϕ = [0 -350 °], the inclination of the sample surface in the reflectivity region was measured. At these angles, the detector was positioned into the reflectivity exit angle which corresponds to the specular reflections. The deviation of the incidence angle with respect to the exit angle ΔQ_{XRR} was plotted with blue open circles in Figure A-27. The difference between ΔQ_{XRD} (ϕ) and ΔQ_{XRR} (ϕ) for each azimuthal defines the angle between the film surface and the

crystal lattice planes. These angles ΔQ_{XRD} (ϕ) and ΔQ_{XRR} (ϕ) were fitted by the function $\Delta Q(\phi)$=A*sin(ϕ - ϕ_0) and the amplitude A of the sinus function with respect to the miscut α of the substrate. The largest miscut α_M = 0.67º was measured for the substrate of the sample M2 while for M1 α_M = 0.08º.

2D-HRXRD maps were used to derive the angular broadening ($FWHM_{ang}$) of the diffraction profiles for symmetric reflections in BaM (BaM006, BaM0010, BaM0014, and BaM0016) and YbFO (YbFO004, YbFO006, YbFO008). Using the Williamson-Hall approach and assimilating that BaM and YbFO layers are composed of misoriented mosaic crystal blocks, the variation of the $FWHM_{ang}$ with the reflection order *00l* enables the determination of the misorientation degree (α). This enables us to deduce the crystal qualities of BaM and YbFO within the M1 and M2 heterostructures as a function of the stacking order. The analysis of X-ray data involved the coordinates determination of maximum peak intensities. These were used for the calculation of both, the out-of-plane and in-plane lattice parameters of the BaM and YbFO crystals, residual strains and lattice misfit among individual layers in both, the M1 and M2 heterostructures.

The lattice misfit $f^{M1}_{BaM/YbFO}$ between the BaM/YbFO (resp. YbFO/BaM) (Equation (7-1) to (7-4)) bilayers which corresponds to M1(resp. $f^{M2}_{YbFO/BaM}$) as well as at the substrate interface YbFO/YSZ (resp. BaM/YSZ) was calculated as follows Equations (7-1) to (7-4)):

$$f^{M1}_{BaM/YbFO}\,[\%] = \frac{a^{M1}_{BaM} - a^{M1}_{YbFO}}{a^{M1}_{YbFO}} * 100 \tag{7-1}$$

$$f^{M1}_{YbFO/YSZ}\,[\%] = \frac{a^{M1}_{YbFO} - 3\mathrm{d}(11\overline{2})_{\mathrm{YSZ}}}{3\mathrm{d}(11\overline{2})_{\mathrm{YSZ}}} * 100 \tag{7-2}$$

$$f^{M2}_{YbFO/BaM}\,[\%] = \frac{a^{M2}_{YbFO} - a^{M2}_{BaM}}{a^{M2}_{BaM}} * 100 \tag{7-3}$$

$$f^{M2}_{BaM/YSZ}\,[\%] = \frac{a^{M2}_{BaM} - 3\mathrm{d}(11\overline{2})_{\mathrm{YSZ}}}{3\mathrm{d}(11\overline{2})_{\mathrm{YSZ}}} * 100 \tag{7-4}$$

The magnitudes a^{M1}_{BaM}, (resp. a^{M2}_{BaM}), a^{M1}_{YbFO} (resp. a^{M2}_{YbFO}) and $\mathrm{d}(11\overline{2})_{\mathrm{YSZ}}$ are the in-plane lattice parameters of the BaM, YbFO and YSZ substrate, respectively.

The in-plane residual strains (i.e. $\varepsilon^{M1}_{YbFO//}$ and $\varepsilon^{M2}_{YbFO//}$) of the YbFO layer and (i.e. $\varepsilon^{M1}_{BaM//}$ and $\varepsilon^{M2}_{BaM//}$) of the BaM layer were determined for M1 and M2 heterostructures using Equations (7-5) to (7-8):

$$\varepsilon^{M1}_{BaM//} = \frac{a^{M1}_{BaM} - a^{FS}_{BaM}}{a^{FS}_{BaM}} \tag{7-5}$$

$$\varepsilon^{M1}_{YbFO//} = \frac{a^{M1}_{YbFO} - a^{FS}_{YbFO}}{a^{FS}_{YbFO}} \tag{7-6}$$

$$\varepsilon_{BaM//}^{M2} = \frac{a_{BaM}^{M2} - a_{BaM}^{FS}}{a_{BaM}^{FS}} \quad (7\text{-}7)$$

$$\varepsilon_{YbFO//}^{M2} = \frac{a_{YbFO}^{M2} - a_{YbFO}^{FS}}{a_{YbFO}^{FS}} \quad (7\text{-}8)$$

The out-of-plane residual strains ($\varepsilon_{YbFO\perp}^{M1}$, $\varepsilon_{YbFO\perp}^{M2}$) of the YbFO layer and ($\varepsilon_{BaM\perp}^{M1}$, $\varepsilon_{BaM\perp}^{M2}$) of the BaM layer were calculated by the following Equations (7-9) to (7-12):

$$\varepsilon_{BaM\perp}^{M1} = \frac{c_{BaM}^{M1} - c_{BaM}^{FS}}{c_{BaM}^{FS}} \quad (7\text{-}9)$$

$$\varepsilon_{YbFO\perp}^{M1} = \frac{c_{YbFO}^{M1} - c_{YbFO}^{FS}}{c_{YbFO}^{FS}} \quad (7\text{-}10)$$

$$\varepsilon_{BaM\perp}^{M2} = \frac{c_{BaM}^{M2} - c_{BaM}^{FS}}{c_{BaM}^{FS}} \quad (7\text{-}11)$$

$$\varepsilon_{YbFO\perp}^{M2} = \frac{c_{YbFO}^{M2} - c_{YbFO}^{FS}}{c_{YbFO}^{FS}} \quad (7\text{-}12)$$

$a_{BaM}^{FS} = 5.892$ Å, $c_{BaM}^{FS} = 23.183$ Å and $a_{YbFO}^{FS} = 5.9652$ Å, $c_{YbFO}^{FS} = 11.7020$ Å correspond to the lattice parameters of the BaM and YbFO bulks in the free standing states.

XRR

XRR was carried out by utilizing a Rigaku Smartlab diffractometer which emits $Cu_{K\alpha}$ radiation at a wavelength of 1.54056 Å. The collected data were evaluated by using the Parratt formalism developed for the analysis of multilayers with rough interfaces[176]. The fit model was adapted for the XRR curves of M1 and M2 and it comprised a series of layers: a rough YSZ substrate, a thin interlayer between the substrate and the primary layer. The first layer exhibits a rough interface, and a rough top layer. The fit process was performed by using a custom script based on the least-squares fit algorithm.

TEM

For the TEM measurement of the M1(BaM/YbFO/YSZ) and M2(YbFO/BaM/YSZ) heterostructure systems, cross-sectional specimens were prepared by FIB milling in an FEI Helios G4 dual-beam microscope. Prior to the FIB preparation, a thin gold layer was sputtered on the sample surface to prevent the M1 and M2 heterostructures from damage by the Ga^+-ion bombardment. Subsequently, a standard FIB preparation of TEM lamellae was realized which a Pt protection layer was deposited on top of the samples first. Then, coarse FIB milling was carried out at a primary ion energy of 5 keV. The lamellae were attached to Cu lift-out grids and finally polished by a Ga^+-ion beam with a low energy of 1 keV to minimize Ga^+ implantation and material amorphization. TEM investigations of the M1 and M2 were carried out on two different transmission

electron microscopes by possessing thermally assisted field emission cathodes (Schottky emitters). In more detail, an image-corrected 300 kV FEI Titan 80-300 microscope was used for a conventional TEM investigation of the general layer properties (e.g., layer thickness, crystal structure). The crystal structure and microchemistry of the interfacial regions and BaM as well as YbFO layers of the M1 and M2 heterostructures were investigated in detail by combined high-angle annular dark-field (HAADF) imaging in the STEM mode and energy-dispersive X-ray spectroscopy (EDX) at an accelerating voltage of 300 kV with a probe-corrected Thermo Fisher Themis 300 microscope. This microscope is equipped with a Super-X EDX detector (Thermo Fisher) which combines four SDDs. X-ray maps were recorded in the STEM mode with typical measurement times of about 10 to 20 min which a possible drift of the sample was automatically corrected by the cross-correlation of corresponding reference images. By employing the Velox software (Thermo Scientific), raw-data X-ray maps were quantified by using the thin-film approximation after Cliff-Lorimer[148] to obtain element-concentration maps and quantitative EDX line profiles. Moreover, the crystal-structure information was obtained by two-dimensional fast Fourier transformation of selected areas in atomically resolved STEM images.

VSM

Magnetic characterizations, both in-plane (IP) and out-of-plane (OOP), were conducted by utilizing a VersaLab vibrating sample magnetometer from Quantum Design, equipped to handle magnetic fields up to 2 Tesla and a sweeping rate (SR) of 10 Oe/s. Two distinct setups were employed: the standard mode for conventional OOP and IP measurements, which ranges from 50K to 400K, and a specialized VSM Oven setup for the Curie temperature measurement in the IP direction from 300K to 1000K by using a unique heating holder with the sample encased in copper foil.

Experiments were carried out on M1(BaM/YbFO/YSZ) and M2(YbFO/BaM/YSZ) systems at various temperatures: 50, 70, 100, 120, 150, 200, 250, 300, and 400 K. Key magnetic parameters were extracted from the IP and OOP magnetization loops which include the saturation magnetization ($M_{s//}(T)$, $M_{s\perp}(T)$), remanent magnetization ($M_{r//}(T)$, $M_{r\perp}(T)$), perpendicular and parallel squareness ($S_{\perp}(T)= M_{r\perp}(T) / M_{s\perp}(T)$ and $S_{//}(T) = M_{r//}(T) / M_{s//}(T)$), out-of-plane and in-plane coercivity fields ($H_{c\perp}(T)$, $H_{c//}(T)$), the coercivity ratio ($R_c(T)=H_{c//}/H_{c\perp}$), and the anisotropy field ($H_a(T)$).

An advanced method was utilized to determine the anisotropy fields ($H_a(T)$) which considers factors such as misalignment between the hard axis and the direction of the applied magnetic field, sweeping speed, domain structure and multiphase magnetism, as elucidated by Zehner et al.[283]. Average anisotropy fields ($H_a(T)$) for M1(BaM/YbFO/YSZ) and M2(YbFO/BaM/YSZ) were determined from the intersection of the extrapolation of the linear portion of the IP hysteresis magnetization curve with the OOP saturation magnetization level. This approach was applied to all hysteresis loops measured across the range of temperatures.

Additionally, the Curie temperature (T_c) of M1(BaM/YbFO/YSZ) and M2(YbFO/BaM/YSZ) systems was measured by monitoring the IP magnetic moment ($M_{//}$ where H is perpendicular to the c-axis). Zero field cooling (ZFC) and field cooling (FC) magnetization profiles were recorded parallel to the c-axis in the temperature range of 50 to 400 K, with applied fields (H) of 0 and 2000 Oe, respectively.

7.3 Characterization of the heterostructures M1 and M2

Figure 7.1a compares the diffraction patterns of M1 and M2 which include the reflections of BaM, YbFO, and the YSZ substrate. The schematic representation of the heterostructures M1 and M2 can be found in Figure 7.1h and Figure 7.1k. Both diffraction curves contain peaks for BaM (000l) and YbFO (000l), as well as reflections for YSZ (111) and YSZ (222) (marked by magenta stars). Additionally, 2D-HRXRD reciprocal space maps were recorded for BaM such as BaM006, BaM008, BaM0012, BaM0016 and YbFO reflections like YbFO002, YbFO004, YbFO008. The presence of high reflection orders, such as BaM0016 and YbFO008, justifies the c-axis orientation for both samples, M1 and M2 as well as the growth of hexagonal structures for the BaM and YbFO layers. The layer orientation is YSZ [111] // BaM [0001] // YbFO [0001] regardless of the stacking order. In the diffraction patterns, the reflections of BaM and YbFO cannot be resolved due to the small difference in the diffraction peak positions. The XRD pattern of sample M2 exhibits a higher background and diffuse scattering intensity than that of the M1 sample which may be caused by the higher defect concentration. In addition to the diffuse scattering, the intensities of the reflections are relatively lower in the case of M2. Figure 7.1f and Figure 7.1g depicts a combined RSMs of the BaM008 and YbFO0016 reflections. The lattice parameters of YbFO and BaM layers were calculated by using the Q-positions at the maximum intensities which were determined from HR-RSMs of the symmetric and asymmetric reflections. The results are displayed in Table 7-2. We found that the out-of-plane lattice parameter of BaM in M1 $c_{BaM}^{M1} = 23.25$ Å is lower than that of BaM in M2 $c_{BaM}^{M2} = 23.2942$ Å. This variation in the lattice parameter is also evident from the peak shift of the M2 towards a lower diffraction angle (see Figure 7.1a). Furthermore, the out-of-plane lattice parameter of YbFO in M1 $c_{YbFO}^{M1} = 11.693$ Å is slightly lower than that in M2, $c_{YbFO}^{M2} = 11.715$ Å. This can be related to the difference in the chemical compositions of the BaM and of YbFO layers generated by the growth sequence in the M1 and M2 heterostructures.

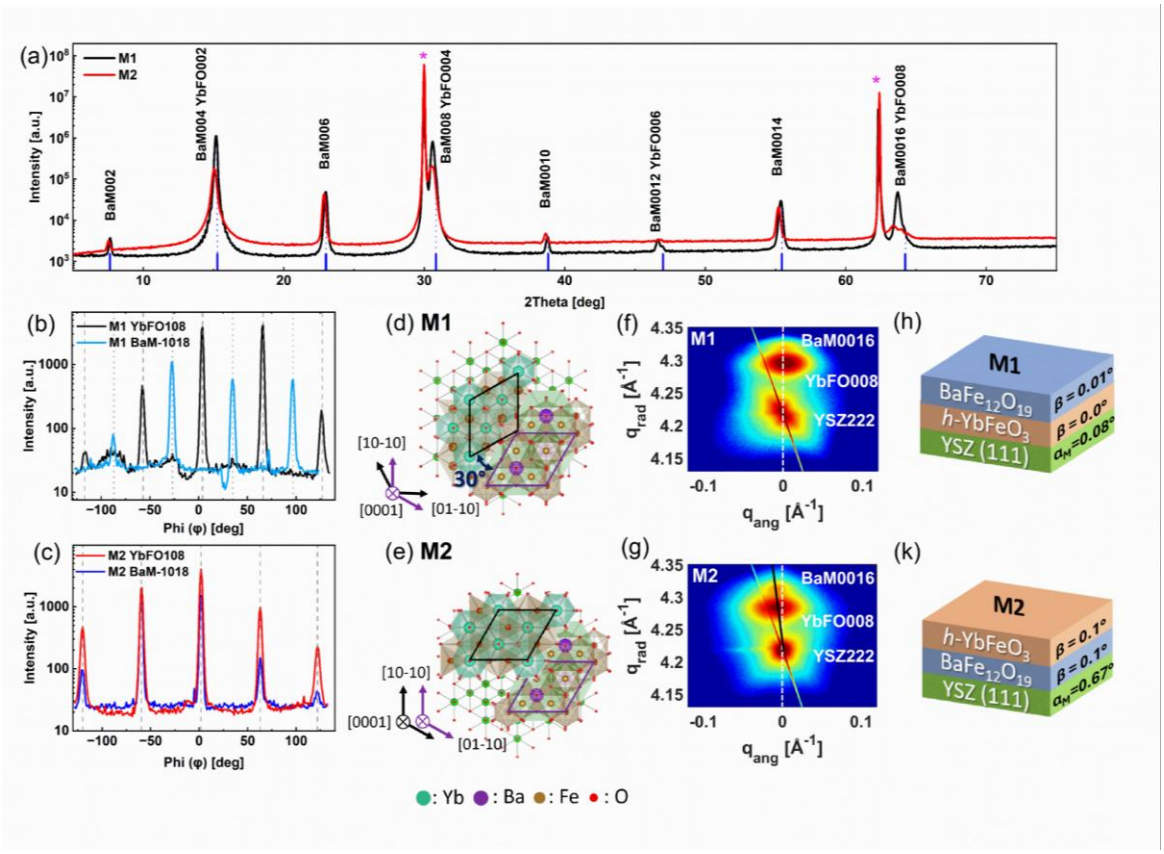

Figure 7.1: (a) Diffraction patterns of the heterostructures M1(BaM/YbFO/YSZ) (solid black curve) and M2(YbFO/BaM/YSZ) (solid red curve), (b), (c) Azimuthal scans of asymmetric reflection BaM (-1018) and YbFO (108) for M1 and M2, respectively. (d), (e) Visualization of the in-plane rotation relationship of the atomic layers which relate to the crystalline structures as it is simulated along [0001] for M1 and M2 respectively. (f), (g) 2D-HRXRD reciprocal space maps which contains the BaM(0016), YbFO(008) and YSZ(222) diffraction spots. (h), (k) Schematic presentation of the heterostructures M1(BaM/YbFO/YSZ) and M2(YbFO/BaM/YSZ) which possess two different stacking sequences together with the miscut and misalignment values noted on the schematic representation. For magnified view refer to Figure A-28[242].

The change of the stacking order between M1 and M2 strongly affects the interfacial lattice misfit between the individual layers. This results in a different residual strain in the individual layers. Furthermore, the lattice misfit at BaM/YbFO interface in M1 is $f_{BaM/YbFO}^{M1} = -3.56\,\%$, whereas the misfit at BaM/YSZ interface in M2 is $f_{BaM/YSZ}^{M2} = -5.3\,\%$ ($a_{BaM}^{M1} = 5.8151 \pm 0.001$ Å, $a_{BaM}^{M2} = 5.967 \pm 0.001$ Å). Residual strain values were calculated by using the bulk lattice parameter of BaM as a free-standing layer[284]. The in-plane residual strain of BaM changes from $\varepsilon_{BaM//}^{M1} = -1.3\,\%$ to $\varepsilon_{BaM//}^{M2} = 1.3\,\%$ (see Table 7-4). Although, the misfit values are not significantly different from each other, the residual strain of BaM varies from compressive to tensile.

The lattice misfit for YbFO layer is dramatically reduced from $f_{YbFO/YSZ}$ [%] = -4.42 % in M1 to $f_{YbFO/BaM}$ [%] = 0.35 % in M2 (Table 7-3). On the other side, the in-plane lattice parameters of YbFO layer range from a_{YbFO}^{M1} = 6.0221 ± 0.001 Å to a_{YbFO}^{M2}= 5.9881 ± 0.001 Å, with only slight

variations. Additionally, the in-plane residual strain also decreases from $\varepsilon_{YbFO//}^{M1}$ = 0.96% to $\varepsilon_{YbFO//}^{M2}$ = 0.39 % (refer to Table 7-4).

Figure 7.1b and Figure 7.1c displays the azimuthal scans which were obtained for BaM-1018 and YbFO108 reflections by rotating M1 and M2 samples about their surfaces normal. BaM and YbFO layers exhibit a 6-fold symmetry, as evidenced by the presence of reflections every 60 degrees. In Figure 7.1b, the reflection intensities indicate that the YbFO layer is rotated 30 degrees with respect to the BaM layer along the surface normal for sample M1. In Figure 7.1c, BaM and YbFO layers are well aligned with each other. For the M1 and M2 heterostructures, the in-plane rotation relationship of the individual layers is visualized in the Figures 6.1d and 6.1e by corresponding crystal-structure models simulated along the [0001] direction.

In comparison with M2 (Figure 7.1c) , for the M1 sample, the azimuthal scans of YbFO108 and BaM-1018 (Figure 7.1b) show comparable peak intensities. Furthermore, the decrease of reflections intensities for BaM-1018 at ϕ = 0° and ϕ = 120° during the M2 sample rotation may be attributed to a disturbance in the c-axis orientation (Figure 7.1c). This degree of misorientation is confirmed by the peak shift observed in the BaM0016 Yb008 reflections in Figure 7.1g.

Figure 7.1f and Figure 7.1g show that the peak maximum of the reflections in M1 are aligned along (111) of the YSZ substrate. In M2, the maximum of BaM0016 and YbFO008 peaks are aligned and slightly misoriented with respect to the YSZ (111) direction. This indicates that the diffraction planes of BaM and YbFO layers are inclined with respect to those of the YSZ (111) lattice planes. The derived inclination values of the layers are determined from the XRD reflections of the BaM and YbFO layers. The values are for M1 $\beta \cong 0°$, whereas for M2, it is about $\beta \cong$ 0.1° for both individual layers.

In order to investigate the cause of misalignment, the miscut of the substrates in M1 and M2 were measured and are presented the results in Figure A-27. One can find that α^{M1} = 0.08° and α^{M2} = 0.67°. This miscut could be also seen as surface steps at the BaM/YSZ interface visualized by the TEM images which are shown in Figure A-35 in the appendix. This inclination of the bilayer M2 with respect to YSZ(111) could be rather induced by the degree of substrate miscut. A more reliable determination of the true misalignment of the YbFO and BaM bilayers with respect to the YSZ(111) lattice planes normal would require the comparison of RSMs recorded for different azimuthal angles and fit sinusoidal functions, similarly to the miscut case.

Figure 7.2a and Figure 7.2b show a comparison between M1 and M2 of the angular diffraction profiles (i.e., along Q_x indicated by white dashed lines on RSMs in the insets) which correspond to the BaM0014 and YbFO006 reflections, respectively. Figure 7.2a shows that M1 has the largest angular broadening for the BaM0014 reflection compared to M2 which indicates a higher defect concentration in the BaM layer of M1. In Figure 7.2c and Figure 7.2e, the Williamson-Hall (WH) plots are given by the variation $FWHM_{ang}$ of the BaM and YbFO layer with the reflection order (00l). The $FHWM_{ang}$ values are extracted from the angular diffraction profile fits by a Pseudo-Voigt function of the BaM (006), (0010), (0014) and (0016) reflections and the reflections of YbFO (004), (006) and (008), respectively.

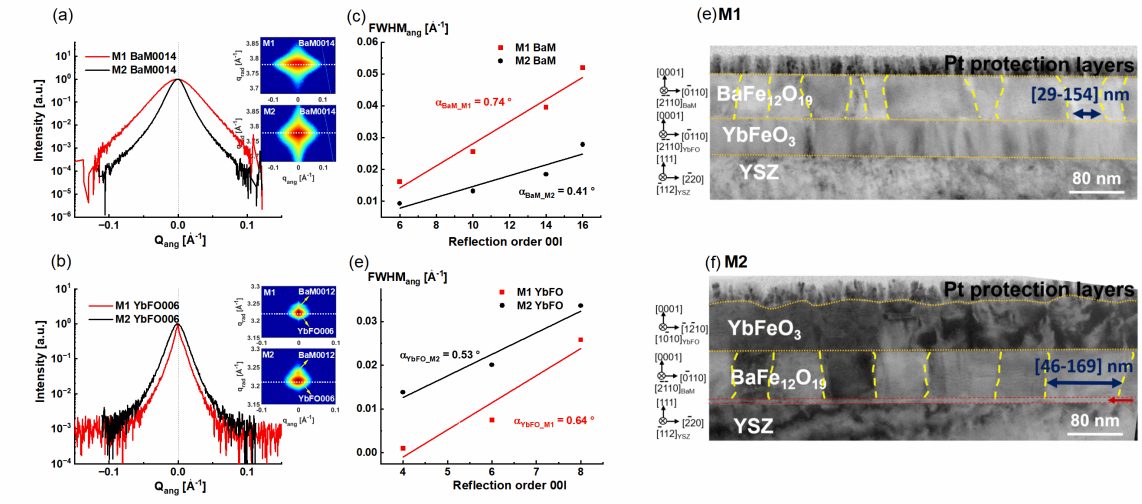

Figure 7.2: (a), (b) Comparison between the M1(BaM/YbFO/YSZ) and M2(YbFO/BaM/YSZ) heterostructures of the angular diffraction profiles of the BaM0014 and YbFO006 reflections, respectively. (c), (d) Comparison between M1 and M2 of variation of the full width half maximum of the corresponding angular broadening *FWHM*$_{ang}$ with the reflection order 00l for the BaM and YbFO layers, respectively. (e), (f) TEM cross-sections images of the M1 and M2, respectively, which indicate the phase boundaries by yellow dashed lines. For magnified view refer to Figure A-29[242].

It turns out that the degree of misorientation of mosaic blocks α_{BaM_M1} = 0.74° was higher for the BaM layer in M1 compared to the M2 heterostructures (α_{BaM_M2} = 0.41°) whereas BaM is directly grown on YSZ(111). The mosaicity of the YbFO layers in terms of being tilted are not affected by the change in the stacking order. In fact, the slope of WH for Yb reflections are found comparable, where α_{YbFO_M2} = 0.53° and α_{YbFO_M1} = 0.64°, Figure 7.2e.

Figure 7.2c and Figure 7.2f shows the HR-TEM images of M1 and M2 systems. Yellow dashed lines on the BaM layers are used to visualize the mosaic boundaries/mosaic blocks of the BaM layer. Orange dashed lines show the interfaces of both layers, and the red dashed lines in M2 indicate the interlayer which was formed at the interface BaM/YSZ. We deduce that the BaM layer in the M1 system has a higher number of phase boundaries which also means smaller lateral mosaic block sizes. The BaM layer of M1 is composed of blocks with mean lateral size of $<L_{//}>$ = 68 nm which varies between 29 and 154 nm while the BaM mosaic blocks of M2 have a mean lateral size of $<L_{//}>$ = 98 nm which varies from 46 to 169 nm. In conclusion, the TEM results are correlated with the finding derived from the comparison of the diffraction angular broadening (Figure 7.2a).

Figure 7.3a and Figure 7.3h show the micrographs of the M1 and M2 multiferroic systems which include the different orientations of the different individual layers such as YSZ, YbFO and BaM. For both M1 and M2 heterostructures, BaM and YbFO are grown along the (001) direction which is parallel to the YSZ (111) direction. There exists an approximately 2 nm thick transition layer from YSZ to YbFO instead, which will be discussed via chemical mapping. This transition layer may be the reason of a strain contrast in the HR-TEM images. Oppositely, YbFO has a sharp interface with the BaM layer in M2. The clear distinction of the interface YbFO/BaM in the M1

heterostructure is mostly due to the reduction of the misfit from $f^{M1}_{YbFO/YSZ}$= -4.42 % to $f^{M2}_{YbFO/BaM}$ = 0.35 %.

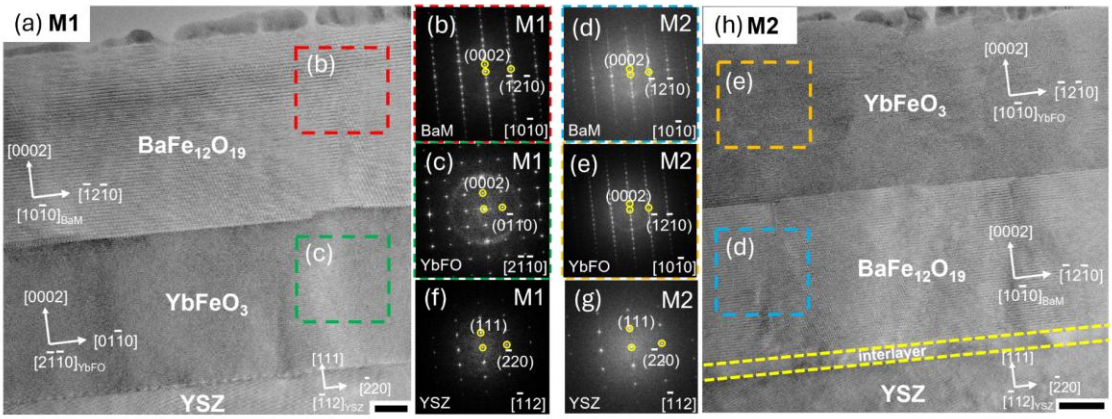

Figure 7.3: (a, h) TEM image of the M1(BaM/YbFO/YSZ) and M2(YbFO/BaM/YSZ) cross sections with the crystallographic orientation of the individual layers BaM, YbFO and YSZ. (b), (c), (f) Diffractograms which corresponds to M1(BaM/YbFO/YSZ) of the BaM layer drawn by red box in (a), of YbFO layer illustrated by green box (a) and of YSZ(111) substrate, respectively. (d), (e), (g) Diffractograms corresponding to M2(BaM/YbFO/YSZ) of the BaM layer drawn by blue box in (a), of YbFO layer illustrated by orange box (h) and of YSZ(111) substrate, respectively. The scale bars are in 20 nm for (a) and (h). For magnified view refer to Figure A-29[242].

The diffractograms of Figure 7.3c and Figure 7.3e correspond to the dashed green square in Figure 7.3a and to the orange square in Figure 7.3h for the YbFO layers in M1 and M2, respectively. They prove a change in the in-plane crystalline orientation of YbFO layer from [2-1-10] in the M1 to [10-10] in the M2 heterostructure. This indicates that the YbFO layer, grown on BaM(001) in M2, is twisted about 30° (± 60°) along the (001) direction with respect to the YbFO layer grown on YSZ(111) in M1 (Figure 7.3e and Figure 7.3c). In similar way, we compare the crystal structure and orientation of the BaM layer in the M1 and M2 diffractograms of Figure 7.3b and Figure 7.3d. It is obvious that the in-plane orientation of the BaM layer is not affected by the stacking order as it could be demonstrated by Figure 7.3a, Figure 7.3b) and Figure 7.3d, Figure 7.3h). However, the quality of BaM/YbFO in M1 and BaM/YSZ in M2 interfaces are different. TEM micrograph of M1 indicates a distinct BaM/YbFO interface which is accordance with the low misfit value $f^{M1}_{BaM/YbFO}$ [%] = -3.56 % while an interlayer was formed between the BaM layer and the YSZ substrate in M2 where $f^{M2}_{BaM/YSZ}$ [%] = -5.3 %.

HRTEM images of Figure A-35d and Figure A-35e, which correspond to M2 and M1, respectively, demonstrates the existence of a well resolved atomic step at the interfaces YbFO (AF)/BaM (FM) and BaM (FM)/YbFO (AF). This atomic step can induce a spin frustration at the AF/FM interface as it has been discussed by Chen et al.[285].

In order to evaluate the interfaces qualities and to determine the thickness of the layers and interlayers, we measured XRR curves for the M1 and M2 heterostructures as shown in Figure 7.4a. The results derived from the XRR curves fits are detailed in Table 7-5. A simple reflectivity model[102] was used to create mass density profiles for the bilayers which are depicted in Figure

7.4b. In order to enhance clarity, magnified mass density (ρ) profiles of the interfaces are presented in Figure 7.4c. The black profile in this representation corresponds to M1 while the red profile corresponds to M2. *Th* = 0 nm denotes the surface termination of the bilayer system.

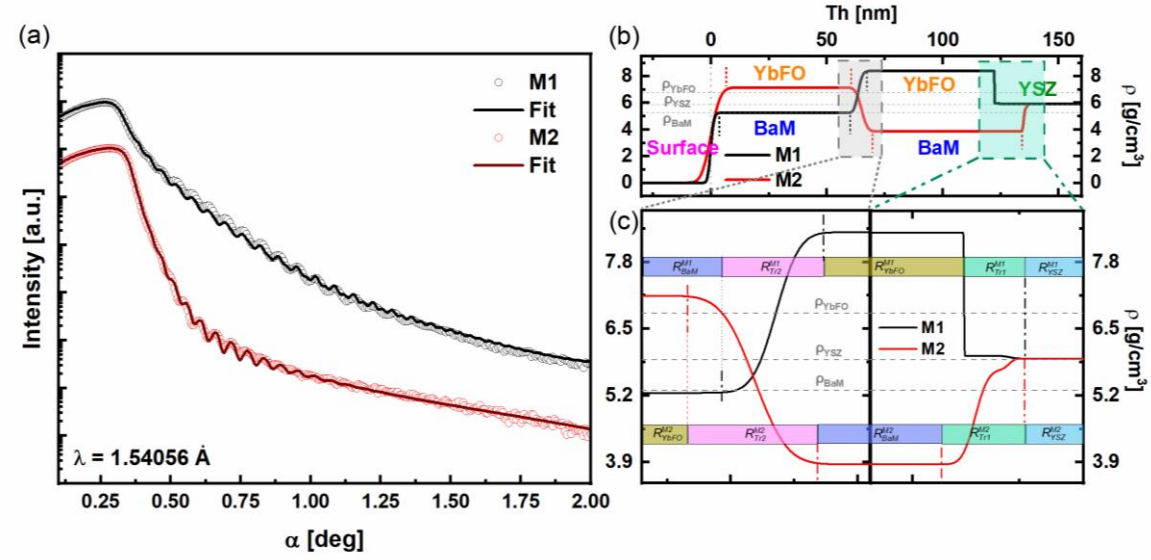

Figure 7.4: (a) Measured XRR curves (points) for and the obtained fits (lines) for M1 (black), M2 (red), and BaM (purple). The curves are vertically shifted for better visibility. (b) Density profiles obtained from the fits of M1 (black) and M2 (red). The insets (c) show the interface YSZ/first layer and the interface between layers respectively. The density profiles in the insets are shifted with respect to each other for better comparison of the interfaces. For magnified view refer to Figure A-31[242].

The model assumes a constant mass density distribution throughout the layers, with vertical dashed lines delimiting the layer thicknesses. The density variations between different layers of the heterostructures M1 and M2 indicate the presence of transition regions which the mass density deviates from the constant values. Figure 7.4b present mass density profiles for BaM, YbFO, and YSZ across the overall heterostructures thicknesses of M1 and M2. Furthermore, the mass densities of the targets $BaFe_{12}O_{19}$, YbFO, and YSZ(111) are given by ρ_{BaM} = 5.296 g/cm^3, ρ_{YbFO} = 6.8 g/cm^3, and ρ_{YSZ} = 5.92 g/cm^3, respectively, and are drawn by the horizontal grey dashed lines in Figure 7.4b. The transition regions which correspond to the interfaces with the YSZ(111) substrate (i.e. YSZ/BaM for M2, YSZ/YbFO for M1) and between the bilayers (BaM/YbFO for M1 and YbFO/BaM for M2) are highlighted by green and grey rectangles and are measured with a higher magnification for the thickness x-axis scale in Figure 7.4c.

When comparing the profiles of M1 and M2, it is evident that the first transition region from the substrate to the first layer is larger for M2 at BaM/YSZ (R_{Tr1}^{M2} = 3.95 nm) than for M1 at YbFO/YSZ (R_{Tr1}^{M1} = 2.81 nm). This indicates that the interdiffusion between YSZ and the BaM layer is more significant than that between YSZ and YbFO. Moreover, Figure 7.4c shows a sudden increase in the density profile in the R_{Tr1}^{M1} region and rather a gradual change in the mass density within the R_{Tr1}^{M2} region. Regarding the transition between the bilayers which is illustrated by the grey rectangle in Figure 7.4b and magnified in Figure 7.4c the mass density profiles show larger transition region in the case of M2 than in M1 (R_{Tr2}^{M2} = 10.29 nm and R_{Tr2}^{M1} = 8.19 nm).

Additionally, the mass density profiles reveal deviations of the individual layer densities from the theoretical values. In M1, the density of YbFO exceeds the theoretical density, as does the YbFO layer density in M2 does. However, it is worth noting that the YbFO density in M1 is higher than in M2. When comparing the mass densities of the BaM layers the BaM density in M2 is higher than in M1. It is interesting to observe that in the M2 system, the BaM density is lower than the theoretical density, which corresponds to the higher interdiffusion layer (R_{Tr1}^{M2}). Conversely, in the M1 system, the BaM density is higher than the theoretical density of BaM. This may indicate that the reduced density of the layers lacks certain elements, which have voids or an incomplete filling over the substrate surface.

In order to identify density variations and chemical transition zones, HR-STEM HAADF images and generated atomic resolution EDX maps were generated (see Figure 7.5). The HAADF image of the M1 system at the YbFO/YSZ interface (Figure 7.5a) shows a crystalline interlayer that is approximately 2-3 nm thick, marked by magenta dashed lines. The Yb atoms in the YbFO layer exhibit a 2up/1down configuration which is a characteristic of the ferroelectric metastable phase of hexagonal YbFO. Figure 7.5b and Figure 7.5c present diffractograms obtained by the FFT analysis of marked regions in Figure 7.5a. These diffractograms confirm the desired orientation and crystallographic alignment. The YSZ is oriented along the [111] direction, which promotes the metastable $P6_3cm$ YbFO layer to grow in the [0001] orientation.

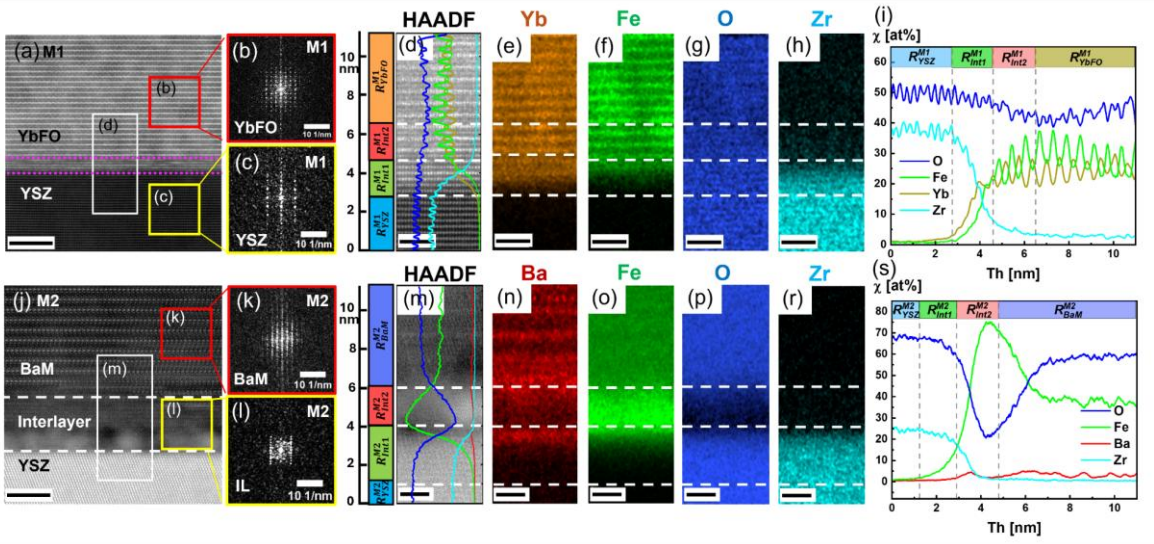

Figure 7.5: (a, j) High-resolution STEM HAADF images near the bilayer interface regions (YbFO/YSZ) and (BaM/YSZ) for M1 and M2 heterostructures, respectively. (b, c) Diffractograms corresponding to red and yellow rectangles drawn in BaM layer and YSZ substrate, respectively. (k, I) Diffractograms of the red and yellow rectangles drawn in BaM layer and YSZ substrate, respectively. The regions marked with white rectangles are the regions selected for the corresponding X-ray maps given in (d, e, f, g, h) for M1 and in (m, n, o, p, r) for M2, (i, s) comparison of the quantitative EDX line profiles for the elements O, Fe, Ba, and Yb for M1 and M2, respectively. Scale bars of (a, j) are 5 nm and of (d-h) and (m-r) are 2 nm in size. For magnified view refer to Figure A-32[242].

Figure 7.5d to 7.5h show the atomic resolution EDX maps for M1. These maps illustrate that the interfacial region consists of a mixture of chemical elements which belong to YSZ and YbFO and exhibit a gradient transition through the YbFO layer from the substrate. The elemental profiles of

O, Ba, Fe and Yb in Figure 7.5i reveals that the transition regions (R_{int1}^{M1} + R_{int2}^{M1}) correspond to the local region R_{Tr1}^{M1} estimated by mass density profiles of XRR curves. The values are listed in Table 7-5 whereas R_{Tr1}^{M1} = 2.81 nm from the XRR fit and R_{int1}^{M1} = 1.85 nm, and R_{int2}^{M1}= 1.9 nm from the element profiles of Figure 7.5i. R_{int1}^{M1} demonstrates a gradient decrease in the Zr atom concentration, while the Yb atom concentration increases towards the layer direction which indicates diffusion of Zr atoms into the layer. R_{int2}^{M1} shows residual Zr atoms, synchronized with the onset of visually observed Yb and Fe atomic layers which show Yb and Fe oscillation in the mass concentrations χ.

Figure 7.5j shows the HR-STEM HAADF image of the M2 layer at the interface between BaM/YSZ. It reveals an interlayer with a thickness of approximately 5 nm and a bad atomic resolution. Diffractograms obtained by the FFT analysis from the marked square regions are shown in Figure 7.5k and Figure 7.5l for BaM and the interlayer, respectively. Figure 7.5k illustrates that the BaM layer exhibits the *pnma* space group[284] of the hexagonal phase of the BaM film, known for its magnetic applications. Figure 7.5l illustrates that the interlayer region is an iron rich crystalline phase and/or phases. Figure 7.5m to Figure 7.5r present the atomic resolution EDX maps of the interface region squared in Figure 7.5j, while Figure 7.5s shows the concentration profile. The elemental profile indicates two transition regions which correspond to the summation of R_{Tr1}^{M2}= R_{int1}^{M2} + R_{int2}^{M2}. According to Table 7-5, R_{Tr1}^{M2} = 3.95 nm, while R_{int1}^{M2} = 1.65 nm. As the Zr content decreases and the Fe content increases until R_{int2}^{M2} = 1.9 nm, the Ba content starts to increase. Subsequently, the Ba content enables the stoichiometric composition while Fe content gradually degrades it.

Comparing the interlayers formed with YSZ for M1 and M2, one can see that the M2 transition interlayer R_{int1}^{M2} + R_{int2}^{M2}= 3.55 nm is slightly smaller than R_{int1}^{M1}+ R_{int2}^{M1} = 3.75 nm. Nevertheless, the element profiles given by Figures 7.5i and 7.5s display different behaviors. In the case of BaM (M2), the Fe content peaks at the interface, while for YbFO (M1), the chemical composition gradually approaches the theoretical stoichiometry. The increase of the Fe content at the interface may affect the magnetic contribution of the single layer.

Figure 7.6a to Figure 7.6g show a detailed study of chemical composition at the YbFO/BaM interface in sample M2 with atomic resolution. The corresponding EDX mapping to the TEM images of Figure 7.6a (not shown) illustrate the element profiles in Figure 7.6g. In addition, atomically resolved STEM HAADF images and EDX maps (see white framing) drawn in Figure 7.6a are displayed in Figure 7.6b to Figure 7.6f. In element profiles of Figure 7.6g, three different characteristic regions R_{BaM}^{M2}, R_{int3}^{M2} and R_{YbFO}^{M2} where R_{BaM}^{M2} and R_{YbFO}^{M2} are defined by constant Ba and Yb concentrations, respectively. The R_{int3}^{M2} region is the transition zone at the YbFO/BaM interface in M2. It contains a chemical mixture over a thickness of R_{int3}^{M2} = 8.7 ± 0.05 nm (listed in Table 7-6). The inset (Figure 7.6g) shows the elemental profiles at atomic resolution from the turquise colored region, which captures in particular, the interdiffusion of Ba atoms into the YbFO layer. The measured region of R_{int3}^{M2} is well correlated with R_{Tr2}^{M2} = 10.3 ± 0.05 nm derived from mass density profiles of XRR curves (see Figure 7.4c). HRTEM images (Figure A-35) reveal an atomic step at the YbFO/BaM interface in M2 that could potentially be a source of spin frustration

at this interface and conseqently prevent the occurrence of the exchange bias at the AF/FM interface[285]. Comparatively, Figure 7.6h shows atomically resolved STEM HAADF images of the M1 (BaM/YbFO/YSZ) system, specifically near the YbFO/BaM interface. For M1, EDX have been collected and quantified, as indicated by the orange rectangle (Figure 7.6i to Figure 7.6m). The resulting elemental concentration profiles for Ba, Yb, Fe and O are plotted in Figure 7.6n.

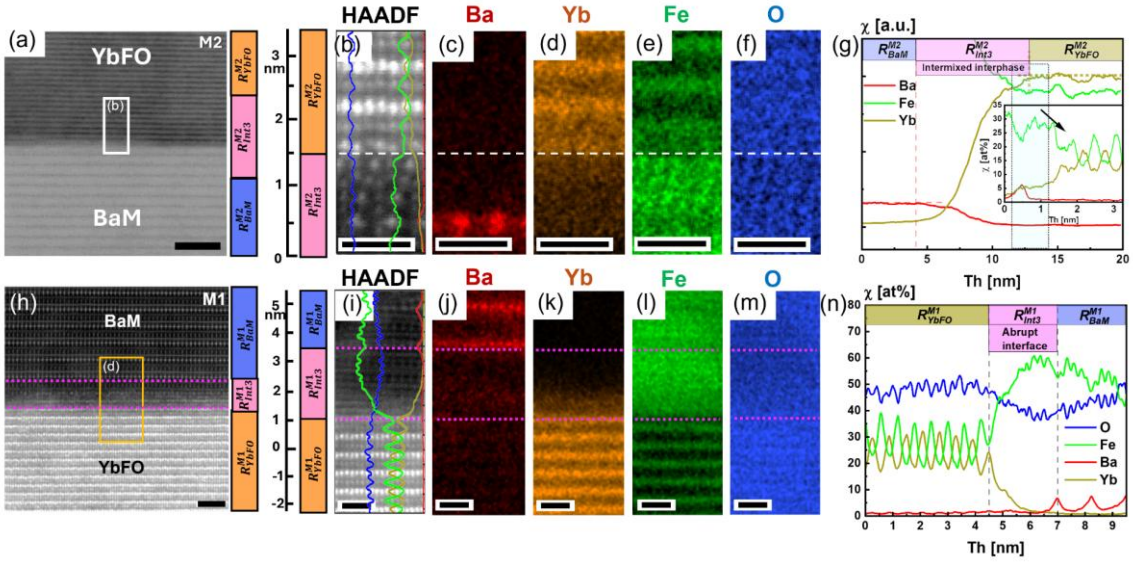

Figure 7.6: (a, j) High-resolution STEM HAADF images near the bilayer interface regions (BaM/YbFO) and (YbFO/BaM) for M1 and M2 heterostructures, respectively. (b, c) Diffractograms which correspond to white and red rectangles drawn in BaM and YbFO layers, respectively. (k, I) Diffractograms of the black and yellow rectangles drawn in YbFO and BaM layers, respectively. The regions marked with orange and red rectangles are the regions selected for the which correspond to X-ray maps given in (d, e, f, g, h) for M1 and in (m, n, o, p, r) for M2, (i, s) comparison of the quantitative EDX line profiles for the elements O, Fe, Ba, and Yb for M1 and M2. Scale bars of (a) is 5 nm, of (h) is 2 nm and of (b-f) and (i-m) are 1 nm in size. For magnified view refer to Figure A-33[242].

Three distinct regions: R_{YbFO}^{M1}, R_{BaM}^{M1} and R_{int3}^{M1} could be identified where R_{int3}^{M1} = 2.5 nm ± 0.05 nm is the transition region at the YbFO/BaM interface, which is significantly smaller than R_{int3}^{M2} = 8.7 ± 0.05 nm and shows no chemical intermixture between the BaM and YbFO layers. (see Figure 7.6n). It should be emphasized that the transition region R_{Tr2}^{M2}, determined from the mass density profile in Figure 7.4c to be 8.2 ± 0.1 nm is relatively larger than R_{int3}^{M2} (2.5 ± 0.05 nm) as measured from the elemental profiles (Table 7-6). In conclusion, the extent of the Yb/Ba intermixture depends on the stacking order of the layers. Specifically, in M1 an abrupt atomic interface is observed at the BaM/YbFO interface, whereas in M2 there is significant chemical intermixture at the YbFO/BaM interface. In addition, atomic steps at the interfaces observed in atomically resolved TEM images (Figure A-35, 7.2d) are a consistent feature in both heterostructures, irrespective of the growth sequence, and could induce magnetic frustration as reported by Chen et al[285]. The crystalline structure of the BaM and YbFO layers, which include the number of boundaries and the degree of misorientation of the BaM mosaic blocks, appears to be influenced by the layer stacking order, as shown in Figure 7.2.

Figure 7.7 shows HR-STEM HAADF images of the YbFO layers for M1 and M2 bilayer systems across the 12 nm x 12 nm region. Diffractograms obtained by the FFT analysis of selected square regions within the YbFO layers are shown in Figure 7.7b for M1 and Figure 7.7c for M2. The diffractograms confirm that both layers, whether directly grown on YSZ (M1) or on BaM (M2), represent the ferroelectric metaphase of YbFO which belongs to space group $P6_3cm$. Figure 7.7a and Figure 7.7d illustrate the atomic arrangement of the YbFO layer with representative colored spheres. Green and yellow spheres represent Yb atoms with bright contrast in HAADF images (green spheres displaced upwards, and yellow spheres displaced downwards), while brown spheres represent Fe atoms with darker contrast in the HAADF images.

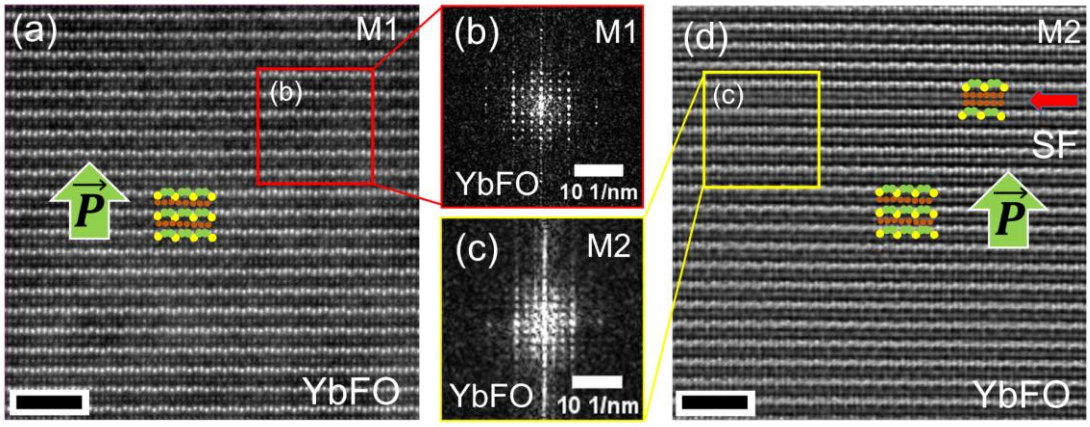

Figure 7.7: High resolution STEM HAADF images and diffractograms of YbFO layers in the M1 and M2 systems. (a, d) HAADF images of YbFO layers in M1 and M2, respectively, illustrate the atomic arrangements with colour-coded spheres for Yb (green and yellow) and Fe (brown) atoms. Note a stacking defect in M2 (d). (b, c) FFT analysis diffractograms of M1 (b) and M2 (c) which confirm the ferroelectric metaphase of $YbFeO_3$ in both layers. The scale bars for (a, d) are 2 nm in size[242].

A comparison of the atomic arrangements of M1 (Figure 7.7a) and M2 (Figure 7.7d) shows that both layers consist of ferroelectric domains. In these domains, a non-centrosymmetric shift of Yb atoms generates charge polarization. Specifically, two Yb atoms are shifted vertically upwards, while one is shifted downwards which results in ferroelectric polarization in the upward direction. Furthermore, Figure 7.7d shows a stacking fault (SF) which could accidentally originate from a specific imaged region. Significant variations, which lead to differences in stacking faults between the two layers, could not be observed, except for the absence of Yb atoms and in the case of two Fe layers.

7.4 Effect of the growth sequence on the magnetic properties

Figure 7.8 shows comprehensive magnetization measurements for the heterostructure systems M1 and M2. Figures 7.8a and 7.8b show different behaviors for the out-of-plane (OOP) and in-plane (IP) hysteresis loops measured at different temperatures in the range of 50 K to 400 K. This reflects the growth of highly c-axis anisotropy M1 and M2 heterostructures, independent of the

stacking order. OOP was recorded along the easy axis with an applied magnetic field *H* parallel to the c-axis while IP was measured along the hard axis at which the applied magnetic field *H* is perpendicular to the c-axis. The top and the bottom panels of Figures 7.8a and 7.8b corresponds the OOP and IP hysteresis loops of the M1 and M2 heterostructures, respectively. It should be noted that the saturation magnetization $M_{s//}(T)$ and $M_{s\perp}(T)$ decreased with the temperature. For better clarity, Figure 7.8c compares the OOP hysteresis loops for M1 and M2, measured at 50 K and 300 K. The inset graph in Figure 7.8c magnifies a specific region to clearly demonstrate the difference in the coercivity values $H_{c\perp}$ between M1 and M2 as well as the temperature dependence of the magnetic properties. Earlier studies[286] pointed out the effect of the grain size, defect concentration and mosaic boundaries on the coercivity field. Furthermore, Figures 7.2e and 7.2f proved that M2 contains a higher number of mosaic boundaries in comparison with M1. This has a profound effect on the magnetic coercivity of the heterostructures M1 and M2.

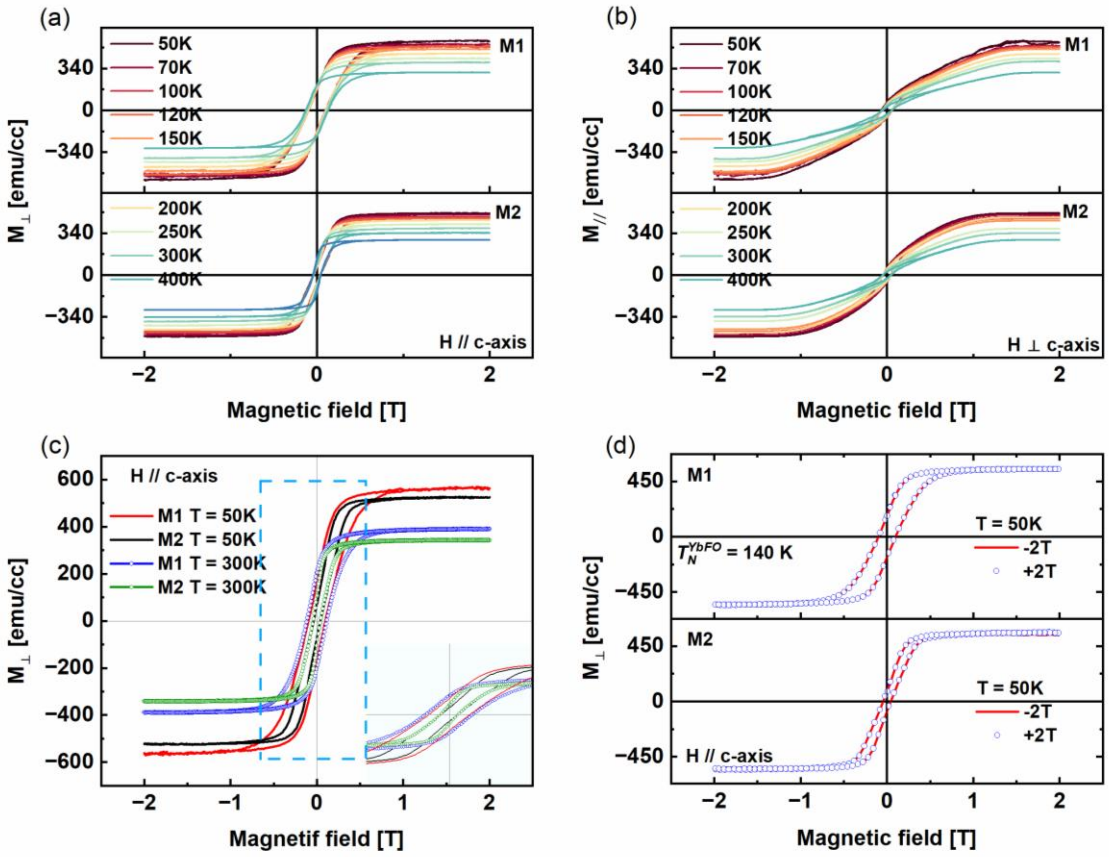

Figure 7.8: (a, b) Out-of-plane (OOP) and in-plane (IP) magnetization polarization curves for M1 (top panel) and M2 (bottom panel), respectively, recorded in the temperature range T = 50 K – 400 K. (c) Comparison between the OOP magnetization of M1 and M2 at T = 50 K and 300 K with the inset as a magnification in the region of H = -1 T – 1 T. (d) OOP magnetization loop measured at 50 K and for an applied magnetic field H = 2 T and -2 T for M1 (top panel) and M2 (bottom panel) [242].

In addition, Figure 7.8d focuses on the EB measurement performed by applying magnetic fields of +2 T and -2 T at 50 K. The heterostructures were cooled to this temperature during an applied field in accordance with the methodology for studying EB below the Neel temperature of YbFO

($T_N^{YbFO} \approx 125$ K, in this work in chapter 6) mentioned to be around ~125K[137,231,235]. However, the absence of a horizontal shift in the hysteresis loops suggests the absence of an exchange bias possibly due to spin frustration. This observation is consistent with the results of field-cooled hysteresis loops measured for both M1 and M2 heterostructures which did not show a detectable EB. Despite the chemical mixing of Yb and Ba cations over an intermixed region of R_{int3}^{M2} = 8.7 ± 0.05 nm at the YbFO/BaM interface in M2 (as shown in Figure 7.6g and Table 7-6), the spins of the YbFO layer at the interface appear to be fully compensated. This configuration energetically favors a spin-flopping state which does not induce EB in agreement with the findings of Chen et al[285] in similar systems. In addition, studies[287] have confirmed the absence of EB in systems with chemically abrupt interfaces like the one observed in M1. It is crucial to emphasize the tilted antiferromagnetic spin orientation in YbFO which significantly affects the spin ordering near the interface and contributes to the spin-flop phase as reported by Jensen et al[271]. In order to further understand and compare the temperature dependence of the magnetic properties in M1 and M2, the values of $M_{s\perp}$ *(T)*, $H_{c\perp}$ *(T)* and H_a *(T)* were derived from Figure 7.8 and plotted against the temperature in Figure 7.9.

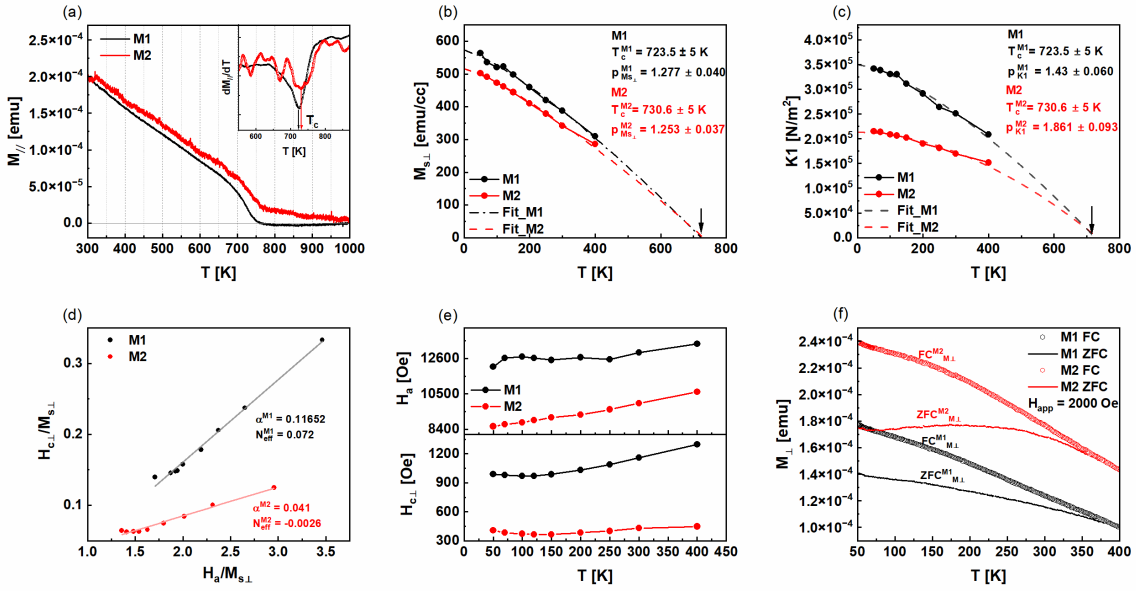

Figure 7.9: (a) Variation of the in-plane moment $M_{//}$ versus temperature in the range T = 300 – 1000 K for M1 and M2, inset corresponds to the derivative dM/dT as a function of temperature, the minima corresponds to Curie temperature T_c, (b) variation of the out-of-plane moment at the saturation $Ms_\perp$ with the temperature for M1 (black full circle) and M2 (red full circle), the fit curves are the power law curves, (c) temperature dependence of the fist anisotropy constant K1 for M1 (black full circle) and M2 (red full circle), (d) variation of $H_{c\perp}$ / $M_\perp$ as function of the $H_a/Ms_\perp$ (black full circle) and M2 (red full circle) dedicated to determination of microstructural and demagnetizing factors α and N_{eff}, respectively, (e) anisotropy field H_a temperature dependence (top panel) for M1 and M2 and comparison between M1 and M2 of temperature dependence of perpendicular coercivity $H_{c\perp}$ with temperature (bottom panel), (f) zero field cooling (ZFC) and field cooling (FC) recorded at an applied field H = 2000 Oe for M1 (open circle) and M2 (solid lines). For magnified view refer to Figure A-34[242].

In Figure 7.9a, the Curie temperature, T_c, measurements for the M1 and M2 heterostructures are presented. The Curie temperature for free-standing BaM single crystalline material was previously identified by Shirk et al[287]. as T_c = 740 K. The inset of the graph displays the derivative of

the magnetic moment ($dM_{//}/dT$) with the curve's minima which indicate the Curie temperatures. In this study, a slight variation in T_c between the two systems is observed and attributable to the influence of the stacking order to in-plane residual strain and to the consequent alteration of an in-plane misfit. The measured Curie temperatures are T_c^{M1} = 723.5 ± 5 K for M1 and T_c^{M2} = 730.6 ± 5 K for M2, both lower than that of the free-standing BaM layer.

The impact of residual strain on Curie temperatures in strained films was previously discussed by Gan et al.[268]. Furthermore, Španková et al[288] conducted studies on the strain relationship of $La_{0.9}Sr_{0.1}MnO_3$ films on various substrates who concluded that compressive strain suppresses ferromagnetism and reduces T_c. For the heterostructures in the present work, the in-plane residual strain for the BaM layers shifts from a compressive state in M1 ($\varepsilon_{BaM//}^{M1}$ = -1.3 %) to a tensile state in M2 ($\varepsilon_{BaM//}^{M2}$ = 1.3 %) while the out-of-plane residual strain increases from $\varepsilon_{BaM\perp}^{M1}$ = 0.29 % to $\varepsilon_{BaM\perp}^{M2}$ = 0.48 %, as listed in Table 7-4. Therefore, the observed increase in T_c from 723.5 K in M1 to 730.6 K in M2 can be linked to the transition from compressive to tensile strain which corroborates the findings of Španková et al[288].

In Figure 7.9b and Figure 7.9c, one can compare between M1 and M2 regarding the temperature dependence of the magnetization saturation $M_{s\perp}$ (T) and the first anisotropy constant *K1(T)*. The latter is related to the anisotropy field H_a *(T)* and $M_{s\perp}$ *(T)* as follows in Equation (6-13)[214,289,290,291].

$$K1(T) = \frac{M_{s\perp}(T) * H_a(T)}{2} \tag{7-13}$$

It turned out that in the measured temperature range, $M_{s\perp}$ *(T)* values are lower for M2 than for M1. The decrease of $M_{s\perp}$ *(T)* in M2 could be caused by the presence of the chemical intermixture region revealed by EDX in M2, R_{int3}^{M2} = 8.7 ± 0.05 nm. *K1(T)* represents the magneto-crystalline anisotropy energy (MAE) and, therefore, the energy required to break the anisotropy. *K1(T)* decreases with the temperature due to weakening of the spin orbital coupling (SOC) because of thermal fluctuations. We found that the anisotropy constant *K1(T)* is higher for M1 than in M2 heterostructures which means that the corresponding SOC was affected by the stacking order. In conclusion, due to high values of *K1(T)* M1 would be more suitable for a storage device which requires higher MAE. *K1(T)* is in accordance with the c-axis orientation of the layers. This was proven by Figure 7.1f and Figure 7.1g where the layer inclination with respect to substrate lattice planes is higher for M2 (β = 0.1).

$M_{s\perp}$ *(T)* decreases by increasing the temperature for the M1 and M2 heterostructures. This behavior results from breaking the spin order with the temperature increase (see Figure 7.9b). In order to analyze the variation of $M_{s\perp}$ *(T)* and *K1(T)* as a function of temperature, both curves were fitted to the power law as a modified Bloch`s law[290] as provided in Equations (7-14) and Eq (7-15). It has been argued that the well-known $T^{3/2}$ Bloch law, derived from the spin wave theory and the thermal excitation of magnons, is insufficient to explain the complex magnetic structure of hexaferrites [290,292]

$$M_{s\perp}(T) = M_{s\perp}(0) * \left[1 - (\frac{T}{T_c})^P\right] \tag{7-14}$$

$$K1\,(T) = K1\,(0) * \left[1 - (\frac{T}{T_c})^P\right] \tag{7-15}$$

for which ($M_{s\perp}$ *(0), P*) and (*K1 (0), P*) are the fit parameters obtained from the best fit of the $Ms_{\perp}$ *(T)* and *K1 (T)*, respectively, which uses the non-linear square fit algorithms with chi-square values R = 0.999.

In the case of homogeneous ferromagnetic systems, the exponent *P*, satisfies the Bloch`s law to be 3/2. However, the exponent *P* depends on the dimensionality, predominant spin, and the crystal structure of the systems. The fit is realized by using the T_c for both systems as a fixed parameter due to having Curie temperature measurement beforehand which apply the fit for $T_{c,M1}$ = 723.5 ± 5 K and $T_{c,M2}$ = 730.6 ± 5 K, respectively.

Silica-coated $BaFe_{12}O_{19}$ nanoparticles have found to be that the temperature-dependent *K1* and M_s satisfy the power law and the exponents *P* = 1.58 and *P* = 1.56, respectively[290]. In the case of M1 and M2 heterostructures, $M_{s\perp}$ *(T)* and *K1(T)* deviate from the Block $T^{3/2}$ behavior for which *P* may be dependent on several features. For M1, the exponents *P* derived from the fits of $M_{s\perp}$ *(T)* and *K1 (T)* are $P_{M_{s\perp}}^{M1}$ = 1.277 ± 0.040 and P_{K1}^{M1} =1.432 ± 0.060, respectively. In the case of M2, $P_{M_{s\perp}}^{M2}$ =1.253 ± 0.037 and P_{K1}^{M2} =1.861 ± 0.093, (see Table 7-8). For M1, we found that $Ms_{\perp}$ *(T)* behaves closer to the Bloch $T^{3/2}$ law. The exponents $P_{M_{s\perp}}^{M1}$ and $P_{M_{s\perp}}^{M2}$ are comparable for M1 and M2. However, P_{K1}^{M2} dramatically deviated from 3/2 in the case of M2. As mentioned above, the inhomogeneity/intermixture region at the BaM/YbFO interface for M2 could be the reason for such a deviation. In other words, P which deviates from the Bloch`s law could confirm the intermixture and generation of the inhomogeneity region for the magnetic properties (R_{int3}^{M2} = 8.7 ± 0.05 nm). Similarly, Garcia et.al[292]. also reported that the higher value of exponent P was interrelated with the atomic disorder and with the magnetic frustration in doped yttrium iron garnets.

In order to conclude the mechanism which controls the coercivity and to figure out the influence of the change in the growth sequence, the micromagnetic model (Equation (7-16)) was applied to analyze the temperature dependent hysteresis loops as follow: [24,25,214,216,286].

$$\frac{H_{c\perp}(T)}{M_{s\perp}\,(T)} = \alpha\,\frac{H_a\,(T)}{M_{s\perp}\,(T)} - N_{eff} \tag{7-16}$$

N_{eff} is the demagnetization factor which is relevant for the grain surface and for the volume changes of the material. This would generate a negative effect on the total magnetization of the samples. The magnitude α corresponds to the microstructural parameter also called structural reduction factor defined as $\alpha = \alpha_1$ x α_2 by Kronmüller[214]. α_1 represents the pinning or nucleation factor of the domains whereas α_2 is related to the misalignment factor of the grains with respect to the easy-axis/c-axis or to the applied field.

In Figure 7.9d, H_c / M_s vs H_a / M_s values are plotted for the M1 and M2 systems and are linearly fitted by the micromagnetic model to determine the structural reduction factors, α and N_{eff}. From the slopes of the curves, α_{M1} = 0.116 and α_{M2} = 0.04, the coercivity control mechanism could not be clearly determined since the factor α < 0.5 and, therefore, the analysis was indecisive between nucleation and the domain wall pinning[214,216]. Considering the inclination values of the layer (in

Figure 7.1f, Figure 7.1g), β = 0.1 for M2 and β = 0.01 for M1, the extracted structural results suggest that α_{M2} would be higher for the M2 heterostructure. Controversially, the obtained higher value of α_{M1} = 0.116 could be interpreted in a way so that M1 possesses a higher number of pinning and the nucleation centers in the magnetic layer which are located at the phase boundaries (i.e. TEM images in Figure 7.2e). This result justified the high values of the coercivity field for M1 in comparison to M2 which revealed less phase boundaries and, therefore, less pinning centers (see TEM of Figure 7.9e). Furthermore, demagnetization the factors are relatively small, N_{eff}^{M1}= 0.072 and N_{eff}^{M2}= -0.003 for both heterostructures which indicate the formation of a limited number of nonmagnetic phases in both hetereostructures[214]. Nevertheless, N_{eff}^{M1} of M1 is still higher than $N_{eff}^{M2}$of M2 which is probably related to the high defect density as revealed by the diffraction angular broadening of the BaM reflections and by the HRTEM images (Figure 7.2).

Bance et.al[286] demonstrated that the N_{eff} decreases as the lateral mosaic block size and the grain misalignment increases. That correlates with the findings of β^{M2} = 0.1 which is higher than β^{M1} = 0.01 (Figure 7.1h and Figure 7.1k), and the lateral size of the mosaic blocks is larger than in M1 (Figure 7.2e and Figure 7.2f).

Figure A.5a presents the initial magnetization curves of the M1 and M2 heterostructures which were measured at T = 300 K to investigate the domain wall motion and to determine the susceptibility of these systems. The curves are displayed in Figure A-36a, with an inset, which provides a magnified view of the initial slope at lower magnetic fields. The curves of M1 and M2 exhibit a two-slope behavior which suggests the potential existence of two distinct domain-wall motion mechanisms. In the first slope up to approximately 1000 Oe, one can possibly observe the mechanism of predominant domain wall pinning. The initial slope (H < 1000 Oe) is less steep than the second slope of (H > 1000 Oe) which indicates a greater material resistance for the applied magnetic field (H < 1000 Oe) to move the domain walls. Once the critical coercivity (H_{crit} ≥ 1000 Oe) is reached the curve slope increases which indicates a reduction of the resistance for the applied field. This phase is likely indicative for domain wall depinning in which domain walls move more unhindered when the applied field becomes higher than H_{crit}. In order to determine H_{crit} accurately, the second and third derivatives of the magnetization curves (d^2M/dH^2 and d^3M/dH^3) were analyzed, as shown in Figure A-36b for M1 and Figure A-36c for M2. H_{crit} is identified at the point where the third derivative equals zero which marks the change in the slope of the initial magnetization curve. For M1, H_{crit} is determined to be 1217 Oe, while for M2, it is identified to be 913 Oe. This finding indicates that the depinning of domains in M1 occurs at a higher external field which supports the hypothesis that a higher concentration of defects in a material requires a stronger field for domain wall depinning[26].

Figure 7.9e shows the variation of the OOP coercivity field $H_{c\perp}$ *(T)* and anisotropy field H_a *(T)* with the temperature T in the range 50 K to 400 K at the bottom and the top panel, respectively. The two M1 and M2 heterostructures show an increase of H_c and H_a fields with the temperature. However M1 displays a higher H_c, $H_{c\perp}{}^{M1}$ = 990 (50 K) – 1296 Oe (400 K) which is due to a higher number of domain wall pinning centers, located at phase boundaries (Figure 7.2c and Figure 7.2f). Previous studies[214,289] investigated the temperature dependence behavior of $H_{c\perp}$ *(T)* and H_a *(T)* for a BaM hexaferrite single layer. They revealed an increase of $H_{c\perp}$ *(T)* and H_a *(T)* until attaining the

maximum between 400 K - 500 K, then followed by decay until the Curie temperature T_c = 740 K for a BaM single crystal.

In Figure 7.9f, zero-field cooling ($ZFC_{M\perp}^{M1}$, $ZFC_{M\perp}^{M2}$) and field cooling ($FC_{M\perp}^{M1}$, $FC_{M\perp}^{M2}$) curves of both systems M1 and M2 are plotted in the temperature range T = 50 K - 400 K, with the externally applied field of H = 0 and H = 2000 Oe. Here, the applied external field H is higher than $H_{c\perp}^{M1}(T)$ and $H_{c\perp}^{M2}(T)$ for M1 and M2 whereupon $H_{c\perp}^{M1}$= 990 (50 K) – 1296 Oe (400 K) and with $H_{c\perp}^{M2}$= 407 (50 K) – 448 Oe (400 K). Due to higher values of H_a^{M1} for M1 the magnetic moment recorded during ZFC curves were reduced in comparison to M2 (see Figure 7.9f). This means that M1 requires a higher external field than M1 to rotate the spins in a certain direction. This results into a lower magnetization at the FC curves ($FC_{\perp}^{M1} < FC_{\perp}^{M2}$, Figure 7.9f). Additionally, thermal irreversibility has been recorded for which the FC magnetic moment is higher than the ZFC magnetic moment ($FC_{M\perp} > ZFC_{M\perp}$). This suggested the relation to spin frustration[293]. As it discussed by Kumar et al.[293] this spin frustration could occur due to the irregularities at the interfaces of the magnetic layer. In our study, these irregularities correspond to the regions with the chemical mixture at the YbFO/BaM interface in M2 which induced spin frustration and disturbance at the regular spin alignments. This led to a reduced moment shown by the ZFC curves. In return for the bifurcation degree (the separation between ZFC and FC ($ZFC_{M\perp}$ - $FC_{M\perp}$)) is expected to be higher for M2 as seen in Figure 7.9f.

7.5 Summary and conclusions

A detailed study on the structure and the magnetic properties was carried out by using complementary analysis methods (i.e. 2D-HRXRD, HRTEM, Atomic resolution EDX) on two heterostructures M1, M2 which possess two different stacks of BaM layer as FM and YbFO as canted AF and FE layers. The different interfacial strain, which was induced by the variation of the growth sequence in M1 and M2 was demonstrated to affect the crystal quality and the chemical composition of the individual BaM and YbFO layers as well as the degree of the chemical homogeneity at the interfaces.

By mean of atomic resolution EDX, the chemical composition at interfaces with YSZ substrate and at BaM/YbFO in M1 and YbFO/BaM in M2 was explored. An interdiffusion phenomenon has occurred for M1 and M2 with different chemical compositions at the substrate YSZ interfaces where a Fe-rich crystalline phase was predominantly formed at the interface BaM/YSZ in M2. The determined values of the misfit at the YSZ interface in M1 and M2 are comparably compressive (i.e. $f_{YbFO/YSZ}^{M1}$= -4.42 %, $f_{BaM/YSZ}^{M2}$ = -5.53 %). The chemical composition of the layer which interfaces with the substrate was found different from the stoichiometry of the target as it has been demonstrated by the measurement of the mass densities.

While the interface BaM/YbFO in M1 was distinctive and without any chemical interdiffusion over a thickness of R_{int3}^{M1} = 2.5 ± 0.05 nm, the interface in M2 YbFO/BaM has revealed a chemical intermixture over an extend of R_{int3}^{M2} = 8.7 ± 0.05 nm. This is most probably related to the change in the interfacial misfit from compressive $f_{BaM/YbFO}^{M1}$= -3.56 % to tensile $f_{YbFO/BaM}^{M2}$= 0.35 %. For

the M1 and M2 heterostructures, there was no detectable exchange bias even in the case of the chemically intermixed interface for the M2 heterostructure.

It should be emphasized that below the Neel temperature of YbFO < $T_N \cong 140$ K, the heterostructures M1 and M2 act as FM/CAF and CAF/FM while in the temperature range beyond $T_N \cong 140$ K, the heterostructures M1 and M2 are rather FM/PM and PM/FM. Furthermore, the YbFO layers do not exhibit any variation in the metastable hexagonal $P6_3cm$ ferroelectric order of Yb atoms. Even with a varying stress and stacking order both systems exhibit the ferroelectric order, which is known as a non-centrosymmetric displacement of the rare earth element (also known as 2Up/1Down vice versa).

The measured magnetic properties of the heterostructures were found strongly influenced by the ferromagnetic BaM layer due to the weakness of the antiferromagnetic YbFO. The magnetic behavior of M1 and M2 was remarkably related to the crystal quality of the BaM layer which was crucially influenced the interfacial features (i.e., residual strain, misfit, chemical homogeneity of the layer and at the interface).

For BaM layers, there is a slight inclination with respect to the substrate lattice planes in the M2 system. Even if the misalignment originates from the miscut of the substrate the addition of an interlayer (such as YbFO for M1) would suppress the miscut effect generated during the production of the substrate crystal. TEM and XRD investigations reveal that BaM layers have a higher crystalline quality when grown on YSZ, with less defect concentration (fewer mosaic boundaries and smaller mosaic tilt), despite the occurrence of an unwanted interlayer formation at the substrate interface. The mass density of the BaM layer deviates from the theoretical value, with M1 being higher and M2 being smaller than the theoretical value. In this case, the increase in mass density could again be due to compression for M1 (BaM/YbFO).

A large chemical mixture region of M2 at the YbFO/BaM interface disturbs the homogeneity of the magnetic layers and deviates the material behavior from the Bloch $T^{3/2}$ law. Furthermore, the intermixture of materials affects the ZFC-FC behavior, whereupon film irregularities result in spin frustration which generate thermal irreversibility and disturbs the regular spin alignment. It ultimately increases the degree of bifurcation. Additionally, it has been proven that tensile stress increases T_c for BaM, while compressive strain suppresses ferromagnetism and reduces T_c. In conclusion, M1 with a more distinct interface exhibits more homogeneous and regular magnetic properties. On the other hand, M1 exhibits larger coercivity, N_{eff}, a higher density of defects (mosaic boundaries), a higher anisotropy constant, and a higher MAE. These characteristics suggest that M1 is more suitable for magnetic storage applications.

Table 7-2: Summary of the lattice parameters corresponding to the different layers BaM, YbFO and YSZ of the heterostructures M1 and M2[242].

Sample name	**M1 ($BaFe_{12}O_{19}$/$YbFeO_3$/YSZ111)**	**M2 ($YbFeO_3$/$BaFe_{12}O_{19}$/YSZ111)**
$d_{(11-2)YSZ}$ [Å]	2.1 ± 0.001	2.1 ± 0.001
$d_{(111)YSZ}$ [Å]	2.969 ± 0.001	2.969 ± 0.001
a_{YbFO}^{M1} [Å]	6.0221 ± 0.001	
a_{YbFO}^{M2} [Å]		5.9881 ± 0.001
c_{YbFO}^{M1} [Å]	11.693 ± 0.001	
c_{YbFO}^{M2} [Å]		11.7149 ± 0.001
a_{BaM}^{M1} [Å]	5.8151 ± 0.001	
a_{BaM}^{M2} [Å]		5.967 ± 0.001
c_{BaM}^{M1} [Å]	23.25 ± 0.001	
c_{BaM}^{M2} [Å]		23.2942 ± 0.001

Table 7-3: Summary of the lattice misfit determined at different interfaces BaM/YbFO, YbFO/YSZ for M1 and YbFO/BaM, BaM/YSZ for M2. (C): Compressive, (T): Tensile[242].

Sample name	**M1 ($BaFe_{12}O_{19}$/$YbFeO_3$/YSZ111)**	**M2 ($YbFeO_3$/$BaFe_{12}O_{19}$/YSZ111)**
$f_{YbFO/YSZ}^{M1}$ [%]	-4.42 (C)	
$f_{BaM/YbFO}^{M1}$ [%]	-3.56 (C)	
$f_{BaM/YSZ}^{M2}$ [%]		-5.3 (C)
$f_{YbFO/BaM}^{M2}$ [%]		0.35 (T)

Table 7-4: Summary oft he in-plane and out-plane residuals determined in the BaM and YbFO layers in the two different heterostructures M1 and M2[242].

Sample name	**M1 ($BaFe_{12}O_{19}$/$YbFeO_3$/YSZ111)**	**M2 ($YbFeO_3$/$BaFe_{12}O_{19}$/YSZ111)**
$\varepsilon_{YbFO//}^{M1}$ [%]	0.96 (T)	
$\varepsilon_{YbFO\perp}^{M1}$ [%]	-0.08 (C)	
$\varepsilon_{BaM//}^{M1}$ [%]	-1.3 (C)	
$\varepsilon_{BaM\perp}^{M1}$ [%]	0.29 (T)	
$\varepsilon_{BaM//}^{M2}$ [%]		1.3 (T)
$\varepsilon_{BaM\perp}^{M2}$ [%]		0.48 (T)
$\varepsilon_{YbFO//}^{M2}$ [%]		0.39 (T)
$\varepsilon_{YbFO\perp}^{M2}$ [%]		0.11 (T)

Table 7-5: Summary of the fitting parameters such as mass densities ρ_{BaM} of BaM and ρ_{YbFO} of YbFO layer derived from the XRR curves of M1 and M2 and the corresponding densities profiles across the heterostructures films thicknesses[242].

Sample name	**M1 ($BaFe_{12}O_{19}$/$YbFeO_3$/YSZ111)**	**M2 ($YbFeO_3$/$BaFe_{12}O_{19}$/YSZ111)**
BaM thickness Th_{BaM} [nm]	61.0 ± 0.2	70.0 ± 0.2
YbFO thickness Th_{YbFO} [nm]	58.8 ± 0.2	65.0 ± 0.2
Mass density $\rho_{B\alpha M}$ [g/cm^3]	5.24 ± 0.05 ≅ ρ_{BaM} = 5.296 g/cm^3	3.86 ± 0.05 < ρ_{BaM} = 5.296 g/cm^3
Mass density ρ_{YbFO} [g/cm^3]	8.38 ± 0.05 > ρ_{YbFO} = 6.8 g/cm^3	7.14 ± 0.07 slightly > ρ_{YbFO} = 6.8 g/cm^3
Transition region YbFO/YSZ R_{Tr1}^{M1} [nm]	2.81 ± 0.1	
Transition region BaM/YbFO R_{Tr2}^{M1} [nm]	8.2 ± 0.1	
Transition region BaM/YSZ R_{Tr1}^{M2} [nm]		3.95 ± 0.1
Transition region YbFO/BaM R_{Tr2}^{M2} [nm]		10.3 ± 0.1

Table 7-6: Summary of the characteristics of regions with their corresponding thicknesses of the EDX profiles of the two heterostructures as they are derived from Figures 7.5 and 7.6[242].

Sample name	**M1 ($BaFe_{12}O_{19}/YbFeO_3/YSZ111$)**	**M2 ($YbFeO_3/BaFe_{12}O_{19}/YSZ111$)**
BaM thickness Th_{BaM} [nm] TEM	63 ± 0.2	67 ± 0.2
YbFO thickness Th_{YbFO} [nm] TEM	53 ± 0.2	74 ± 0.2
YbFO/YSZ R_{int1}^{M1} [nm] EDX profiles	2.75 < *Th* < 4.6 1.85 ± 0.05 nm Interdiffusion of Zr atoms	
YbFO/YSZ R_{int2}^{M1} [nm] EDX profiles	4.6 < *Th* < 6.5 1.9 ± 0.05 nm Residual Zr atoms	
BaM/YbFO R_{int3}^{M1} [nm] EDX profiles	4.5 < *Th* < 7 2.5 ± 0.05 nm Sharp interface without intermix-ing	
BaM/YSZ R_{int1}^{M2} [nm] EDX profiles		1.25 < *Th* < 2.9 1.65 ± 0.05 nm Interdiffusion of Zr atoms
BaM/YSZ R_{int2}^{M2} [nm] EDX profiles		2.9 < *Th* < 4.8 1.9 ± 0.05 nm Fe rich phase
BaM/YbFO R_{int3}^{M2} [nm] EDX profiles		4.2 < *Th* < 12.93 8.7 ± 0.05 nm Chemical intermixing

Table 7-7: Summary of the concentration χ [at %] of the Yb, Fe and Ba derived from the EDX profiles of Figure 7.5i and Figure 7.6n for M1 and from EDX profiles of Figure 7.5s and Figure 7.6g for M2[242].

Sample name	**M1 ($BaFe_{12}O_{19}/YbFeO_3$/YSZ111)**	**M2 ($YbFeO_3/BaFe_{12}O_{19}$/YSZ111)**
BaM thickness Th_{BaM} [nm]	63 ± 0.2	67 ± 0.2
YbFO thickness $Th_{Y\text{-}bFO}$ [nm]	53 ± 0.2	74 ± 0.2
R_{YbFO}^{M1} χ [at %]	χ_{Yb} (Max)= 30 ± 1 $<\chi_{Yb}>$ = 23.57 $<\chi_{Fe}>$ = 27.12	
R_{BaM}^{M1} χ [at %]	$\chi_{B\alpha M}$ (Max) = 7 ± 0.5 $<\chi_{B\alpha}>$ = 3.7 $<\chi_{Fe}>$ = 54.03	
R_{YbFO}^{M2} χ [at %]		χ_{Yb} (max) = 18 ± 0.5 Large scan $<\chi_{Yb}>$ = 19.85, $<\chi_{Fe}>$ = 17.97 Atomic resolution $<\chi_{Yb}>$ = 13.89, $<\chi_{Fe}>$ = 18.53
R_{BaM}^{M2} χ [at %]		$\chi_{B\alpha M}$ (Max) = 6 ± 0.5 Large scan $<\chi_{B\alpha}>$ = 3.18, $<\chi_{Fe}>$ = 36.77 Atomic resolution $<\chi_{B\alpha M}>$ = 3.39, $<\chi_{Fe}>$ = 27.1

Table 7-8: Summary of the characteristic magnetic parameters for M1 and M2 such as moment at saturation T = 0 K, $M_{s\perp}(0)$ and exponents P which were derived from the fitting of temperature dependence moment with the power law $M_{s\perp}(0)*(1-(T/T_c)^P)$ and $K1(0)*(1-(T/T_c)^P)$. Microstructural parameter α and demagnetization factor N_{eff} which were derived from $H_{c\perp}/M_{s\perp}$ as function of the $H_a/M_{s\perp}$[242].

Sample name	**M1 ($BaFe_{12}O_{19}/YbFeO_3$/YSZ111)**	**M2 ($YbFeO_3/BaFe_{12}O_{19}$/YSZ111)**
Moment at saturation T = 0 K $M_{s\perp}(0)$ [emu/cc]	$M_{s\perp}^{M1}(0)$ = 573.43 ± 5.97	$M_{s\perp}^{M2}$ (0) = 513.77 ± 5.68
Exponent P	$P_{M_{s\perp}}^{M1}$ =1.277 ± 0.040	$P_{M_{s\perp}}^{M2}$ =1.253 ± 0.037
Curie Temperature T_c [K]	T_c^{M1} =723.5 ± 5	T_c^{M2} = 730.6 ± 5
Anisotropy constant $K1$, T = 0 $K1$ (0) [N/m2]	$K1^{M1}(0)$ = 3.5E+6 ± 4.4E+3	$K1^{M2}(0)$ = 2.1E+6 ± 2.6E+3
Exponent P	P_{K1}^{M1} = 1.432 ± 0.060	P_{K1}^{M2} = 1.861 ± 0.093
Microstructural parameter α	α^{M1} = 0.116	α^{M2} = 0.041
Demagnetization factor N_{eff}	N_{eff}^{M1} = 0.072	N_{eff}^{M2} = -0.0026

8 Conclusions

This PhD thesis is concerned with the optimisation of pulsed laser deposition (PLD) growth parameters for the fabrication of multiferroic heterostructures, with the objective of achieving room-temperature operational devices. The study systematically investigates the individual layers, namely platinum (Pt) as the bottom electrode, barium hexaferrite (BaM) as the ferromagnetic layer, and *h*-$YbFeO_3$ (YbFO) as the ferroelectric layer, and their combination into heterostructures. The objective is to understand how the growth conditions affect the structural, morphological, and physical properties of these layers and their interfaces, ultimately leading to the realization of efficient multiferroic devices.

This study initially investigated the optimal conditions for subsequent layers of a platinum layer on YSZ(111) substrates, deposited via PLD, with a view to establishing the growth temperature. The importance of fixing the growth temperature lies in its variability with different growth methods and subsequent procedures. While previous studies have extensively examined the growth of Pt and its morphological and crystalline structure influenced by specific growth methods and temperatures, they have not adequately addressed the influence of the Pt underlayer during the overgrowth of a capping layer. To address this gap in the literature, we first investigated the optimal growth temperature for Pt by exploring temperatures of 300 °C, 500 °C, 700 °C, and 900 °C. To ensure similar thicknesses across samples, we calibrated the number of shots.

The results demonstrated that as the growth temperature increased, the morphology of the Pt layer became smoother, mosaicity decreased, and crystalline quality improved. The optimal growth temperature was observed to be 900 °C. Further investigation showed that annealing, simulating subsequent growth processes, resulted in the least dewetting at higher growth temperatures. Although dewetting was inevitable, it was minimized when the growth temperature was close to the subsequent treatment temperature, reducing the extent of modifications during or after annealing.

With the optimal growth temperature of 900 °C, which matches the capping layer growth temperature, the thickness of the Pt layer was varied from 10 nm to 70 nm in order to understand its effects on surface filling factor, crystalline quality, hillock formation, and robustness against further high-temperature growth. It was found that increasing the Pt thickness improved surface coverage and reduced hillock formation once a critical filling factor was reached. A detailed comparison between the as-grown and encapsulated states of Pt films revealed a number of competing phenomena, including hillock formation, dewetting, and coalescence, which were driven by increased diffusion energy at 900 °C and interactions at grain boundaries.

The optimal Pt thickness was determined to be 70 nm, providing high crystalline quality, minimal thickness fluctuations, and robustness against high-temperature growth – attributes which are desirable for a bottom electrode. The formation of hillocks was observed to be least pronounced at higher thicknesses in both the as-grown and encapsulated states. The rearrangement of the Pt film during subsequent growth effectively acts as an annealing process, reducing residual strains and enhancing film quality.

Following the investigation of the bottom electrode, the growth parameters of the ferromagnetic layer BaM were optimised using Pt-buffered templates. The optimisation process for BaM growth involved two main steps: first, examining the effect of the Pt underlayer thickness on the BaM layer, and second, varying the growth parameters of the BaM layer itself. The objective was to produce high-crystalline-quality, continuous, stoichiometrically stable, and homogeneous BaM layers with desired magnetic properties for perpendicular recording media and multiferroic heterostructure applications.

BaM layers were grown on bare YSZ (111) substrates and Pt-buffered YSZ substrates with Pt underlayer thicknesses ranging from 10 nm to 70 nm, while keeping other BaM growth parameters constant. Investigations utilising HRXRD, HR-STEM, EDX, and other complementary methods have revealed that the dewetting of the Pt underlayer has a significant impact on the continuity of the BaM layer. Discontinuities were attributed to the formation of Pt blocks and voids during BaM layer growth. Consequently, it was determined that a Pt bottom electrode with a thickness of at least 70 nm is crucial for achieving high-quality and continuous BaM layers. Furthermore, the incorporation of a continuous underlayer has been demonstrated to enhance the c-axis orientation of the BaM layer and to influence the domain structure alignment along the c-axis, which is of critical importance for the performance of perpendicular recording media.

Subsequently, the BaM growth process was subjected to further investigation by varying the laser fluence employed in the PLD growth procedure. The laser pulse energy was adjusted from 25 mJ to 75 mJ in order to examine the effects of this parameter. It was observed that higher fluence induces crystal defects, mosaic block boundaries, and stoichiometrically different secondary phases due to the dynamic growth processes and the energy differences in the plasma species between 25 mJ and 75 mJ. Since 75 mJ laser pulses ablate more material and transfer more energy to the ablated plasma, they alter the momentum and diffusion kinetics, leading to stoichiometric and structural defects, which in turn affect the magnetic properties. Furthermore, higher fluence led to the formation of secondary growth on the material surface, resulting in a less flat surface. It was thus demonstrated that laser fluence is a crucial parameter for regulating the microstructure, morphology, and subsequent magnetic properties of BaM layers.

As previously indicated, one of the aims of this investigation is to examine the FE layer of YbFO. In order for ferroelectric YbFO to function properly, it is necessary to use a bottom electrode that serves as a conductor, is continuous, free of hillocks to prevent short circuits, promotes the $P6_3cm$ space group of YbFO, and ensures good crystalline quality for better ferroelectric domain structure. To this end, Pt templates, previously optimised for thickness, were used as bottom electrodes to determine if the YbFO quality was influenced by the underlayer. This section focuses on the low-temperature magnetic properties of the YbFO layer in relation to its film morphology, crystal structure, and mosaicity.

The results demonstrate that increasing Th_{Pt} improves the quality of the YbFO layer in terms of crystalline quality and homogeneity. The presence of hillocks on the Pt underlayer disrupts the continuity and morphology of the YbFO layer, as the YbFO tends to follow the surface structures of the Pt underlayer. In order to achieve a continuous and high-quality YbFO layer, a minimum Th_{Pt} of 55 nm is necessary to avoid hillocks and ensure good crystalline quality.

As the thickness of the Pt layer increases and the quality of the Pt bottom electrode improves, the magnetic properties of the YbFO layers are enhanced. It was observed that the remanent magnetisation (M_r) and the magnitude of the bifurcation between field-cooled (M_{FC}) and zero-field-cooled (M_{ZFC}) magnetisations increase. This indicates that the YbFO layer deposited on a Th_{Pt} thickness of 70 nm exhibits enhanced magnetic properties due to an increased degree of anisotropy and magnetic behaviour.

Following the investigation of individual layers, optimal conditions for combining FE YbFO and FM BaM layers were determined. These layers were deposited on YSZ(111) substrates without a Pt bottom electrode due to limitations in the PLD setup. In order to identify the optimal configuration for multiferroic (MF) heterostructures, a series of investigations were conducted, employing a range of analytical techniques, including HRXRD, HR-TEM, atomic resolution EDX, XRR, and VSM.

The study demonstrated that interfacial strain induced by varying the stacking order significantly affects the crystal quality and chemical composition of the individual layers, as well as the sharpness and degree of chemical homogeneity at the interfaces. Atomic resolution EDX revealed chemical composition variations at the interfaces, with interdiffusion observed at varying extents depending on the stacking order. A Fe-rich crystalline phase was identified at the BaM/YSZ interface in M2, likely due to the complexity of the BaM crystalline structure and the higher interfacial strain/misfit ($f^{M1}_{YbFO/YSZ}$= - 4.42 %, $f^{M2}_{BaM/YSZ}$= - 5.53 %).

The mass density profiles obtained from XRR indicated differences in stoichiometry. M1 (YbFO/BaM) exhibited no chemical interdiffusion, with an interface thickness of R^{M1}_{int3} = 2.5 ± 0.05 nm. In contrast, M2 (BaM/YbFO) exhibited chemical intermixture, with an interface thickness of R^{M2}_{int3} = 8.7 ± 0.05 nm. The misfit transition from compressive in M1 ($f^{M1}_{BaM/YbFO}$= - 3.56 %) to tensile in M2 ($f^{M2}_{YbFO/BaM}$= 0.35 %) is likely to account for these differences.

Both M1 and M2 heterostructures exhibited FM and CAF behaviour below the Neel temperature of YbFO ($T_N \approx 140$ K), and exhibited FM and PM behaviour above $T_N \approx 140$ K. No magnetic exchange bias was observed. The YbFO layer maintained its structural integrity, indicating stable ferroelectricity regardless of stacking order or stress due to misfit.

The magnetic properties of the heterostructures were predominantly influenced by the ferromagnetic BaM layer, given the relatively weak antiferromagnetic behaviour of YbFO. The crystal quality of the BaM layer was influenced by interfacial features such as residual strain, misfit, and chemical homogeneity. In M2, a slight inclination of the BaM layer with respect to the substrate lattice planes was observed, likely originating from the substrate's miscut. The presence of an interlayer in M1 suppressed this effect, leading to better crystalline quality in the BaM layer.

TEM and XRD analyses revealed that BaM layers exhibited higher crystalline quality when grown on YSZ(111), with fewer defects, despite the formation of an unwanted interlayer at the substrate interface. The mass density of the BaM layer deviated from theoretical values, with M1 showing a higher density and M2 a lower density, likely due to compressive strain in M1.

The large chemical mixture region in M2 at the YbFO/BaM interface disrupted the homogeneity of the magnetic layers, deviating from the Bloch $T^{3/2}$ law. This intermixture also affected the ZFC-FC behaviour, causing spin frustration, thermal irreversibility, and increased bifurcation. Additionally, tensile stress increased the Curie temperature (T_c) for BaM, while compressive strain reduced ferromagnetism and lowered T_c. Consequently, M1, with its distinct interface, exhibited more homogeneous and regular magnetic properties, rendering it more suitable for magnetic storage applications. M1 also displayed larger coercivity, higher defect density, higher anisotropy constant, and greater magnetic anisotropy energy (MAE), reinforcing its suitability for such applications.

The study highlights the significance of optimising growth conditions and stacking order in the development of high-performance multiferroic heterostructures, paving the way for the advancement of advanced room-temperature multiferroic devices by combining the bottom electode, FE layer and FM layer into a multilayer heterostructure.

A Appendices

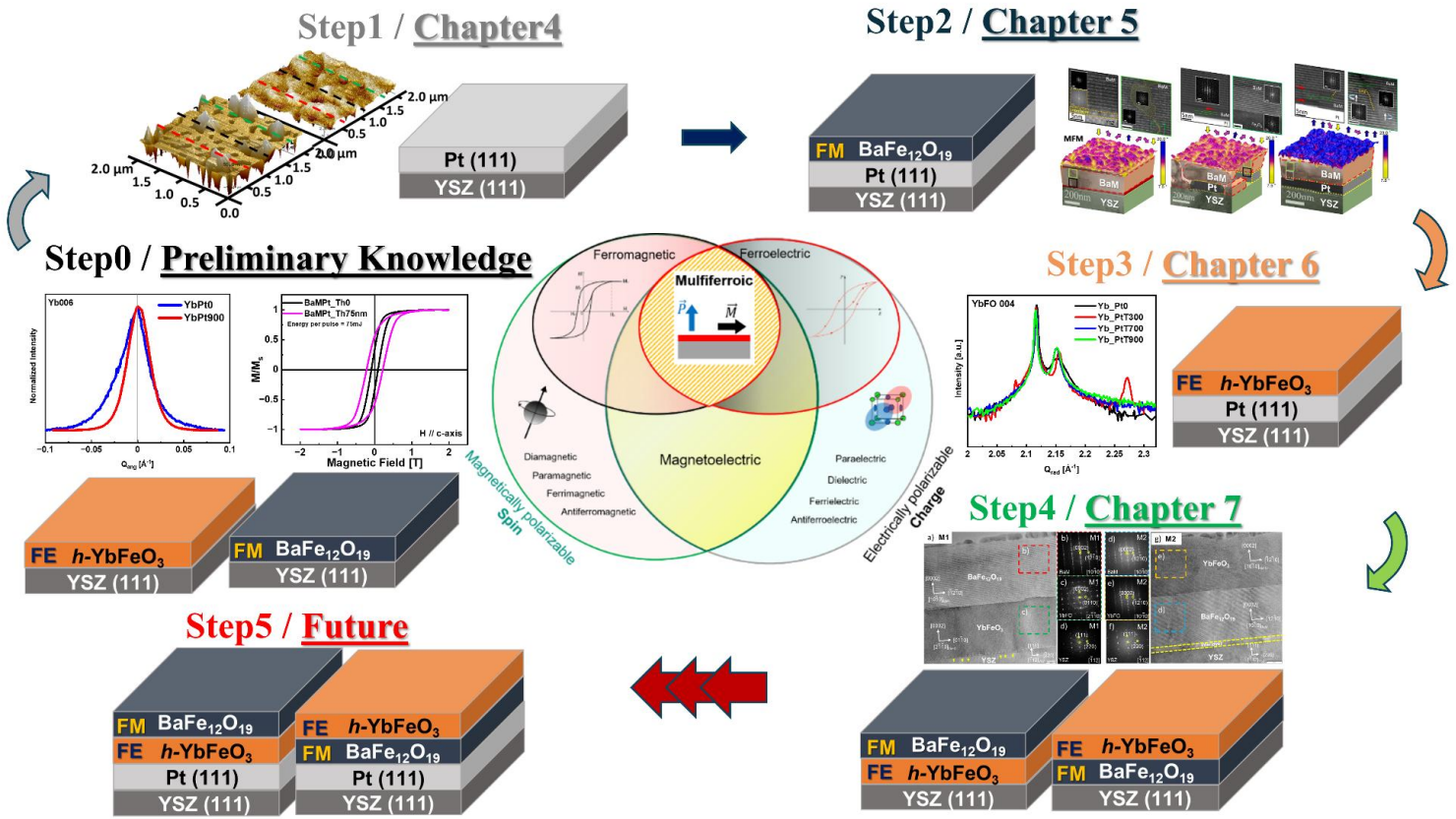

Figure A-1: Schematic representation of the overall scheme for the thesis path, which was represented in Figure 1.2 in the thesis.

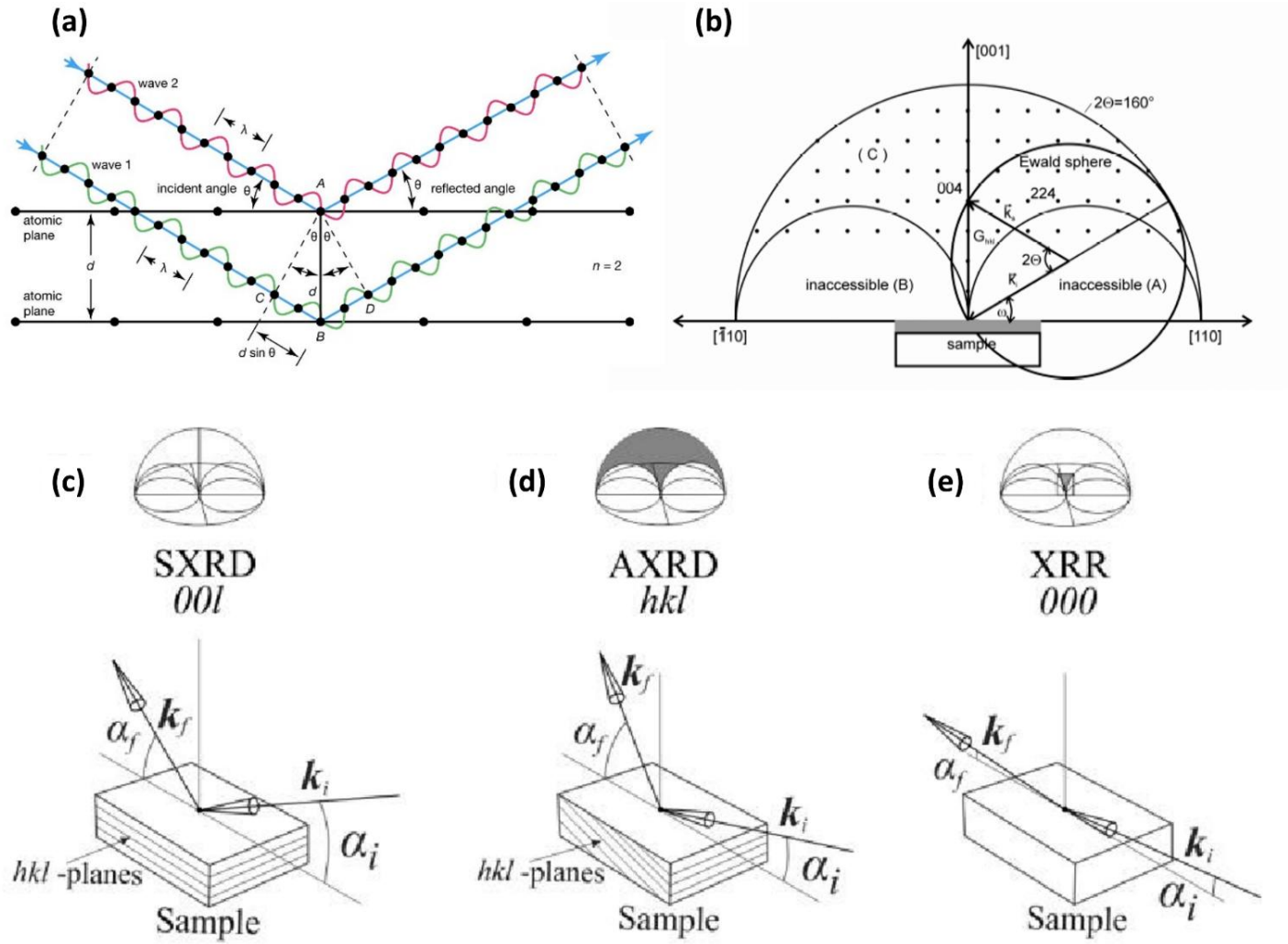

Figure A-2: Schematics of X-ray diffraction which refers to the Figure 2.7[100,101].

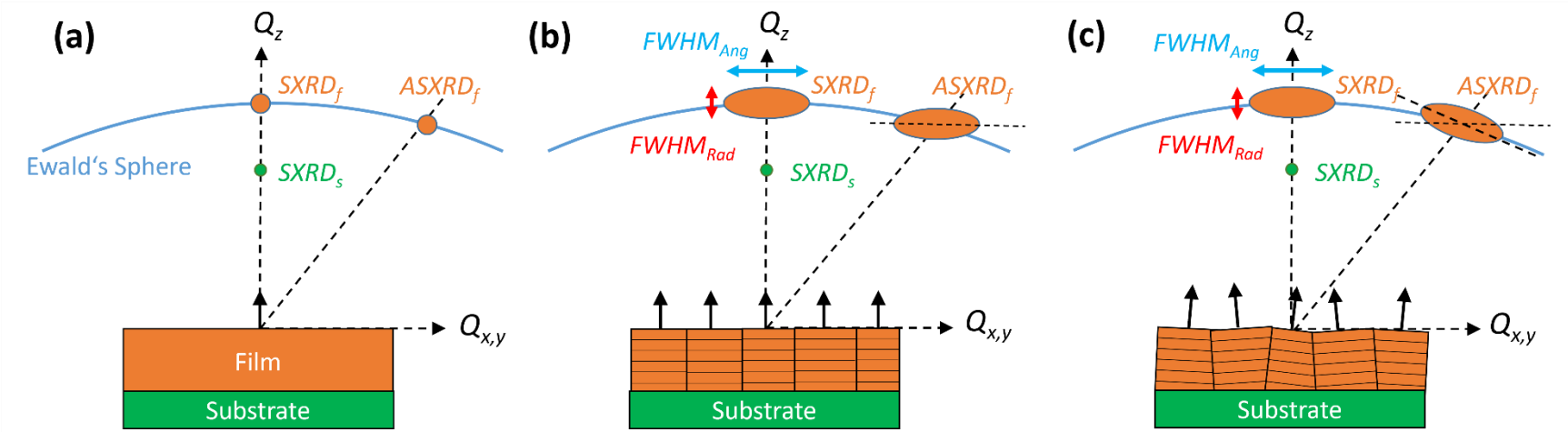

Figure A-3: A schematic of the thin films and the representative RSM influence due to the defects originated in the film structure, which refers to the Figure 2.8.

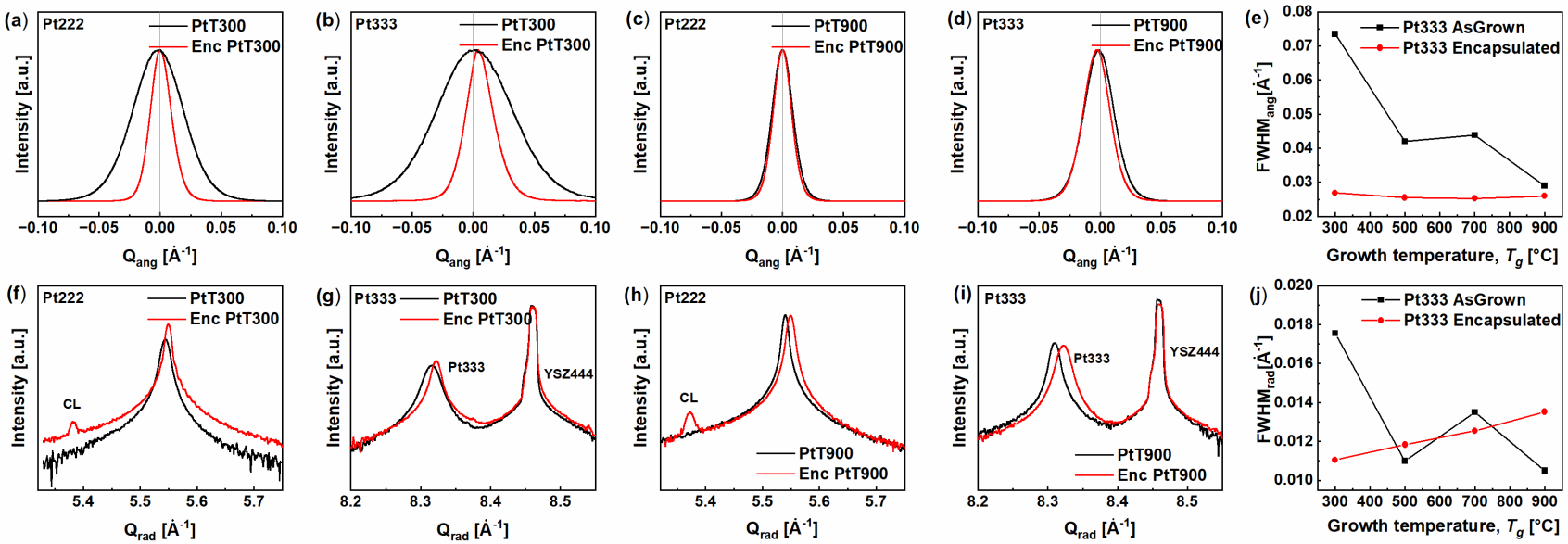

Figure A-4: Angular and radial intensity profiles which refers to the Figure 4.1.

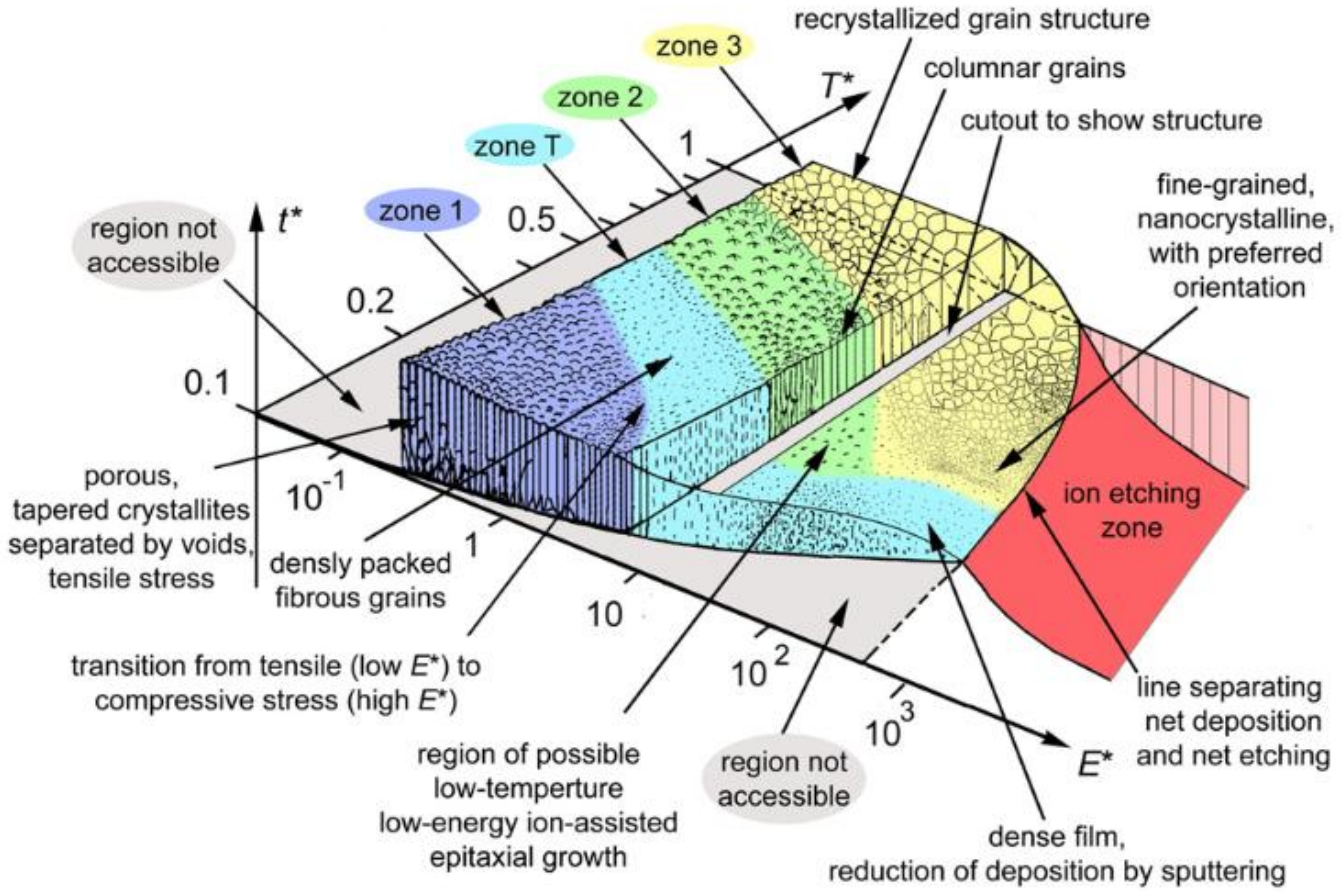

Figure A-5: The structure zone diagram, as introduced by Anders, is applicable to the energetic species deposition. However, it was noted that the exact boundaries and values of the diagram could mislead the readers. It was also observed that specific materials and conditions may vary the results, therefore a value reading must be avoided[86].

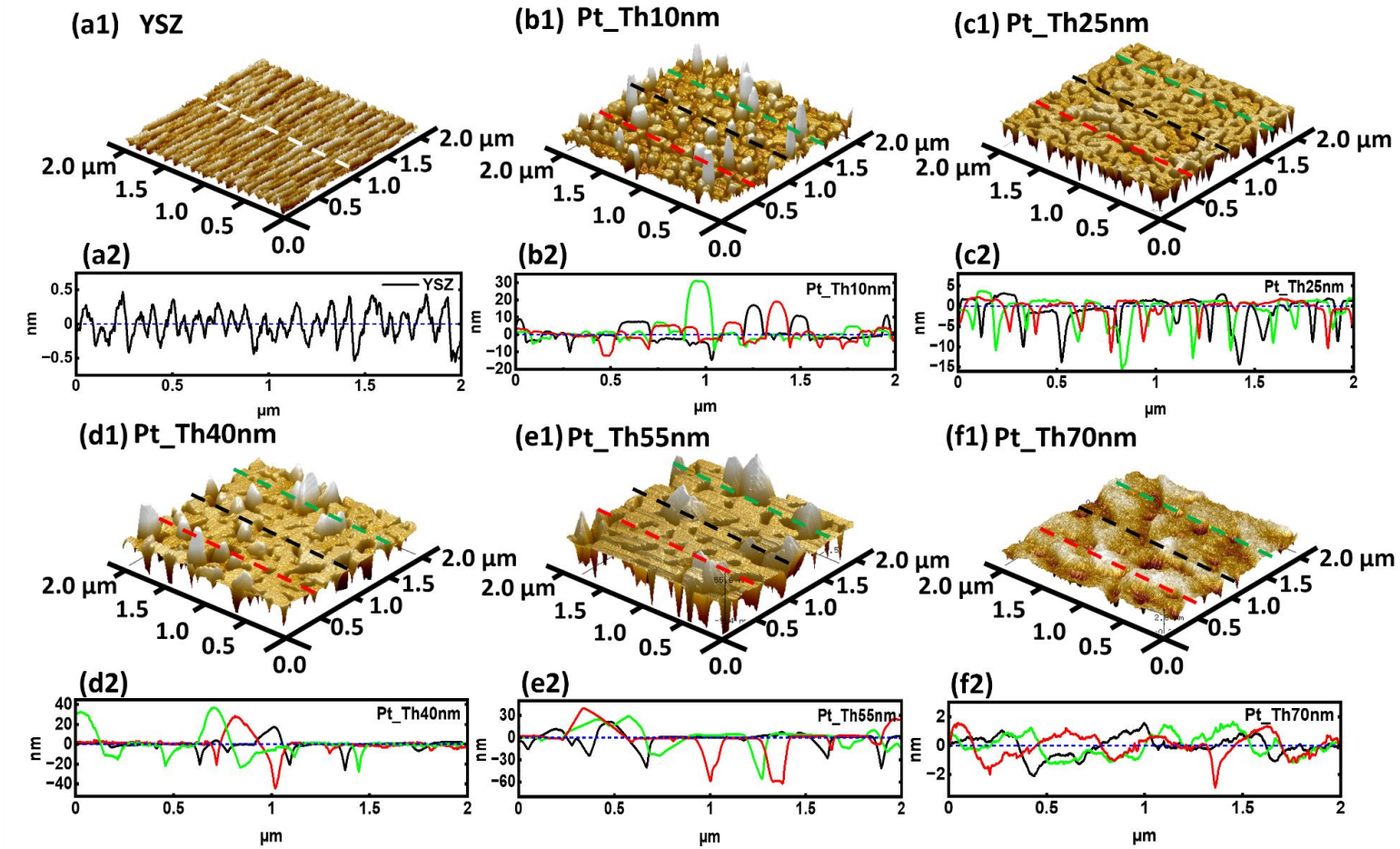

Figure A-6: A magnified version of Figure 4.6[172].

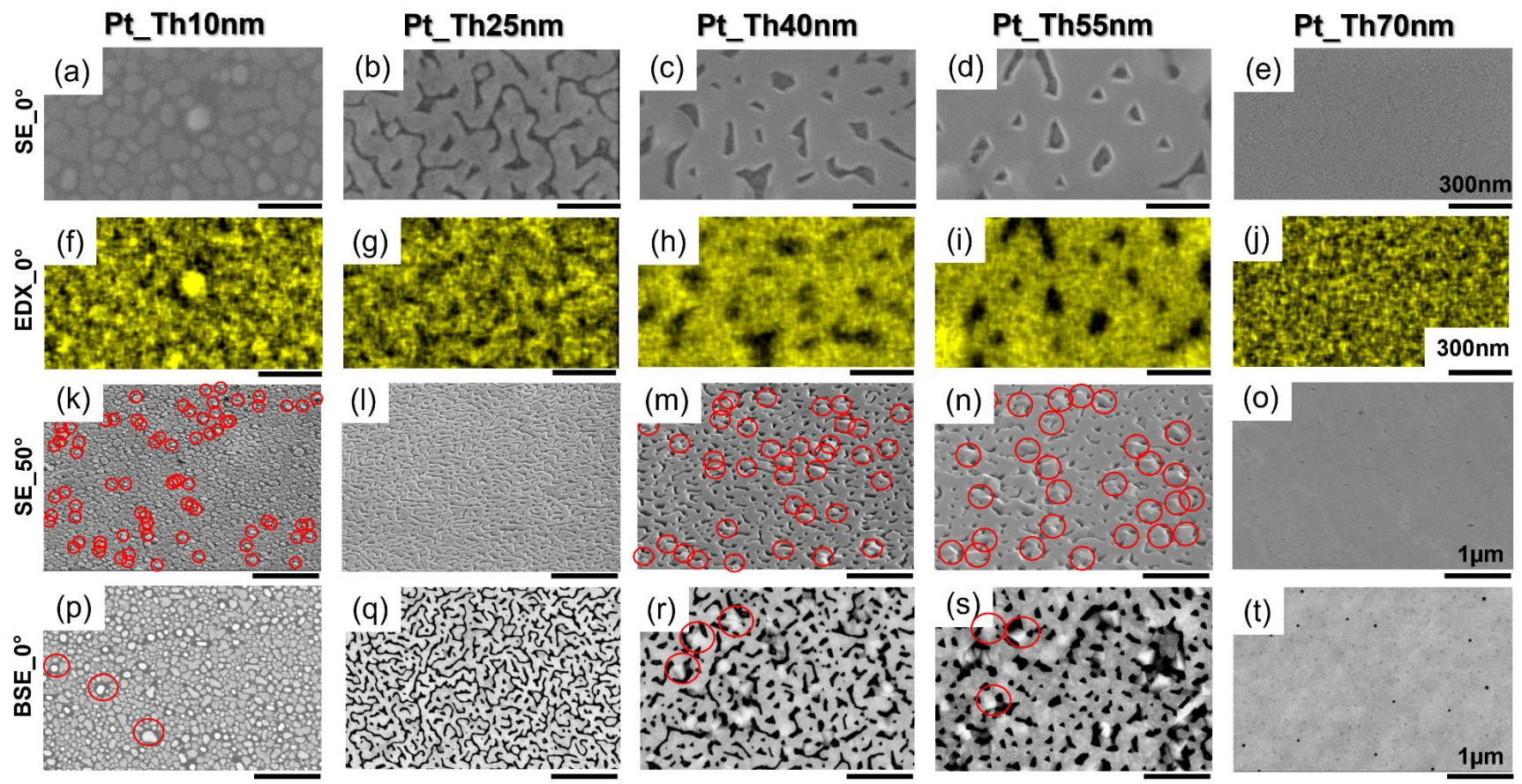

Figure A-7: A magnified version of Figure 4.7[172].

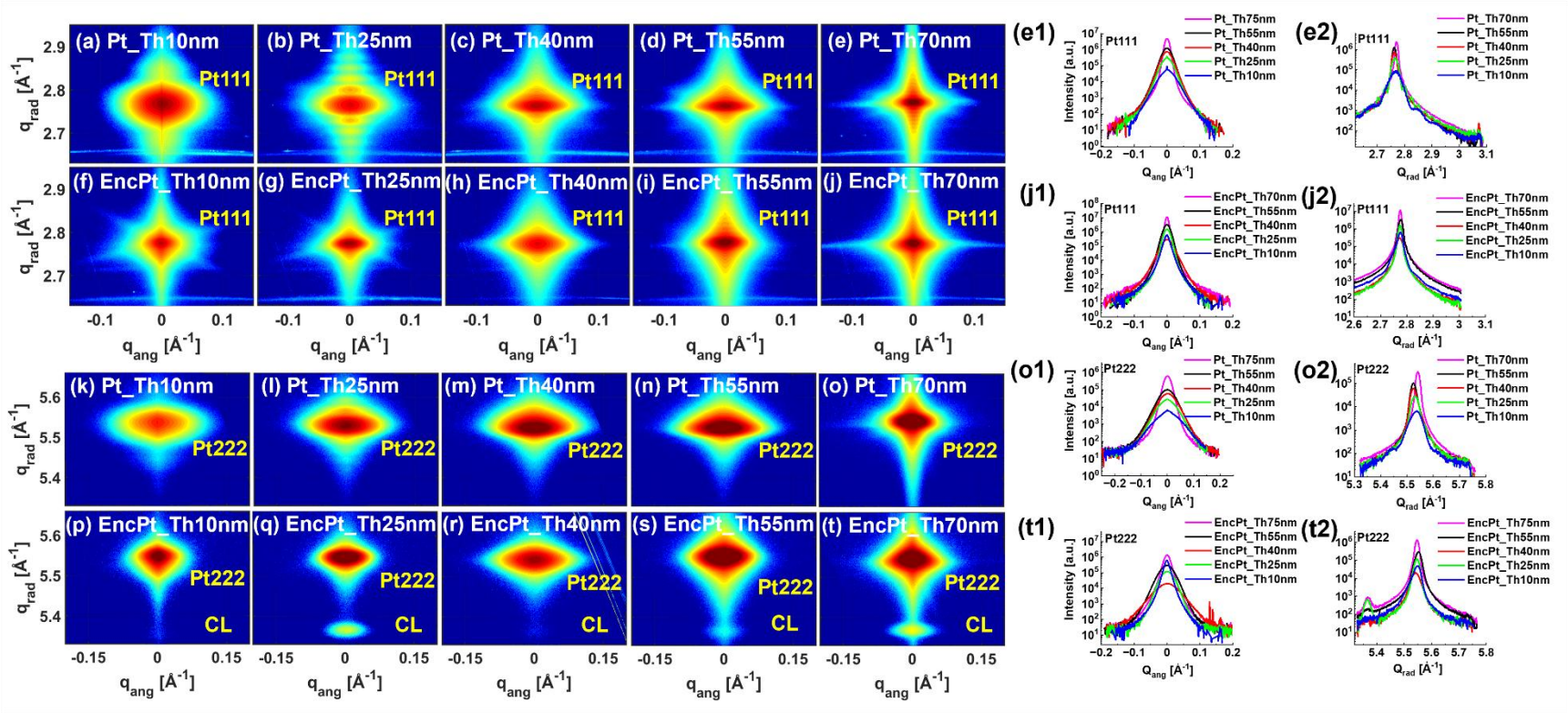

Figure A-8: A magnified version of Figure 4.9[172].

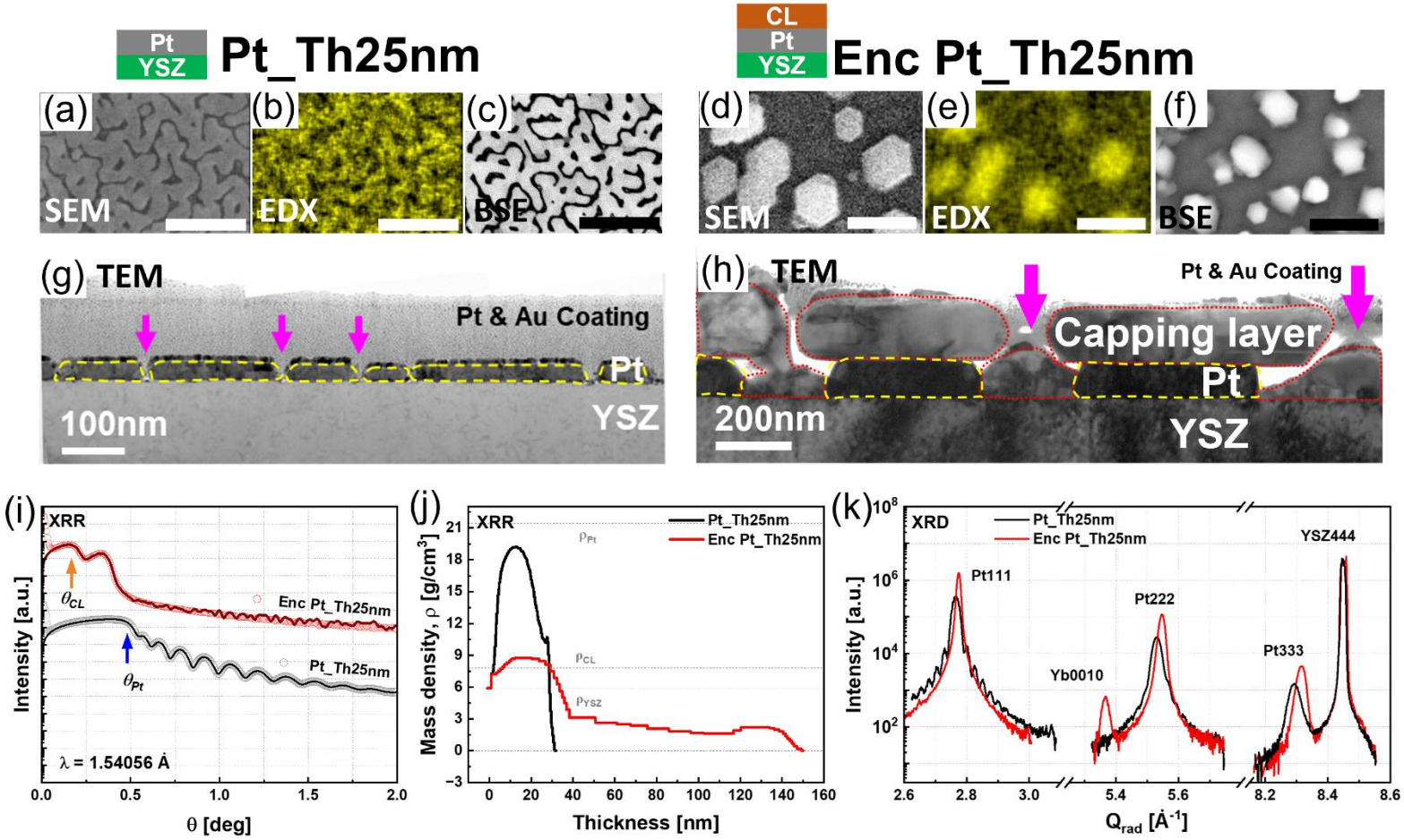

Figure A-9: A magnified version of Figure 4.12[172].

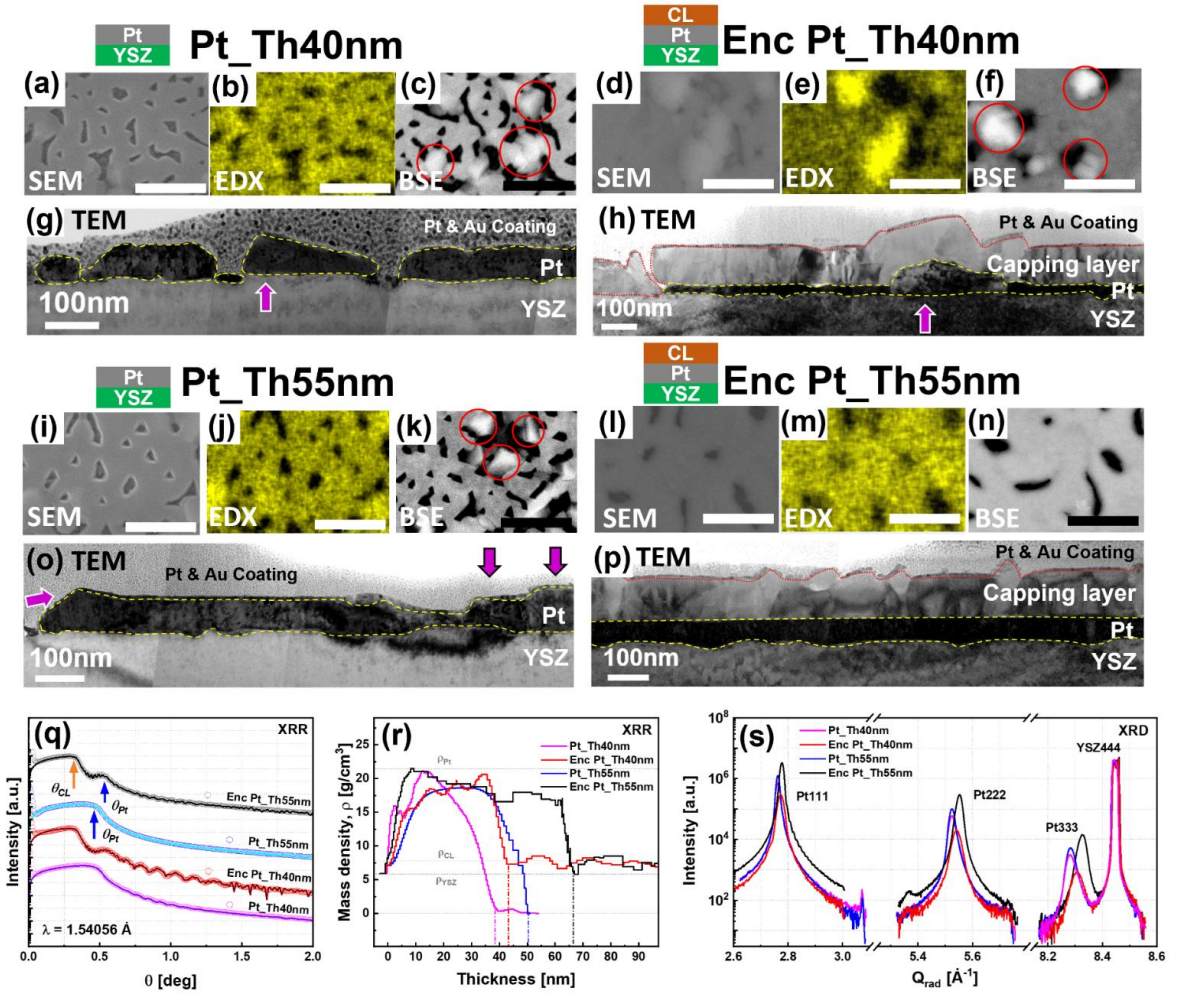

Figure A-10: A magnified version of Figure 4.14[172].

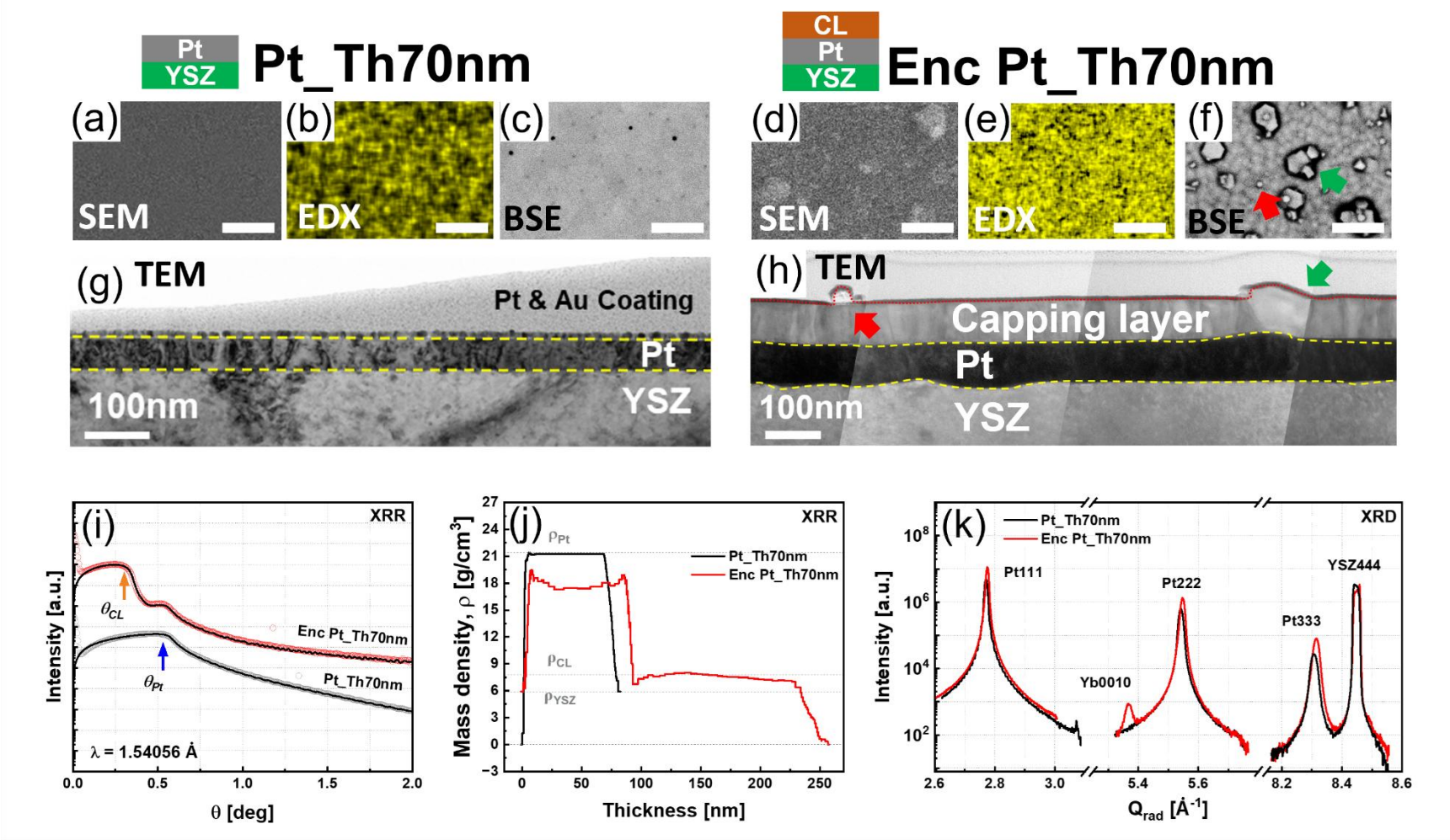

Figure A-11: A magnified version of Figure 4.15[172].

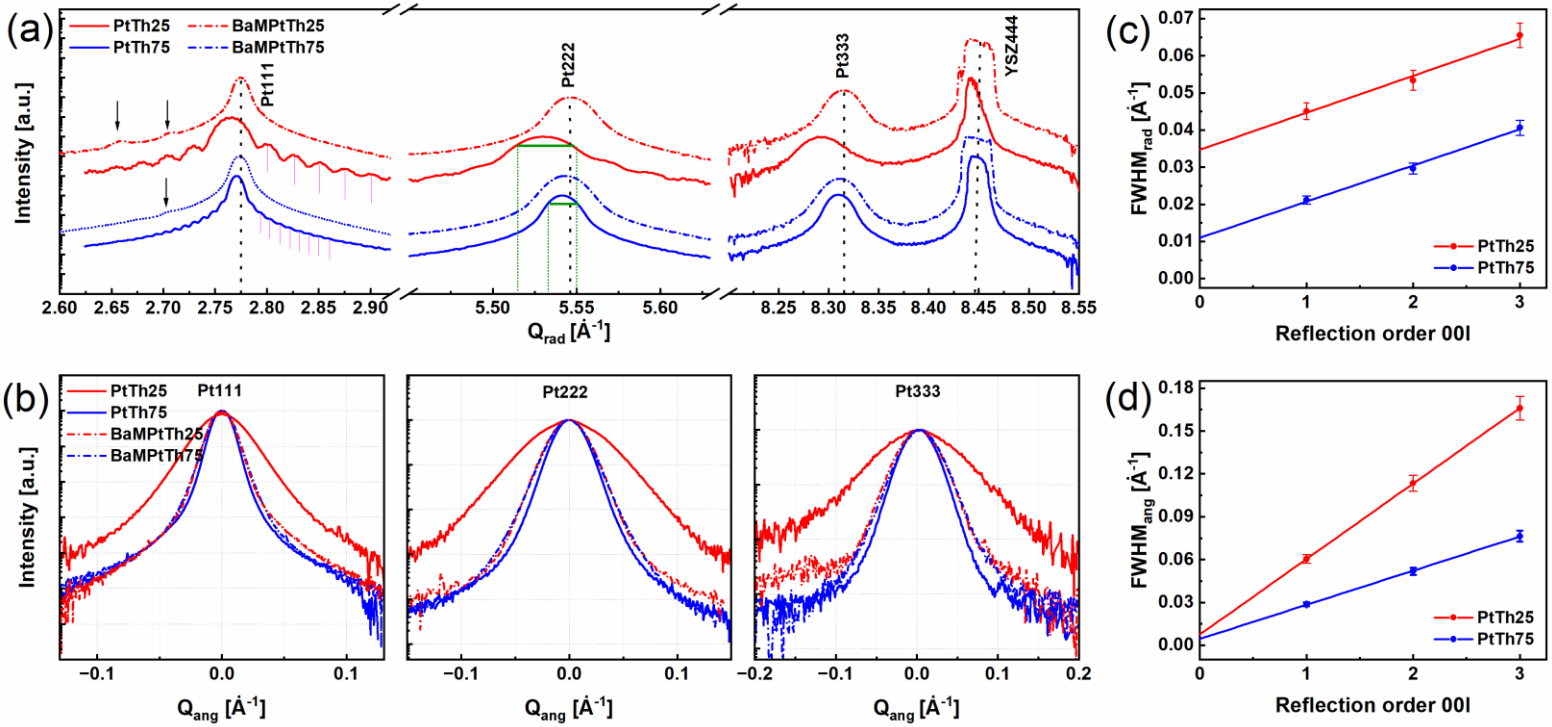

Figure A-12: A magnified version of Figure 5.2[107].

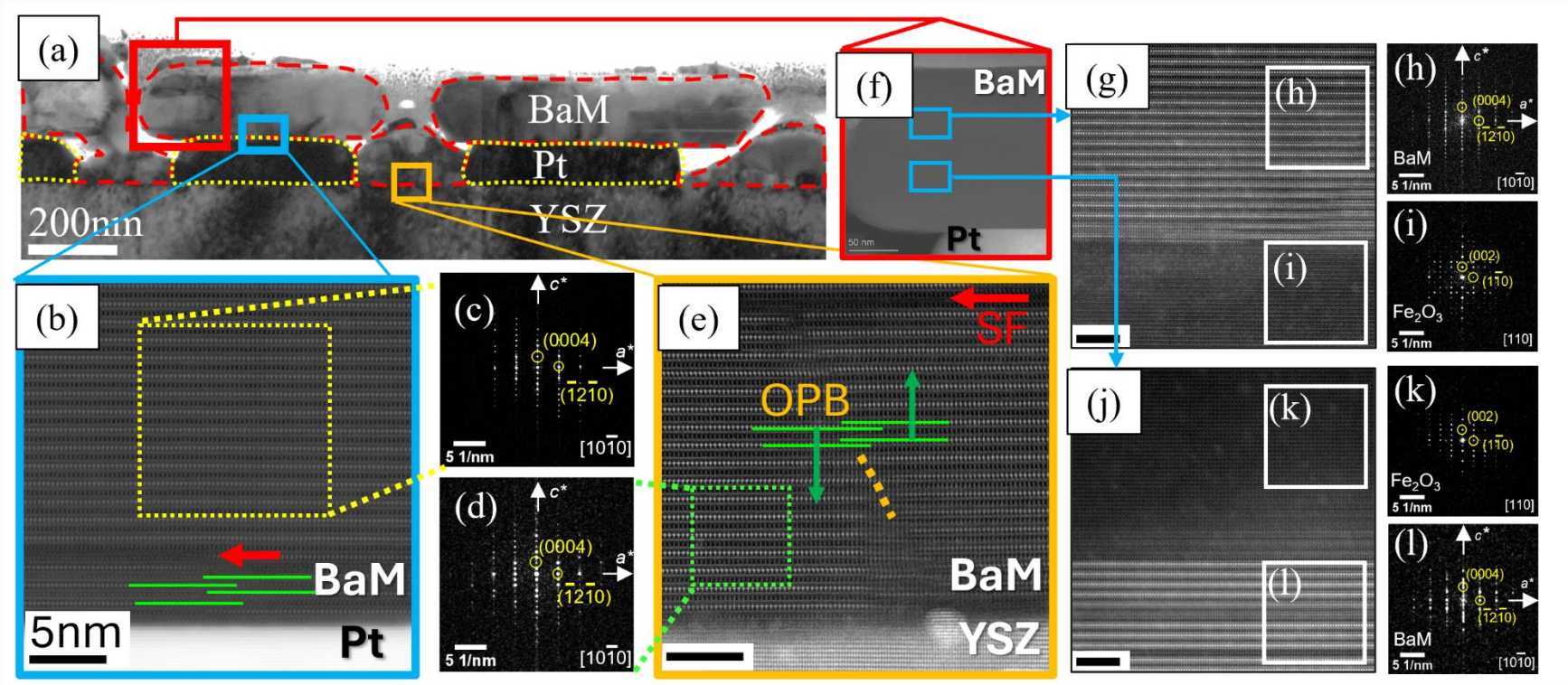

Figure A-13: A magnified version of Figure 5.8[107].

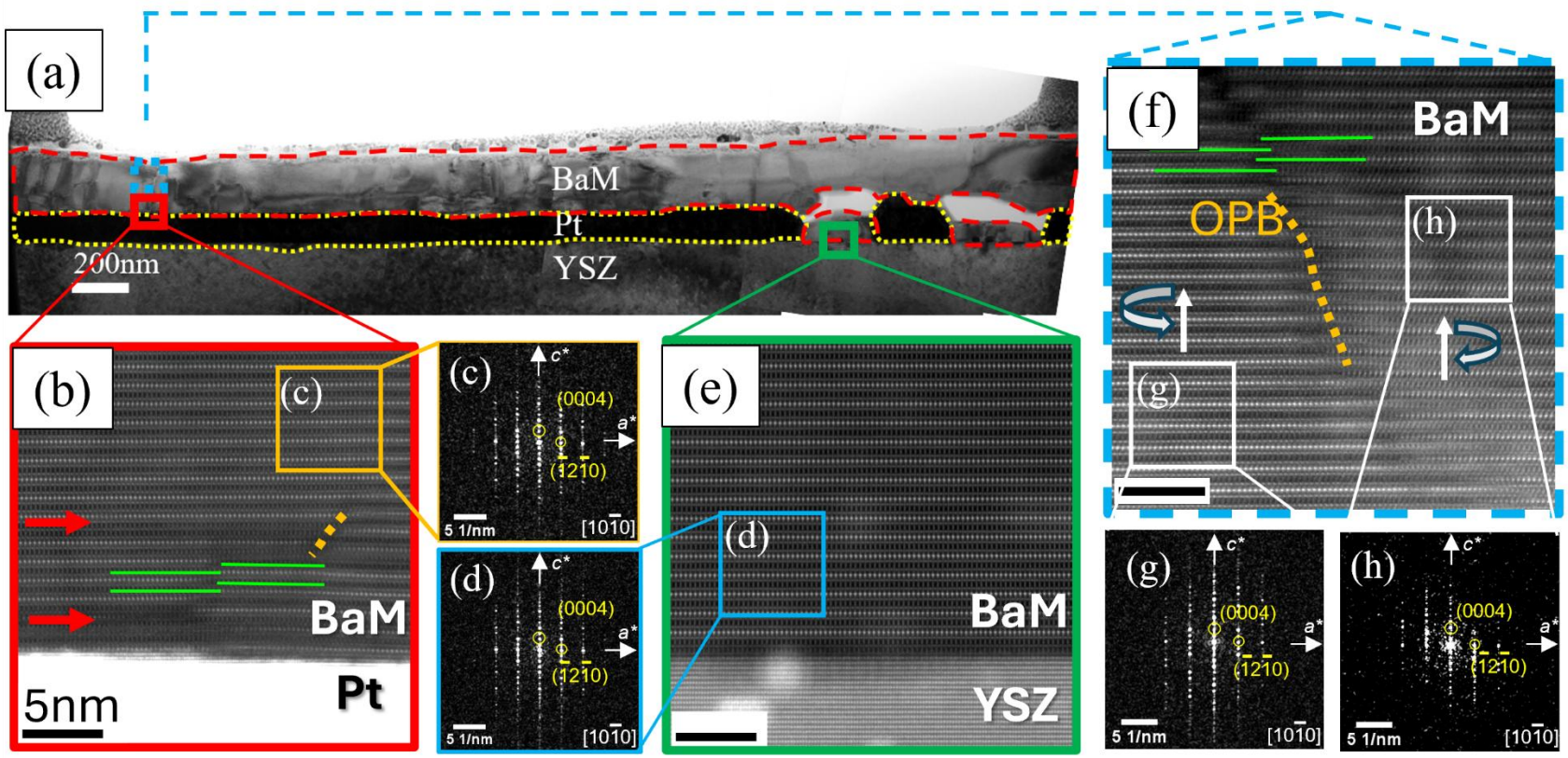

Figure A-14: A magnified version of Figure 5.9[107].

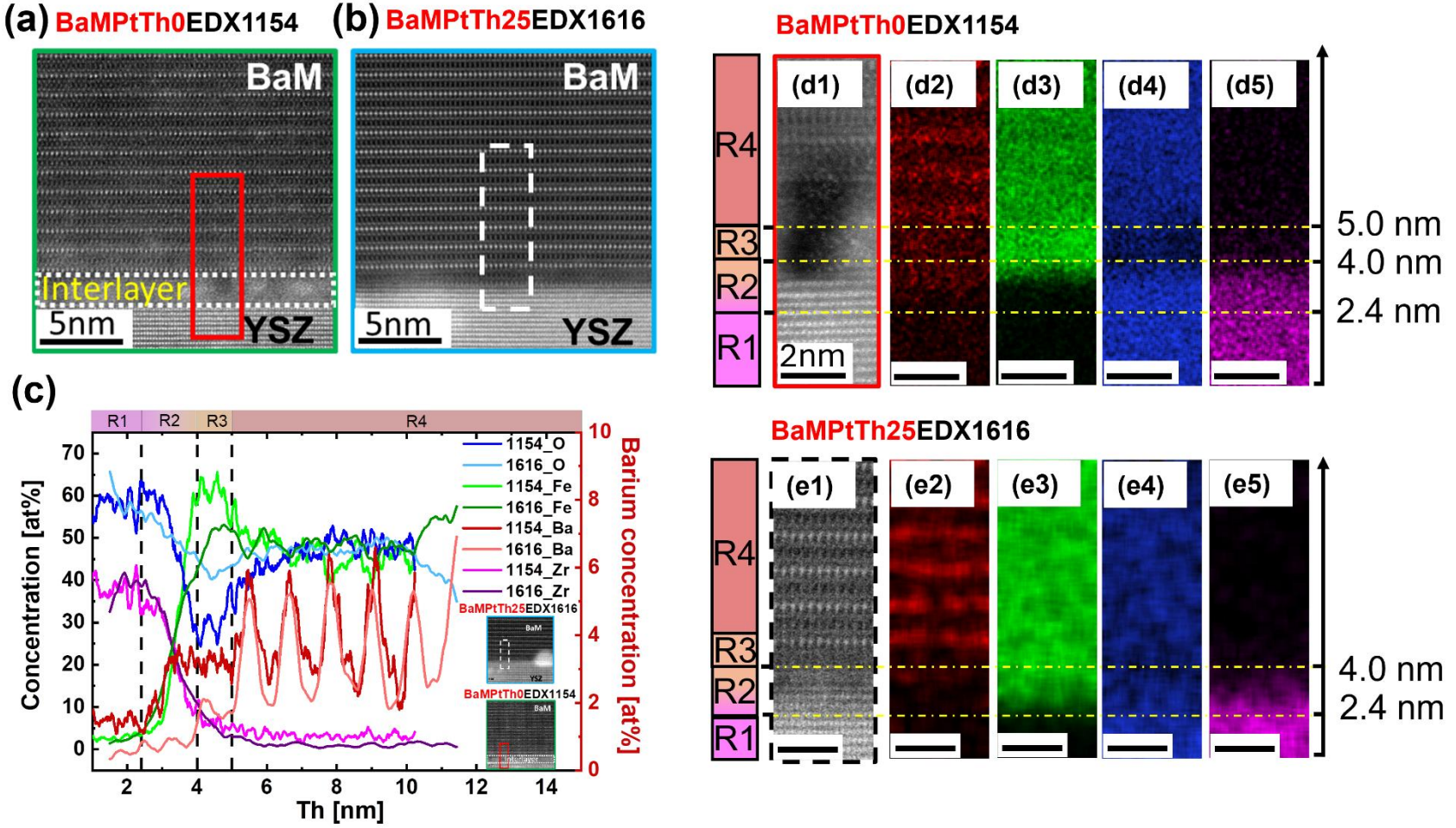

Figure A-15: A magnified version of Figure 5.11[107].

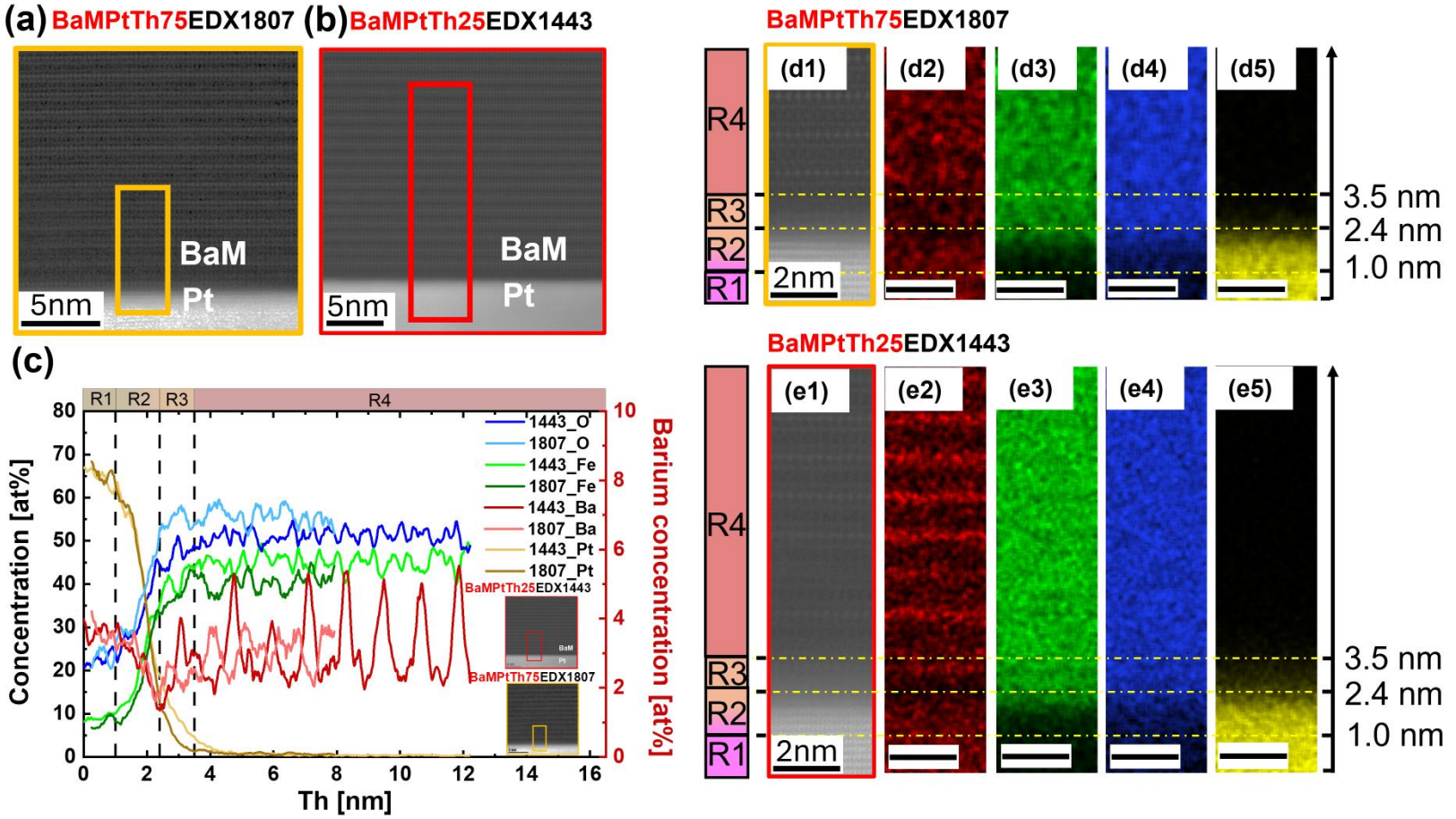

Figure A-16: A magnified version of Figure 5.12[107].

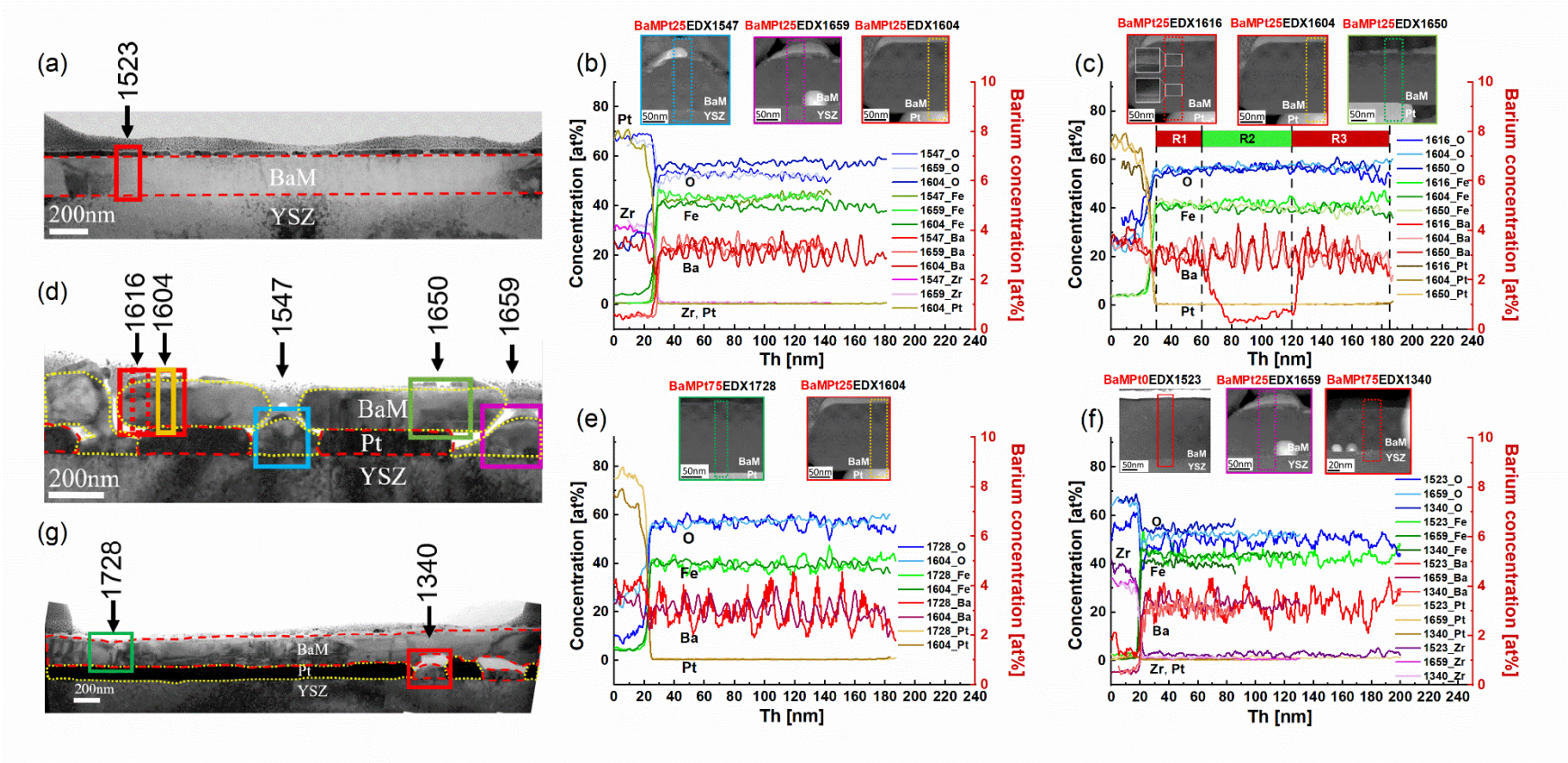

Figure A-17: A magnified version of Figure 5.13[107].

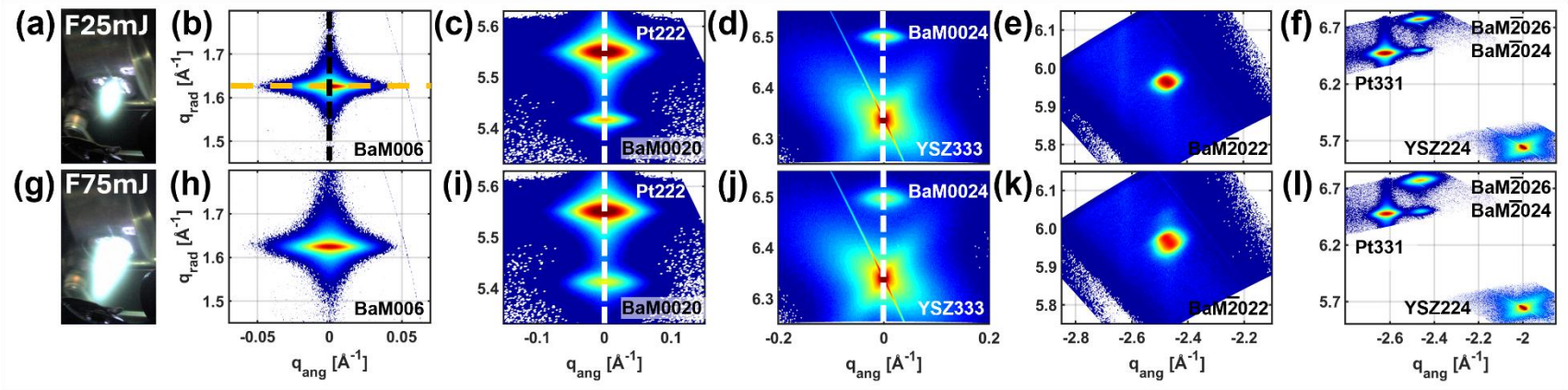

Figure A-18: A magnified version of Figure 5.17[80].

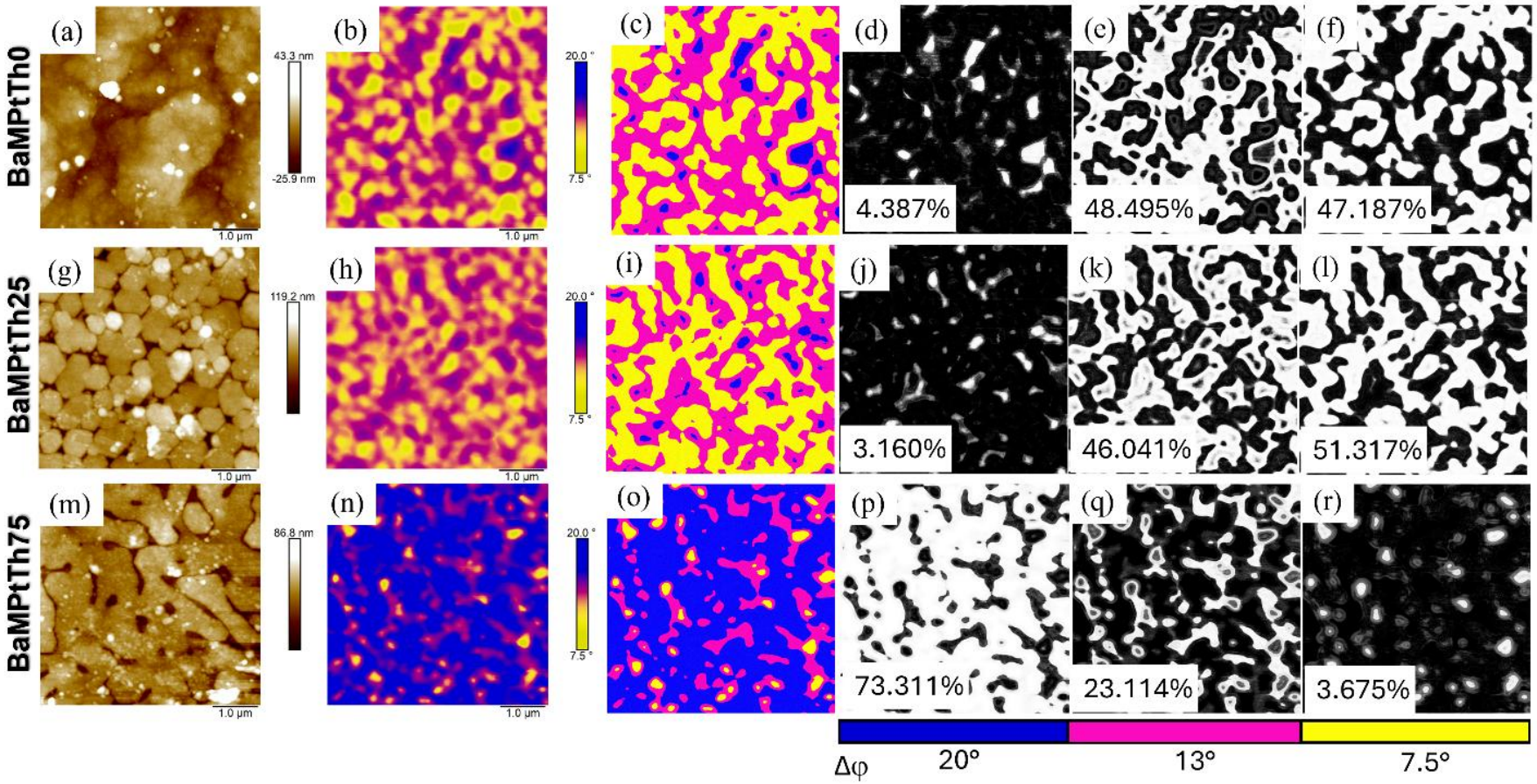

Figure A-19: The images of AFM (a, g, m), MFM (b, h, n), corresponding segmented images of MFM by using Weka Trainable Segmentation plug-in of ImageJ (c, i, o), blue (d, j, p), magenta (e, k, q) and yellow (f, l, r) channel binary images of BaMPtTh0, BaMPtTh25 and BaMPtTh75 samples, respectively. The blue regions (d, j, p) correspond to magnetic domains with the highest spin orientation with phase shift $\Delta\varphi$ = 20 degrees while the yellow regions (f, l, r) refer to the magnetic grains with the lowest spin orientation of phase shift $\Delta\varphi$ = 7.5 degrees. The magenta regions were originated by the intermediate spin orientation with phase shift $\Delta\varphi$ = 13 degrees[80].

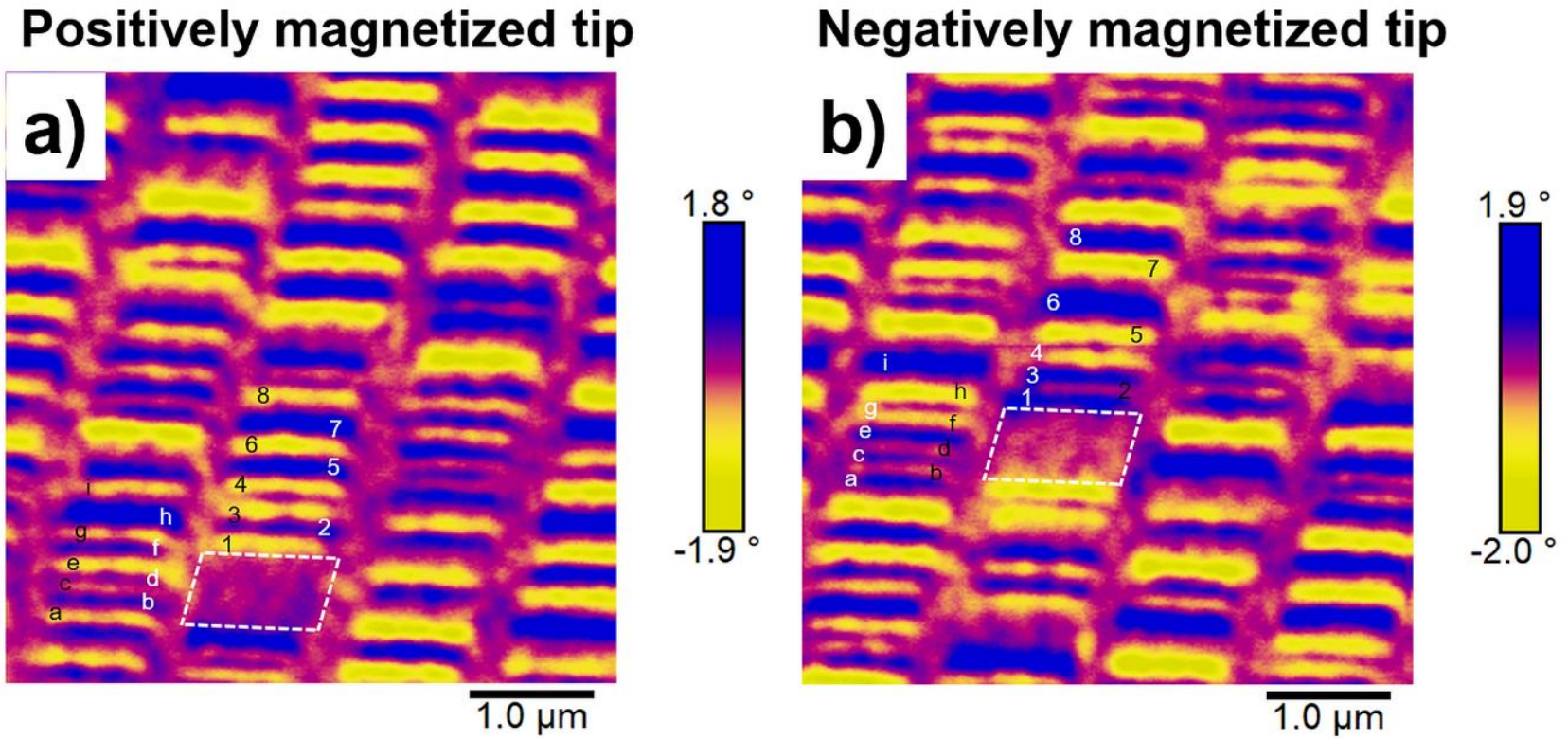

Figure A-20: MFM images of the HDD surface showing topographic and magnetic contrast. (a) MFM image obtained using a positively magnetized tip, and (b) MFM image obtained using a negatively magnetized tip[80].

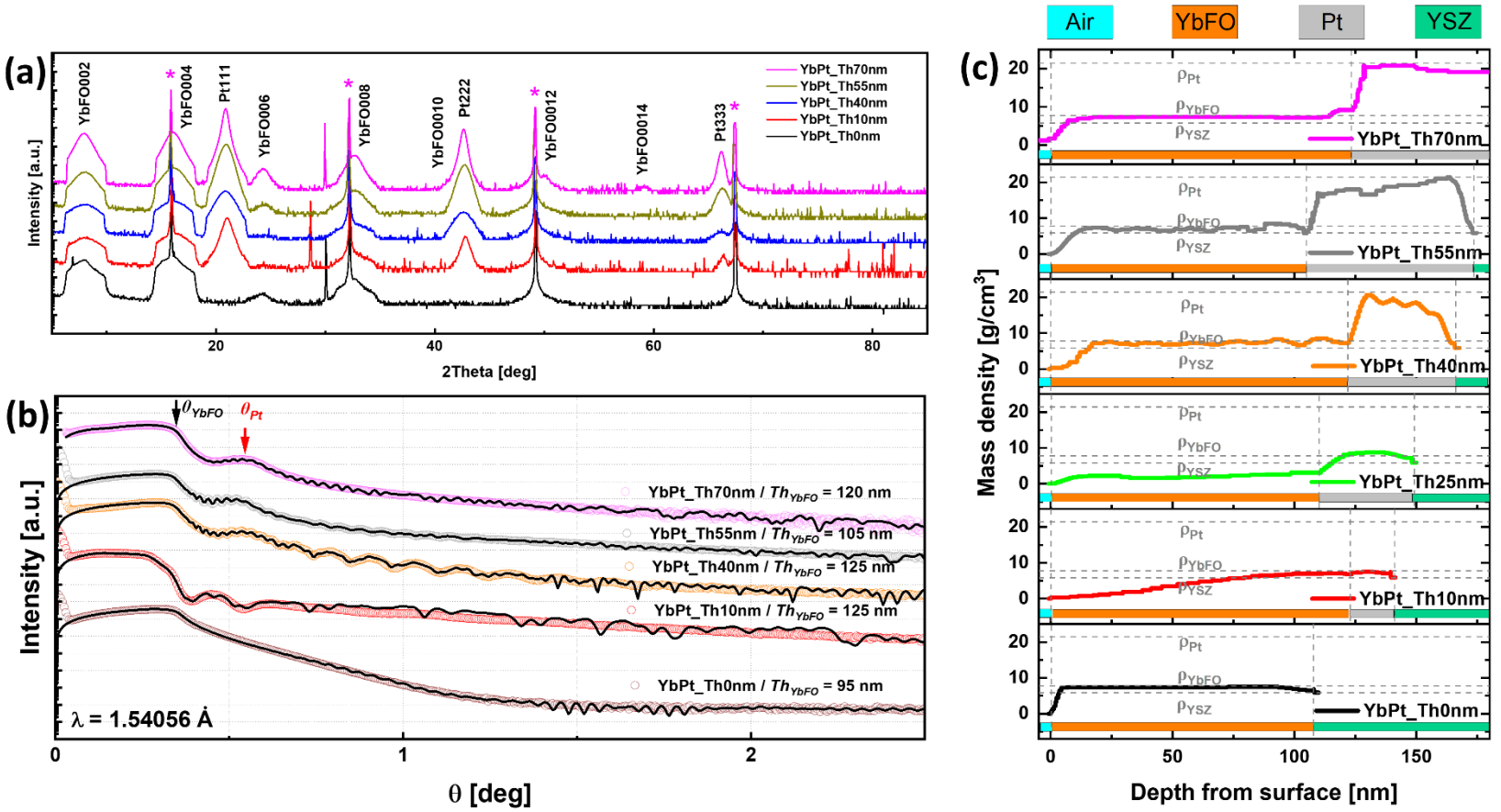

Figure A-21: A magnified version of Figure 6.1[241].

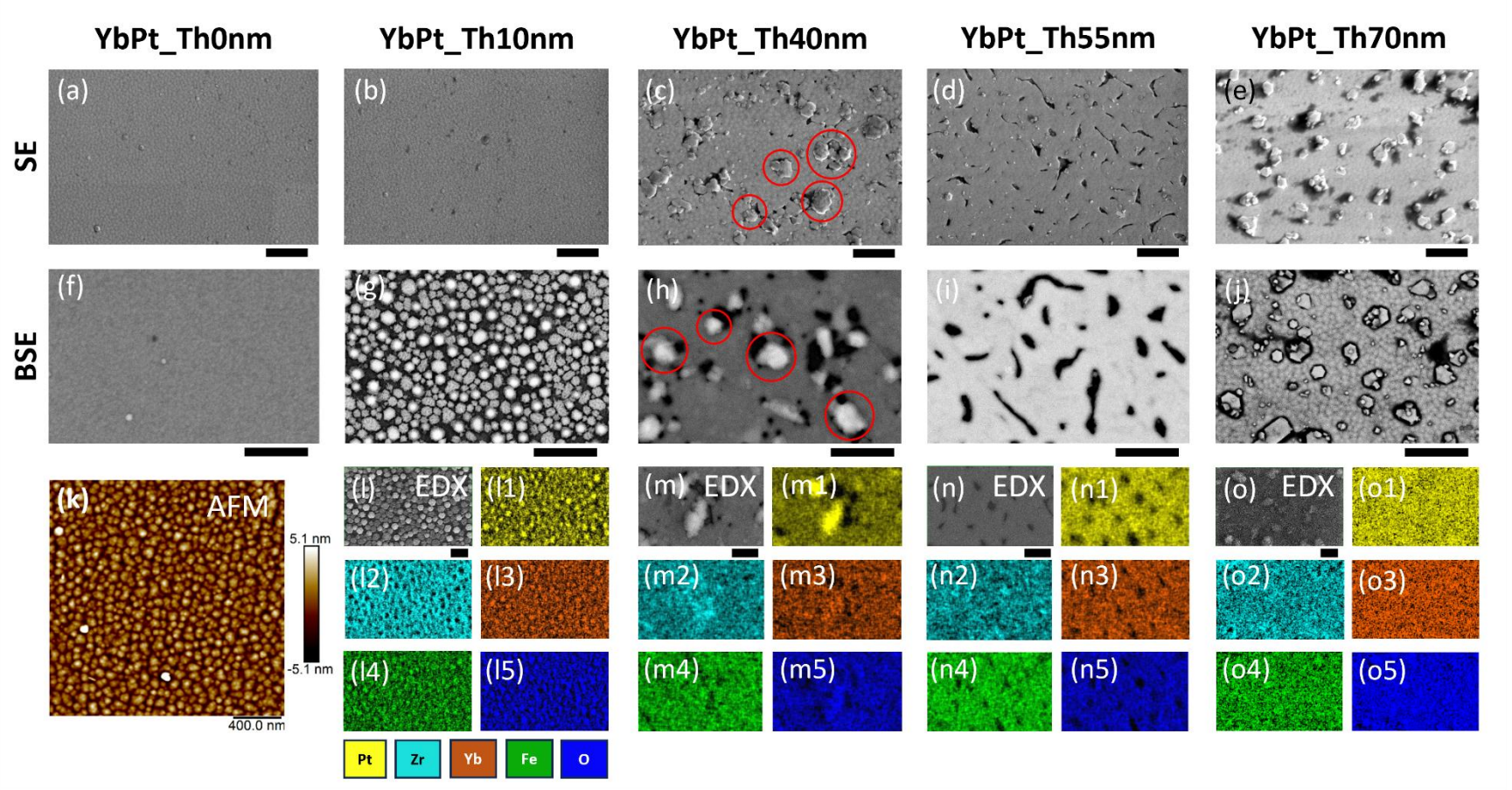

Figure A-22: A magnified version of Figure 6.2[241].

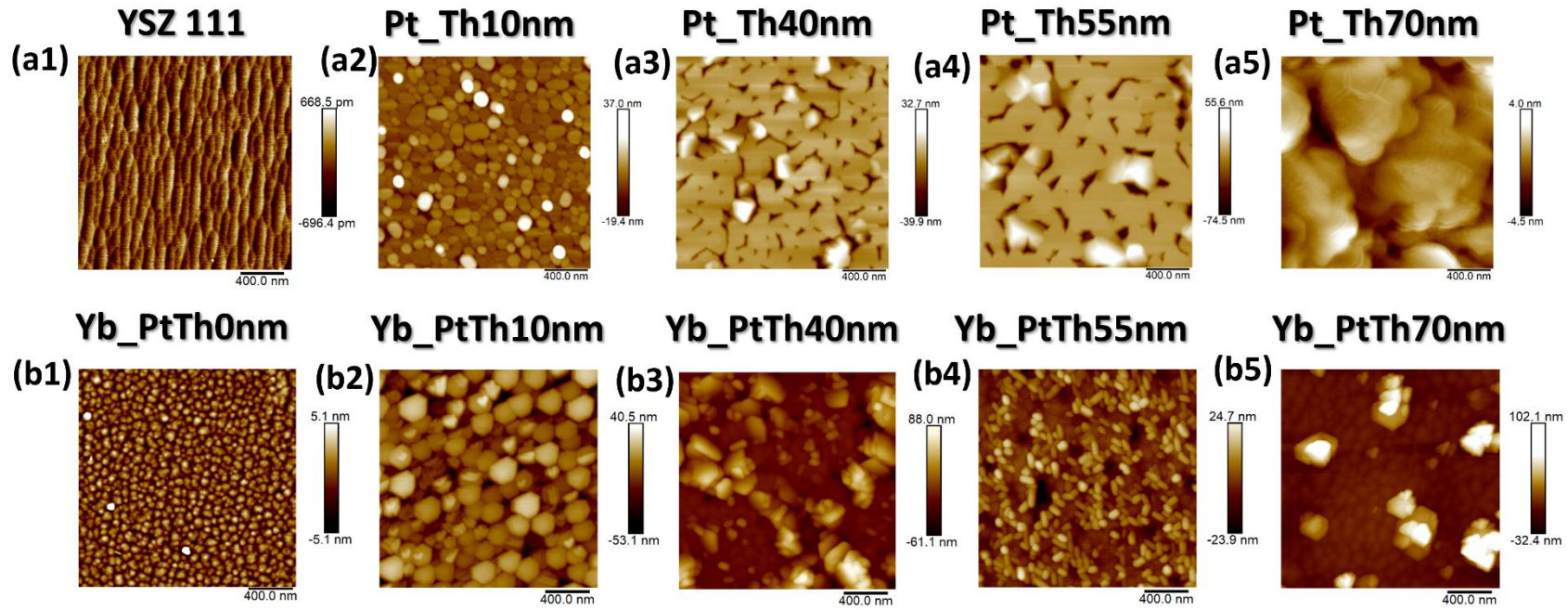

Figure A-23: A magnified version of Figure 6.3[241].

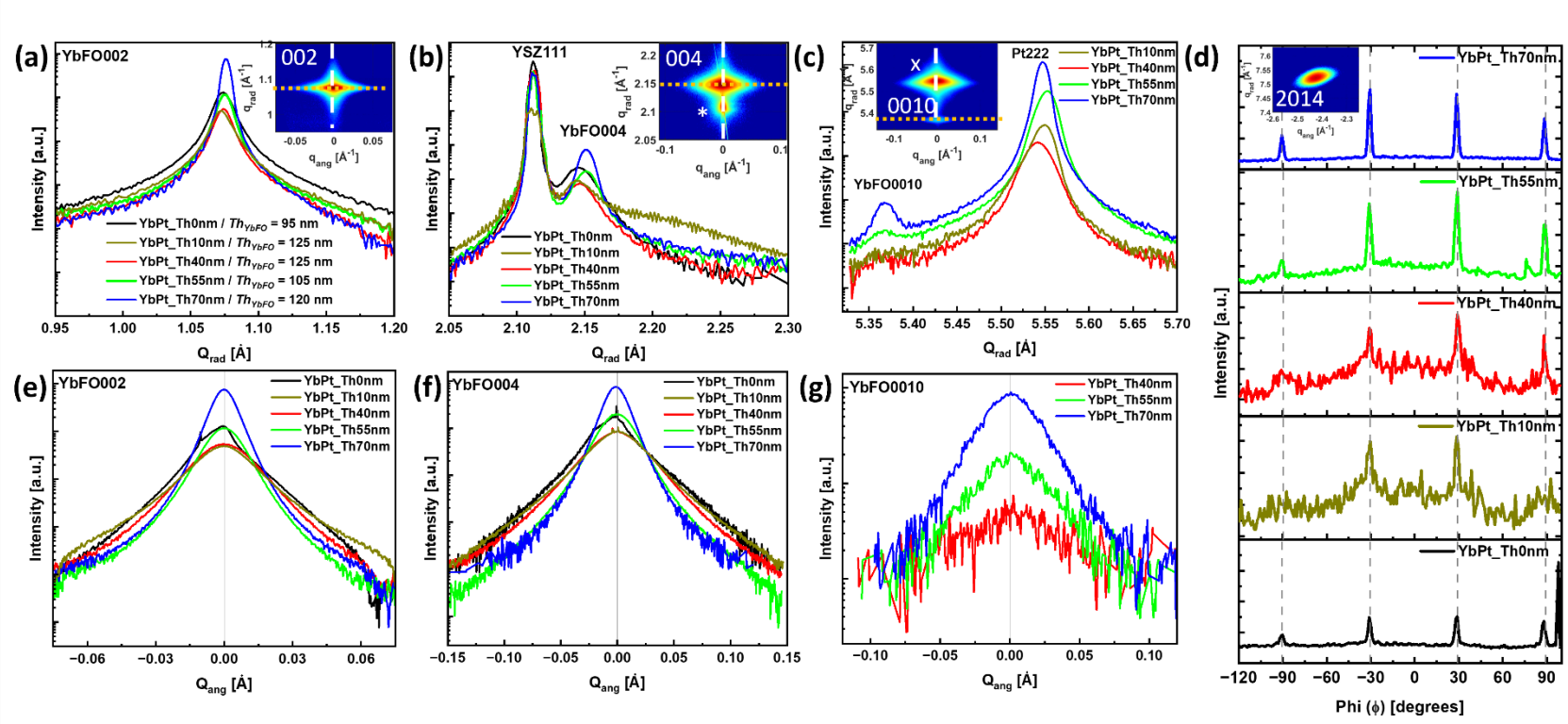

Figure A-24: A magnified version of Figure 6.4[241].

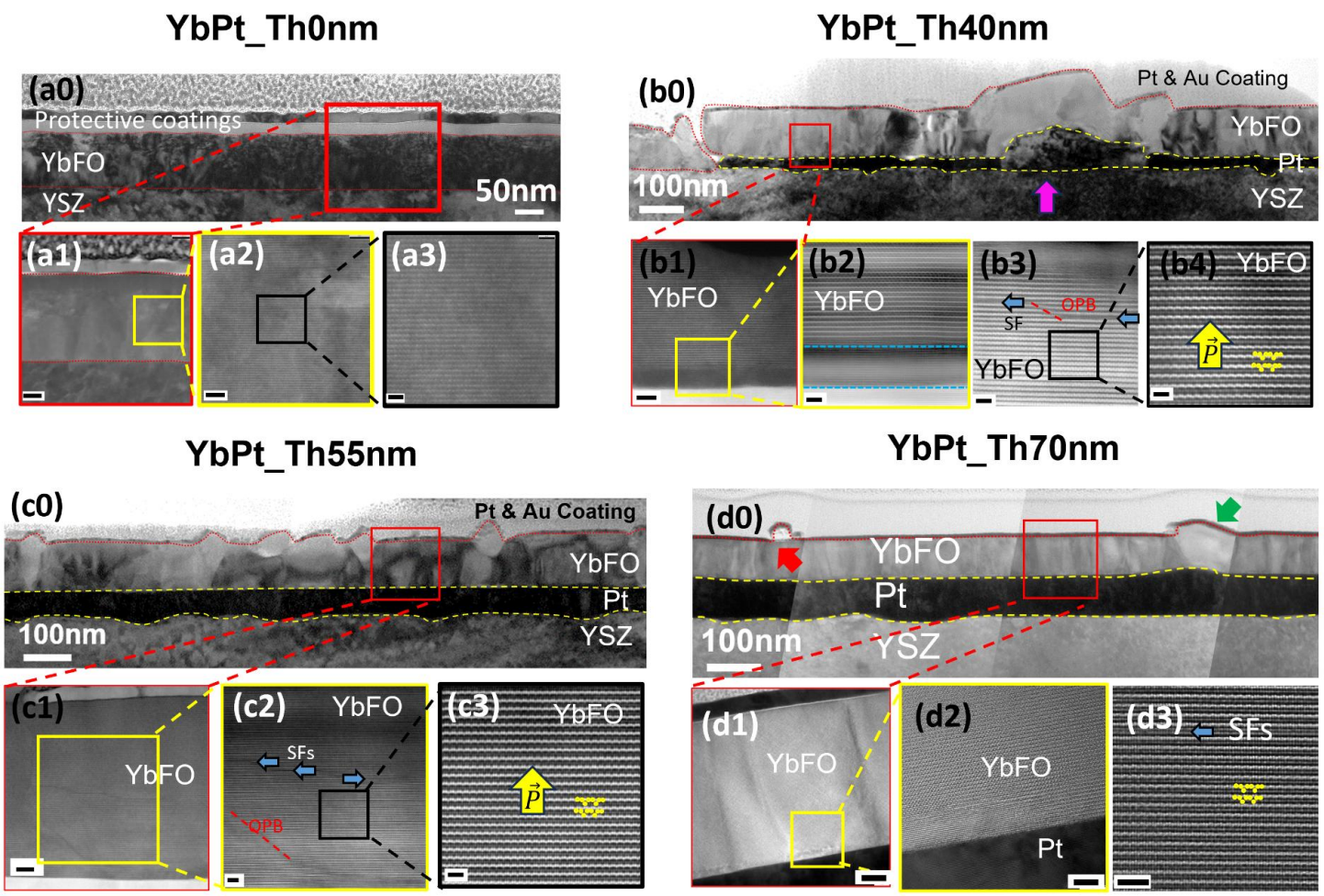

Figure A-25: A magnified version of Figure 6.6[241].

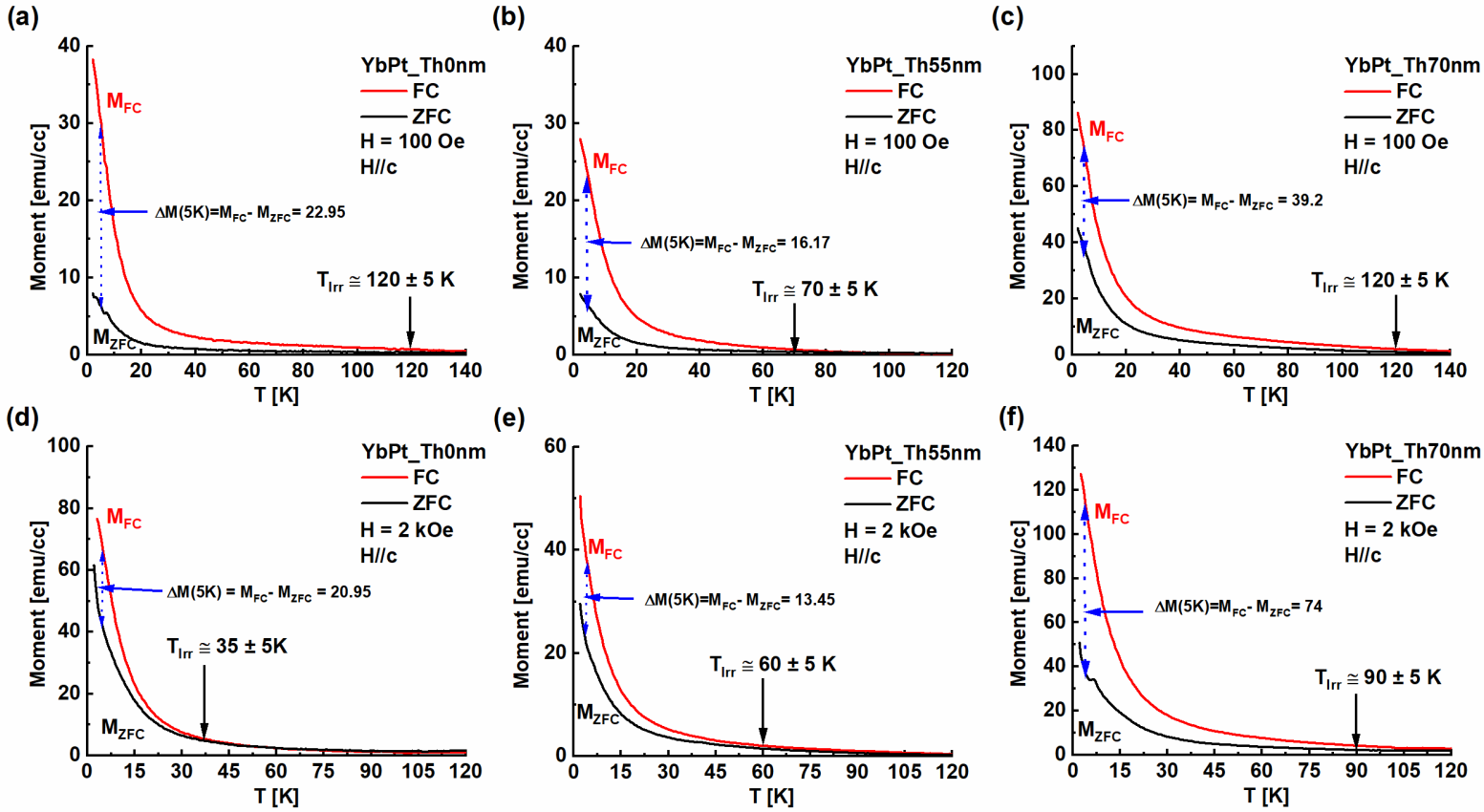

Figure A-26: A magnified version of Figure 6.8[241].

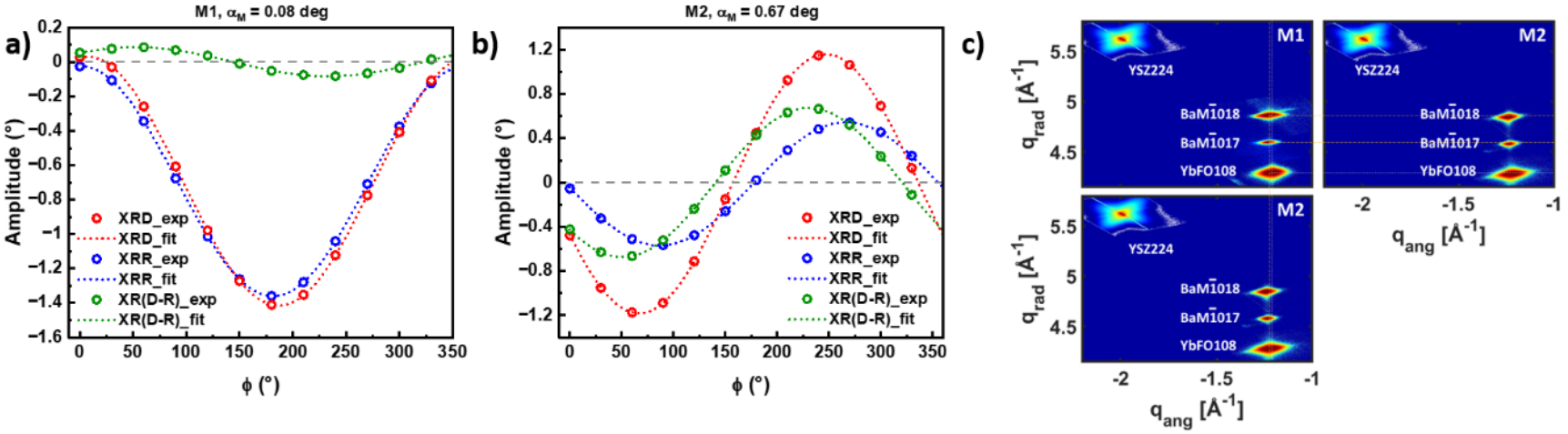

Figure A-27: (a) M1, (b) M2, and the tilt of the surface and the YSZ crystal lattice is presented. The surface inclination is marked by blue points, the tilt of the YSZ substrate's crystal lattice by red points, and the green points represent the discrepancy in inclination, namely, the miscut, across various azimuths. The lines in the graph are the result of fitting the experimental data. (c) HR-RSMs for M1 and M2 heterostructures of BaM-1018, BaM-1017, YbFeO108, YSZ 222 and YSZ133 reflections. Dashed lines are showing the relative shift of the reflections with respect to each other to emphasize the lattice parameter change[242].

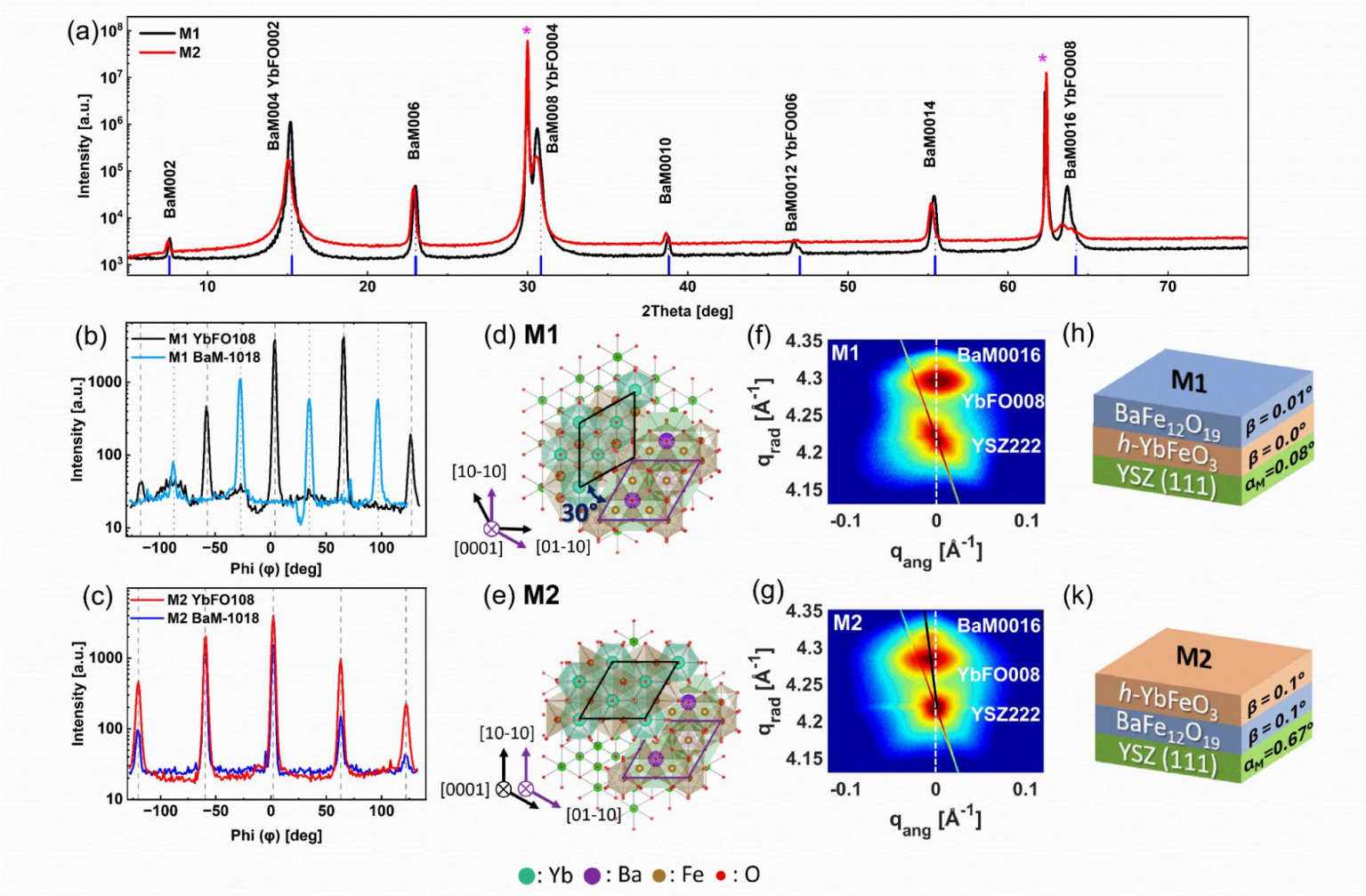

Figure A-28: A magnified version of Figure 7.1[242].

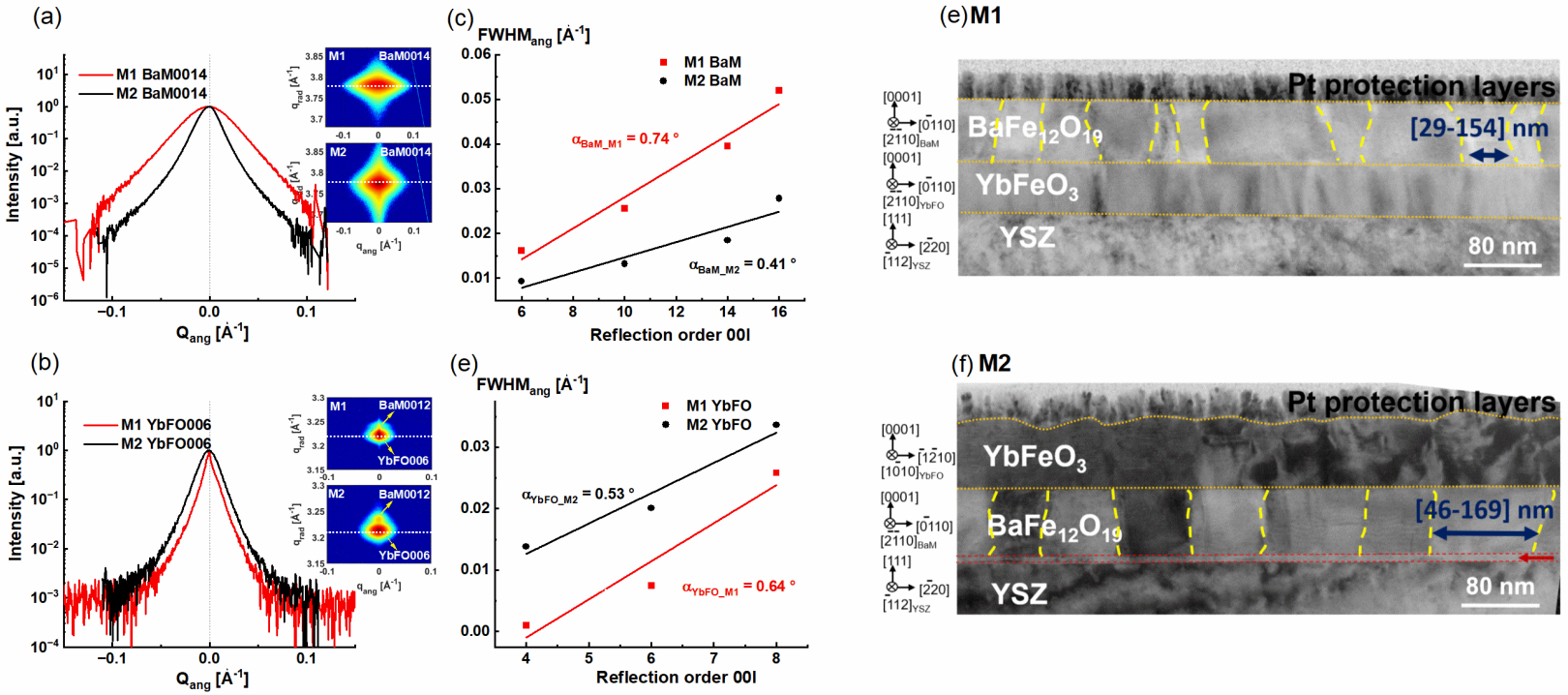

Figure A-29: A magnified version of Figure 7.2[242].

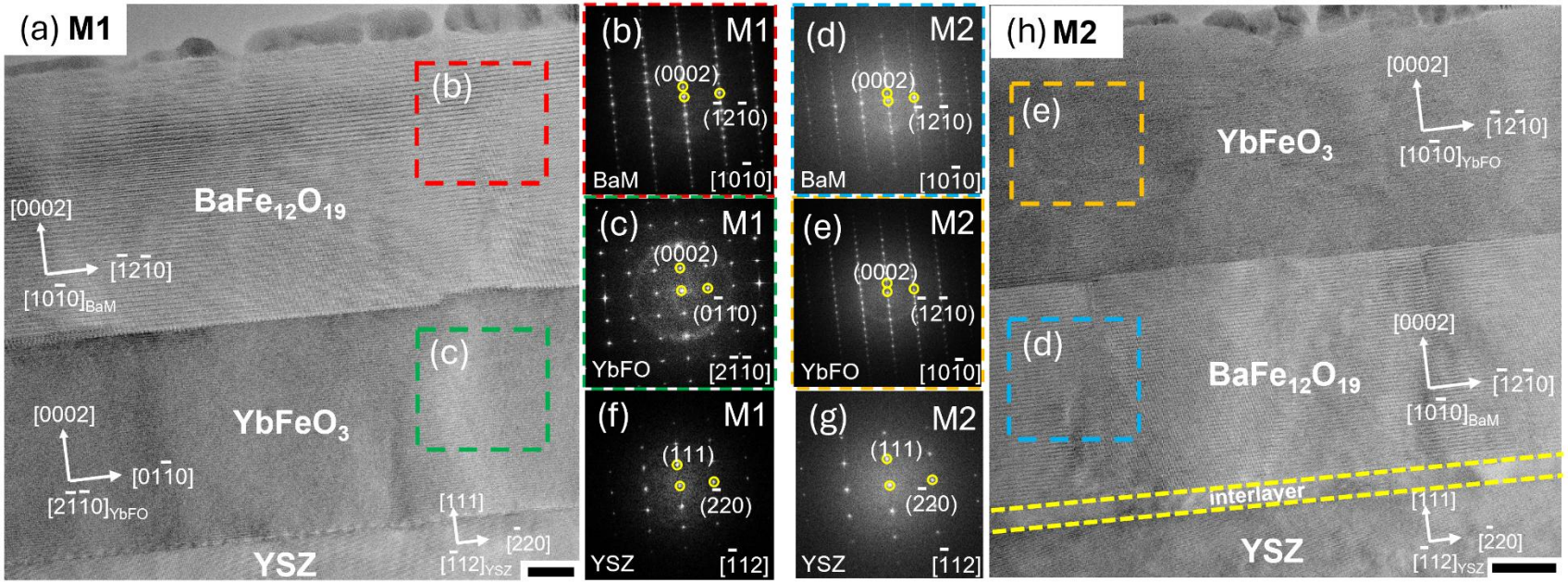

Figure A-30: A magnified version of Figure 7.3[242].

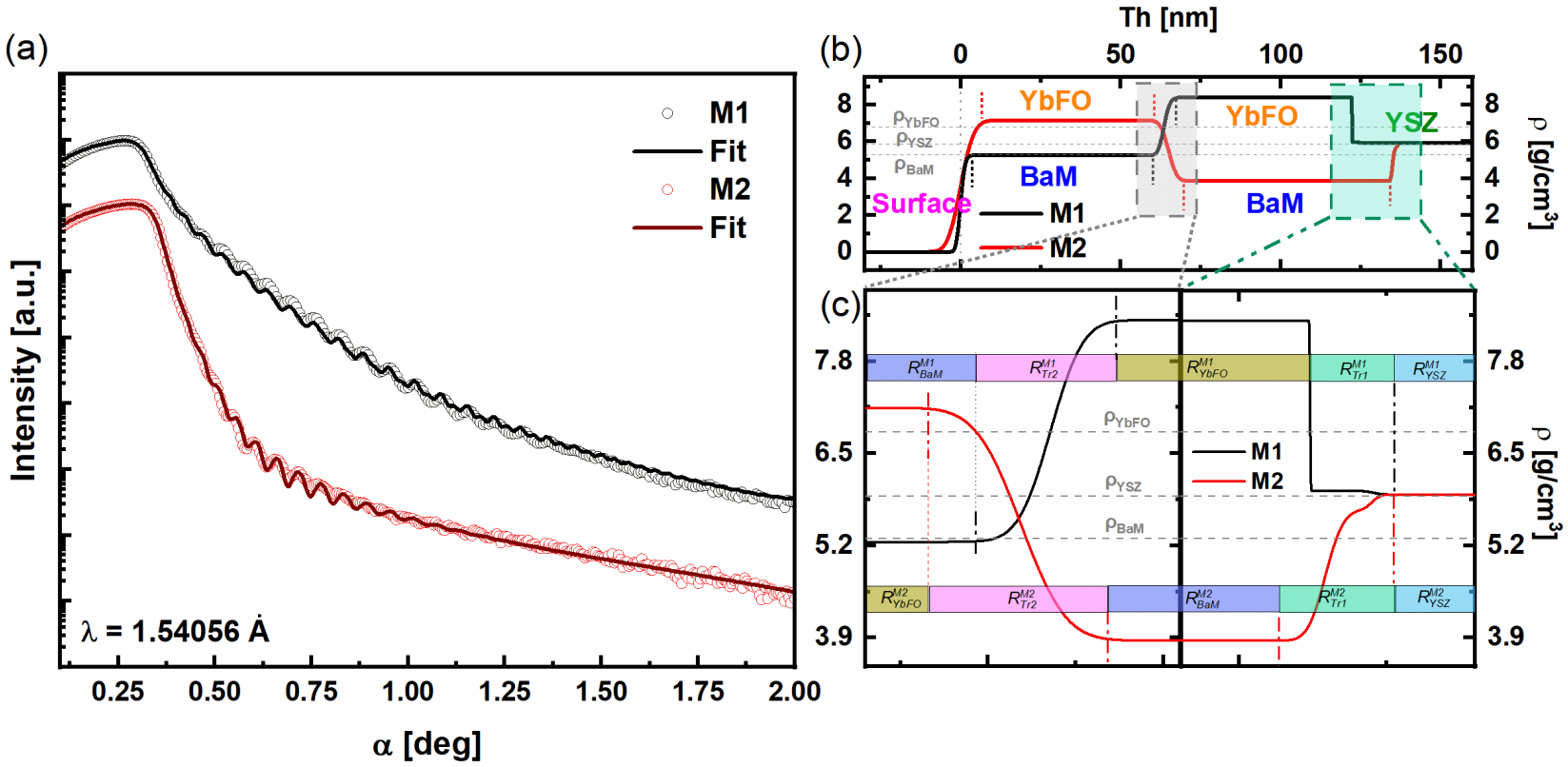

Figure A-31: A magnified version of Figure 7.4[242].

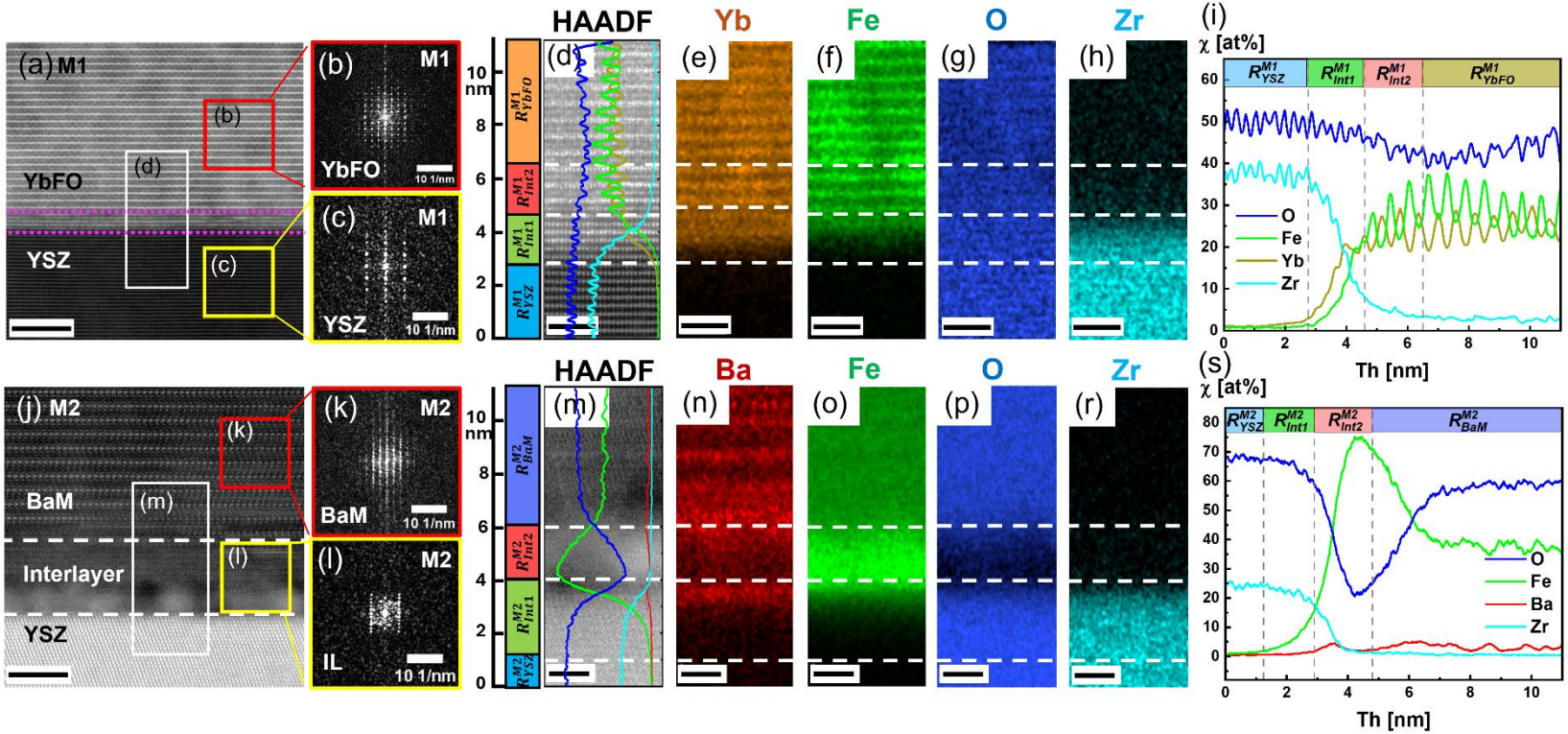

Figure A-32: A magnified version of Figure 7.5[242].

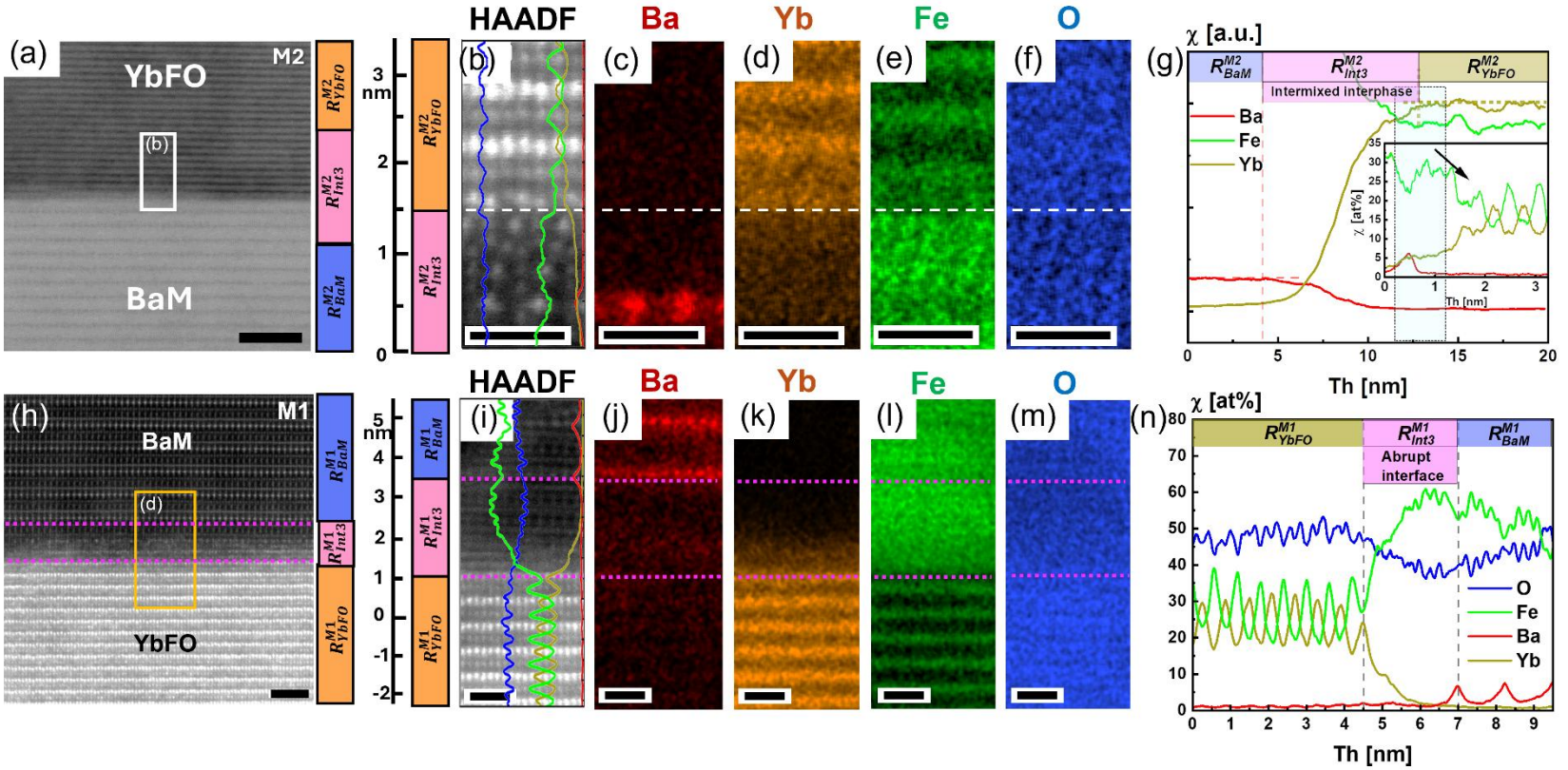

Figure A-33: A magnified version of Figure 7.6[242].

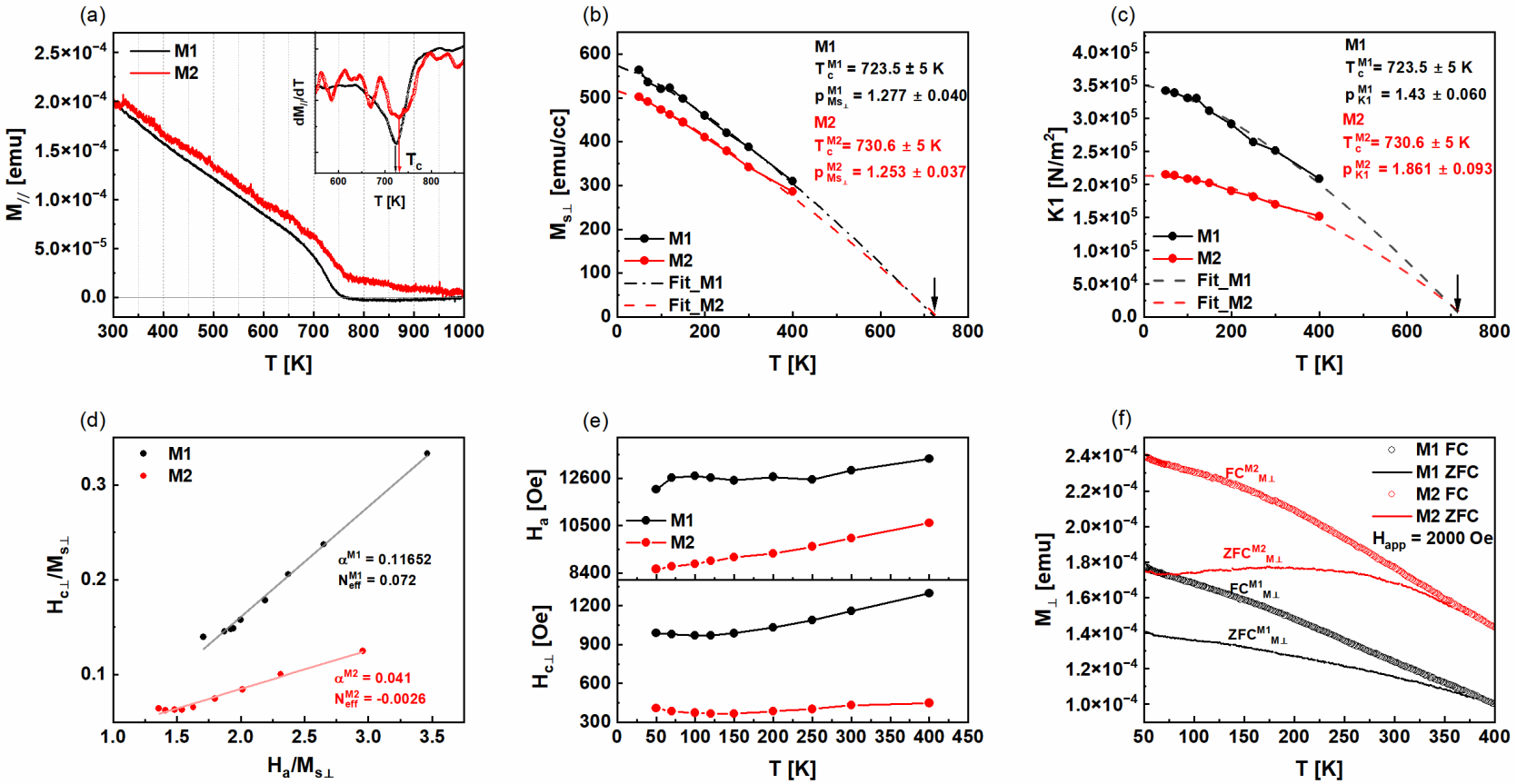

Figure A-34: A magnified version of Figure 7.9[242].

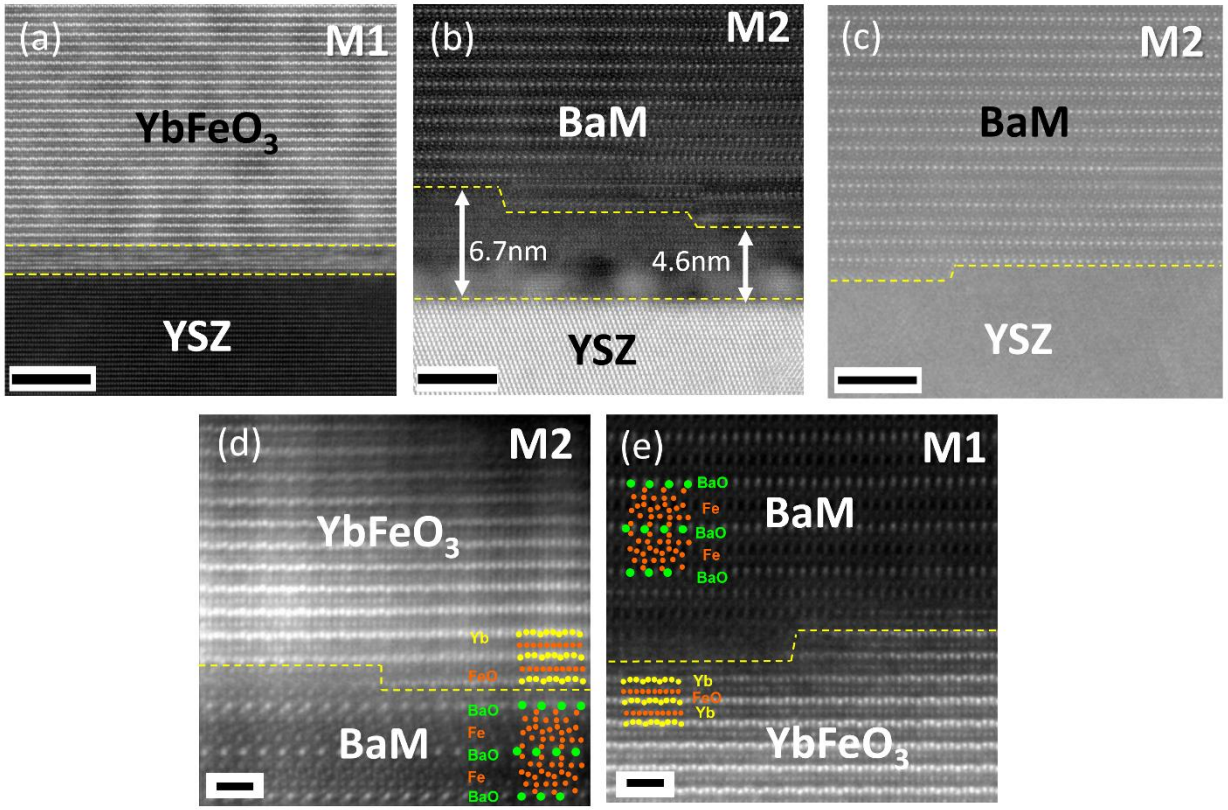

Figure A-35: Additional atomic resolution HAADF images of the M1 and M2 systems focusing on the interfaces: (a) Shows the YbFO/YSZ interface in the M1 system, highlighting an interlayer with a yellow dashed line, (b) depicts the BaM/YSZ interface in the M2 system, where a significant interlayer varying from 4.6 to 6.7 nm is marked by yellow dashed lines along with atomic steps at the BaM interface, (c) illustrates the BaM/YSZ interface in M2 without an interlayer, with miscut-related YSZ surface steps indicated by a yellow dashed line, (d) presents the YbFO/BaM interface in M2, where interface atomic steps are outlined by a yellow dashed line, and individual atoms are identified by colored filled circles, and (e) features the BaM/YSZ interface in M1, showcasing surface steps on YbFO with a yellow dashed line and atom identification using colored circles. The scale bars for (a-c) are 5nm and (d-e) are 1 nm in size[242].

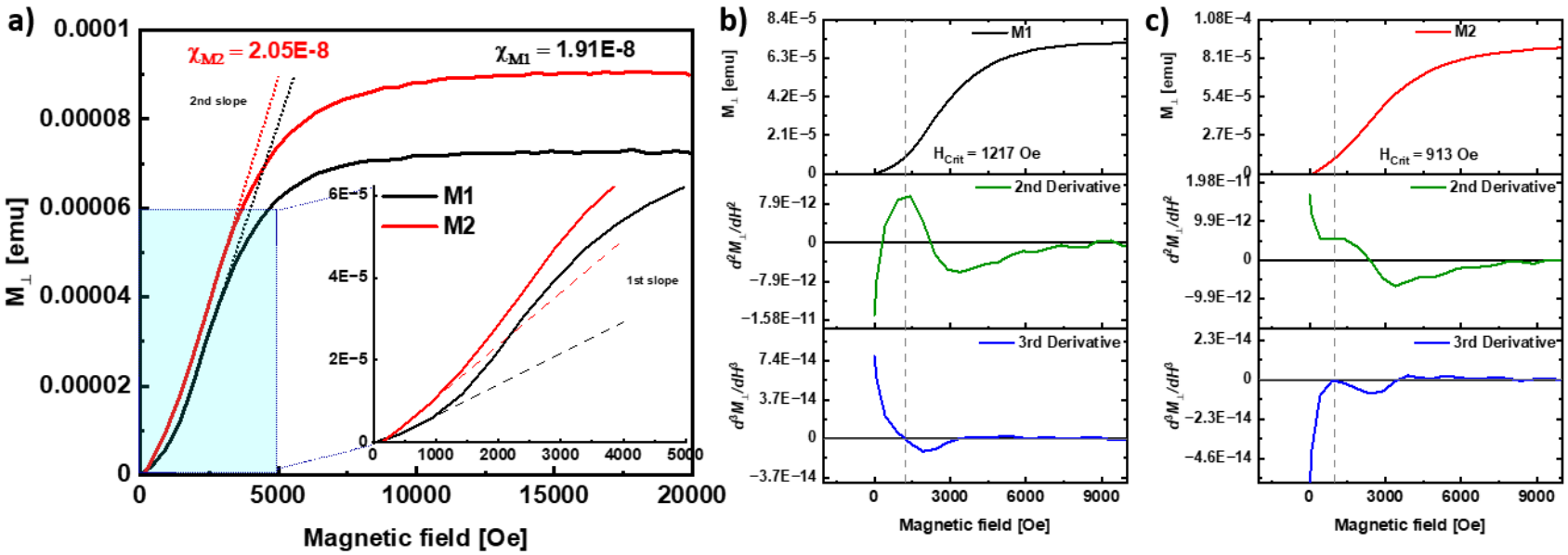

Figure A-36: Initial magnetisation and H_{crit} analysis for M1 and M2 heterostructures (a) shows initial magnetization curves for M1 and M2, with an inset detailing two-slope behaviour and determination of H_{crit} (highlighted by dashed lines). (b, c) Shows the initial magnetisation and its derivatives for (b) M1 and (c) M2, identifying H_{crit} at the zero point of the third derivative, H_{crit} is marked by vertical dashed line[242].

Table A-1: Growth temperatures and calculated homologous temperature T_h according to Movchan and Demchishin[85,86].

	Growth temperature, T_g [°C]	Growth temperature, T_g [K]	$T_h = T_g / T_m$
Pt T_m = 1768 °C[294] (2041 K)	300	573	0.28
	500	773	0.38
	700	973	0.48
	900	1173	0.57

Table A-2: The FWHM of the angular and radial broadening of BaM (004), (006), (0012), (0014) and (0022) reflections of BaMPtTh0, BaMPtTh25 and BaMPtTh75 samples as it was derived from the fitting with the Pseudo-Voight function[107].

Angular	***FWHM*$_{ang}$ (004) [Å^{-1}]**	***FWHM*$_{ang}$ (006) [Å^{-1}]**	***FWHM*$_{ang}$ (0012) [Å^{-1}]**	***FWHM*$_{ang}$ (0014) [Å^{-1}]**	***FWHM*$_{ang}$ (0022) [Å^{-1}]**
BaMPtTh0	0.00665	0.01022	0.01833	0.02216	0.03514
BaMPtTh25	0.00746	0.01114	0.02221	0.02588	0.04061
BaMPtTh75	0.0074	0.0118	0.02357	0.02769	0.04278
Radial	***FWHM*$_{rad}$ (004) [Å^{-1}]**	***FWHM*$_{rad}$ (006) [Å^{-1}]**	***FWHM*$_{rad}$ (0012) [Å^{-1}]**	***FWHM*$_{rad}$ (0014) [Å^{-1}]**	***FWHM*$_{rad}$ (0022) [Å^{-1}]**
BaMPtTh0	0.0063	0.00877	0.0152	0.01662	0.02407
BaMPtTh25	0.00671	0.00809	0.01367	0.01595	0.02265
BaMPtTh75	0.00656	0.00937	0.01501	0.01763	0.02387

Table A-3: Summary of different thicknesses for the BaM, Pt underlayer and other found interlayer as it could be determined from XRR, (TEM/EDX) investigations methods[107].

	Layer material	BaM thickness (XRR) Th_{BaM} [nm]	BaM thickness (TEM-EDX) Th_{BaM} [nm]	Interlayer thick-ness (XRR) Th_{int} [nm]	Interlayer thick-ness (TEM-EDX) Th_{int} [nm]	Pt thickness (XRR) Th_{Pt} [nm]	Pt thickness (TEM) Th_{Pt} [nm]
PtTh0	YSZ	-	-	-	-	-	-
PtTh25	Pt/YSZ	-	-	-	-	6.73 ± 0.31 25.83 ± 0.05	25.5 [20 – 31]
PtTh75	Pt/YSZ	-	-	-	-	68.64 ± 0.72	51.0 [47 – 55]
BaMPtTh0	BaM/YSZ	169.67 ± 0.86	178.70	7.04 ± 2.14		-	-
BaMPtTh25	BaM/Pt	151.19 ± 1.57	155.00	-	-	114.22 ± 1.45	95.42 [88.90-109.09]
BaMPtTh75	BaM/Pt	163.00 fixed	163.00	-	-	100.75 ± 1.87	84.13 [69.90-92.40]

Table A-4: Summary of the surface and interfaces roughness, which were derived from the XRR fitting curves using the Leptos software. Interlayer corresponds to the amorphous interlayer revealed in from the TEM micrographs of Figure 6. The type and the number of interfaces are Pt/YSZ (PtTh0, PtTh25, PtTh75, BaMPth25, BaMPtTh75), BaM/Pt (BaMPth25, BaMPtTh75), BaM/interlayer (BaMPtTh0), and Interlayer/YSZ (BaMPtTh0) [107].

	Layer material	Surface roughness R_{surf} at BaM or Pt [nm]	Interface roughness R_{int} at BaM/Inter-layer [nm]	Interface roughness R_{int} at Interlayer/YSZ [nm]	Interface roughness R_{int} at BaM/Pt [nm]	Interface roughness R_{int} at Pt/YSZ [nm]
PtTh0	YSZ		-	-	-	0.34 ± 0.04 YSZ/Air
PtTh25	Pt/YSZ	2.54 ± 0.33	-	-	-	R_{int} at Pt/Pt 0.37 ± 0.06 R_{int} at Pt/YSZ 0.87 ± 0.08
PtTh75	Pt/YSZ	0.42 ± 0.01	-	-	-	R_{int} at Pt/YSZ 1.46 ± 0.24
BaMPtTh0	BaM/YSZ	4.16 ± 0.18	2.75 ± 0.67	1.32 ± 0.25	-	-
BaMPtTh25	BaM/Pt/YSZ	5.52 ± 0.08	-	-	3.54 ± 0.17	0.37 ± 0.30
BaMPtTh75	BaM/Pt/YSZ	5.19 ± 0.13	-	-	2.96 ± 0.14	0.23 ± 0.30

Table A-5: Summary of the mass densities of the different layers such YSZ substrate, Pt underlayer, amorphous interlayer and BaM layer of the PtTh0, PtTh25, PtTh75, BaMPtTh0, BaMPth25, BaMPtTh75 samples[107].

	Layer material	Density BaM layer ρ_{BaM} [g/cm^3]	Density amorphous interlayer ρ_{int} [g/cm^3]	Density Pt underlayer ρ_{Pt} [g/cm^3]	Density YSZ substrate ρ_{YSZ} [g/cm^3]
PtTh0	YSZ	-	-	No Pt	5.91 ± 0.04
PtTh25	Pt/YSZ	-	-	8.89 ± 0.40 16.33 ± 0.18	4.04 ± 1.04
PtTh75	Pt/YSZ	-	-	21.36 ± 0.16	5.90 ± Fixed
BaMPtTh0	BaM/YSZ	5.29 ± 0.11	9.08 ± 1.53	-	7.98 ± 2.27
BaMPtTh25	BaM/Pt/YSZ	4.69 ± 0.03	-	10.09 ± 0.19	6.50 ± 0.28
BaMPtTh75	BaM/Pt/YSZ	5.01 ± 0.03	-	11.96 ± 0.23	7.34 ± 1.32

Table A-6: Locally calculated in-plane lattice parameters, lattice mismatch values of YSZ, Pt and BaM by using FFTs of HAADF images of the samples BaMPtTh0, BaMPtTh25 and BaMPtTh75[107].

Diffraction patterns	In-plane (-220) YSZ [Å]	In-plane (-220) Pt [Å]	In-plane (1-210) BaM on YSZ [Å]	In-plane (1-210) BaM on Pt [Å]	BaM/YSZ mismatch	BaM/Pt mismatch
BaMPtTh0	1.8870	No Pt	3.0301	No Pt	-19.71%	No Pt
BaMPtTh25	1.8568	1.4314	3.0091	3.0319	-18.97%	5.11%
BaMPtTh75	1.8788	1.4372	3.0308	3.0250	-19.34%	5.44%

Table A-7: Summary of the atomic fraction for the Ba, Fe and O elements as it could be derived from the EDX elemental profiles for the different BaMPtTh0, BaMPtTh25 and BaMPtTh75 samples[80].

	Column 1	**Column 2**	**Column 3**	**Column 4**	**Column 5**	**Column 6**	**Column 7**	**Column 8**
Row 1	Sample name	EDX map indice	Th (nm) Time (min)	Growth rate (nm/min)	BaM type	Concentration Ba [Min-Max] Mean (at%)	Concentration Fe [Min-Max] Mean (at%)	Concentration O [Min-Max] Mean (at%)
Row 2	BaMPtTh0	**EDX1523** **[24 – 200nm]**	**176 nm** **111 min**	**1.58**	**BaM/YSZ**	[2.10 - 4.39] **3.22**	[38.10 - 48.60] **42.64**	[43.16 - 54.07] **49.74**
Row 3	BaMPtTh25	**EDX1659** **[33 – 139nm]**	**106 nm** **141 min**	**0.75**	**BaM/YSZ**	[2.80 - 3.96] **3.30**	[41.7 - 45.8] **43.50**	[49.60 - 53.90] **52.15**
Row 4	BaMPtTh25	**EDX1547** **[33 - 144nm]**	**111 nm** **141 min**	**0.78**	**BaM/YSZ**	[2.88 - 3.80] **3.30**	[40.30 - 46.50] **43.00**	[49.10 - 55.50] **52.70**
Row 5	BaMPtTh25	**EDX1604** **[33.4 - 181.0nm]**	**147.6 nm** **141 min**	**1.05**	**BaM/Pt/YSZ**	[2.30 - 3.90] **3.02**	[36.90 - 42.40] **39.50**	[54.10 - 59.70] **57.10**
Row 6	BaMPtTh25	**EDX1616** **[30 - 185nm]**	**155 nm** **141 min**	**1.10**	**BaM/Pt/YSZ**	[**2.60** - 3.70] **2.60**	[38.60 - 47.40] **41.70**	[49.60 - 59.50] **55.80**
Row 7	BaMPtTh25	**EDX1650** **[30.3 - 178.5nm]**	**148 nm** **141 min**	**1.05**	**BaM/Pt/YSZ**	[1.90 - 4.28] **2.93**	[35.40 - 44.0] **40.50**	[52.60 - 61.20] **56.20**
Row 8	BaMPtTh75	**EDX1340** **[24.0 – 85.7nm]**	**61.7 nm** **111 min**	**0.55**	**BaM/YSZ**	[2.62 - 3.67] **3.09**	[35.90 - 42.64] **40.05**	[52.18 - 58.60] **54.83**
Row 9	BaMPtTh75	**EDX1728** **[25.6 - 186.4nm]**	**160.8 nm** **111 min**	**1.44**	**BaM/Pt/YSZ**	[1.77 - 4.56] **2.79**	[34.80 - 47.40] **39.32**	[49.50 - 61.20] **56.85**

Table A-8: Fitting parameters of Ba 3d doublets listing binding energies, FWHM and integrated areas of individual peaks fitted by Voigt profiles after a linear-type background subtraction. The percentages of I_{Ba1}, I_{Ba2} were determined from the integrated areas of $I_{Ba} + I_{Fe} + I_O$ peaks. Intensity ratios of $I_{5/2}$:$I_{3/2}$=2/3 and Spin orbit splitting (S.O.S.) is 15.33 eV[80].

Ba3d	**Peak3 Pos [eV] Ba1 $3d_{3/2}$**	**Peak1 Pos [eV] Ba1 $3d_{5/2}$**	**Ia of Ba1 I_{Ba1} [%]**	**Peak4 Pos [eV] Ba2 $3d_{3/2}$**	**Peak2 Pos [eV] Ba2 $3d_{5/2}$**	**Ia of Ba2 I_{Ba2} [%]**	**Ia of Ba $*I_{Ba}$ [%]**
BaMF25mJ	793.98 ± 0.10	778.65 ± 0.10	**7.48 ± 0.60**	795.33 ± 0.10	780.00 ± 0.10	**6.87 ± 0.55**	**14.35 ± 1.15**
FWHM [eV]	1.57 ± 0.02	1.57 ± 0.02		1.57 ± 0.02	1.57 ± 0.02		
BaMF75mJ	793.91 ± 0.10	778.58 ± 0.10	**5.52 ± 0.50**	795.28 ± 0.10	779.95 ± 0.10	**4.10 ±0.40**	**9.62 ± 0.90**
FWHM [eV]	1.57 ± 0.02	1.57 ± 0.02		1.57 ± 0.02	1.57 ± 0.02		

$*I_{Ba}=100*(I_{Ba1} + I_{Ba2})/(I_{Ba} + I_{Fe} + I_O)$, $I_{Ba1\{2\}}=100*(I_{Ba1}\{I_{Ba2}\})/(I_{Ba} + I_{Fe} + I_O)$, SoS=15.33 eV, $I_{5/2}$:$I_{3/2}$=2/3

Table A-9: Fitting parameters of Fe 2p doublets listing binding energies, FWHM and integrated areas of individual peaks fitted by Voigt profiles after a linear-type background subtraction. The percentages of I_{Fe1}, I_{Fe2} were determined from the integrated areas of I_{Ba} + I_{Fe} + I_O peaks. Intensity ratios of $I_{3/2}$:$I_{1/2}$=2 and Spin orbit splitting (S.O.S.) is 13.6 eV[80].

Fe2p	**Peak3 Pos [eV] Fe_1 $2p_{1/2}$ (Fe2+)**	**Peak1 Pos [eV] Fe_1 $2p_{3/2}$ (Fe2+)**	**Ia of Fe_1 I_{Fe1} (Fe2+) [%]**	**Peak4 Pos [eV] Fe_2 $p_{1/2}$ (Fe3+)**	**Peak2 Pos [eV] Fe_2 $2p_{3/2}$ (Fe3+)**	**Ia of Fe_2 I_{Fe2} (Fe3+) [%]**	**Peak Pos [eV] Fe $2p_{3/2}$ satellite**	**Ia of Fe $2p_{3/2}$ Satellite $I_{Fe2p3/2}$ Sat [%]**	**Peak Position [eV] Fe $2p_{1/2}$ satellite**	**Ia of Fe $2p_{1/2}$ Satellite $I_{Fe2p1/2}$ Sat [%]**	**Peak Pos [eV] Fe LMM**	**Ia of FeLMM-peak I_{FeLMM} [%]**	**Ia of Fe* *I_{Fe} [%]**
BaMF25mJ	723.78 ± 0.10	710.18 ± 0.10	**17.06 ± 0.95**	726.40 ± 0.10	712.80 ± 0.10	**6.97 ± 0.23**	718.27 ± 0.10	**15.00 ± 1.50**	730.75 ± 0.10	**9.92 ± 1.00**	783.30 ± 0.10	**23.56 ± 1.40**	**72.25 ± 5.00**
FWHM [eV]	3.15 ± 0.05	3.15 ± 0.05		3.15 ± 0.05	3.15 ± 0.05		9.92 ± 0.05		9.92 ± 0.05		12.24 ± 0.05		
BaMF75mJ	723.84 ± 0.10	710.24 ± 0.10	**16.58 ± 1.97**	726.45 ± 0.10	712.85 ± 0.10	**6.83 ± 0.54**	718.27 ± 0.10	**14.97 ± 1.44**	730.75 ± 0.10	**10.45 ± 1.00**	783.30 ± 0.10	**28.91 ± 1.80**	**77.75 ± 7.00**
FWHM [eV]	3.15 ± 0.05	3.15 ± 0.05		3.15 ± 0.05	3.15 ± 0.05		9.92 ± 0.05		9.92 ± 0.05		12.24 ± 0.05		

Ia: Integrated area, Pos: Position

$*I_{Fe}=100*(I_{Fe1} + I_{Fe2} + I_{Fe2p3/2Satellite} + I_{Fe2p1/2Satellite} + I_{FeLMM}) / (I_{Ba} + I_{Fe} + I_O)$

SoS=13.6 eV

$I_{3/2}$:$I_{1/2}$=2

Table A-10: Fitting parameters of O 1s listing binding energies, FWHM and integrated areas of individual peaks fitted by Voigt profiles after a linear-type background subtraction. The percentages of I_{O1}, I_{O2}, I_{O3} were determined from the integrated areas of $I_{Ba} + I_{Fe} + I_O$ peaks[80].

O1s	**Peak1 Pos [eV]** **O1**	**Ia of O_1** **I_{O1} [%]**	**Peak2 Pos [eV]** **O2**	**Ia of O_2** **I_{O2} [%]**	**Peak3 Pos [eV]** **O3**	**Ia of O_3** **I_{O3} [%]**	**Ia of O** **I_O [%]**
BaMF25mJ	529.42 ± 0.10	**10.12 ± 0.95**	531.49 ± 0.10	**2.73 ± 0.25**	532.94 ± 0.10	**0.64 ± 0.05**	**13.45 ± 1.25**
FWHM [eV]	1.74 ± 0.01		1.74 ± 0.01		1.74 ± 0.01		
BaMF75mJ	529.46 ± 0.10	**9.72 ± 0.97**	531.53 ± 0.10	**2.42 ± 0.24**	533.14 ± 0.10	**0.49 ± 0.04**	**12.63 ± 1.25**
FWHM [eV]	1.74 ± 0.01		1.74 ± 0.01		1.74 ± 0.01		

*$I_O = 100*(I_{O1} + I_{O2} + I_{O3})/(I_{Ba} + I_{Fe} + I_O)$

List of Figures

List of Tables

Bibliography

[1] Murugavel, P., Saurel, D., Prellier, W., Simon, C., & Raveau, B. (2004). Tailoring of ferromagnetic Pr0.85Ca0.15MnO3⁄ferroelectric Ba0. 6Sr0. 4TiO3 superlattices for multiferroic properties. *Applied Physics Letters*, *85*(19), 4424-4426.

[2] Singh, M. P., Prellier, W., Simon, C., & Raveau, B. (2005). Magnetocapacitance effect in perovskite-superlattice based multiferroics. *Applied Physics Letters*, *87*(2).

[3] Hill, N. A. (2000). Why are there so few magnetic ferroelectrics? *The Journal of Physical Chemistry B*, *104*(29), 6694-6709.

[4] Schmid, H. (1994). Multi-ferroic magnetoelectrics. *Ferroelectrics*, *162*(1), 317-338.

[5] Khomskii, D. (2009). Classifying multiferroics: Mechanisms and effects. *Physics*, *2*, 20.

[6] Disseler, S. M., Borchers, J. A., Brooks, C. M., Mundy, J. A., Moyer, J. A., Hillsberry, D. A., Thies, E. L., Tenne, D. A., Heron, J., Holtz, M. E., Clarkson, J. D., Stiehl, G. M., Schiffer, P., Muller, D. A., Schlom, D. G., & Ratcliff, W. D. (2015). Magnetic structure and ordering of multiferroic hexagonal LuFeO3. *Physical review letters*, *114*(21), 217602.

[7] Heron, J. T., & Chiang, T. (2021). Magnetoelectrics and multiferroics: Materials and opportunities for energy-efficient spin-based memory and logic. *MRS Bulletin*, 1-8.

[8] Kim, Y., Pham, C., & Chang, J. P. (2015). Potentials and challenges of integration for complex metal oxides in CMOS devices and beyond. *Journal of Physics D: Applied Physics*, *48*(6), 063001.

[9] Chang, S. J., Chung, M. H., Kao, M. Y., Lee, S. F., Yu, Y. H., Kaun, C. C., Nakamura, T., Sasabe, N., Chu, S. J., & Tseng, Y. C. (2019). GdFe0.8Ni0.2O3: a multiferroic material for low-power spintronic devices with high storage capacity. *ACS applied materials & interfaces*, *11*(34), 31562-31572.

[10] Paul, J., Bhardwaj, S., Sharma, K. K., Kotnala, R. K., & Kumar, R. (2015). Room temperature multiferroic behaviour and magnetoelectric coupling in Sm/Fe modified Bi4Ti3O12 ceramics synthesized by solid state reaction method. *Journal of Alloys and Compounds*, *634*, 58-64.

[11] Yau, H. M., Yan, Z. B., Chan, N. Y., Au, K., Wong, C. M., Leung, C. W., Zhang, F. Y., Gao, X. S., & Dai, J. Y. (2015). Low-field switching four-state nonvolatile memory based on multiferroic tunnel junctions. *Scientific reports*, *5*(1), 12826.

[12] Harris, V. G. (Ed.). (2022). Modern Ferrites, Volume 2: Emerging Technologies and Applications.

[13] Jalaja, M. A., & Dutta, S. (2015). Ferroelectrics and multiferroics for next generation photovoltaics. *Adv. Mater. Lett*, *6*(7), 568-584.

[14] Lee, K., Hajra, S., Sahu, M., & Kim, H. J. (2021). Colossal dielectric response, multiferroic properties, and gas sensing characteristics of the rare earth orthoferrite LaFeO3 ceramics. *Journal of Alloys and Compounds*, *882*, 160634.

[15] Ramesh, R., & Manipatruni, S. (2021). Electric field control of magnetism. *Proceedings of the Royal Society A*, *477*(2251), 20200942.

[16] Hyun, S., Seo, H., Yang, I.-K., Kim, Y., Jeon, G., Lee, B., Jeong, Y. H., Kim, Y., & Kim, J. K. (2015). High density array of multiferroic nanoislands in a large area. *Journal of Materials Chemistry C*, *3*(10), 2237-2243.

[17] Wang, J., Neaton, J. B., Zheng, H., Nagarajan, V., Ogale, S. B., Liu, B., Viehland, D., Vaithyanathan, V., Schlom, D. G., Waghmare, U. V., Spaldin, N. A., Rabe, K. M., Wuttig, M., & Ramesh, R. (2003). Epitaxial BiFeO3 multiferroic thin film heterostructures. *Science*, *299*(5613), 1719-1722.

[18] Eerenstein, W., Mathur, N. D., & Scott, J. F. (2006). Multiferroic and magnetoelectric materials. *nature*, *442*(7104), 759-765.

[19] Bowles, J. F. W., Howie, R. A., Vaughan, D. J., & Zussman, J. (2011). Rock-forming minerals: Non-silicates: Oxides, hydroxides and sulphides. *Geological Society*.

[20] Jiles, D. (2015). *Introduction to magnetism and magnetic materials*. CRC press.

[21] Bertotti, G. (1998). *Hysteresis in magnetism: for physicists, materials scientists, and engineers*. Gulf Professional Publishing.

[22] Chikazumi, S., & Graham, C. D. (1997). *Physics of ferromagnetism* (No. 94). Oxford university press.

[23] Stoner, E. C., & Wohlfarth, E. P. (1991). A mechanism of magnetic hysteresis in heterogeneous alloys. *IEEE Transactions on Magnetics*, *27*(4), 3475-3518.

[24] Kou, X. C., Kronmüller, H., Givord, D., & Rossignol, M. F. (1994). Coercivity mechanism of sintered Pr17Fe75B8 and Pr17Fe53B30 permanent magnets. *Physical Review B*, *50*(6), 3849.

[25] Ma, J., Zhao, X., Liu, W., Li, Y., Liu, L., Song, Y., Xie, Y., Zhao, X., & Zhang, Z. (2021). Coercivity Mechanism and Magnetization Reversal in Anisotropic Ce-(Y)-Pr-Fe-B Films. *Materials*, *14*(16), 4680.

[26] Qiu, L., Zhao, L., Weng, X., Shen, L., Zhao, G., Wang, F., & Xie, L. (2019). A hybrid coercivity mechanism for exchange-coupled nanocomposite permanent magnets. *Journal of Rare Earths*, *37*(10), 1030-1033.

[27] Fidler, J., & Schrefl, T. (2000). Micromagnetic modelling-the current state of the art. *Journal of Physics D: Applied Physics*, *33*(15), R135.

[28] Schäfer, R. (2001). Magnets, soft and hard: Domains. *Encyclopedia of Materials: Science and Technology*, 5130-5141.

[29] Stamps, R. L. (2000). Mechanisms for exchange bias. *Journal of Physics D: Applied Physics*, *33*(23), R247.

[30] Schuller, I. (2017, December 20). *Exchange bias*. Schuller Nanoscience Group. https://ischuller.ucsd.edu/research/exchange-bias/

[31] Parkin, S. S. P., Roche, K. P., Samant, M. G., Rice, P. M., Beyers, R. B., Scheuerlein, R. E., O'Sullivan, E. J., Brown, S. L., Bucchigano, J., Abraham, D. W., Lu, Y., Rooks, M., Trouilloud, P. L., Wanner, R. A., & Gallagher, W. J. (1999). Exchange-biased magnetic tunnel junctions and application to nonvolatile magnetic random access memory. *Journal of Applied Physics*, *85*(8), 5828-5833.

[32] Blachowicz, T., Ehrmann, A., & Wortmann, M. (2023). Exchange bias in nanostructures: An update. *Nanomaterials*, *13*(17), 2418.

[33] Binek, C., Hochstrat, A., Chen, X., Borisov, P., Kleemann, W., & Doudin, B. (2005). Electrically controlled exchange bias for spintronic applications. *Journal of applied physics*, *97*(10).

[34] Guo, Y., Ouyang, Y., Sato, N., Ooi, C. C., & Wang, S. X. (2017). Exchange-biased anisotropic magnetoresistive field sensor. *IEEE Sensors Journal*, *17*(11), 3309-3315.

[35] Ai, H., Li, F., Bai, H., Liu, D., Lo, K. H., Yang, S. A., Kawazoe, Y., & Pan, H. (2022). Ferroelectricity coexisted with p-orbital ferromagnetism and metallicity in two-dimensional metal oxynitrides. *npj Computational Materials*, *8*(1), 60.

[36] Lu, Y., Fei, R., Lu, X., Zhu, L., Wang, L., & Yang, L. (2020). Artificial multiferroics and enhanced magnetoelectric effect in van der waals heterostructures. *ACS Applied Materials & Interfaces*, *12*(5), 6243–6249.

[37] Mbam, S. O., Nwonu, S. E., Orelaja, O. A., Nwigwe, U. S., & Gou, X.-F. (2019). Thin-film coating; historical evolution, conventional deposition technologies, stress-state micro/nano-level measurement/models and Prospects Projection: A critical review. *Materials Research Express*, *6*(12), 122001.

[38] Fayomi, O. S. I., Akande, I. G., Abioye, O. P., & Fakehinde, O. B. (2019). New trend in thin film composite coating deposition: A Mini Review. *Procedia Manufacturing*, *35*, 1007–1012.

[39] Curtis, H. D. (1911). Methods of silvering mirrors. *Publications of the Astronomical Society of the Pacific*, *23*(135), 13–13.

[40] Grundy, P. J. (1998). Thin Film Magnetic Recording Media. *Journal of Physics D: Applied Physics*, *31*(21), 2975–2990.

[41] Matsuoka, M., Naoe, M., & Hoshi, Y. (1985). Ba–ferrite thin-film disk for Perpendicular magnetic recording. *Journal of Applied Physics*, *57*(8), 4040–4042.

[42] Georgobiani, A. N. (1974). Wide-band II-VI semiconductors and the prospects of their application. *Soviet Physics Uspekhi*, *17*(3), 424–437.

[43] Shima, H., Kawae, T., Morimoto, A., Matsuda, M., Suzuki, M., Tadokoro, T., Naganuma, H., Iijima, T., Nakajima, T., & Okamura, S. (2009). Optical properties of bifeo3-system multiferroic thin films. *Japanese Journal of Applied Physics*, *48*(9).

[44] Gong, C., Kim, E. M., Wang, Y., Lee, G., & Zhang, X. (2019). Multiferroicity in atomic van der Waals heterostructures. *Nature communications*, *10*(1), 2657.

[45] Martin, L. W., Crane, S. P., Chu, Y. H., Holcomb, M. B., Gajek, M., Huijben, M., C-H Yang, C-h., Balke, N., & Ramesh, R. (2008). Multiferroics and magnetoelectrics: thin films and nanostructures. *Journal of Physics: Condensed Matter*, *20*(43), 434220.

[46] Tokunaga, Y., Iguchi, S., Arima, T. H., & Tokura, Y. (2008). Magnetic-field-induced ferroelectric state in DyFeO 3. *Physical review letters*, *101*(9), 097205.

[47] Hohenberger, S., Lazenka, V., Temst, K., Selle, S., Patzig, C., Höche, T., Grundmann, M., & Lorenz, M. (2018). Effect of double layer thickness on magnetoelectric coupling in multiferroic BaTiO3-Bi0. 95Gd0. 05FeO3 multilayers. *Journal of Physics D: Applied Physics*, *51*(18), 184002.

[48] Wu, H., Ao, H., Li, W., Zeng, Z., Gao, R., Fu, C., Chen, G., Deng, X., Wang, Z., Lei, X., & Cai, W. (2021). Improvement of magnetoelectric coupling effect in Ba0. 8Sr0. 2TiO3-Co0. 5Cu0. 5Fe2O4 multiferroic fluids by tuning the composition. *Materials Today Chemistry*, *21*, 100511.

[49] Le, M. T., Bui, T. Q., Nguyen, T. G., & Dinh, V. H. (2020). Tuning magnetoelectric effect in Pb (1− x) SrxTiO3/CoFe2O4 multiferroic nanocomposites by varying Sr content. *Journal of Physics and Chemistry of Solids*, *138*, 109293.

[50] Palkar, V. R., Anisha, R., Pinto, R., & Bhattacharya, S. (2007). Multiferroic properties of Dy modified BiFeO 3 thin films in comparison with Tb modified BiFeO 3 thin films. *Journal of materials research*, *22*, 2068-2073.

[51] Amrillah, T., Hermawan, A., Bitla, Y., Baqiya, M. A., Quynh, L. T., Taufik, A., Yin, S., & Juang, J. Y. (2021). Preferentially oriented nanometer-sized CoFe2O4 mesocrystals embedded in the BiFeO3 matrix for opto-magnetic device applications. *ACS Applied Nano Materials*, *4*(10), 11249-11259.

[52] Puebla, J., Kim, J., Kondou, K., & Otani, Y. (2020). Spintronic devices for energy-efficient data storage and energy harvesting. *Communications Materials*, *1*(1), 24.

[53] Amrillah, T., Hermawan, A., Wulandari, C. P., Muthi'Ah, A. D., & Simanjuntak, F. M. (2021). Crafting the multiferroic BiFeO3-CoFe2O4 nanocomposite for next-generation devices: A review. *Materials and Manufacturing Processes*, *36*(14), 1579-1596.

[54] Kumar, A., Pawar, S., Pandey, A., Dutta, S., & Kaur, D. (2020). Anisotropic magnetoelectric functionality of ferromagnetic shape memory alloy heterostructures for MEMS magnetic sensors. *Journal of Physics D: Applied Physics*, *53*(39), 395302.

[55] Markov, I., & Stoyanov, S. (1987). Mechanisms of epitaxial growth. *Contemporary Physics*, *28*(3), 267–320.

[56] Van Der Merwe, J. H. (1993). Theoretical considerations in growing uniform epilayers. Interface Science, 1(1), 77–86.

[57] Ohring, M. (2002). Materials science of thin films: Deposition and structure. Academic Press.

[58] Bauer, S., Rodrigues, A., Horák, L., Nergis, B., Jin, X., Schneider, R., Gröger, R., Baumbach, T., & Holý, V. (2021). Time-Resolved Morphology and Kinetic Studies of Pulsed Laser Deposition-Grown Pt Layers on Sapphire at Different Growth Temperatures by in Situ Grazing Incidence Small-Angle X-ray Scattering. *Langmuir*, *37*(2), 734-749.

[59] Lorenz, M., Wei, H., Jung, F., Hohenberger, S., Hochmuth, H., Grundmann, M., Patzig, C., Selle, S., & Höche, T. (2017). Two-dimensional frank–van-der-merwe growth of functional oxide and nitride thin film superlattices by pulsed laser deposition. *Journal of Materials Research*, *32*(21), 3936–3946.

[60] Albrecht, M., Hansson , P. O., Christiansen, S., Dorsch, W., Strunk, H. P., & Bauser, E. (1994). Balancing Surface Energy Terms For Stable Growth of Planar Surface. *Scanning Microscopy*, *8*(4), 925–934.

[61] Martin, P. M. (2010). *Handbook of Deposition Technologies for Films and coatings: Science, applications and technology*. Elsevier.

[62] Gatzen, H. H., Saile, V., & Leuthold, J. (2015a). Deposition Technologies. *Micro and Nano Fabrication*, 65–203.

[63] Kelly, P. J., & Arnell, R. D. (2000). Magnetron sputtering: a review of recent developments and applications. *Vacuum*, *56*(3), 159-172.

[64] Rossnagel, S. M. (2003). Thin film deposition with physical vapor deposition and related technologies. *Journal of Vacuum Science & Technology A: Vacuum, Surfaces, and Films*, *21*(5), S74-S87.

[65] Mattox, D. M. (2010). *Handbook of physical vapor deposition (PVD) processing*. William Andrew.

[66] Singh, J., Quli, F., Wolfe, D. E., Schriempf, J. T., & Singh, J. (1999). An overview: Electron beam-physical vapor deposition technology-Present and future applications. *Applied Research Laboratory, Pennsylvania State University, USA*.

[67] Al Taleb, A., Majer, L. N., Selfors, E. W., Smink, S., Holst, B., Mannhart, J., Braun, W., & Farías, D. (2022). Ultrasmooth graphene-coated metal thin films on sapphire grown by thermal laser epitaxy. *Thin Solid Films*, *758*, 139449.

[68] Christen, H. M., & Eres, G. (2008). Recent advances in pulsed-laser deposition of complex oxides. *Journal of Physics: Condensed Matter*, *20*(26), 264005.

[69] Liang, J., Liu, Q., Li, T., Luo, Y., Lu, S., Shi, X., Zhang, F., Asiri, A. M., & Sun, X. (2021). Magnetron sputtering enabled sustainable synthesis of nanomaterials for energy electrocatalysis. *Green Chemistry*, *23*(8), 2834-2867.

[70] Dally, A., Coat, V., & Hill, A. (2023, December 27). *Introduction to pulsed laser deposition (PLD):8 applications*. VacCoat. https://vaccoat.com/blog/what-is-pulsed-laser-deposition-pld/

[71] Axente, E., & Socol, G. (2022). Special Issue "Pulsed Laser Deposition of Thin Films: Recent Advances and Challenge". *Coatings*, *12*(3), 368.

[72] Chrisey, D. B., & Hubler, G. K. (Eds.). (1994). Pulsed laser deposition of thin films.

[73] Gee, S. H., Hong, Y. K., Erickson, D. W., Tanaka, T., & Park, M. H. (2003). Ex situ annealing method for c-axis oriented barium ferrite thick films. *Journal of applied physics*, *93*(10), 7507-7509.

[74] Abuzir, A. R., & Yeh, W. J. (2005). Comparison Between In-situ Annealing and External Annealing For Barium Ferrite Thin Films Made by RF Magnetron Sputtering. *MRS Online Proceedings Library (OPL)*, *875*.

[75] Bassim, N. D., Schenck, P. K., Donev, E. U., Heilweil, E. J., Cockayne, E., Green, M. L., & Feldman, L. C. (2007). Effects of temperature and oxygen pressure on binary oxide growth using aperture-controlled combinatorial pulsed-laser deposition. *Applied Surface Science*, *254*(3), 785-788.

[76] Min, C. H., Cho, S., Lee, S. H., Cho, D. Y., Park, W. G., Chung, J. G., Lee, E., Lee, J. C., Anass, B., Lee, J. H., Hwang, C. S., & Oh, S. J. (2010). Effect of oxygen partial pressure on the Fermi level of ZnO1− x films fabricated by pulsed laser deposition. *Applied Physics Letters*, *96*(20).

[77] Kunti, A. K., Sekhar, K. C., Pereira, M., Gomes, M. J. M., & Sharma, S. K. (2017). Oxygen partial pressure induced effects on the microstructure and the luminescence properties of pulsed laser deposited TiO2 thin films. *AIP advances*, *7*(1).

[78] Gabriel, V., Kocán, P., Bauer, S., Nergis, B., Rodrigues, A., Horák, L., Jin, X., Schneider, R., Baumbach, T., & Holý, V. (2022). Effect of pulse laser frequency on PLD growth of LuFeO3 explained by kinetic simulations of in-situ diffracted intensities. *Scientific Reports*, *12*(1), 5647.

[79] Gabriel, V., Kocán, P., & Holý, V. (2022). Growth-rate model of epitaxial layer-by-layer growth by pulsed-laser deposition. *Physical Review E*, *106*(3), 035302.

[80] Nergis, B., Bauer, S., Jin, X., Seemann, K., Horak, L., Schneider, R., Holý, V., Ulrich, S., & Baumbach, T. (2023). Effect of the laser fluence on the microstructure and the relating magnetic properties of BaFe12O19 films grown on YSZ (111) by PLD for optimized perpendicular recording. *Journal of Materials Science*, *58*(2), 718-739.

[81] Ojeda-G-P, A., Döbeli, M., & Lippert, T. (2018). Influence of plume properties on thin film composition in pulsed laser deposition. *Advanced Materials Interfaces*, *5*(18), 1701062.

[82] Hwang, T. J., Ha, D. H., Kim, D. H., Lee, K. W., & Park, Y. K. (2000). Fabrication of YBCO/STO/YBCO multilayer by PLD. *Physica C: Superconductivity*, *341*, 2347-2348.

[83] Hau, S. K., Wong, K. H., Chan, P. W., & Choy, C. L. (1995). Intrinsic resputtering in pulsed-laser deposition of lead-zirconate-titanate thin films. *Applied physics letters*, *66*(2), 245-247.

[84] Krebs, H. U., Weisheit, M., Faupel, J., Süske, E., Scharf, T., Fuhse, C., Störmer, M., Sturm, K., Seibt, M., Kijewski, H., Nelke, D., Panchenko, E., & Buback, M. (2003). Pulsed laser deposition (PLD)--a versatile thin film technique. *Advances in Solid State Physics*, 505-518.

[85] Movchan, B. A., & Demchishin, A. V. (1969). Structure and properties of thick condensates of nickel, titanium, tungsten, aluminum oxides, and zirconium dioxide in vacuum. *Fiz. Metal. Metalloved. 28: 653-60 (Oct 1969).*

[86] Anders, A. (2010). A structure zone diagram including plasma-based deposition and ion etching. *Thin Solid Films*, *518*(15), 4087-4090.

[87] Ohnishi, T., Koinuma, H., & Lippmaa, M. (2006). Pulsed laser deposition of oxide thin films. *Applied surface science*, *252*(7), 2466-2471.

[88] Fa, S., & Krebs, H. U. (1996). Calculations and experiments of material removal and kinetic energy during pulsed laser ablation of metals. *Applied surface science*, *96*, 61-65.

[89] Arregi, J. A., Caha, O., & Uhlíř, V. (2020). Evolution of strain across the magnetostructural phase transition in epitaxial ferh films on different substrates. *Physical Review B*, *101*(17).

[90] Lazarev, S., Bauer, S., Forghani, K., Barchuk, M., Scholz, F., & Baumbach, T. (2013). High resolution synchrotron X-ray studies of phase separation phenomena and the scaling law for the threading dislocation densities reduction in high quality Algan heterostructure. *Journal of Crystal Growth*, *370*, 51–56.

[91] Chierchia, R., Böttcher, T., Figge, S., Diesselberg, M., Heinke, H., & Hommel, D. (2001). Mosaicity of GaN epitaxial layers: simulation and experiment. *physica status solidi (b)*, *228*(2), 403-406.

[92] Kafashan, H. (2018). Structural characterizations of pure SnS and In-doped SnS thin films using isotropic and anisotropic models. *Materials Research Express*, *5*(4), 046417.

[93] Chierchia, R., Böttcher, T., Heinke, H., Einfeldt, S., Figge, S., & Hommel, D. (2003). Microstructure of heteroepitaxial GaN revealed by x-ray diffraction. *Journal of Applied physics*, *93*(11), 8918-8925.

[94] Hejral, U., Shipilin, M., Gustafson, J., Stierle, A., & Lundgren, E. (2020). High energy surface x-ray diffraction applied to model catalyst surfaces at work. *Journal of Physics: Condensed Matter*, *33*(7), 073001.

[95] Moram, M. A., & Vickers, M. E. (2009). X-ray diffraction of III-nitrides. *Reports on progress in physics*, *72*(3), 036502.

[96] Borzì, A., Dolabella, S., Szmyt, W., Geler-Kremer, J., Abel, S., Fompeyrine, J., Hoffmann, P., & Neels, A. (2020). Microstructure analysis of epitaxial BaTiO3 thin films on SrTiO3-buffered Si: Strain and dislocation density quantification using HRXRD methods. *Materialia*, *14*, 100953.

[97] Dolabella, S., Borzì, A., Dommann, A., & Neels, A. (2022). Lattice strain and defects analysis in nanostructured semiconductor materials and devices by high-resolution X-ray diffraction: theoretical and practical aspects. *Small Methods*, *6*(2), 2100932.

[98] Liu, J. Q., Qiu, Y. X., Wang, J. F., Xu, K., & Yang, H. (2011). Analysis of modified Williamson-Hall plots on GaN layers. *Chinese Physics Letters*, *28*(1), 016101.

[99] Moseley, H. G. J. (1913). XCIII. The high-frequency spectra of the elements. *The London, Edinburgh, and Dublin Philosophical Magazine and Journal of Science*, *26*(156), 1024-1034.

[100] Encyclopædia Britannica, inc. (n.d.). *Bragg Law*. Encyclopædia Britannica. https://www.britannica.com/science/Bragg-law

[101] Lazarev, S. (2013). *X-ray investigation of defects in III-nitrides and their alloys* (Doctoral dissertation, Karlsruhe, Karlsruher Institut für Technologie (KIT), Diss., 2013).

[102] Yasaka, M. (2010). X-ray thin-film measurement techniques. *The Rigaku Journal*, *26*(2), 1-9.

[103] Chason, E., & Mayer, T. M. (1997). Thin film and surface characterization by specular X-ray reflectivity. *Critical Reviews in Solid State and Material Sciences*, *22*(1), 1-67.

[104] Kiessig, H. (1931). Untersuchungen zur totalreflexion von röntgenstrahlen. *Annalen der Physik*, *402*(6), 715-768.

[105] Jin, X., Popescu, R., Pasha, A., Schneider, R., Hariskos, D., Witte, W., Pawalla, M., & Gerthsen, D. (2019). Structural and microchemical characterization of Cu (In, Ga) Se2 solar cells with solution-grown CdS, Zn (O, S), and Inx (O, S) y buffers. *Thin Solid Films*, *671*, 133-138.

[106] Bauer, S., Rodrigues, A., Horák, L., Jin, X., Schneider, R., Baumbach, T., & Holý, V. (2019). Structure quality of LuFeO3 epitaxial layers grown by pulsed-laser deposition on sapphire/Pt. *Materials*, *13*(1), 61.

[107] Bauer, S., Nergis, B., Jin, X., Schneider, R., Wang, D., Kübel, C., Holý, V., Horák, L., Seemann, K., Ulrich, S., & Baumbach, T. (2023). Effect of Interface layer Quality on Microstructure, Stoichiometry, and Magnetic Properties of Hexaferrite BaFe12O19 Grown on YSZ (111) by Pulsed Laser Deposition. *Langmuir*, *39*(40), 14308-14327.

[108] Scheu, C., & Kaplan, W. D. (2012). Introduction to Scanning Electron Microscopy. *In-situ Electron Microscopy*, 3-37.

[109] Banerjee, S., Yang, R., Courchene, C. E., & Conners, T. E. (2009). Scanning electron microscopy measurements of the surface roughness of paper. *Industrial & engineering chemistry research*, *48*(9), 4322-4325.

[110] Gao, N., Wang, S. C., Ubhi, H. S., & Starink, M. J. (2005). A comparison of grain size determination by light microscopy and EBSD analysis. *Journal of materials science*, *40*(18), 4971-4974.

[111] Mirsaidov, U., Timashev, S. F., Polyakov, Y. S., Misurkin, P. I., Musaev, I., & Polyakov, S. V. (2011). Analytical method for parameterizing the random profile components of nanosurfaces imaged by atomic force microscopy. *Analyst*, *136*(3), 570-576.

[112] Lobo, R. F. M., Pereira-da-Silva, M. A., Raposo, M., Faria, R. M., & Oliveira Jr, O. N. (1999). In situ thickness measurements of ultra-thin multilayer polymer films by atomic force microscopy. *Nanotechnology*, *10*(4), 389.

[113] Mischler, S., Vogel, A., Mathieu, H. J., & Landolt, D. (1991). The chemical composition of the passive film on Fe-24Cr and Fe-24Cr-11Mo studied by AES, XPS and SIMS. *Corrosion Science*, *32*(9), 925-944.

[114] Mikhlin, Y. L., Nasluzov, V. A., Romanchenko, A. S., Shor, A. M., & Pal'yanova, G. A. (2014). XPS and DFT studies of the electronic structures of AgAuS and Ag3AuS2. *Journal of alloys and compounds*, *617*, 314-321.

[115] Thøgersen, A., Rein, M., Monakhov, E., Mayandi, J., & Diplas, S. (2011). Elemental distribution and oxygen deficiency of magnetron sputtered indium tin oxide films. *Journal of Applied Physics*, *109*(11).

[116] Panzmer, G., & Egert, B. (1984). The bonding state of sulfur segregated to α-iron surfaces and on iron sulfide surfaces studied by XPS, AES and ELS. *Surface Science*, *144*(2-3), 651-664.

[117] Maticiuc, N., Katerski, A., Danilson, M., Krunks, M., & Hiie, J. (2017). XPS study of OH impurity in solution processed CdS thin films. *Solar Energy Materials and Solar Cells*, *160*, 211-216.

[118] Abd Mutalib, M., Rahman, M. A., Othman, M. H. D., Ismail, A. F., & Jaafar, J. (2017). Scanning electron microscopy (SEM) and energy-dispersive X-ray (EDX) spectroscopy. In *Membrane characterization* (pp. 161-179). Elsevier.

[119] Bozuyuk, U., Suadiye, E., Aghakhani, A., Dogan, N. O., Lazovic, J., Tiryaki, M. E., Schneider, M., Karacakol, A. C., Demir, S. O., Richter, G., & Sitti, M. (2022). High-performance magnetic FePt (L10) surface microrollers towards medical imaging-guided endovascular delivery applications. *Advanced Functional Materials*, *32*(8), 2109741.

[120] Chen, X., Hochstrat, A., Borisov, P., & Kleemann, W. (2006). Magnetoelectric exchange bias systems in spintronics. *Applied physics letters*, *89*(20).

[121] Nogués, J., & Schuller, I. K. (1999). Exchange bias. *Journal of Magnetism and Magnetic Materials*, *192*(2), 203-232.

[122] *Physical Property Measurement System*. Quantum Design North America - Products - Physical Property Measurement System – Quantum Design PPMS® VersaLab®. (n.d.). https://qdusa.com/products/versalab.html

[123] Kunzmann, M. (2024). *Sensitivity and noise at VSM measurements – take a look behind the curtain* . https://qd-europe.com/de/en/news/product-application-news-spectrum/sensitivity-and-noise-at-vsm-measurements-take-a-look-behind-the-curtain/

[124] Kraft, A., Rupprecht, C., & Yam, Y. C. (2017). Superconducting quantum interference device (squid). *UBC Phys*.

[125] Quantum Design. (2019). *Squid magnetometer*. Quantum Design North America - Products - SQUID Magnetometer – Quantum Design MPMS®3. https://www.qdusa.com/products/mpms3.html

[126] Budakian, R., Finkler, A., Eichler, A., Poggio, M., Degen, C. L., Tabatabaei, S., Lee, I., Hammel, C., Eugene, S. P., & Gauger, E. M. (2024). Roadmap on nanoscale magnetic resonance imaging. *Nanotechnology*.

[127] Grütter, P., Wadas, A., Meyer, E., Heinzelmann, H., Hidber, H. R., & Güntherodt, H. J. (1990). High resolution magnetic force microscopy. *Journal of Vacuum Science & Technology A: Vacuum, Surfaces, and Films*, *8*(1), 406-410.

[128] Hartmann, U. (1999). Magnetic force microscopy. *Annual review of materials science*, *29*(1), 53-87.

[129] Kazakova, O., Puttock, R., Barton, C., Corte-León, H., Jaafar, M., Neu, V., & Asenjo, A. (2019). Frontiers of magnetic force microscopy. *Journal of applied Physics*, *125*(6).

[130] Awan, M. S., Bhatti, A. S., Qing, S., & Ong, C. K. (2010). Fabrication of LSS bottom electrode by pld. *Vacuum*, *85*(1), 55–59.

[131] Comes, R., Liu, H., Khokhlov, M., Kasica, R., Lu, J., & Wolf, S. A. (2012). Directed self-assembly of epitaxial cofe2O4–bifeo3 multiferroic nanocomposites. *Nano Letters*, *12*(5), 2367–2373.

[132] Sung-Min Yoon, S.-M. Y., Eisuke Tokumitsu, E. T., & Hiroshi Ishiwara, H. I. (1998). Electrical properties of la0.7sr0.3coo 3/pb(zr0.52ti0.48)o 3/la0.7sr0.3coo 3 thin film capacitors formed on mgo substrates using the sol-gel method. *Japanese Journal of Applied Physics*, *37*(8A).

[133] Ramesh, R., Gilchrist, H., Sands, T., Keramidas, V. G., Haakenaasen, R., & Fork, D. K. (1993). Ferroelectric La-sr-co-O/PB-Zr-ti-O/La-SR-Co-O heterostructures on silicon via template growth. *Applied Physics Letters*, *63*(26), 3592–3594.

[134] Jia, Q. X., Wu, X. D., Foltyn, S. R., & Tiwari, P. (1995). Structural and electrical properties of ba0.5sr0.5tio3 thin films with conductive SRRUO3 bottom electrodes. *Applied Physics Letters*, *66*(17), 2197–2199.

[135] Mardare, A. I., Mardare, C. C., & Savu, R. (2006). Ferroelectric properties of pb(zr,ti)o3 thin film capacitors made by RF magnetron sputtering and heat-treated by the bottom electrode crystallization method. *Materials Science Forum*, *514–516*, 1348–1352.

[136] Sheng, S., & Ong, C. K. (2011). Multifunctional dual-tunable multiferroic BA0.25sr0.75tio3–bifeo3–ba0.25sr0.75tio3 trilayered structure for tunable microwave applications. *Journal of Physics D: Applied Physics*, *44*(16), 165406.

[137] Rai, R. C., Horvatits, C., Mckenna, D., & Du Hart, J. (2019). Structural studies and physical properties of hexagonal-YbFeO3 thin films. *AIP Advances*, *9*(1).

[138] Markelova, M., Nygaard, R., Tsymbarenko, D., Shurkina, A., Abramov, A., Amelichev, V., Makarevic, A., Vasiliev, A., & Kaul, A. (2021). Multiferroic h-LuFeO3 thin films on (111) and (100) surfaces of YSZ substrates: An experimental and theoretical study. *ACS Applied Electronic Materials*, *3*(2), 1015-1022.

[139] Hwang, S. J., Lee, J. H., Jeong, C. O., & Joo, Y. C. (2007). Effect of film thickness and annealing temperature on hillock distributions in pure Al films. *Scripta Materialia*, *56*(1), 17-20.

[140] Sharma, S. K., & Spitz, J. (1980). Hillock formation, hole growth and agglomeration in thin silver films. *Thin Solid Films*, *65*(3), 339-350.

[141] Gadkari, P. R., Warren, A. P., Todi, R. M., Petrova, R. V., & Coffey, K. R. (2005). Comparison of the agglomeration behavior of thin metallic films on SiO2. *Journal of Vacuum Science & Technology A*, *23*(4), 1152-1161.

[142] Schaefer, B. T., Cheung, J., Ihlefeld, J. F., Jones, J. L., & Nagarajan, V. (2013). Stability and dewetting kinetics of thin gold films on Ti, TiOx and ZnO adhesion layers. *Acta materialia*, *61*(20), 7841-7848.

[143] Sudheer, S., Mondal, P., Rai, V. N., & Srivastava, A. K. (2017). A study of growth and thermal dewetting behavior of ultra-thin gold films using transmission electron microscopy. *AIP Advances*, *7*(7).

[144] Barrozo, P., Småbråten, D. R., Tang, Y. L., Prasad, B., Saremi, S., Ozgur, R., Thakare, V., Steinhardt, R. A., Megan, E. H., Stoica, V. A., Martin, L. W., Schlom, D. G., Selbach, S. M., & Ramesh, R. (2020). Defect-enhanced polarization switching in the improper ferroelectric LuFeO3. *Advanced Materials*, *32*(23), 2000508.

[145] Tanaka, H., & Taniguchi, M. (2016). Single-crystalline epitaxial platinum film on yttrium-stabilized zirconia (111) prepared by sputtering deposition. *Japanese Journal of Applied Physics*, *55*(12), 120304.

[146] Bauer, S., Lazarev, S., Molinari, A., Breitenstein, A., Leufke, P., Kruk, R., Hahn, H., & Baumbach, T. (2014). The power of *in situ* pulsed laser deposition synchrotron characterization for the detection of domain formation during growth of ba0.5sr0.5tio3on mgo. *Journal of Synchrotron Radiation*, *21*(2), 386–394.

[147] Williamson, G. K., & Hall, W. H. (1953). X-ray line broadening from filed aluminium and Wolfram. *Acta Metallurgica*, *1*(1), 22–31.

[148] Cliff, G., & Lorimer, G. W. (1975). The quantitative analysis of thin specimens. *Journal of Microscopy*, *103*(2), 203–207.

[149] Wojdyr, M. (2010). *fityk*: A general-purpose peak fitting program. *Journal of Applied Crystallography*, *43*(5), 1126–1128.

[150] CasaXPS Processing Software, CasaXPS Manual 2.3.15 Rev 1.2Casa Software Ltd, Copyright © 2009

[151] Anthony, M. T., & Seah, M. P. (1984). XPS: Energy calibration of electron spectrometers. 2—results of an interlaboratory comparison. *Surface and Interface Analysis*, *6*(3), 107–115.

[152] Holý, V., Bauer, S., Rodrigues, A., Horák, L., Jin, X., Schneider, R., & Baumbach, T. (2020). In situ grazing-incidence x-ray scattering study of pulsed-laser deposition of Pt layers. *Physical Review B*, *102*(12), 125435.

[153] Nguyen, A. H. T., Nguyen, M. C., Nguyen, A. D., Yim, J. Y., Kim, J. H., Park, N. H., Jeon, S-J., Kwon, D., & Choi, R. (2022). Impact of Pt grain size on ferroelectric properties of zirconium hafnium oxide by chemical solution deposition. *Nano Convergence*, *9*(1), 1-6.

[154] Roshchin, V. M., Silibin, M. V., Yakovlev, V. B., & Yakovleva, E. N. (2014). Effect of bottom-electrode morphology on the dielectric characteristics of the metal-ferroelectric-metal planar structure. *Semiconductors*, *48*, 1704-1709.

[155] Jeong, Y. P. M., Moon, S. I., Jeong, K. W., Kim, S. H., Song, J. T., & Yi, J. Y. J. (1999). Pt and RuO2 bottom electrode effects on Pb (Zr, Ti) O3 memory capacitors. *Japanese Journal of Applied Physics*, *38*(12R), 6801.

[156] Larsen, P. K., Cuppens, R., & Spierings, G. A. C. M. (1992). Ferroelectric memories. *Ferroelectrics*, *128*(1), 265-292.

[157] Koochekzadeh, A., Alamdari, E. K., Barzegar, A. A. G., & Salardini, A. A. (2010). Thermal Effects of Platinum Bottom Electrodes on PZT Sputtered Thin Films Used in MEMS Devices. *Key Engineering Materials*, *437*, 598-602.

[158] Cao, J. L., Solbach, A., Klemradt, U., Weirich, T., Mayer, J., Horn-Solle, H., Böttger, U., Schorn, P. J., Schneller, T., & Waser, R. (2006). Structural investigations of Pt⁄ TiOx electrode stacks for ferroelectric thin film devices. *Journal of Applied Physics*, *99*(11).

[159] Jahangir, S., Cheng, X., Huang, H. H., Ihlefeld, J., & Nagarajan, V. (2014). In-situ investigation of thermal instabilities and solid state dewetting in polycrystalline platinum thin films via confocal laser microscopy. *Journal of Applied Physics*, *116*(16).

[160] Eichorst, D. J., Blanton, T. N., Barnes, C. L., & Bosworth, L. A. (1994). Influence of processing conditions on hillock formation in electron-beam evaporated platinum/titanium films. *Integrated Ferroelectrics*, *4*(3), 239-246.

[161] Hren, P. D., Al-Shareef, H., Rou, S. H., Kingon, A. I., Buaud, P., & Irene, E. A. (1992). Hillock formation in platinum films. *MRS Online Proceedings Library*, 575-580.

[162] Matsui, Y., Hiratani, M., Kumagai, Y., Miura, H., & Fujisaki, Y. (1998). Thermal stability of Pt bottom electrodes for ferroelectric capacitors. *Japanese journal of applied physics*, *37*(4B), L465.

[163] Kweon, S. Y., Yeom, S. J., Sun, H. J., Kim, N. K., Yu, Y. S., & Lee, S. K. (1999). Intrinsic stress dependence of Pt hillock formation and its related electrical properties of SBT capacitor. *Integrated ferroelectrics*, *25*(1-4), 299-309.

[164] Galinski, H., Ryll, T., Schlagenhauf, L., Gauckler, L. J., Stender, P., & Schmitz, G. (2012). Hillock formation of Pt thin films on single-crystal yttria-stabilized zirconia. *Physical Review B*, *85*(12), 125408.

[165] Ciftyürek, E., Sabolsky, K., & Sabolsky, E. M. (2013). Platinum thin film electrodes for high-temperature chemical sensor applications. *Sensors and Actuators B: Chemical*, *181*, 702-714.

[166] Galinski, H., Ryll, T., Elser, P., Rupp, J. L. M., Bieberle-Hütter, A., & Gauckler, L. J. (2010). Agglomeration of Pt thin films on dielectric substrates. *Physical Review B*, *82*(23), 235415.

[167] Ryll, T., Galinski, H., Schlagenhauf, L., Elser, P., Rupp, J. L., Bieberle-Hutter, A., & Gauckler, L. J. (2011). Microscopic and nanoscopic three-phase-boundaries of platinum thin-film electrodes on YSZ electrolyte. *Advanced Functional Materials*, *21*(3), 565-572.

[168] Tasaka, Y., Kuroda, H., Tanaka, M., & Usami, S. (1996). Velocity analysis of ablated particles in pulsed laser deposition of NiO film. *Thin solid films*, *281*, 441-444.

[169] Masumoto, H., & Kobayashi, T. (1965). On the thermal expansion coefficient and the temperature coefficient of Young's modulus of iron-platinum alloys. *Transactions of the Japan Institute of Metals*, *6*(2), 113-115.

[170] YASUDA, I., & HISHINUMA, M. (2000). Lattice Expansion of Acceptor-doped Lanthanum Chromites under High-temperature Reducin'g Atmospheres. *Electrochemistry*, *68*(6), 526-530.

[171] Stress and strain. (n.d.). https://www.tf.uni-kiel.de/matwis/amat/semitech_en/kap_3/backbone/r3_2_3.html

[172] Nergis, B., Bauer, S., Jin, X., Horak, L., Schneider, R., Holy, V., Seemann, K., Ulrich, S., & Baumbach, T. (2024). Structural and Morphological Studies of Pt in the As-Grown and Encapsulated States and Dependency on Film Thickness. *Nanomaterials*, *14*(8), 725.

[173] Skoupy, R., & Krzyzanek, V. (2020). Beam energy dependent calibration of STEM and BSE detectors for thin film thickness estimation. *Microscopy and Microanalysis*, *26*(S2), 1946-1948.

[174] Sheng, Y. Q., Munz, P., & Schultheiss, R. (1985). The determination of the thickness of ultrathin metal and semiconductor films on conventional semiconductor substrates. *physica status solidi (a)*, *92*(1), 121-128.

[175] Timma, A., Caubet, P., Chenevier, B., Thomas, O., Kaouache, B., Dumas, L., Normandon, P., & Giraudin, J. C. (2010). Post Si (C) N hillock nucleation and growth in IC copper lines controlled by diffusional creep. *Microelectronic engineering*, *87*(3), 361-364.

[176] Parratt, L. G. (1954). Surface studies of solids by total reflection of X-rays. *Physical review*, *95*(2), 359.

[177] Yoon, S. D., Vittoria, C., & Oliver, S. A. (2003). Magnetic and microwave magnetic properties of barium hexaferrite permanent magnet films having the c-axis in the film plane. *Journal of applied physics*, *93*(7), 4023-4026.

[178] Harris, V. G., Chen, Z., Chen, Y., Yoon, S., Sakai, T., Gieler, A., Yang, A., He, Y., Ziemer, K. S., Sun, N. X., & Vittoria, C. (2006). Ba-hexaferrite films for next generation microwave devices. *Journal of Applied Physics*, *99*(8).

[179] Zhang, X., Meng, S., Song, D., Zhang, Y., Yue, Z., & Harris, V. G. (2017). Epitaxially grown BaM hexaferrite films having uniaxial axis in the film plane for self-biased devices. *Scientific Reports*, *7*(1), 44193.

[180] Rafique, M. S., Khaleeq-ur-Rahman, M., Anjum, S., Anwar, M. S., Bhatti, K. A., Saeed, S., & Awan, M. S. (2008). Effect of external magnetic field on the deposition of BaFe12O19. *Vacuum*, *82*(11), 1233-1237.

[181] Shono, K., Gomi, M., & Abe, M. (1982). Magneto-optical properties of magnetoplumbites BaFe12O19, SrFe12-xAlxO19 and PbFe12O19. *Japanese Journal of Applied Physics*, *21*(10R), 1451.

[182] Futamoto, M., Hirayama, Y., Honda, Y., & Kikukawa, A. (2001). Perpendicular recording media for ultra-high-density magnetic recording. *Magnetic Storage Systems Beyond 2000*, 103-116.

[183] Kryder, M. H., & Gustafson, R. W. (2005). High-density perpendicular recording—advances, issues, and extensibility. *Journal of Magnetism and Magnetic Materials*, *287*, 449-458.

[184] Cideciyan, R. D., Dellmann, L., Eleftheriou, E., Haeberle, W., Jelitto, J., Kartik, V., Lantz, M. A., Ölçer, S., Fellow, IEEE., Pantazi, A., Rothuizen, H. E., Berman, D., Imaino, W., Jubert, P. O., McClelland, G., Koeppe, P. V., Tsuruta, K., Harasawa, T., Murata, Y., Musha, A., Noguchi, H., Ohtsu, H., Shimizu, O., & Suzuki, R. (2011). 29.5 Gb/in^2 recording areal density on barium ferrite tape. *IEEE Trans. Magn.*, *47*(1).

[185] SUI, X., CHEONG, B. K., LAUGHLIN, D. E., & KRYDER, M. H. (1994). Growth of perpendicular barium hexaferrite thin film media on a Pt interface layer for high density perpendicular magnetic recording. *Journal of The Magnetics Society of Japan*, *18*(S_1_PMRC_94_1), S1_319-322.

[186] Zheng, H., Han, M., Zheng, L., Deng, J., Zheng, P., Wu, Q., Deng, L., & Qin, H. (2016). Magnetic properties of hexagonal barium ferrite films on Pt/MgO (111) substrates annealed at different temperatures. *Journal of Magnetism and Magnetic Materials*, *413*, 25-29.

[187] Lazarov, V. K., Hasnip, P. J., Cai, Z., Yoshida, K., & Ziemer, K. S. (2011). Growth and interface phase stability of barium hexaferrite films on SiC (0001). *Journal of Applied Physics*, *109*(7).

[188] Erickson, D. W., Hong, Y. K., Gee, S. H., Tanaka, T., Park, M. H., & Nam, I. T. (2004). The Role of (111) MgO Interface layer in Growth of c-axis Oriented Barium Ferrite Films. *Journal of Magnetics*, *9*(4), 116-120.

[189] Zheng, H., Han, M., Wu, Y., Zhao, W., & Deng, L. (2016, May). Magnetic properties of hexagonal barium ferrite films on Pt (111)/Al 2 O 3 (0001) substrate based on optimized thickness of Pt. In *2016 IEEE International Nanoelectronics Conference (INEC)* (pp. 1-2). IEEE.

[190] Kaewrawang, A., Ghasemi, A., Liu, X., & Morisako, A. (2010). Interface layer dependence of microtexture, microstructure and magnetic properties of c-axis oriented strontium ferrite thin films. *Thin Solid Films*, *518*(23), 7059-7063.

[191] Li, Q. F., Su, X. D., Li, H., Zhang, L., Liu, Z. H., & Zhong, H. J. (2009). Modulating microstructure and magnetic properties of BaFe12O19 thin films by using Pt and yttria stabilized zirconia interface layers. *Journal of Applied Physics*, *106*(12).

[192] Shams, N. N., Liu, X., Matsumoto, M., & Morisako, A. (2005). Manipulation of crystal orientation and microstructure of barium ferrite thin film. *Journal of Magnetism and Magnetic Materials*, *290*, 138-140.

[193] Kim, D. H., Nam, I. T., Hong, Y. K., Gee, S. H., & Park, M. H. (2002). Microstructure and magnetic properties of hexagonal barium ferrite thin films with various interface layers. *Journal of applied physics*, *91*(10), 8751-8753.

[194] Nakagawa, S., Matsushita, N., & Naoe, M. (2001). Perpendicular magnetic recording media using hexagonal ferrite thin films deposited on Pt interface layers and interlayers. *Journal of magnetism and magnetic materials*, *235*(1-3), 337-341.

[195] Morisako, A., Naka, T., Ito, K., Takizawa, A., Matsumoto, M., & Hong, Y. K. (2002). Properties of Ba-ferrite/AlN double layered films for perpendicular magnetic recording media. *Journal of magnetism and magnetic materials*, *242*, 304-310.

[196] Sokolov, A. S., Yu, C., Beam, E., Gu, X., Obi, Y., & Harris, V. (2018, April). AlN Interlayers Allow Robust Hexagonal Barium Ferrite Heteroepitaxy on 6H-SiC. In *2018 IEEE International Magnetics Conference (INTERMAG)* (pp. 1-1). IEEE.

[197] Zheng, H., Luo, J., Wu, Q., Zheng, P., Zheng, L., Han, M., & Zhang, Y. (2019). Hexagonal barium ferrite films on a Pt (1 1 1)/Si (0 0 1) substrate and their local magnetic properties. *Journal of Magnetism and Magnetic Materials*, *479*, 99-104.

[198] Zhuang, Z., Rao, M., Laughlin, D. E., & Kryder, M. H. (1999). The effect of Pt interlayers on the magnetic and structural properties of perpendicularly oriented barium ferrite media. *Journal of applied physics*, *85*(8), 6142-6144.

[199] Oliver, S. A., Chen, M. L., Kozulin, I., & Vittoria, C. (2000). Structure and magnetic properties of barium hexaferrite films deposited at low oxygen pressures. *Journal of magnetism and magnetic materials*, *213*(3), 326-334.

[200] Dorsey, P. C., Chrisey, D. B., Horwitz, J. S., Lubitz, P., & Auyeung, R. C. Y. (1994). Oriented barium hexaferrite thick films grown on c-plane and m-plane sapphire substrates. *IEEE Transactions on magnetics*, *30*(6), 4512-4517.

[201] Shinde, S. R., Lofland, S. E., Ganpule, C. S., Ogale, S. B., Bhagat, S. M., Venkatesan, T., & Ramesh, R. (1999). Realization of epitaxial barium ferrite films of high crystalline quality with small resonance losses. *Journal of applied physics*, *85*(10), 7459-7466.

[202] Zhuang, Z., Rao, M., White, R. M., Laughlin, D. E., & Kryder, M. H. (2000). Barium ferrite thin film media with perpendicular c-axis orientation and small grain size. *Journal of Applied Physics*, *87*(9), 6370-6372.

[203] Kronmüller, H. (1987). Theory of nucleation fields in inhomogeneous ferromagnets. *physica status solidi (b)*, *144*(1), 385-396.

[204] Schrefl, T., Schmidts, H. F., Fidler, J., & Kronmüller, H. (1993). The role of exchange and dipolar coupling at grain boundaries in hard magnetic materials. *Journal of magnetism and magnetic materials*, *124*(3), 251-261.

[205] Zheng, H., Han, M., Zheng, P., Zheng, L., Deng, J., & Qin, H. (2016, December). The influence of oxygen pressure on the crystallographic structure and magnetic properties of BaM films on Al2O3 (0001) substrate. In *International Symposium on Mechanical Engineering and Material Science (ismems-16)* (pp. 67-72). Atlantis Press.

[206] Wei, X., Zheng, H., Chen, W., Wu, Q., Zheng, P., Zheng, L., & Zhang, Y. (2020). Crystal structure, morphology and magnetic properties of hexagonal M-type barium ferrite film based on the substrate temperature. *Chemical Physics Letters*, *752*, 137541.

[207] Schrefl, T., Schmidts, H. F., Fidler, J., & Kronmüller, H. (1993). Nucleation of reversed domains at grain boundaries. *Journal of applied physics*, *73*(10), 6510-6512.

[208] Schrefl, T., Schmidts, H. F., Fidler, J., & Kronmuller, H. (1993). Nucleation fields and grain boundaries in hard magnetic materials. *IEEE transactions on magnetics*, *29*(6), 2878-2880.

[209] Lazarov, V. K., Cai, Z., Yoshida, K., Hasnip, P., & Ziemer, K. S. (2010). TEM analysis of Pulse Laser Deposited BaFe12O19 films on SiC. *Microscopy and Microanalysis*, *16*(S2), 1232-1233.

[210] Patel, R., Ikeda, Y., Onoda, H., Tainosho, T., Hisamatsu, Y., Sharmin, S., Kita, E., & Yanagihara, H. (2017). Magnetic Properties of Epitaxial Barium Hexaferrite (0001) Thin Films Deposited by Radio Frequency Magnetron Sputtering. *IEEE Transactions on Magnetics*, *54*(2), 1-4.

[211] Yu, C., Sokolov, A. S., Kulik, P., & Harris, V. G. (2020). Stoichiometry, phase, and texture evolution in PLD-grown hexagonal barium ferrite films as a function of laser process parameters. *Journal of Alloys and Compounds*, *814*, 152301.

[212] Bauer, S., Rodrigues, A., & Baumbach, T. (2018). Real time in situ x-ray diffraction study of the crystalline structure modification of Ba0. 5Sr0. 5TiO3 during the post-annealing. *Scientific reports*, *8*(1), 11969.

[213] Leu, C. C., Chien, C. H., Hsu, C. C., Leu, C. F., Hsu, F. Y., & Hu, C. T. (2004). Pt nanocrystalline interfacial layer in an SBT/Pt/Ti ferroelectric capacitor. *Electrochemical and solid-state letters*, *7*(11), F67.

[214] Kronmüller, H., Durst, K. D., & Sagawa, M. (1988). Analysis of the magnetic hardening mechanism in RE-FeB permanent magnets. *Journal of Magnetism and Magnetic Materials*, *74*(3), 291-302.

[215] Mishra, B. N.; Chatterjee, S. (2023). Study of Magnetostriction property of Barium Ferrite to design a transducer using simulation. *J. Emerging Technol. Innovative Res*., *10 (2)*, a756– a763

[216] Liu, B. H., Ding, J., Dong, Z. L., Boothroyd, C. B., Yin, J. H., & Yi, J. B. (2006). Microstructural evolution and its influence on the magnetic properties of CoFe2O4 powders during mechanical milling. *Physical Review B*, *74*(18), 184427.

[217] Ciubotariu, O., Semisalova, A., Lenz, K., & Albrecht, M. (2019). Strain-induced perpendicular magnetic anisotropy and Gilbert damping of Tm3Fe5O12 thin films. *Scientific reports*, *9*(1), 17474.

[218] Singh, S., Munjal, S., & Khare, N. (2015). Strain/defect induced enhanced coercivity in single domain CoFe2O4 nanoparticles. *Journal of Magnetism and Magnetic Materials*, *386*, 69-73.

[219] Khodaei, M., Ebrahimi, S. S., Park, Y. J., Ok, J. M., Kim, J. S., Son, J., & Baik, S. (2013). Strong in-plane magnetic anisotropy in (111)-oriented CoFe2O4 thin film. *Journal of magnetism and magnetic materials*, *340*, 16-22.

[220] Jaber, N., Wolfman, J., Daumont, C., Negulescu, B., Ruyter, A., Sauvage, T., Courtois, B., Bouyanfif, H., Longuet, J. L., Autret-Lambert, C., & Gervais, F. (2017). Laser fluence and spot size effect on compositional and structural properties of BiFeO3 thin films grown by Pulsed Laser Deposition. *Thin Solid Films*, *634*, 107-111.

[221] Schou, J. (2009). Physical aspects of the pulsed laser deposition technique: The stoichiometric transfer of material from target to film. *Applied Surface Science*, *255*(10), 5191-5198.

[222] Duclère, J. R., Perrin, A., Guilloux-Viry, M., Olikhovska, L., & Ustinov, A. (2005). Structure of non-stoichiometric Sr–Bi–Nb–O thin films grown by PLD. *Journal of Crystal Growth*, *275*(1-2), e2493-e2498.

[223] Vrejoiu, I., Le Rhun, G., Zakharov, N. D., Hesse, D., Pintilie, L., & Alexe, M. (2006). Threading dislocations in epitaxial ferroelectric PbZr0.2Ti0.8O3 films and their effect on polarization backswitching. *Philosophical Magazine*, *86*(28), 4477-4486.

[224] Greene, J. E. (2010). Thin film nucleation, growth, and microstructural evolution: an atomic scale view. In *Handbook of deposition technologies for films and coatings* (pp. 554-620). William Andrew Publishing.

[225] Zhang, X. Y., Ong, C. K., Xu, S. Y., & Fang, H. C. (1999). Observation of growth morphology in pulsed-laser deposited barium ferrite thin films. *Applied surface science*, *143*(1-4), 323-327.

[226] Panwar, R., Dhingra, A., & Kumar, D. (2011). Study of thermal stability behavior of MoN & WN thin films in ULSI. *International Journal of Advances in Engineering & Technology*, *1*(3), 55.

[227] Scharf, T., & Krebs, H. U. (2002). Influence of inert gas pressure on deposition rate during pulsed laser deposition. *Applied Physics A*, *75*, 551-554.

[228] Atuchin, V. V., Vinnik, D. A., Gavrilova, T. A., Gudkova, S. A., Isaenko, L. I., Jiang, X., Pokrovsky, L. D., Prosvirin, I. P., Mashkovtseva, L. S., & Lin, Z. (2016). Flux crystal growth and the electronic structure of BaFe12O19 hexaferrite. *The Journal of Physical Chemistry C*, *120*(9), 5114-5123.

[229] Bossak, A. A., Graboy, I. E., Gorbenko, O. Y., Kaul, A. R., Kartavtseva, M. S., Svetchnikov, V. L., & Zandbergen, H. W. (2004). XRD and HREM studies of epitaxially stabilized hexagonal orthoferrites RFeO3 (R= Eu− Lu). *Chemistry of materials*, *16*(9), 1751-1755.

[230] Xu, X., & Wang, W. (2014). Multiferroic hexagonal ferrites (h-RFeO 3, R= Y, Dy-Lu): a brief experimental review. *Modern Physics Letters B*, *28*(21), 1430008.

[231] Jeong, Y. K., Lee, J. H., Ahn, S. J., Song, S. W., Jang, H. M., Choi, H., & Scott, J. F. (2012). Structurally tailored hexagonal ferroelectricity and multiferroism in epitaxial YbFeO3 thin-film heterostructures. *Journal of the American Chemical Society*, *134*(3), 1450-1453.

[232] Han, H., Kim, D., Chu, K., Park, J., Nam, S. Y., Heo, S., Yang, C. H., & Jang, H. M. (2018). Enhanced switchable ferroelectric photovoltaic effects in hexagonal ferrite thin films via strain engineering. *ACS applied materials & interfaces*, *10*(2), 1846-1853.

[233] Fu, Q., Zhuang, N., Hu, X., & Chen, J. (2020). Substrate influence on the structure and properties of YbFeO3 films. *Materials Research Express*, *6*(12), 126120.

[234] Iida, H., Koizumi, T., & Uesu, Y. (2011). Physical properties of new multiferroic hexagonal YbFeO3 thin film. *Phase Transitions*, *84*(9-10), 747-752.

[235] Iida, H., Koizumi, T., Uesu, Y., Kohn, K., Ikeda, N., Mori, S., Haumont, R., Janolin, P. E., Kiat, J. M., Fukunaga, M., & Noda, Y. (2012). Ferroelectricity and ferrimagnetism of hexagonal YbFeO3 thin films. *journal of the physical society of japan*, *81*(2), 024719.

[236] Zhang, X., Yin, Y., Yang, S., Yang, Z., & Xu, X. (2017). Effect of interface on epitaxy and magnetism in h-RFeO3/Fe3O4/Al2O3 films (R= Lu, Yb). *Journal of Physics: Condensed Matter*, *29*(16), 164001.

[237] Uesu, Y., Iida, H., Koizumi, T., Kohn, K., Ikeda, N., Mori, S., Haumont, R., & Kiat, J. M. (2010, August). Multi-ferroicity of thin-film-stabilized hexagonal YbFeO 3. In *2010 IEEE International Symposium on the Applications of Ferroelectrics (ISAF)* (pp. 1-3). IEEE.

[238] Xu, X., Yun, Y., Buragohain, P., Thind, A., Yin, Y., Li, X. Jiang, X., Mishra, R., & Gruverman, A. (2020). Absence of critical thickness in improper ferroelectric hexagonal-YbFeO3 thin films.

[239] Li, X., Yun, Y., Thind, A. S., Yin, Y., Li, Q., Wang, W., N'Diaye, A. T., Mellinger, C., Jiag, X., Mishra, R:, & Xu, X. (2023). Domain-wall magnetoelectric coupling in multiferroic hexagonal YbFeO3 films. *Scientific reports*, *13*(1), 1755.

[240] Kaynig, V., Schindelin, J., Cardona, A., Eglinger, J., Freydiere, P., Funke, J., & Arganda-Carreras, I. (2019, May 13). Weka Trainable Segmentation (Version 3.2.33) [Computer software]. Retrieved April 3, 2020, from https://imagej.net/Trainable_Weka_Segmentation.

[241] Bauer, S., Nergis, B., Jin, X., Horak, L., Schneider, R., Holy, V., Seemann, K., Baumbach, T., Ulrich, S. (2024). Relevance of Platinum Underlayer Crystal Quality for the Microstructure and Magnetic Properties of the Heterostructures YbFeO3/Pt/YSZ(111). *Nanomaterials. 14*(12), 1041.

[242] Bauer, S., Nergis, B., Jin, X., Schneider, R., Wang, D., Kübel, C., Machovec, P., Horak, L., Holy, V., Seemann, K., Baumbach, T., & Ulrich, S. (2024). Dependence of the Structural and Magnetic Properties on the Growth Sequence in Heterostructures Designed by YbFeO3 and BaFe12O19. *Nanomaterials*, *14*(8), 711.

[243] Cao, S., Sinha, K., Zhang, X., Zhang, X., Wang, X., Yin, Y., N'Diaye, A. T., Wang, J., Keavney, J. K., Paudel, T. R., Liu, Y., Cheg, X., Tsymbal, E. Y., Dowben, P. A.,& Xu, X. (2017). Electronic structure and direct observation of ferrimagnetism in multiferroic hexagonal YbFeO 3. *Physical Review B*, *95*(22), 224428.

[244] Sahu, B. N., Suresh, K. G., Venkataramani, N., Prasad, S., & Krishnan, R. (2018). Temperature and field dependent magnetization studies on nano-crystalline ZnFe2O4 thin films. *AIP Advances*, *8*(5).

[245] Joy, P. A., Kumar, P. A., & Date, S. K. (1998). The relationship between field-cooled and zero-field-cooled susceptibilities of some ordered magnetic systems. *Journal of physics: condensed matter*, *10*(48), 11049.

[246] Liang. X, Chen. H, Sun. N.X. (2021). Magnetoelectric materials and devices. *APL Mater*. 9 (4), 41114.

[247] Kumar, A., Kaur. Davinder, (2022) Magnetoelectric heterostructures for next-generation MEMS magnetic field sensing applications., *J. Alloys Compd*.897,163091.

[248] Chen. D., Harward. I., Linderman. K., Economou. E., Nie. Y, Celinski. Z. (2014) Properties of ferroelectric/ferromagnetic thin film heterostructures., *J. Appl. Phys.* 115 (17) 17D713.

[249] Dun. Y., Chen. J., An. D., Chen. D., Chen. Y., Li. Y. (2020). Voltage control of millimeter-wave ferromagnetic resonance in multiferroic heterostructures thin films. *Phys Let A* 384 (26), 126639.

[250] Bodeux. R., Michau. D., Maglione. M., Josse. M. (2016). Thin films sputtered from $Ba_2NdFeNb_4O_{15}$ multiferroic targets on $BaFe_{12}O_{19}$ coated substrates, *Mat. Res. Bull* 81, 49-54.

[251] Hajlaoui. T., Harnagea. C., Pignolet. A. (2023). Magnetoelectric Coupling in Room Temperature Multiferroic $Ba_2EuFeNb_4O_{15}$/$BaFe_{12}O_{19}$ Epitaxial Heterostructures Grown by Laser Ablation. *Nanomaterials* 13, 761.

[252] Srinivasan. G., Zavislyak. I.V., Tatarenko. A.S. (2006). Millimeter-wave magnetoelectric effects in bilayers of barium hexaferrite and lead zirconate titanate, *Appl. Phys. Lett*. 89, 152508.

[253] Srinath. S., Frey. N. A., Heindl. R., Srikanth. H., Coffey. K. R, Dudney. N. J. (2005). Growth and characterization of sputtered BSTO⁄BaM multilayers, *J. Appl. Phys*. 97, 10J115.

[254] Das. J., Kalinikos. B. A., Barman. A. R., Patton. C.E (2007) Multifunctional dual-tunable low loss ferrite-ferroelctric heterostructures for microwave devices. *Appl. Phys. Lett*. 91 (17) 172516.

[255] Das. J., Song. Y. Y., Wu. M. (2010). Electric-field control of ferromagnetic resonance in monolithic $BaFe_{12}O_{19}$–$Ba_{0.5}Sr_{0.5}TiO_3$$BaFe_{12}O_{19}$–$Ba_{0.5}Sr_{0.5}TiO_3$ heterostructures. J. Appl. Phys. 108 (4) 043911.

[256] Zandalazini. C. I., Oliva. M. I., Ferrero. J. C. (2021). Structural and magnetic characterization of $BaTiO_3$–$BaFe_{12}O_{19}$ bilayer thin films: Interface effects on the magnetic properties of barium hexaferrite layer, *Ceramics International*, 47 (14) 19384-19393.

[257] Portugal. R. J., Peko. J-C. M., Hernandes. A. C., Guaran C. A., Guerr J. D. S. (2012). Synthesis and Electrical Properties of PZT/$BaFe_{12}O_{19}$ Multiferroic *Ceramics, Key Engineering Materials* 512, 1291-1295.

[258] Guerra. J. D. S., Pal. M, Portugal. R. J., Cótica. L. F., Santos. I. A., Guo. R., Bhalla A. S. (2013). Multiferroism and magnetoelectric coupling in (PbZr0.65Ti0.35O3)0.97–($BaFe_{12}O_{19}$)0.03 ceramic composites. *J. Appl. Phys.* 114 (22), 224113.

[259] Guerra. J.D.S., McIntosh. R., M′Peko. J. C., Hernandes. A. C., Guo. R., Bhalla. A.S. (2015) Frequency dielectric response of ferroelectric–magnetic ceramic composites like $PbZr_{0.6}5Ti_{0.35}O_3$–$BaFe_{12}O_{19}$, *Ceramics International* 41, 7091 – 7096.

[260] Yun. Y., Buragohain. P., Thind. A. S., Yin. Y., Li. X., Jiang. X., Mishra. R., Gruverman. A., Xu. X. (2022). Spontaneous Polarization in an Ultrathin Improper-Ferroelectric/Dielectric Bilayer in a Capacitor Structure at Cryogenic Temperatures, *Phys. Rev. Appl* 18, 034071.

[261] Vrejoiu. I., Ziese. M., Setzer A., Esquinazi. P. D., Birajdar B. I., Lotnyk A., Alexe M., Hesse D. (2008). Interfacial strain effects in epitaxial multiferroic heterostructures of $PbZr_xTi_{1-x}O_3$/$La_{0.7}Sr_{0.3}MnO_3$PbZr grown by pulsed-laser deposition. *Appl. Phys. Lett.* 92 (15)**,** 152506.

[262] Choi. E. M., Sim. K. I., Burch. K. S, Lee. Y. H. (2022). Emergent Multifunctional Magnetic Proximity in van der Waals Layered Heterostructures. *Adv. Sci*. 9, 2200186.

[263] Huang. H., Zhai. X., Wang. J., Meng. D., Yun. Y., Ma. C., Zheng. X., Wu. L., Pan. H., Fu. Z., Lu Y. (2018) effect of interface defects on the magnetoresistance in Bi4Ti3O12/(La, Sr)Mn1−xO_3 heterostructures, *J Mater Sci* 53, 9627-9634.

[264] Vafaee. M., Finizio. S., Deniz. H., Hesse. D., Zabel. H., Jakob.G., Kläui. M. (2016) The effect of interface roughness on exchange bias in $La_{0.7}Sr_{0.3}MnO_3$–$BiFeO_3$ heterostructures. *Appl. Phys. Lett.* 108 (7)**,** 072401.

[265] Chen. B., Gauquelin. N., Green. R. J., Verbeeck. J., Rijnders. G., Koster. G. (2021) asymmetric cation intermixing, magnetic coupling in $LaMnO_3$/$LaFeO_3$ heterostructures, *Frontiers in Physics* 9, 698154.

[266] Neumann. R. F., Bahiana. M., Binggeli. N. (2012). Magnetic properties of La0.67Sr0.33MnO3/BiFeO3(001) heterojunctions: Chemically abrupt vs. atomic intermixed interface, *Europhysics Letters*, 100, 67002.

[267] Bibes. M., Balcells. Ll., Valencia. S., Fontcuberta. J., Wojcik. M., Jedryka. E., Nadolski. S. (2001). Nanoscale Multiphase Separation at La2/3Ca1/3MnO3/SrTiO3 Interfaces, *Phys. Rev. Lett*. 87, 067210.

[268] Q. Gan. Q., Rao. R. A., Eom. C. B., Garrett. J. L, Lee. M., (1998). Direct measurement of strain effects on magnetic and electrical properties of epitaxial SrRuO3 thin film. *A*ppl. Phys. Lett. 72, 978–980.

[269] Huang. Z., Ariando, Renshaw. X. R., Rusydi. A., Chen. J., Yang. H., Venkatesan. T. (2018) Interface Engineering and Emergent Phenomena in Oxide Heterostructures, *Adv. Mater*. 30, 1802439.

[270] Malozemoff A. P. (1987) Random-field model of exchange anisotropy at rough ferromagnetic-antiferromagnetic interfaces, *Phys. Rev. B* 35, 3679-3682.

[271] Jensen. P. J., Dreyssé. H., Kiwi. M. (2005) Magnetic reordering in the vicinity of a ferromagnetic/antiferromagnetic interface. *Eur. Phys. J. B* 46, 541-551.

[272] Sahoo, S., Polisetty, S., Wang, Y., Mukherjee, T., He, X., Jaswal, S. S., & Binek, C. (2012). Asymmetric magnetoresistance in an exchange bias Co/CoO bilayer. *Journal of Physics: Condensed Matter*, *24*(9), 096002.

[273] Zhu, D. Q., Guo, Z. X., Du, A., Xiong, D. R., Xiao, R., Cai, W. L., Shi, K. W., Peng, S. Z., Cao, K. H., Lu, S. Y., Zhu, D. P., Wang, G. F., Liu, H. X., Leng, Q. W., & Zhao, W. S. (2021, December). First demonstration of three terminal MRAM devices with immunity to magnetic fields and 10 ns field free switching by electrical manipulation of exchange bias. In *2021 IEEE International Electron Devices Meeting (IEDM)* (pp. 17-5). IEEE.

[274] Ranjbar, S., Al-Mahdawi, M., Oogane, M., & Ando, Y. (2020). Controlling domain configuration of the sensing layer for magnetic tunneling junctions by using exchange bias. *AIP Advances*, *10*(2).

[275] Koon. N. C. (1997). calculations of Exchange Bias in Thin Films with Ferromagnetic/Antiferromagnetic Interfaces, *Phys. Rev. Lett*. 78, 4865 – 4868.

[276] Folven. E., Scholl. A., Young. A., Retterer. S. T., Boschker. J. E., Tybell. T., Takamura. Y., Grepstad. J. K. (2012). Crossover from Spin-Flop Coupling to Collinear Spin Alignment in Antiferromagnetic/Ferromagnetic Nanostructures, *Nano Lett*. 12, 2386 – 2390.

[277] Schulthess. T. C., Butler. W. H. (1998). Consequences of Spin-Flop Coupling in Exchange Biased Films, Phys. Rev. Lett. 81, 4516–4519.

[278] Berkowitz A.E., Takano. K. (1999) Exchange anisotropy — a review, J. Magn. Magn. Mater. 200, 552 – 570.

[279] Dong. S., Yamauchi. K., Yunoki. S., Yu. R., Liang. S., Moreo. A., Liu. J. M., Picozzi. S., Dagotto. E. (2009) Exchange Bias Driven by the Dzyaloshinskii-Moriya Interaction and Ferroelectric Polarization at G-Type Antiferromagnetic Perovskite Interfaces, *Phys. Rev. Lett*. 103, 127201.

[280] Zhang. W., Krishnan. K. M. (2016) Epitaxial exchange-bias systems: From fundamentals to future spin-orbitronics, *Mater. Sci. Eng. R.* 105, 1–20.

[281] Olsen. F. K., Hallsteinsen. I., Arenholz. E., Tybell. T., Folven. E. (2019). Coexisting spin-flop coupling and exchange bias in LaFeO3/La0.7Sr0.3MnO3 heterostructures, *Phys. Rev. B*. 99, 134411

[282] Gibert. M., Viret. M., Torres-Pardo. A., Piamonteze. C., Zubko. P., Jaouen. N., Tonnerre. J.M., Mougin. A., Fowlie. J., Catalano. S., Gloter. A., Stéphan. O., Triscone. J. M. (2015). Interfacial Control of Magnetic Properties at LaMnO3/LaNiO3 Interfaces, *Nano Lett*. 15, 7355 – 7361

[283] J. Zehner, I. Soldatov, S. Schneider, R. Heller, N. B. Khojasteh, S. Schiemenz, S. Fähler, K. Nielsch, R. Schäfer, K. Leistner, (2020) Voltage-Controlled Deblocking of Magnetization Reversal in Thin Films by Tunable Domain Wall Interactions and Pinning Sites. *Adv. Electron. Mater.* 6, 2000406.

[284] Obradors, X., Collomb, A., Pernet, M., Samaras, D., & Joubert, J. C. (1985). X-ray analysis of the structural and dynamic properties of BaFe12O19 hexagonal ferrite at room temperature. *Journal of Solid State Chemistry*, *56*(2), 171-181.

[285] Chen. X, Ji. T. Z., Sun. L., Miao. B. F., Millev. Y. T., Ding. H. F. (2019) General nature of the step-induced frustration at ferromagnetic/antiferromagnetic interfaces: topological origin and quantitative understanding, *New J. Phys.* 21, 123045.

[286] Bance. S., Seebacher. B., Schrefl. T., Exl. L., Winklhofer. M., Hrkac, G., Zimanyi. G., Shoji. T., Yano. M., Sakuma N., Ito. M., Kato. A., Manabe. A. (2014). Grain-size dependent demagnetizing factors in permanent magnets, *J. Appl. Phys*. 116, 233903.

[287] Shirk. B. T., Buessem. W. R. (1969) Temperature Dependence of Ms and K1 of $BaFe_{12}O_{19}$ and SrFe12O_{19} Single Crystals *J. Appl. Phys.* 40 1294.

[288] Španková, M., Štrbík, V., Dobročka, E., hromik, Š., Sojková, M., Zheng, D.N., Li, J. (2016) Characterization of epitaxial LSMO thin films with high Curie temperature prepared on different substrates, *Vacuum,* 126, 24 – 28.

[289] Zhang. W., Peng. B., Zhang. W., Zhou. S., Schmidt. H. (2010) Ultra large coercivity in barium ferrite thin films prepared by magnetron sputtering, *J. Magn. Magn. Mater* 322, 1859–1862.

[290] Wang. J, Zhao. F., Wu. W., Zhao. G. M. (2011). Unusual temperature dependence of the magnetic anisotropy constant in barium ferrite $BaFe_{12}O_{19}$, *J. Appl. Phys.* 110, 096107.

[291] Singh. H. K., Mohapatra. P. P., Sahu. S., Dobbidi. P. (2022) Dielectric and temperature dependent magnetic studies of $Al3^{+}$ substituted $Ba_{0.4}La_{0.1}Sr_{0.5}Al_xFe_{12}$-$xO_{19}$ hexaferrite for microwave application, *Mater. Sci. Eng. B.* 284, 115876

[292] Peña-Garcia. R., Guerra. Y., de Souza. F.R., Gonçalves. L.A.P., Padrón-Hernández. E (2018). The extended Bloch's law in yttrium iron garnet doped with Zn, Ni and Co, *Physica. E: Low-Dimensional Systems and Nanostruct*. 103, 354–360,

[293] Anil Kumar, P.S., Joy, P.A., Date, S.K. (2000) Comparison of the irreversible thermomagnetic behaviour of some ferro- and ferrimagnetic systems. *Bull Mater Sci* 23, 97–101.

[294] Platinum - element information, properties and uses: Periodic Table. Platinum - Element information, properties and uses | Periodic Table. (n.d.). https://www.rsc.org/periodic-table/element/78/platinum